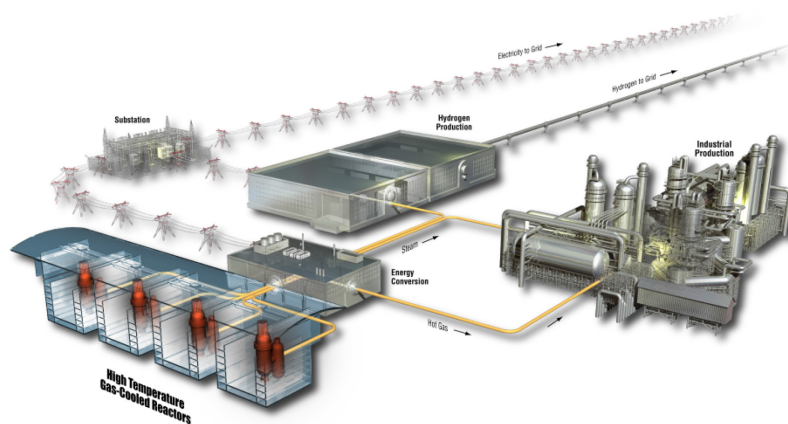# High-Temperature Gas-Cooled Test Reactor Point Design

James W. Sterbentz
Paul D. Bayless
Lee O. Nelson
Hans D. Gougar
Jim C. Kinsey
Gerhard Strydom
Akansha Kumar

April 2016

**INL**
Idaho National
Laboratory

# High-Temperature Gas-Cooled Test Reactor Point Design

**James W. Sterbentz**
**Paul D. Bayless**
**Lee O. Nelson**
**Hans D. Gougar**
**Jim C. Kinsey**
**Gerhard Strydom**
**Akansha Kumar**

**April 2016**

**Idaho National Laboratory**
**INL ART TDO Program**
**Idaho Falls, Idaho 83415**

**http://www.inl.gov**

**INL ART TDO Program**


# High-Temperature Gas-Cooled Test Reactor Point Design
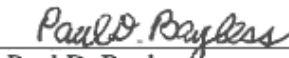
**INL/EXT-16-38296**


**April 2016**


Authors:
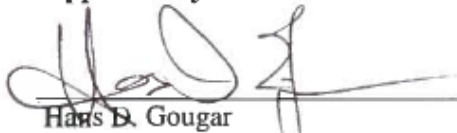
_James W. Sterbentz_      April 8, 2016

James W. Sterbentz               Date
INL ART TDO Nuclear Engineer

_Paul D. Bayless_            4/11/16

Paul D. Bayless                Date
INL ART TDO Nuclear Engineer


Approved by:

                  4/11/16

Hans D. Gougar                Date
INL ART TDO Deputy Technical Director

                  4/11/16

Michelle T. Sharp             Date
INL ART TDO Quality Assurance

# ABSTRACT

A point design has been developed for a 200-MW, high-temperature, gas-cooled test reactor. The point design concept uses standard prismatic blocks and 15.5% enriched uranium oxycarbide fuel. Reactor physics and thermal-hydraulics simulations have been performed to characterize the capabilities of the design. In addition to the technical data, overviews are provided on the technological readiness level, licensing approach, and costs.

# EXECUTIVE SUMMARY

A point design for a graphite-moderated, high-temperature, gas-cooled test reactor (HTGTR) has been developed by Idaho National Laboratory (INL) as part of a United States (U.S.) Department of Energy (DOE) initiative to explore and potentially expand the existing U.S. test reactor capability. This report provides an initial summary description of the design and its main attributes. Although there are no high-temperature, gas-cooled reactors (HTGRs) operating today in the U.S., the design of the HTGTR has leveraged design information and experience from both previously-constructed and -operated commercial U.S. HTGRs and more modern HTGR designs with annular cores. In addition, the HTGTR has drawn heavily on recent advancements in tristructural isotropic (TRISO) particle fuel, graphite, and in-core HTGR materials from the very successful DOE Advanced Gas Reactor Program and the associated U.S. Nuclear Regulatory Commission (NRC) interactions. These advancements, along with recent and past HTGR technology, have been incorporated into the design of the HTGTR.

The HTGTR core is composed of hexagonal prismatic fuel blocks and graphite reflector blocks. Figure ES-1 shows a cross section of the reactor vessel and core. Twelve fuel columns (96 fuel blocks total) are arranged in two hexagonal rings (Rings 2 and 3) to form a relatively compact, high-power density, annular core sandwiched between inner, outer, top, and bottom graphite reflectors. The fuel columns are eight blocks high. TRISO particle fuel from the DOE Advanced Gas Reactor Program has been adopted with the larger 425-μm uranium oxycarbide kernel with an enrichment of 15.5-wt% $^{235}$U. The reactor power is 200 MW and has a power cycle length of 110 days. Assuming a 4-week shutdown time between cycles, it also has an availability factor of 80%.
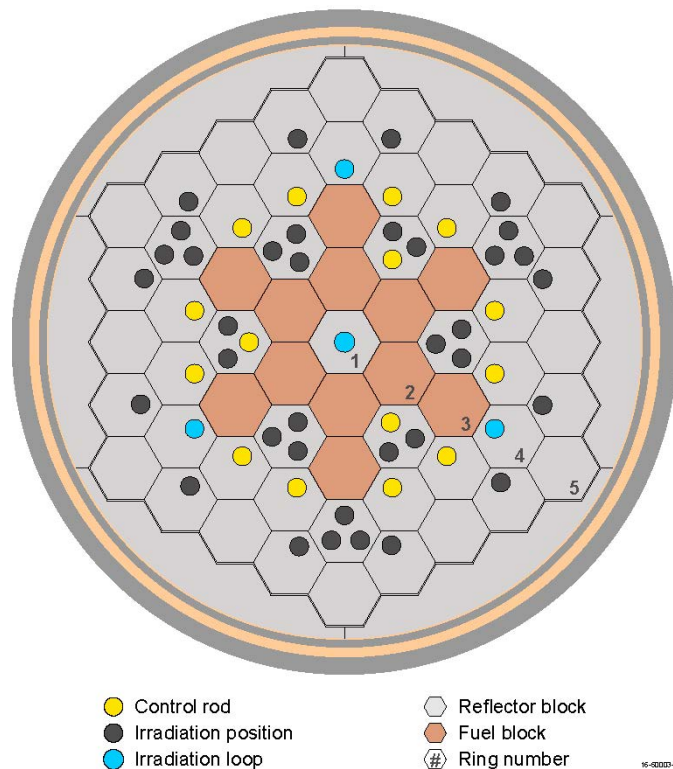


Figure ES-1. Reactor vessel cross section in the core region.

The HTGTR is predominantly a thermal-neutron spectrum reactor with a sizable graphite pile cooled by helium gas. The highest thermal-neutron flux occurs in the outer reflector (Ring 3). High fast-flux irradiation levels are more difficult to achieve. The maximum fast-flux levels are produced in the annular core; however, because of high temperature concerns in the high-power density core under accident

conditions, all irradiation test facilities have been initially located in the inner and outer reflectors where fast neutrons are moderated and fast-flux levels decline. Fast flux can be enhanced in the central reflector column (Ring 1) with the removal of graphite from the column blocks; this is where the maximum fast flux occurs.

The core features a large number of irradiation positions with large test volumes and long test lengths, which is ideal for thermal-neutron irradiation of large test articles (e.g., full length partial fuel rod assemblies and composite reactor structures and components). Up to four test loop facilities can be accommodated with pressure tube boundaries to isolate test articles and test fluids from the primary helium coolant system. One of these test loop facilities is located in the center of the core (Ring 1) and has a maximum thermal and fast flux of 1.61E+14 n/cm$^2$/s and 1.17E+14 n/cm$^2$/s (E$_n$>0.18 MeV), respectively. The three other loop facilities can be located in the outer reflector (Ring 4) with a maximum thermal and fast flux of 2.82E+14 n/cm$^2$/s and 2.28E+13 n/cm$^2$/s (E$_n$>0.18 MeV). The in-core loop facilities have test volumes of about 14 L.

It is expected that one of these loop locations in the outer reflector would contain a pneumatically-driven rabbit system. The core can also accommodate at least 36 irradiation positions for drop-in test capsules in the outer graphite reflector. In Ring 3 these positions have a maximum thermal and fast flux of 3.90E+14 n/cm$^2$/s and 5.24E+13 n/cm$^2$/s, respectively. All test positions can be the full length of the active core (6.34 m), and the Ring 3 and 4 positions could be up to 16 cm in diameter. The 8-cm-diameter irradiation positions shown in Figure ES-1 each have a test volume of 30 L, resulting in a total test volume over 1100 L. The positions shown in Figure ES-1 are just one example of a possible configuration; larger or smaller diameter facilities could be accommodated without much difficulty.

A modern commercial HTGR will operate at relatively high gas pressure (7 MPa) and high outlet gas temperature (750–850ºC). The point design HTGTR is also designed to operate at 7 MPa, but at a lower outlet gas temperature (650°C). The lower outlet temperature was selected to ensure sufficient thermal margin under normal operating conditions to prevent melting of metallic in-pile tubes during accident conditions. Penetration of the top-head reactor pressure vessel boundary by both control rod guide tubes and loop pressure tubes could potentially result in top-head crowding. Future engineering assessments will need to consider possible crowding issues and penetration design and maintenance of the pressure boundary integrity due to frequent loading and unloading of fuel and experiments.

The primary mission of the HTGTR is material irradiation; therefore the core has been specifically designed and optimized to provide the highest possible thermal and fast neutron fluxes. A helium-cooled test reactor can support independent irradiation loops that contain a variety of coolant fluids (e.g., liquid metal, liquid salt, light water, and other gases or steam). Power levels and coolant conditions are such that it can serve as a test bed supporting developments in high-efficiency electricity production (steam and Brayton cycle) and process heat-driven energy products, including hydrogen. Other secondary missions such as isotope production can also be supported. The range of temperatures and test loop coolants afforded by the HTGTR would be most useful to molten salt and gas-cooled reactor developers. Loop experiments for investigating fuel, material, and coolant interactions in a radiation field are supported by only a few facilities in the U.S. and around the world. Because of the large volumes within the multiple loop positions, advanced water-cooled reactor fuels can also be tested. Much of the customer base of INL's Advanced Test Reactor could be served by the HTGTR, with half-sized or even full-sized fuel assemblies for smaller light water reactor (LWR) concepts (such as NuScale) being accommodated.

The use of a HTGR with materials irradiation as its *primary* mission is unprecedented, and thus the engineered systems used to support irradiations in past and current test reactors would have to be modified or even designed from scratch to be compatible with the geometry and pressure of the HTGR. The associated challenges and mitigating strategies are enumerated and described in *Design Attributes and Considerations for a Gas-Cooled Graphite Moderated Irradiation Test Reactor* (Mayer, Lommers, and Shahrikhi 2016), a study performed by AREVA, Inc. in support of this point design.

The HTGTR has strong negative fuel and moderator temperature coefficients. Under normal critical operation and over the entire power cycle length, the reactor will operate safely because of the strong negative temperature feedback and the high-thermal inertia of the graphite. One aspect of reactor control that was not considered in the design is the use of burnable poisons. Burnable poisons will eventually play an important role in holding down the initial core excess reactivity over the 110-day power cycle and in flattening the power profile. Because the primary performance goal in this study was to maximize the irradiation flux, optimization of the burnable poison loading was omitted, but it will be required in the next design phase. Axial and radial placement of the burnable poison rods ($B_4C$) in the fuel columns will need to be done judiciously to minimize any effect on the flux profiles in the irradiation spaces. Once burnable poisons are incorporated into the reactor design, the movable control rod pattern can be adjusted to optimize core performance.

The reactor design is passively safe and peak fuel temperatures during design-basis conduction cooldown (loss of forced cooling) accidents are below the steady-state operating temperatures and well below safety limits. Long-term decay heat removal is provided by a natural-circulation driven, water-cooled system such that no energized systems are required. Heat is transferred from the reactor vessel to the cooling system by passive radiation and natural convection mechanisms.

The large irradiation volumes and long (110-day) cycle length, plus the competitive thermal neutron irradiation flux and large operational safety margins are the main strengths of the HTGTR. This translates into greater flexibility for a variety of irradiation experiments and test materials. Another potential strength is the possibility to increase the cycle length. Although the HTGTR meets the 90-day metric criterion, a much longer cycle length can readily be achieved with simple increases in the TRISO particle packing fraction (up to 280 days with a packing fraction of 35%). Longer irradiations can potentially accumulate fluence faster with fewer reactor shutdowns, despite a slightly reduced flux.

As part of the overall Advanced Test/Demonstration Reactor Options Study, an assessment of the maturity of Generation IV reactor technologies was conducted by a multi-laboratory panel of experts. A technology readiness scale developed by DOE was used to evaluate the HTGTR system. For the HTGR, the lowest technical maturity scores were assigned to certain metallic components inside the pressure vessel. When exposed to core conditions under accident conditions, these may be subjected to failure. If coolant temperatures are limited to 850°C, SA508/533 (the steel alloy used in LWRs) is adequate for the pressure vessel. For the most severe loss-of-forced-cooling events, significant fuel particle degradation is not expected, although some metallic components in the core region (such as control rod guide tubes) may need to be replaced. Qualification of new alloys or use of carbon or silicon carbide composites for the guide tubes may be beneficial. For these reasons, the reactor enclosure subsystem for the demonstration plant was assigned a technology readiness level of 5. The overall conclusion of the panel was that the HTGR, with outlet temperatures limited to 850°C, is suitable for near-term deployment as either a test or demonstration reactor.

The capital, operating, and decommissioning costs for the HTGTR are based on information presented in the *Next Generation Nuclear Plant (NGNP) Pre-Conceptual Design Report* for a 350-MW first-of-a-kind reactor with a single reactor module (INL 2007). The costs include indirect costs and contingencies. The detailed cost model used for this cost estimate was developed as part of the NGNP Project using data from three vendors. The total capital cost for an HTGR is comprised of the following cost categories: preconstruction costs, direct costs, indirect costs, and project contingency. Operating costs include staffing requirements, annual fees, insurance, taxes, material supplies, outage costs, and administration and general cost overhead. The total capital investment required to build a 200-MW HTGTR is estimated at $3,942 million, within a −50% and +50% uncertainty range of $1,971–5,913 million.

The HTGTR aligns with the NRC's definition of a Test Facility, as found in 10 CFR 50.2. Test reactors are one of the non-power reactors that the NRC licenses under the authority of Subsection 104c

of the Atomic Energy Act and issues "Class 104c" licenses. Congress directed the NRC to impose the minimum amount of regulation on Subsection 104(c) research reactor and test reactor licensees. In keeping with this direction, the NRC staff utilizes NUREG-1537 as the primary guidance for review of research reactors and test reactor technologies and license applications. DOE and NRC established a joint initiative in July 2013 to develop guidance for advanced reactor developers and other stakeholders on how the existing general design criteria reflected in 10 CFR 50, Appendix A, can be adapted to non-LWRs. A proposed set of general design criteria adaptations specific to modular HTGRs was developed by a DOE/national laboratory team and submitted to NRC for review in December 2014.

A self-assessment has been performed on the HTGTR scoring against the DOE-developed criteria. This self-assessment is presented in Appendix A of this document and shows that the HTGTR scores 76%.

# CONTENTS

# FIGURES

# TABLES

# ACRONYMS

AGR          Advanced Gas Reactor

ART          Advanced Reactor Technologies

ATR          Advanced Test Reactor

BOC          beginning-of-cycle

CP          construction permit

DCC          depressurized conduction cooldown

DOE          Department of Energy

EFPD          effective full-power day

FHM          fuel handling machine

FIMA          fissions of initial heavy metal atoms

FOAK          first-of-a-kind

FSV          Fort St. Vrain

GA          General Atomics

HFIR          High-Flux Isotope Reactor

HTGR          high-temperature, gas-cooled reactor

HTGTR          high-temperature, gas-cooled test reactor

HTR          high-temperature reactor

INL          Idaho National Laboratory

LWR          light water reactor

MHTGR          modular high-temperature, gas-cooled reactor

NA          not applicable

NGNP          Next Generation Nuclear Plant

NRC          Nuclear Regulatory Commission

O&M          operations and maintenance

PCC          pressurized conduction cooldown

PF          packing fraction

PSR          permanent side reflector

R&D          research and development

RCCS          reactor cavity cooling system

SAR          safety analysis report

TEDE          total effective dose equivalent

TRISO          tristructural isotropic

| | |
|---|---|
| TRL | technology readiness level |
| UCO | uranium oxycarbide |
| U.S. | United States |

# High-Temperature Gas-Cooled Test Reactor Point Design

## 1.  Introduction

A point design for a graphite-moderated, high-temperature, gas-cooled test reactor (HTGTR) has been developed by Idaho National Laboratory (INL) as part of a United States (U.S.) Department of Energy (DOE) initiative to explore and potentially expand the existing U.S. test reactor capability. This report provides an initial summary description of the design and its main attributes. Although there are no high-temperature, gas-cooled reactors (HTGRs) operating today in the U.S., the design of the HTGTR has leveraged design information and experience from both previously-constructed and -operated commercial U.S. HTGRs and more modern HTGR designs with annular cores. In addition, the HTGTR has drawn heavily on recent advancements in tristructural isotropic (TRISO) particle fuel, graphite, and in-core HTGR materials from the very successful DOE Advanced Gas Reactor (AGR) Program and the associated U.S. Nuclear Regulatory Commission (NRC) interactions. These advancements, along with recent and past HTGR technology, have been incorporated into the design of the HTGTR.

The design accommodates independently-cooled irradiation positions (loops) in the central and outer reflectors that can contain different working fluids, such as high-pressure water, liquid metal, or molten salt. The graphite reflector can also accommodate a large number of non-loop irradiation holes for "drop-in" capsule experiments that are cooled by helium. Reactor physics and thermal-hydraulic analyses have been performed to provide quantitative estimates of the reactor's capabilities.

The rationale behind the selected design is provided in Chapter 2. Chapters 3 and 4 describe the reactor design and safety basis, respectively. Details of the reactor physics and thermal hydraulics investigations are provided in these chapters. Chapter 5 addresses technology readiness, Chapter 6 licensing, development, and deployment aspects, and Chapter 7 costs and schedule. References are listed in Chapter 8. A self-assessment against the design criteria is provided in Appendix A. Appendix B contains descriptions of the reactor physics and thermal-hydraulics computer models used in the analyses. Descriptions of earlier scoping analyses that led to this core configuration are provided in Appendix C. Sterbentz et al. (2016) provides a summarized version of the information presented in this report, focusing on the final core design configuration.

# 2. Objectives and Motivation for Concept Selection

The primary objective of the HTGTR design was to provide a versatile, multi-purpose, high flux facility for advanced reactor fuels and materials irradiations. Currently, this capability in the U.S. is provided mainly by the High-Flux Isotope Reactor (HFIR) at Oak Ridge National Laboratory and the Advanced Test Reactor (ATR) at INL. HFIR and ATR are both light water reactors (LWRs) with over 40 years of safe and reliable operating and irradiation experience. Table 2-1 provides a comparison of pertinent test positions and reactor data for HFIR, ATR, and the HTGTR design.

Table 2-1. Comparison of irradiation characteristics of HFIR, ATR, and HTGTR.

| Reactor | Test Position | Test Position Diameter (cm) | Test Position Length (cm) | Peak Thermal Flux (n/cm$^2$/s) | Peak Fast Flux (n/cm$^2$/s) | Core Power (MW) | Core Power Density (W/cm$^3$) | Cycle Length (days) |
|---------|---------------|------------------------------|----------------------------|---------------------------------|------------------------------|------------------|-------------------------------|----------------------|
| HFIR | Permanent beryllium reflector | 3.8–7.6 | 50.8 | 2-10E+14 | ≤1.5E+14 ($E_n$>0.111 MeV) | 85 | 1251 | 23 |
| ATR | Flux trap | 13.3 | 121.9 | 4.4E+14 | 2.2E+14 ($E_n$>0.1 MeV) | 110$^a$ | 116 | 30–60 |
| HTGTR | Graphite reflector | ≤16.0 | 640.0 | 3.9E+14 | 1.2E+14 ($E_n$>0.18 MeV) | 200 | 23 | 110 |
| a. This is a more typical ATR cycle power than the rated power of 250 MW. | | | | | | | | |

Flux levels in the HTGTR are below those of HFIR and ATR, but they are not substantially lower despite the large differences in core power density. Note that in the HFIR center flux trap the thermal flux is much higher, with an average 2.35E+15; these super-high flux positions are usually reserved for isotope production ($^{252}$Cf). The 110-day power cycle length of the HTGTR is substantially longer than the 23-day HFIR cycle and 30- to 60-day ATR cycles. Furthermore, the product of the flux and irradiation time and relatively large number of test positions and large test volumes available in the HTGTR help increase the usefulness of the HTGTR relative to HFIR and ATR in terms of irradiation sample throughput. The main irradiation spaces are large enough to accommodate (in loops) full-length partial fuel assemblies from an LWR, fast reactor, or fluoride salt-cooled reactor.

Another very important and useful feature of the HTGTR is the chemical compatibility with a wide variety of loop and target materials, including fuel, structural materials, and loop coolant fluids. The center loop can be filled with liquid salt (e.g., FLiBe), liquid metal (sodium), high-pressure and high-temperature light water or steam, or other primary coolant gases and the change in loop coolants is estimated to have a small or minimal reactivity impact on the relatively large HTGR core.

Other useful features of the HTGTR include the ability to generate electricity and produce isotopes. The electricity could be sold to a local utility for revenue and any surplus could be supplied to the national laboratory reactor site. Production of commercial isotopes could also generate substantial revenue by employing the huge 'drop-in' test volume space available in the reflector regions. Other secondary missions, such as hydrogen production and process heat testing, may be the most important, especially for U.S. energy security research and development (R&D). Secondary heat transfer loops could be connected via state-of-the-art heat exchangers to provide prototypical conditions for liquid salt and light water secondary loop coolants.

# 3. Design Description

The point design effort has been focused on the core and reactor vessel behavior. Results of the reactor physics and core thermal-hydraulic evaluations are provided, followed by a brief discussion of the ex-vessel systems.

Figure 3-1 shows a cross section of the reactor vessel and core. The size and location of the irradiation positions in the figure illustrate one possible configuration. The graphite blocks could accommodate larger or smaller holes, providing a versatile and variable core configuration, because the irradiation positions could be changed with each operating cycle if desired. Conversely, the locations of the irradiation loops are fixed.
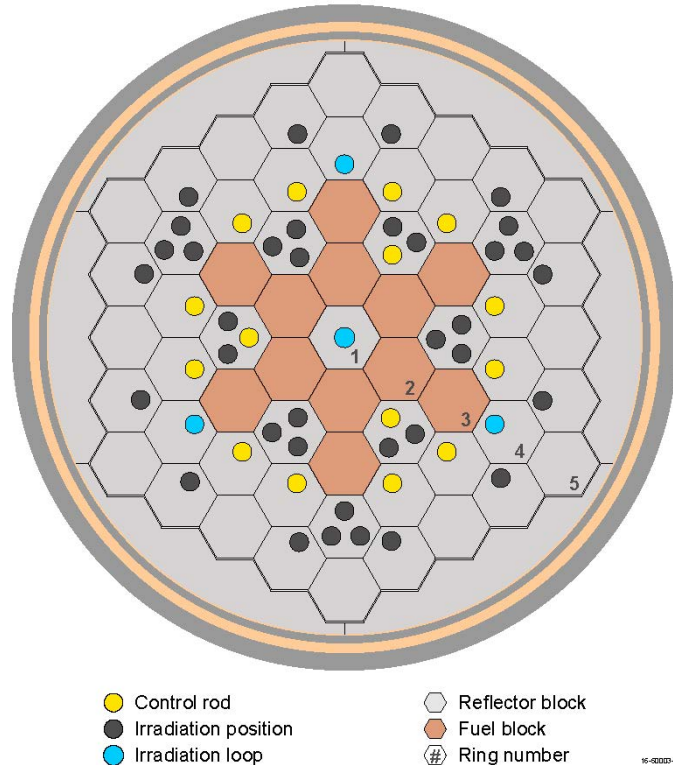


Figure 3-1. Reactor vessel cross section in the core region.

The primary coolant system consists of the reactor vessel, a concentric duct or pipe containing the hot vessel outlet flow in the center with the cooler inlet flow on the outside, a steam generator, and a gas circulator to provide the forced convection flow through the loop. Given the primary coolant system operating temperatures, superheated steam will be exiting the steam generator. A portion of this could be used for electricity generation, some for process heat, and some or all of the heat rejected to atmosphere. If desired, an intermediate heat exchanger could be installed in parallel with the steam generator, so that process heat could be provided as well.

Coolant flow enters near the bottom of the reactor vessel cylinder, flows up through the annulus between the core barrel and reactor vessel, and enters the upper plenum. Helium then flows down through a number of parallel channels in the core: the coolant holes in the fuel blocks, the gaps between the hexagonal blocks, the gap between the permanent side reflector (PSR) and the core barrel, and gaps between the graphite reflector blocks and the control rods or irradiation tubes. These flow paths all meet in the lower plenum, from which the coolant exits the reactor vessel.

The core consists of a central graphite reflector block (Ring 1) with an irradiation loop facility located in the center. Moving radially, the next ring contains fuel blocks, and Ring 3 contains six fuel blocks and six reflector blocks. Three of these reflector blocks contain control rods, and all six of them have irradiation positions. The first ring of the side reflector contains holes for 12 control rods, three irradiation loops, and nine irradiation tubes. Ring 5 has side reflector blocks containing some irradiation tubes, and is surrounded by the PSR and the core barrel. The nominal core power is 200 MW. The core is eight blocks high, with top and bottom reflectors of 1.189 and 1.585 m, respectively. Standard gas-reactor components are used. The fuel is 15.5% enriched uranium oxycarbide (UCO). The fuel blocks are the typical General Atomics (GA) design (DOE 1986), containing 210 fuel rods and 108 coolant holes in a 0.793-m high, 0.360-m wide hexagonal graphite block.

The irradiation loops are designed to allow different coolants to be used, including water, sodium, molten salts, or gas. An experiment well is connected to the reactor vessel upper head, providing the pressure boundary for the primary coolant system. The in-vessel portion of the experiment loop with its own pressure boundary would be lowered into this well. A helium cooling flow would be provided between the outside of the experiment loop facility and the inside of the experiment well. One of the loop locations could house a pneumatically-driven rabbit system to allow insertion and removal of experiments while the reactor is operating.

The irradiation positions are flow-through tubes cooled by primary coolant, designed for "drop-in" capsule experiments. A long tube of a high melting point material, such as titanium, molybdenum, or zirconium, is placed in the hole and is open at both the top and bottom. The experiment hardware would be inserted into the tube.

A simple model of a cavity cooling system has also been developed to allow scoping accident calculations to be performed. Water at 27°C flows through cooling panels that completely surround the reactor vessel, driven by natural circulation from a large overhead tank from which heat can be rejected to the atmosphere.

Details of the reactor physics and thermal hydraulics investigations are provided in the subsections that follow. These analyses also address different core heights and powers.

## 3.1   Neutronic Conditions

The HTGTR point design uses TRISO particle fuel in the form of fuel compacts loaded into prismatic fuel blocks with both fuel and coolant channels. The prismatic fuel blocks are based on a GA design (DOE 1986) that was used at Fort St. Vrain (FSV) (Figure 3-2). This block design offers great flexibility in enrichment zoning, particle packing fraction (PF) zoning, placement of burnable poison rods, and cooling. Figure 3-3 shows a detailed computer model rendering of the FSV fuel block used in the test reactor physics analysis. Optimization of the fuel block dimensions, fuel rod pitch, fuel rod diameter, and number of fuel and coolant channels remains for future work.

The TRISO particles matrixed in cylindrical fuel compacts form an integral high-temperature ceramic system specifically designed for the Next Generation Nuclear Plant (NGNP) HTGR commercial reactors. The same TRISO fuel is used for the HTGTR. Recent irradiation testing of TRISO fuel in the DOE AGR Program has demonstrated the robustness and high performance of the fuel under high temperature (1300°C), burnup (20% fissions of initial heavy metal atoms [FIMA]), and fast fluence (5.5E+21 n/cm$^2$) conditions. The tests have been very successful, with no fuel particle degradation in most cases. The AGR-1, AGR-2, and AGR-3/4 irradiation tests have included a variety of particle designs that have provided substantial particle performance data. The specific TRISO particle design adopted for the HTGTR is based on the AGR-5/6/7 qualification test particle design that features a large 425-μm-diameter $UC_{0.5}O_{1.5}$ kernel, 15.5-wt% enrichment, and PF=25 or 38%.
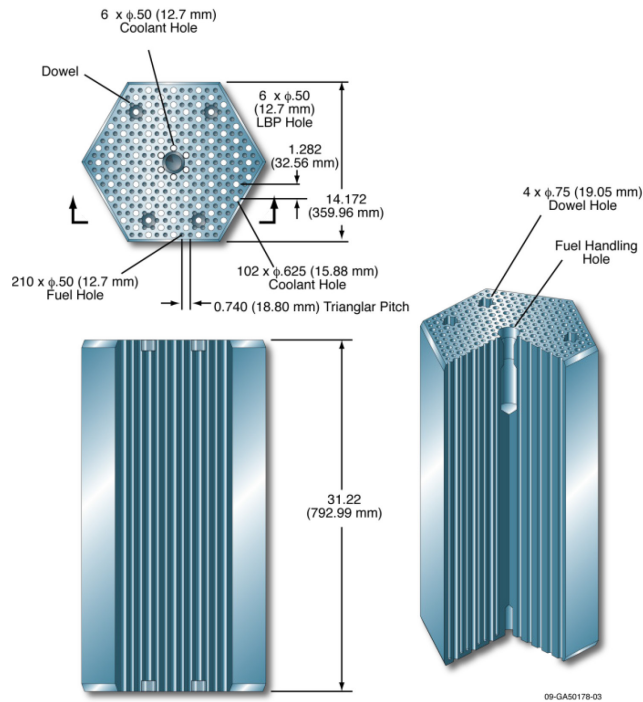
Figure 3-2. FSV fuel block.
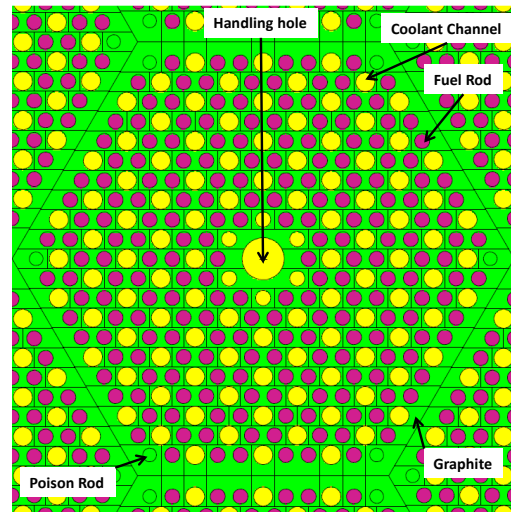


Figure 3-3. Fuel block model.

However, compacts for the HTGTR will have a much lower particle PF (15%) to boost the irradiation fluxes. The following list contains four relatively recent and notable particle and compact design improvements:

- The larger kernel diameter (425 versus 350 μm)

- Higher UCO density (11.04 versus 10.40 g/cm$^3$)

- Higher graphite binder density (1.70 versus 1.2 g/cm$^3$)

- Higher bulk graphite density (1.83 versus 1.74 g/cm$^3$).

These improvements boost HTGR core reactivity.

The test reactor core configuration (baseline) is shown in Figure 3-1 and features the following characteristics:

- Prismatic hexagonal fuel and graphite reflector blocks

- High-leakage annular core

- Block pitch of 36 cm

- Five-ring core: Ring 1 (inner reflector), Rings 2 and 3 (annular core), Rings 4 and 5 (outer reflector)

- 12 fuel columns

- Eight fuel blocks per column

- 210 fuel and 108 coolant channels per fuel block

- Core height of 9.2 m with an active height of 6.4 m

- Core diameter of 3.4 m

- 200 MW thermal power.

The baseline point design is similar in many respects to modern commercial HTGRs. Both are large graphite piles with annular, high-leakage cores formed by prismatic fuel and graphite hexagonal blocks. The helium coolant, pressure, temperature, down flow, and flow path through the pressure vessel are essentially the same. Both have inner, outer, top, and bottom graphite reflectors. The HTGTR core configuration, however, diverges from the much larger commercial reactor in the number of fuel blocks and power as the test reactor mission changes to include material irradiation. To boost irradiation flux in the outer reflectors where the irradiation test facilities are located, the test reactor core size is reduced to increase core power density (20–25 W/cm$^3$). Commercial HTGRs typically operate at much lower core power densities (6–8 W/cm$^3$).

The HTGTR fueled core is an annular core sandwiched between inner and outer graphite reflectors. The annular core has only 12 fuel columns: six in Ring 2 and six more in Ring 3, where the fuel blocks alternate with graphite blocks around Ring 3 (Figure 3-1). Each fuel column is eight fuel blocks high. Modern commercial cores can have up to 102 fuel columns and are 10 blocks high. Three of the six graphite block columns in Ring 3 contain control rods; the other three have irradiation test positions. These three test positions have the highest thermal flux in the core (3.90E+14 n/cm$^2$/s). The 18 columns of Ring 4 are all graphite block columns: 12 with control rods and the other six with additional irradiation test positions. Rings 4 and 5 are the outer graphite reflector. Beyond Ring 5 is the PSR, which contains graphite blocks to form-fit the core barrel. The core is approximately 3.4 m in diameter and 9.2 m in total height. The total core thermal power is 200 MW.

There are a total of 15 control rods in the outer reflector (Figure 3-1). The combined worth of these rods is approximately −$50, enough negative reactivity to shut the core down under both hot and cold conditions. Sufficient margin exists for shutdown, even if two or three rods are stuck out. The introduction of burnable poisons, irradiation tubes, and other in-core hardware will also introduce negative core reactivity and enhance the control rod shutdown margin.

Control rod and loop penetrations through the top head of the reactor pressure vessel may compete for the limited room available in the HTGTR head region. An engineering assessment of the number, location, and diameters of tube penetrations will need to be part of the conceptual design phase. The current HTGTR design with its compact core configuration specifically located the control rods in the outer reflector to address this potential problem. The key reactor parameters are summarized in Table 3-1.

Table 3-1. Key reactor parameters.

| Reactor thermal power | 200 MW |
|---|---|
| Primary coolant | Helium gas |
| Primary coolant system pressure | 7.0 MPa |
| Core pressure drop for normal operation | 192 kPa |
| Primary coolant flow rate | 117.3 kg/s |
| Core inlet temperature | 325°C |
| Core outlet temperature | 650°C |
| Number of primary coolant loops | 1 |
| Fuel format | Prismatic block with coolant channels and fuel rods (compacts) |
| Fuel columns | 12 |

Table 3-1. (continued).

| | |
|---|---|
| Fuel blocks per column | 8 |
| Fuel blocks per core | 96 |
| Fuel type | $UC_{0.5}O_{1.5}$ TRISO-coated particle |
| Fuel PF | 15.0% |
| $^{235}U$ enrichment | 15.5 wt% |
| Average core power density | 23.4 W/cm$^3$ |
| Power cycle length | 110 days |
| Fuel cycle mode | Single batch |
| Reflector material | Graphite |
| Reactor vessel internals material | • Alloy 800H (control rod sheath)<br>• Stainless-steel 316L (irradiation loop pressure tube)<br>• Molybdenum, zirconium, and/or titanium (irradiation tubes in outer reflector) |
| Core structural material | Graphite |
| Control rod material | • B$_4$C in graphite<br>• Boron-10 enrichment 30–50% |
| Vessel material | Steel |
| Core fueled height | 6.4 m |
| Core outer diameter | 3.4 m |
| Core total height | 9.2 m |

## 3.2    Reactor Physics

The proposed test reactor design shown in Figure 3-1 represents the initial optimization and an evolved design derived from coupled physics and thermal hydraulic evaluations; it is based on results from five different core configurations. The five core configurations considered annular core configurations of 6, 7, 12, or 18 fuel columns, all in Rings 1, 2, and 3 only for compactness. (Appendix C contains more detailed descriptions of the five configurations.) Allowing fuel columns in Ring 4 would have required an additional outer reflector ring of 30 graphite columns, plus more PSR blocks. This would also increase the core and pressure vessel diameter by 0.72 m. Because the top priority for the physics evaluations was maximization of the thermal flux in the inner and outer reflector block test positions, keeping the annular core as small as possible to boost core power density was the main focus. Higher power density translates into higher fluxes and a smaller core with fewer fuel blocks meant fewer fuel blocks to reload each cycle.

In the physics analyses, there were six primary design variables:

- Core power (50–250 MW)
- Particle PF (5–50%)
- Power cycle length
- Arrangement of fuel columns in core
- Number of fuel columns (6, 7, 12, and 18)
- Number of fuel blocks in a fuel column (4, 5, 6, 7, and 8).

Some design variables were fixed. While these fixed variables simplified the design analyses, it left open the possibility for a more optimized test reactor for future designs. The fixed design variables included the following:

- FSV fuel block design
- Single 15.5% enrichment
- AGR-5/6/7 particle design.

There were also the following TRISO particle fuel and thermal hydraulic limits that had to be considered:

- Particle power (<400 mW)
- Compact burnups (<20% FIMA)
- Compact fast fluence (<5.5E+21 n/cm$^2$ at $E_n$>0.18 MeV)
- Fuel rod power-peaking (<2.0 peak-to-average)
- Peak fuel temperature (1250°C) during normal steady-state operations
- Peak fuel temperature (within the AGR time-at-temperature envelope) under accident conditions.

The following assumptions were also made in the physics evaluations:

- Uniform core PF
- Un-rodded core
- No burnable poison rods
- Compact fuel radius of 0.6225 cm
- Homogenized compacts.

The combination of design variables, fixed-value variables, and limitations resulted in a complex interplay between the design variables, where some variables were diametrically opposed to one another and others were closely aligned. In all cases, variable ranges were restricted by the fuel and thermal-hydraulic limitations.

## 3.2.1    General Physics Design Characteristics

To achieve the goal of the highest possible thermal-neutron irradiation flux, several variables needed to be maximized or minimized. These included maximization of the total core power, minimization of the particle PF (Figure 3-4), and reduction of the number of fuel blocks in the core either through a reduced number of fuel columns and/or by a reduced height of the fuel columns (number of stacked fuel blocks). Arrangement of the maximum number of fuel blocks around a reflector block with an irradiation position enhanced the local thermal flux. All of these factors helped increase the core power density and thermal-neutron irradiation fluxes. Core power density had a limit, however. Excessive power densities stress the TRISO particle fuel through excessive power output (>400 mW per particle) and time-at-temperature (>1250°C). High power density also leads to excessive $^{235}$U fuel burnup rates and shorter power cycle lengths. The test reactor design attempted to maximize the power density while observing the fuel and the temperature limitations and cycle length goals.

The final optimal core configuration or fuel column arrangement and number of fuel columns is shown in Figure 3-1. The design balances core power, particle PF, particle power, fuel temperature, and cycle length. The result is a 12-fuel column, 8-block-high core configuration, uniform particle PF=15%,

and a total core power of 200 MW. A single-batch core load can sustain a 110-day power cycle length. Calculated results for these design parameters are presented in the following subsections.

## 3.2.2    Calculated Physics Results

The neutronic calculations used the Monte Carlo N-Particle 5 Version 1.60 computer code (X-5 Monte Carlo Team 2003) and INL-developed depletion methods and software. Detailed Monte Carlo N-Particle core models were developed based on the GA FSV fuel block design and the baseline core configuration depicted in Figure 3-1. The calculated results are specifically for the core configuration in Figure 3-1 at 200 MW, particle PF=15%, and 8-block-high fuel columns with no burnable poisons, enrichment grading, PF grading, or control rod insertion (except in the section on control rod worth).
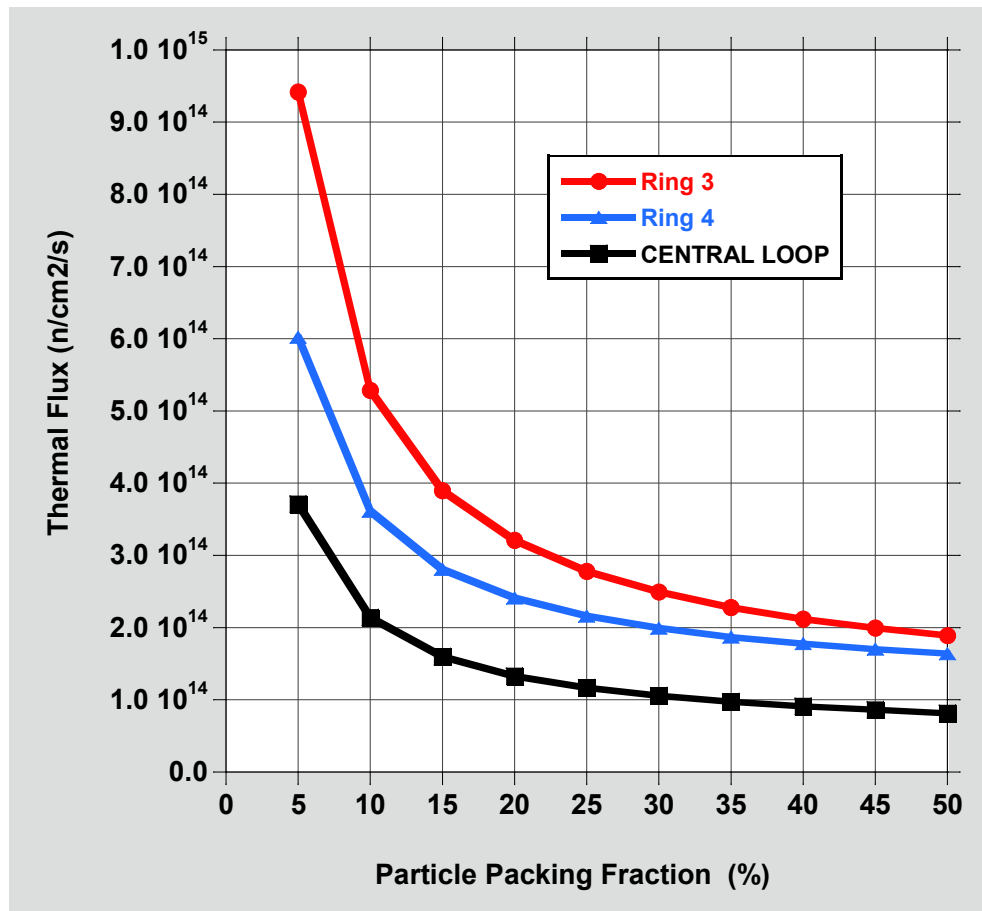


Figure 3-4. Thermal flux versus packing fraction.

***3.2.2.1    Maximum Irradiation Flux.*** The maximum thermal and fast neutron fluxes calculated for the un-rodded core occur above core midplane at the fifth fuel block level due to the axial temperature gradient in the core. The top of the core is cooler than the bottom. Although the highest fast flux occurs in the core fuel blocks, the high fuel block temperatures (800–1000ºC) prevent the use of irradiation test facilities (tubes) and control rods (sleeves) with metallic components in the fuel blocks. Rather, all irradiation test positions are located in the inner and outer graphite reflector blocks, where the reflector blocks are much cooler (500–600°C) and experiments can be directly cooled by primary helium coolant.

Maximum thermal and fast fluxes are presented for three irradiation positions in Table 3-2. The center loop position is a graphite block column with a centrally-located thick-walled steel pressure tube.

The Ring 3 irradiation positions are those three high-flux irradiation positions up against the Ring 2 fuel blocks (Figure 3-1). The Ring 4 positions consist of three irradiation positions and three loop positions up against the Ring 3 fuel blocks. The maximum thermal flux occurs in the Ring 3 positions and is calculated to be 3.90E+14 $n/cm^2/s$. These high thermal flux test positions could have a thin-walled, low thermal-neutron-absorbing containment tube for "drop-in" capsule experiments.

It should be noted that a thick-walled pressure containment tube (stainless steel) for loop experiments can reduce the local thermal flux by a factor of 2. The highest useable fast flux is calculated to be 1.17E+14 $n/cm^2/s$ ($E_n>0.18$ MeV) and occurs in the central loop facility. This fast flux is achieved by removing the graphite mass in the Ring 1 graphite blocks. Without graphite removal, the fast flux is 4.64E+13 $n/cm^2/s$.

Table 3-2. Maximum fast and thermal irradiation fluxes by position.

| Irradiation Position | Core Ring | Maximum Thermal Flux ($n/cm^2/s$) | Maximum Fast Flux ($n/cm^2/s$) |
|---|---|---|---|
| Center loop | 1 | 1.61E+14 | 1.17E+14 |
| Outer reflector | 3 | 3.90E+14 | 5.24E+13 |
| Outer reflector | 4 | 2.82E+14 | 2.28E+13 |

**3.2.2.2    Cycle Length and Burnup.** The cycle length for the baseline HTGTR is calculated to be 110 days. Assuming a 4-week shutdown time between cycles, it has a maximum availability factor of 80%.The fuel rod average burnup ranges from 4.62 to 9.56% FIMA with a core average of 7.36% FIMA. These burnups are slightly less than the AGR-2 UCO burnups that ranged from 4.90 to 10.30% FIMA, with an average burnup of 8.18% FIMA. The AGR-2 TRISO particles were also 425-μm-diameter UCO kernels, but with a slightly lower enrichment of 14-wt% $^{235}$U and a higher PF of 36%. The AGR-5/6/7 qualification and margin tests will use a 425-μm-diameter UCO kernel with an enrichment of 15.5-wt% $^{235}$U, just like this test reactor, but with higher PFs of 25 and 35%. The AGR-5/6/7 compacts should sustain burnups of 8.0–18.6% FIMA, which is substantially higher than the 9.56% FIMA maximum burnup predicted at end-of-cycle for the HTGTR.

The 110-day cycle length could potentially be extended by increasing the PF. A penalty will be paid in lower thermal-neutron irradiation fluxes by factors of 1.33 and 1.74, respectively for PF=25% or 35% (Figure 3-4). The cycle lengths, however, can be substantially extended to 210 and 281 days, respectively (Figure 3-5). Variable cycle length through changes in PF could be a useful feature of the HTGTR. Average compact burnups will also increase to approximately 8.85 and 9.26% FIMA for PF=25 and 35%, respectively.

Using burnable poison rods in the six available corner positions in the prismatic fuel blocks can reduce power-peaking at the core-reflector interfaces. Poison rods designed to be graphite containing $B_4C$ with very low concentrations of $^{10}$B (<1%) should be sufficient to hold down interface reactivity and local power-peaking.

**3.2.2.3    Control Rod Worth.** A preliminary control rod design consists of $B_4C$ compacts in an 800H alloy sleeve. $^{10}$B enrichment of 30–50% would be sufficient. A total of 15 control rods are located in the outer graphite reflector block; three control rods in Ring 3, and 12 control rods in Ring 4. The total worth of the 15 rods is $50.2; hot shutdown requires $30.8, and hot-to-cold shutdown requires $35.0. Cold shutdown can be achieved with 2 of 3 Ring 3 rods and 10 of 12 Ring 4 rods, showing sufficient shutdown margin for stuck rods or accidental rod withdrawals.

**3.2.2.4    Reactivity of Alternative Loop Test Fluids.** An important mission of the test reactor is irradiation of a variety of primary coolant fluids from alternative reactor technologies. Alternative loop fluids may include light water, liquid salt, liquid metal, and gases or steam. To evaluate the reactivity impact to the core, pressurized light water, FLiBe, and liquid sodium were separately

evaluated based on assumed placement in the central irradiation loop facility. Table 3-3 gives the negative core reactivity incurred for each fluid inserted in place of helium coolant in the central test loop (Ring 1).

Table 3-3. Test fluid reactivity impact.

| Fluid Type | Fluid Symbol | Temperature (°C) | Pressure (MPa) | Reactivity ($) |
|---|---|---|---|---|
| Helium gas | He | 650 | 7.0 | — |
| Liquid sodium | Na | 300–600 | 1.01E-4 | −0.17 |
| Light water | $H_2O$ | 329 | 15.0 | −1.57 |
| Liquid salt-FLiBe[a] | $LiF_2$-$BeF_2$ | 548 | 0.3 | −0.21 |

a.: $^7$Li enrichment = 99.99%
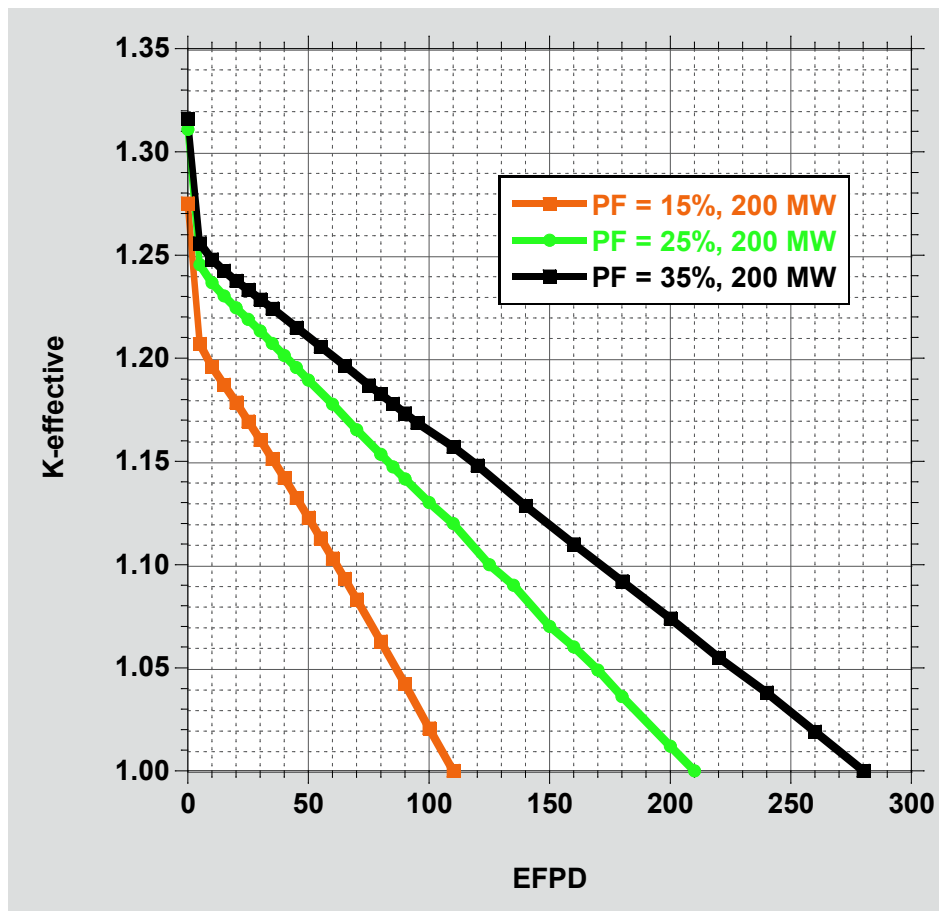


Figure 3-5. Reactivity letdown versus burnup.

The introduction of these three test fluids has minor reactivity impact to the core overall. Other fluids would also be easily accommodated in the central loop facility. The introduction of gases or steam into the central loop would also have a small or negligible reactivity effect.

### 3.2.3    Physics Parameter Summary

Table 3-4 provides a summary of the key reactor physics parameters related to the baseline design.

Table 3-4. Summary of reactor physics parameters.

| | |
|---|---|
| Fuel columns | 12 |
| Fuel blocks per column | 8 |
| Fuel blocks per core | 96 |
| Fuel block type: | Prismatic hexagonal |
|   - Height | 79.3 cm |
|   - Flat-to-flat width | 36 cm |
| Fuel rods per fuel block | 210 |
| Coolant channels per fuel block | 108 |
| Poison rods per fuel block | 0 |
| Compact diameter | 1.245 cm |
| Compacts per block | 3,126 |
| Compacts per core | 300,096 |
| Compact binder matrix graphite density | 1.70 g/cm$^3$ |
| Particle UCO kernel diameter | 425 μm |
| Particle PF | 15.0% |
| Particles per compact | 2,706 |
| Particles per core | 812M |
| $^{235}$U enrichment | 15.5 wt% |
| $^{235}$U loading per fuel block | 525.6 g |
| $^{238}$U loading per fuel block | 2,865.5 g |
| Power cycle length | 110 days |
| Maximum fuel burnup | 9.56% FIMA |
| Maximum thermal flux | 3.90E+14 n/cm$^2$/s |
| Maximum fast flux | 1.17E+14 n/cm$^2$/s |
| Maximum fast fluence | 1.72E+21 n/cm$^2$ |
| Peak fuel temperature under normal operation | <1250°C |
| Average particle power | 246 mW |
| Temperature coefficients of reactivity: | — |
|   - Isothermal | −9.7 to −9.5 pcm/°C (20–1000°C) |
|   - Fuel | −4.9 to −2.4 pcm/°C (20–2500°C) |
|   - Moderator | −3.2 to −5.2 pcm/°C (20–1800°C) |
| Control rods | 3 (Ring 3) + 12 (Ring 4) |
| Control rod worth | $50.2 |
| Beta-effective | 0.0073 |
| Neutron generation time | 642 μs |

## 3.2.4   Next Design Steps

The following activities are recommended to further improve and refine the HTGTR design.

(1) Re-design the fuel block to optimize its flat-to-flat dimensions and number of fuel and coolant channels. For example, a larger flat-to-flat dimension will increase the radial thickness of the annular core, increase the uranium loading at each axial level, and allow for a shorter core height.

(2) Reduce the current 8-block high fuel columns to 4, 5, or 6 blocks. A reduction in the number of vertically stacked fuel blocks in each fuel column would reduce the vertical height of the core and the total number of fuel blocks in the core, which translates directly into reduced fuel costs. Shutdown time to reload the core with fuel and experiments would also be reduced.

(3) Include TRISO particle PF grading as a design variable to help reduce block-average particle power and interface power-peaking. Particle PF increases will also increase cycle length and capacity factor.

(4) Burnable poison rod study. Placement of burnable poison rods in strategic core locations will hold down beginning-of-cycle excess reactivity, reduce interface power-peaking, and reduce control worth requirements. Evaluate different types of burnable poisons, poison concentration, number of rods, and core location.

(5) Re-evaluate the control rod design, number, and placement in the core in conjunction with burnable poison rod placement.

## 3.3 Core Thermal-hydraulic Conditions

Steady-state calculations were performed using the RELAP5-3D computer code (INL 2015) to characterize the core and reactor vessel temperatures. Both nominal and sensitivity cases were studied.

### 3.3.1 Nominal Core Configurations

Steady-state calculations were performed for a range of reactor powers; block-to-block gaps of 2, 3, and 4 mm; and 4, 6, and 8 axial levels of fuel blocks. A 2-mm gap between blocks is about as close together as they can be loaded in the core. Through thermal cycling and irradiation, the gaps are expected to widen over the core life. Therefore, block-to-block gap widths of 2, 3, and 4 mm were modeled to provide an indication of how the response might change during the core life. Figure 3-6 shows peak fuel temperatures from these calculations. At a constant power, the peak fuel temperature may increase by about 100°C over the life of the reflector, as the gap between the blocks increases; this suggests that higher powers and fluxes could be tolerated earlier in the core life when the gaps are smaller.

Figure 3-6 also shows that, at a constant power density, the peak fuel temperatures decrease slightly as the core gets taller. For example, with a 4-mm gap (the top curve in each set of three), the peak temperature is 1277°C for the 100-MW, 4-level core; 1258°C for the 150-MW, 6-level core; and 1240°C for the 200-MW, 8-level core.

Keeping the peak fuel temperature in the 1250-1300°C range is consistent with historical practice and is within the range of fuel testing that has been performed more recently; the temperature could probably be increased with no negative impacts. As will be seen in Section 4, the peak fuel temperatures during conduction cooldown transients are generally well below the steady-state values for this core design. This suggests that higher temperatures could be tolerated during steady-state operation, which would result in higher neutron flux levels.

To be consistent with keeping the peak fuel temperatures below 1300°C during steady state, the nominal power levels are 100 MW for the 4-level core, 150 MW for the 6-level core, and 200 MW for the 8-level core. Steady state conditions from these cases are contained in Tables 3-5 through 3-7. The total bypass includes all flow that is not in a coolant channel. The effective bypass is defined as all flow not in a coolant channel or in a gap around a fuel block, because this particular gap flow will provide direct cooling to the fuel rods, especially those near the edges of the blocks. The bypass at both the core inlet and outlet is also shown; the effective bypass is higher at the bottom of the core than at the top, because
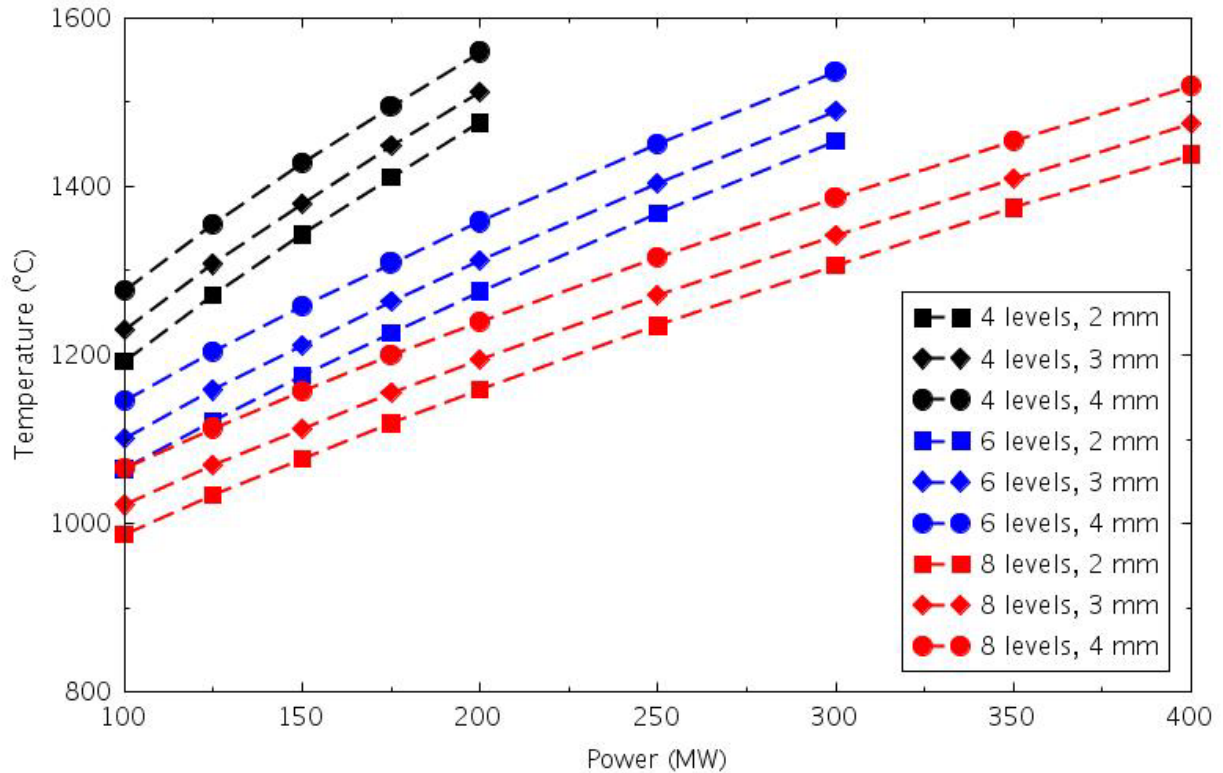
Figure 3-6. Peak fuel steady state temperatures.

some of the helium in the gaps moves to cooler regions farther from the core as it flows downward. The total bypass does not change between the inlet and outlet because leakage from the coolant channels to the gaps is not modeled. Heat removed by both the reactor cavity cooling system (RCCS) and the coolant flowing inside the central irradiation loop is included.

Table 3-5. Steady state conditions for the 4-level, 100-MW core.

| Parameter | 2-mm Gaps | 3-mm Gaps | 4-mm Gaps |
|---|---|---|---|
| Coolant inlet temperature (°C) | 325 | 325 | 325 |
| Coolant outlet temperature (°C) | 650 | 650 | 650 |
| Coolant flow rate (kg/s) | 58.9 | 58.9 | 58.9 |
| Effective core bypass at core inlet (%) | 26 | 30 | 33 |
| Effective core bypass at core outlet (%) | 27 | 31 | 35 |
| Peak fuel temperature (°C) | 1193 | 1230 | 1277 |
| Center reflector peak temperature (°C) | 702 | 696 | 693 |
| Ring 3 reflector peak temperature (°C) | 641 | 622 | 611 |
| Ring 4 reflector inner peak temperature (°C) | 591 | 579 | 572 |
| Ring 4 reflector outer peak temperature (°C) | 430 | 415 | 408 |
| Ring 5 reflector peak temperature (°C) | 378 | 362 | 355 |
| PSR peak temperature (°C) | 344 | 338 | 336 |
| Core barrel peak temperature (°C) | 331 | 330 | 330 |
| Reactor vessel peak temperature (°C) | 316 | 316 | 316 |
| RCCS heat removal (MW) | 0.31 | 0.31 | 0.31 |
| Irradiation loop heat removal (MW) | 0.16 | 0.16 | 0.16 |

14

Table 3-6. Steady state conditions for the 6-level, 150-MW core.

| Parameter | 2-mm Gaps | 3-mm Gaps | 4-mm Gaps |
|---|---|---|---|
| Coolant inlet temperature (°C) | 325 | 325 | 325 |
| Coolant outlet temperature (°C) | 650 | 650 | 650 |
| Coolant flow rate (kg/s) | 88.2 | 88.2 | 88.3 |
| Effective core bypass at core inlet (%) | 26 | 30 | 33 |
| Effective core bypass at core outlet (%) | 27 | 31 | 35 |
| Peak fuel temperature (°C) | 1175 | 1212 | 1258 |
| Center reflector peak temperature (°C) | 661 | 656 | 654 |
| Ring 3 reflector peak temperature (°C) | 584 | 566 | 561 |
| Ring 4 reflector inner peak temperature (°C) | 567 | 556 | 551 |
| Ring 4 reflector outer peak temperature (°C) | 401 | 391 | 386 |
| Ring 5 reflector peak temperature (°C) | 361 | 351 | 346 |
| PSR peak temperature (°C) | 337 | 333 | 332 |
| Core barrel peak temperature (°C) | 329 | 329 | 329 |
| Reactor vessel peak temperature (°C) | 317 | 317 | 317 |
| RCCS heat removal (MW) | 0.38 | 0.38 | 0.38 |
| Irradiation loop heat removal (MW) | 0.17 | 0.16 | 0.17 |

Table 3-7. Steady state conditions for the 8-level, 200-MW core.

| Parameter | 2-mm Gaps | 3-mm Gaps | 4-mm Gaps |
|---|---|---|---|
| Coolant inlet temperature (°C) | 325 | 325 | 325 |
| Coolant outlet temperature (°C) | 650 | 650 | 650 |
| Coolant flow rate (kg/s) | 117.2 | 117.3 | 117.3 |
| Effective core bypass at core inlet (%) | 26 | 29 | 33 |
| Effective core bypass at core outlet (%) | 27 | 31 | 35 |
| Peak fuel temperature (°C) | 1159 | 1194 | 1240 |
| Center reflector peak temperature (°C) | 648 | 645 | 651 |
| Ring 3 reflector peak temperature (°C) | 585 | 567 | 558 |
| Ring 4 reflector inner peak temperature (°C) | 562 | 550 | 548 |
| Ring 4 reflector outer peak temperature (°C) | 392 | 383 | 380 |
| Ring 5 reflector peak temperature (°C) | 357 | 348 | 343 |
| PSR peak temperature (°C) | 336 | 332 | 331 |
| Core barrel peak temperature (°C) | 329 | 328 | 328 |
| Reactor vessel peak temperature (°C) | 317 | 317 | 317 |
| RCCS heat removal (MW) | 0.44 | 0.44 | 0.44 |
| Irradiation loop heat removal (MW) | 0.17 | 0.17 | 0.17 |

The steady-state temperature distribution also provides some operational flexibility. With a fresh core and reflector, where the block-to-block gaps are smaller, much higher core powers (and neutron fluxes) can be achieved while maintaining acceptably low fuel operating temperatures. Experiment campaigns

desiring higher fluxes could be planned for earlier in a core life, with longer exposure or lower flux tests being scheduled during periods with larger gaps.

The reason the fuel temperatures increase as the block-to-block gaps get larger is that more helium is bypassing the coolant channels to flow through the gaps.

To make comparisons between the three core heights more convenient, Table 3-8 contains the steady-state conditions for the 4-mm gap nominal cases. The fuel power fractions are slightly different for the three cases, but are within the statistical variation of the MCNP calculations that generated them. The core bypass fractions are the same for the different heights. RCCS heat removal increases with increasing core height. The principal difference is that the fuel and reflector temperatures decrease somewhat as the core power increases. The higher coolant flow required to maintain the same reactor vessel inlet and outlet temperatures at higher power means that the coolant velocities are also higher, which increases the convective heat transfer coefficient and lowers the structure temperatures. Heat removal through the irradiation loop coolant is insensitive to the core height or power.

Tables 3-9 through 3-11 present steady state conditions for the three cores at different power levels. These results reflect the same effect of core power and coolant flow rate on temperatures. The fuel temperatures increase as the power increases, but the reflector temperatures decrease as the flow rate increases. The reactor vessel and core barrel temperatures are virtually unchanged in any of the calculations, indicating that their temperature is dependent only on the coolant inlet temperature. RCCS heat removal is independent of the core power and dependent only on the height of the reactor vessel; this is consistent with a constant temperature reactor vessel, where only the heat transfer area matters. Heat removal by the helium flowing on the inside of the central irradiation tube decreases slowly with increasing power and flow rate, reflecting the temperature change in the central reflector.

Table 3-8. Steady-state conditions for the three nominal core cases with 4-mm gaps.

| Parameter | 4-Level 100 MW | 6-Level 150 MW | 8-Level 200 MW |
|---|---|---|---|
| Fuel power fraction | 0.978 | 0.992 | 0.982 |
| Coolant inlet temperature (°C) | 325 | 325 | 325 |
| Coolant outlet temperature (°C) | 650 | 650 | 650 |
| Coolant flow rate (kg/s) | 58.9 | 88.3 | 117.3 |
| Effective core bypass at core inlet (%) | 33 | 33 | 33 |
| Effective core bypass at core outlet (%) | 35 | 35 | 35 |
| Peak fuel temperature (°C) | 1277 | 1258 | 1240 |
| Center reflector peak temperature (°C) | 693 | 654 | 651 |
| Ring 3 reflector peak temperature (°C) | 611 | 561 | 558 |
| Ring 4 reflector inner peak temperature (°C) | 572 | 551 | 548 |
| Ring 4 reflector outer peak temperature (°C) | 408 | 386 | 380 |
| Ring 5 reflector peak temperature (°C) | 355 | 346 | 343 |
| PSR peak temperature (°C) | 336 | 332 | 331 |
| Core barrel peak temperature (°C) | 330 | 329 | 328 |
| Reactor vessel peak temperature (°C) | 316 | 317 | 317 |
| RCCS heat removal (MW) | 0.31 | 0.38 | 0.44 |
| Irradiation loop heat removal (MW) | 0.16 | 0.17 | 0.17 |

Table 3-9. Steady-state conditions for the 4-level core with 4-mm gaps at different core powers.

| Parameter | 100 MW | 125 MW | 150 MW | 175 MW | 200 MW |
|---|---|---|---|---|---|
| Coolant inlet temperature (°C) | 325 | 325 | 325 | 325 | 325 |
| Coolant outlet temperature (°C) | 650 | 650 | 650 | 650 | 650 |
| Coolant flow rate (kg/s) | 58.9 | 73.6 | 88.3 | 102.9 | 117.5 |
| Effective core bypass at core inlet (%) | 33 | 33 | 33 | 33 | 33 |
| Effective core bypass at core outlet (%) | 35 | 35 | 35 | 35 | 35 |
| Peak fuel temperature (°C) | 1277 | 1355 | 1427 | 1495 | 1559 |
| Center reflector peak temperature (°C) | 693 | 675 | 659 | 645 | 633 |
| Ring 3 reflector peak temperature (°C) | 611 | 593 | 578 | 565 | 555 |
| Ring 4 reflector inner peak temperature (°C) | 572 | 559 | 548 | 538 | 531 |
| Ring 4 reflector outer peak temperature (°C) | 408 | 398 | 390 | 383 | 378 |
| Ring 5 reflector peak temperature (°C) | 355 | 351 | 348 | 345 | 343 |
| PSR peak temperature (°C) | 336 | 334 | 333 | 332 | 331 |
| Core barrel peak temperature (°C) | 330 | 329 | 329 | 329 | 328 |
| Reactor vessel peak temperature (°C) | 316 | 316 | 317 | 317 | 317 |
| RCCS heat removal (MW) | 0.31 | 0.31 | 0.31 | 0.31 | 0.31 |
| Irradiation loop heat removal (MW) | 0.16 | 0.16 | 0.15 | 0.15 | 0.15 |

Table 3-10. Steady-state conditions for the 6-level core with 4-mm gaps at different core powers.

| Parameter | 100 MW | 150 MW | 200 MW | 250 MW | 300 MW |
|---|---|---|---|---|---|
| Coolant inlet temperature (°C) | 325 | 325 | 325 | 325 | 325 |
| Coolant outlet temperature (°C) | 650 | 650 | 650 | 650 | 650 |
| Coolant flow rate (kg/s) | 58.9 | 88.3 | 117.4 | 146.2 | 174.6 |
| Effective core bypass at core inlet (%) | 33 | 33 | 33 | 33 | 33 |
| Effective core bypass at core outlet (%) | 35 | 35 | 35 | 35 | 35 |
| Peak fuel temperature (°C) | 1147 | 1258 | 1358 | 1450 | 1536 |
| Center reflector peak temperature (°C) | 681 | 654 | 637 | 623 | 611 |
| Ring 3 reflector peak temperature (°C) | 584 | 561 | 543 | 529 | 517 |
| Ring 4 reflector inner peak temperature (°C) | 571 | 551 | 537 | 525 | 514 |
| Ring 4 reflector outer peak temperature (°C) | 404 | 386 | 375 | 367 | 360 |
| Ring 5 reflector peak temperature (°C) | 353 | 346 | 342 | 338 | 335 |
| PSR peak temperature (°C) | 335 | 332 | 330 | 329 | 328 |
| Core barrel peak temperature (°C) | 329 | 329 | 328 | 328 | 327 |
| Reactor vessel peak temperature (°C) | 316 | 317 | 317 | 317 | 317 |
| RCCS heat removal (MW) | 0.37 | 0.38 | 0.38 | 0.38 | 0.38 |
| Irradiation loop heat removal (MW) | 0.18 | 0.17 | 0.16 | 0.15 | 0.15 |

Table 3-11. Steady-state conditions for the 8-level core with 4-mm gaps at different core powers.

| Parameter | 100 MW | 150 MW | 200 MW | 250 MW | 300 MW | 350 MW | 400 MW |
|---|---|---|---|---|---|---|---|
| Coolant inlet temperature (°C) | 325 | 325 | 325 | 325 | 325 | 325 | 325 |
| Coolant outlet temperature (°C) | 650 | 650 | 650 | 650 | 650 | 650 | 650 |
| Coolant flow rate (kg/s) | 58.8 | 88.3 | 117.3 | 146.1 | 174.5 | 202.3 | 229.6 |
| Effective core bypass at core inlet (%) | 33 | 33 | 33 | 33 | 33 | 33 | 33 |
| Effective core bypass at core outlet (%) | 34 | 35 | 35 | 35 | 35 | 35 | 35 |
| Peak fuel temperature (°C) | 1065 | 1157 | 1240 | 1315 | 1387 | 1455 | 1519 |
| Center reflector peak temperature (°C) | 688 | 691 | 651 | 638 | 626 | 616 | 606 |
| Ring 3 reflector peak temperature (°C) | 607 | 577 | 558 | 543 | 531 | 520 | 511 |
| Ring 4 reflector inner peak temperature (°C) | 581 | 562 | 548 | 536 | 525 | 516 | 508 |
| Ring 4 reflector outer peak temperature (°C) | 413 | 393 | 380 | 371 | 364 | 358 | 353 |
| Ring 5 reflector peak temperature (°C) | 357 | 348 | 343 | 340 | 337 | 334 | 332 |
| PSR peak temperature (°C) | 336 | 333 | 331 | 329 | 328 | 327 | 325 |
| Core barrel peak temperature (°C) | 328 | 328 | 328 | 328 | 327 | 327 | 326 |
| Reactor vessel peak temperature (°C) | 316 | 317 | 317 | 317 | 317 | 317 | 317 |
| RCCS heat removal (MW) | 0.44 | 0.44 | 0.44 | 0.44 | 0.44 | 0.44 | 0.44 |
| Irradiation loop heat removal (MW) | 0.20 | 0.18 | 0.17 | 0.17 | 0.16 | 0.16 | 0.16 |

## 3.3.2    Sensitivity Studies

Sensitivity calculations were performed to assess the impact of some modeling assumptions and uncertainties. Parameters that varied were the core bypass flow, coolant inlet and outlet temperatures, and the axial power shape.

### 3.3.2.1    Bypass Flow

Reducing the relatively large bypass flow would provide the ability to run at higher powers and fluxes. Sensitivity calculations were performed where the gaps around the Ring 5 outer reflector blocks were covered either at the top of the core or at both the bottom and the top, thereby preventing flow directly from the upper plenum or into the lower plenum. The gap between the PSR and core barrel was left open. Results from these calculations are shown in Table 3-12. As expected, blocking flow in the outer portion of the outer reflector forced more flow to the interior regions, reducing the interior temperatures and allowing the peripheral temperatures to increase. However, the effect was not very large. With only the top blocked, flow was diverted only in the cooler (top) portion of the core, and

Table 3-12. Effect of blocking some core bypass paths for the 200-MW, 8-level core with 4-mm gaps.

| Parameter | Base Model | Top Blocked | Top and Bottom Blocked |
|---|---|---|---|
| Total bypass (%) | 46 | 44 | 42 |
| Effective bypass, core inlet (%) | 33 | 16 | 16 |
| Effective bypass, core outlet (%) | 35 | 33 | 16 |
| Peak fuel temperature (°C) | 1240 | 1225 | 1211 |
| Center reflector peak temperature (°C) | 651 | 643 | 631 |
| Outer reflector Ring 5 peak temperature (°C) | 343 | 347 | 372 |
| PSR peak temperature (°C) | 331 | 332 | 338 |

only small changes in temperature were calculated. The temperature changes were larger with both the top and bottom blocked, because flow was diverted from the outer gaps back toward the center of the core in the hottest region (bottom) of the core. Although the temperature changes were larger, they were not significant enough to warrant concern in Ring 5; the PSR peak temperature increased less than 10°C from the base case.

### 3.3.2.2    Coolant Temperature

The core inlet and outlet temperatures were selected to not overly challenge the primary coolant system piping materials. However, there may be some interest in running with more prototypical temperatures. Sensitivity calculations were performed with reactor vessel inlet and outlet temperatures of 350°C and 750°C, respectively, compared to the 325°C and 650°C for most of the steady state calculations. The 8-level model was used, with 4-mm gaps and core powers of 150 and 200 MW; results are presented in Table 3-13. The fuel, central reflector and Ring 3 reflector peak temperatures all increased by more than the 100°C increase in the coolant outlet temperature because the flow rate decreased, with the lower velocity resulting in a lower heat transfer coefficient. The increases in the reactor vessel, core barrel, and PSR peak temperatures were all consistent with the 25°C increase in the coolant inlet temperature.

Table 3-13. Results of coolant temperature sensitivity calculations.

| Parameter | 150 MW | | 200 MW | |
|---|---|---|---|---|
| Coolant inlet temperature (°C) | 325 | 350 | 325 | 350 |
| Coolant outlet temperature (°C) | 650 | 750 | 650 | 750 |
| Coolant flow rate (kg/s) | 88.3 | 71.8 | 117.3 | 95.7 |
| Effective core bypass at core outlet (%) | 35 | 35 | 35 | 35 |
| Peak fuel temperature (°C) | 1157 | 1293 | 1240 | 1373 |
| Center reflector peak temperature (°C) | 691 | 826 | 651 | 801 |
| Ring 3 reflector peak temperature (°C) | 577 | 684 | 558 | 660 |
| Ring 4 reflector inner peak temperature (°C) | 562 | 661 | 548 | 645 |
| Ring 4 reflector outer peak temperature (°C) | 393 | 448 | 380 | 432 |
| Ring 5 reflector peak temperature (°C) | 348 | 385 | 343 | 378 |
| PSR peak temperature (°C) | 333 | 361 | 331 | 359 |
| Core barrel peak temperature (°C) | 329 | 355 | 328 | 354 |
| Reactor vessel peak temperature (°C) | 317 | 340 | 317 | 341 |
| RCCS heat removal (MW) | 0.44 | 0.50 | 0.44 | 0.51 |
| Irradiation loop heat removal (MW) | 0.18 | 0.17 | 0.17 | 0.21 |

### 3.3.2.3    Power Shape

Sensitivity calculations were performed where a chopped cosine axial power shape with a peak-to-average value of 1.2 was used instead of a flat profile. Gap widths of 2, 3, and 4 mm were used for a 4-level core at 100 MW and an 8-level core at 200 MW; results from the latter set of calculations are provided in Table 3-14. Other than a 15°C increase in the central reflector peak temperature in the 2-mm case, the only real differences are in the peak fuel temperatures. The peak fuel temperatures occur in the bottom fuel block, where the coolant temperature is the highest. With the cosine power shape, less power is generated in this block than with a flat power shape; therefore, the fuel temperature decreases, ranging from 27°C with 2-mm gaps to 38°C with 4-mm gaps.

Radial power shape sensitivity calculations were not performed. The fueled region is essentially one block wide, with peaking expected at the edges next to reflector blocks. The peaking can be mitigated by

using burnable poisons or varying the fuel packing fraction. Estimates of the effect of various radial peaking factors can also be made by using the results of the steady-state calculations at higher power levels. For example, a radial peaking factor of 1.5 with a total core power of 200 MW would yield peak fuel temperatures in those rods near what was calculated for a 300 MW core with no peaking.

Table 3-14. Axial power sensitivity calculations for the 8-level core at 200 MW.

| Parameter | 2-mm Gaps | | 3-mm Gaps | | 4-mm Gaps | |
|---|---|---|---|---|---|---|
| Axial power profile | flat | cosine | flat | cosine | flat | cosine |
| Coolant inlet temperature (°C) | 325 | 325 | 325 | 325 | 325 | 325 |
| Coolant outlet temperature (°C) | 650 | 650 | 650 | 650 | 650 | 650 |
| Coolant flow rate (kg/s) | 117.2 | 117.2 | 117.3 | 117.3 | 117.3 | 117.3 |
| Effective bypass, core outlet (%) | 27 | 27 | 31 | 31 | 35 | 35 |
| Peak fuel temperature (°C) | 1159 | 1132 | 1194 | 1163 | 1240 | 1202 |
| Center reflector peak temperature (°C) | 648 | 663 | 645 | 645 | 651 | 651 |
| Ring 3 reflector peak temperature (°C) | 585 | 584 | 567 | 567 | 558 | 559 |
| Ring 4 reflector inner peak temperature (°C) | 562 | 561 | 550 | 550 | 548 | 548 |
| Ring 4 reflector outer peak temperature (°C) | 392 | 392 | 383 | 383 | 380 | 380 |
| Ring 5 reflector peak temperature (°C) | 357 | 357 | 348 | 347 | 343 | 343 |
| PSR peak temperature (°C) | 336 | 336 | 332 | 332 | 331 | 331 |
| Core barrel peak temperature (°C) | 329 | 329 | 328 | 328 | 328 | 328 |
| Reactor vessel peak temperature (°C) | 317 | 317 | 317 | 317 | 317 | 317 |
| RCCS heat removal (MW) | 0.44 | 0.44 | 0.44 | 0.44 | 0.44 | 0.44 |
| Irradiation loop heat removal (MW) | 0.17 | 0.17 | 0.17 | 0.17 | 0.17 | 0.17 |

### 3.3.3 Summary

Steady-state calculations were performed for the baseline core layout with 4, 6, and 8 levels of fuel blocks and varying powers and block-to-block gap widths. Some sensitivity calculations were also performed.

The combination of a relatively small number of fuel blocks, a large number of reflector blocks and the gaps between the blocks, and the gaps between control rods or irradiation tubes and the reflector result in a core that is effectively cooled by forced convection of the primary helium coolant. The large number of gaps also results in a core bypass flow that is larger than what would be expected in a prototypic power reactor.

With the effective convective cooling around the fuel and inner reflector blocks, the reactor vessel, core barrel, and PSR temperatures are dependent on the coolant inlet temperature and are independent of the core power. Because the reactor vessel temperature is independent of the core power, so is the RCCS heat removal, which varies as the height of the reactor vessel (and therefore the heat transfer surface area) changes with the changes in core height.

The peak fuel temperatures will increase over the life of the core, by about 100°C, as the gaps between the blocks increase from 2 to 4 mm, because the bypass flow increases, reducing the helium flow through the coolant holes. This behavior observed for all three core heights and with different core powers. As expected, the fuel temperatures also increase with power, but decrease slightly with core height with a constant power density in the fuel.

The reflector temperatures decrease with increasing power, because the coolant flow increases to maintain the same temperature rise across the core. The increased flow means the velocity is higher, which results in higher heat transfer coefficients from the structures to the coolant.

Heat removed by the coolant in the central irradiation loop reduces the temperature of the central reflector, but has little effect on the fuel and fuel block temperatures because the amount of heat removed is very small compared to the heat being generated in the fuel and removed by the flow through the coolant channels.

Sensitivity calculations investigated the impacts of trying to reduce the core bypass flow in the outer reflector, increasing the coolant inlet and outlet temperatures, and changing the axial power shape. Only the increased coolant temperatures had a significant impact on the fuel and structure temperatures, but the impact was no greater than would be expected.

## 3.4  Testing Facilities

Test articles to be irradiated are mounted inside capsules held in test trains suspended directly in reflector holes (black circles in Figure 3-1) or in independently-cooled test loops (blue circles). Test trains in the reflector holes are cooled by the primary helium coolant although some temperature control can be achieved by carefully designing the capsule's insulating layers to control the removal of gamma or fission heat generated within. In the configuration proposed for this study, there are 30 such test spaces but there is sufficient reflector volume to add more.

The test loops remain outside the primary pressure boundary and possess their own cooling systems; therefore, they can provide prototypic conditions for testing fuels and materials for essentially any reactor concept. Test wells suspended from the top vessel head extend the primary pressure boundary downward into the reactor core (Mayer, Lommers, and Shahrikhi, 2015), as shown in Figure 3-7. The loops are inserted into the test wells with the test coolant inlet and outlet and the instrumentation leads emerging from the top of the wells. Piping and associated components (e.g., pumps and heaters) are located outside the pressure vessel. Helium flow would be provided between the experiment loop and the well to provide cooling to the well wall. Loop coolant conditions are specified by the experimenter. It is expected that one of these loop locations in the outer reflector would contain a pneumatically-driven rabbit system.

Because helium is chemically inert, leakage between the primary and loop coolants would not lead to chemical interactions between them. Nonetheless, such leakage is all but ruled out by the test well walls, which are designed to meet American Society of Mechanical Engineers Section III Class 8 pressure vessel criteria. The independent cooling loop can keep the test article at temperatures desired by the experimenter but the primary coolant surrounding the test well will be within a temperature range (325–650°C) that can assist in maintaining prototypical and bounding conditions suitable for testing fuels and materials under a wide range of temperatures. In the configuration proposed, there are four such test loops but more can be added in the reflector region.

The central irradiation test loop in Ring 1 is one such facility. It has a stainless-steel 316L tube with an outer diameter of 11.34 cm (4.5 in.) and wall thickness of 1.35 cm (0.531 in.). The outer irradiation positions in Rings 3 and 4 are similarly configured. Loops can accommodate relatively large test specimens cooled by various fluids including high-pressure light water, low-pressure liquid salt, liquid metal, or different gases (e.g., helium). In addition, the Ring 3 and 4 irradiation positions can have thinner-walled metallic containment tubes (e.g., molybdenum, zirconium, or titanium) for drop-in type capsule experiments assembled into test trains. These tube facilities can have diameters up to approximately 16 cm. For the HTGTR design evaluation, these facilities have an outer diameter of 10.16 cm (4.0 in.), which is the same as the control rod holes in the graphite blocks. Table 3-15 lists the irradiation facility by ring, type, and pertinent metrics.
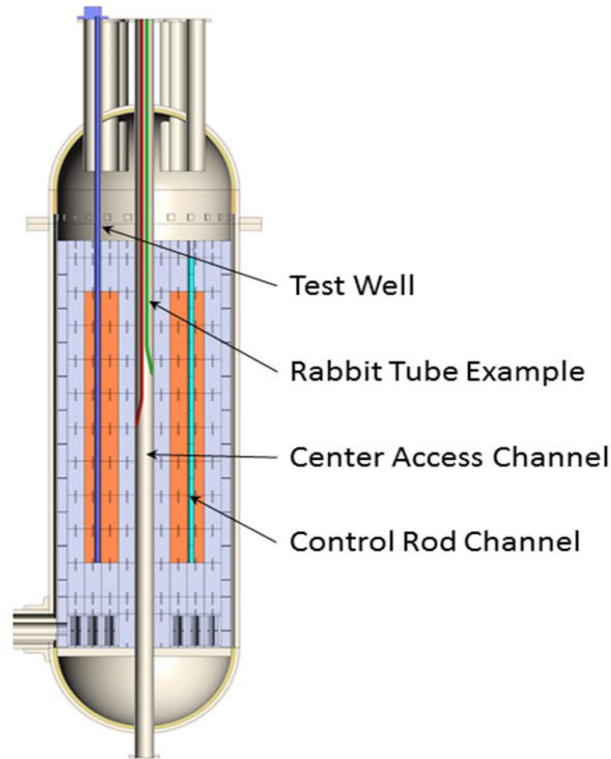
Figure 3-7. Side view of vessel showing vertical test and control structures.

Many of the tests in the flow-through experiment facilities in the side reflector could be contained within the height of a single block. These experiments would be loaded into the block prior to insertion in the reactor and would be removed with the block after irradiation. The holes in the blocks for the experiments would have a counter bore or cutout at the top and bottom of the block that would accommodate hardware to hold the experiments in place.

Table 3-15. Irradiation facilities and characteristics.

| Ring Number | Number of Loops | Number of Tubes | Test Diameter (cm) | Test Length (m) | Test Volume per Facility (L) | Total Test Volume (L) |
|---|---|---|---|---|---|---|
| 1 | 1 | 0 | 5.4 | 6.34 | 14 | 14 |
| 2 | 0 | 0 | — | — | — | — |
| 3 | 0 | 15 | 8.0 | 6.34 | 30 | 450 |
| 4 | 3 | 9 | 5.4/8.0 | 6.34 | 14/30 | 42/270 |
| 5 | 0 | 12 | 8.0 | 6.34 | 30 | 360 |
| Total | 4 | 36 | — | — | — | 1,136 |

## 3.5   Refueling and Replacement of Test Articles

The availability and operational effectiveness of a test reactor is a strong function of the ease and speed with which fuel and test articles can be replaced. High flux reactors must (in general) be refueled more frequently than power reactors. The test samples must be removed after a specified time in the operating core per experimental demands. The refueling and test insertion/replacement schedules may not conveniently overlap at a given power level; therefore, cycle planning becomes a balancing exercise between required test exposure, loop power and temperature, and fuel reactivity. Even if online test

insertion and removal (e.g., with a pneumatic shuttle system) is available, frequent outages are the norm. Design emphasis is placed on simplicity of reloading operations and accessibility to core structures.

The large size of the HTGR fuel and reflector blocks, control rods, and test spaces requires appropriately sized handling equipment. On the other hand, the large size of the core and vessel translates into ample space above the core for maneuvering these structures. Systems and procedures for fuel handling operations were successfully developed and implemented in HTGRs.

Access to the fuel and removable reflector blocks is achieved through vessel head penetrations, most of which are used for control rod drive assemblies and are large enough to accommodate a block. All fuel blocks can be retrieved from the locations indicated in green (Figure 3-8, left) without being obstructed by the loop assemblies (blue circles). Sufficient shutdown reactivity margin exists in the remaining inserted rods. After depressurization, the control rod drive mechanism is lifted from the vessel. The fuel handling machine (FHM) is then lowered through the vessel head and upper plenum from a refueling deck above the reactor vessel. An arm at the end of the FHM extends radially to connect with any block in its immediate vicinity. In this test reactor design, this would include all blocks in the 120-degree sector centered on the FHM shaft. In the GA modular HTGR (MHTGR) design, the block is then transferred to a Fuel Elevator that is suspended through a different head penetration (Figure 3-8, right). In the FSV reactor, no separate device was used. Instead, the FHM and fuel transfer cask were integrated into a single machine. Each captured block was lifted by the FHM through a single access opening and placed within the cask. When the cask was full, it was moved to an available storage cell where it was positioned for unloading. This is likely to be the best option for the HTGTR.

Control rods (yellow circles) inside the nearby reflector blocks would have to be removed or at least detached from their drive assemblies for these blocks to be removed. Shorter (< 160 cm) test trains cooled by the primary coolant (locations indicated by black circles in Figure 3-8) would come out with the reflector block from which they are suspended. Core-length test assemblies (~500 cm) may go in the test
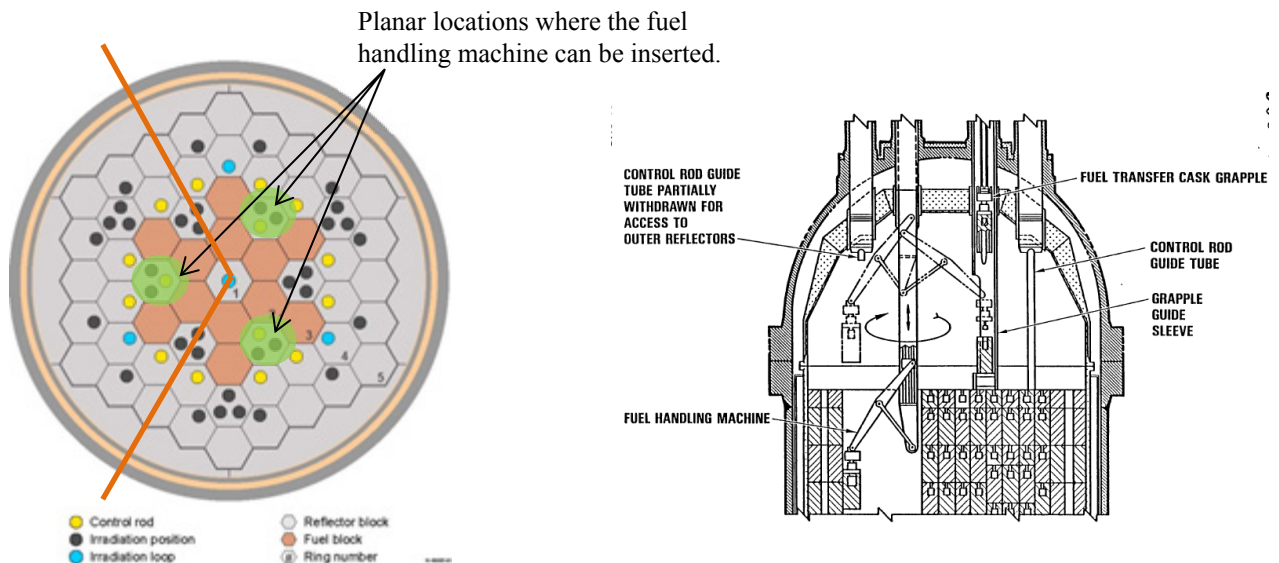


Figure 3-8. Core layout indicating access to fuel and reflector blocks (left) and side view of the MHTGR FHM (right)

spaces directly under the FHM and would be removed with the entire column of blocks. Insertion and removal of test trains or specimens from reflector blocks that are not being replaced remains to be addressed; however, this may not be much different from withdrawing and inserting the control rod guide tubes during refueling. Detailed engineering design may lead to other options for these handling evolutions.

As access to the fuel, test spaces, and control rods are likely to be from above the core, the pressure vessel head will be crowded with penetrations, as shown in Figure 3-9 (Mayer, Lommers, and Shahrikhi, 2015). As demonstrated at FSV, each penetration for Ring 4 would service two independently-controlled control rods. Preliminary evaluation indicates the required penetration configuration is workable. Further design calculations are needed to optimize the location of penetrations and interior structures.
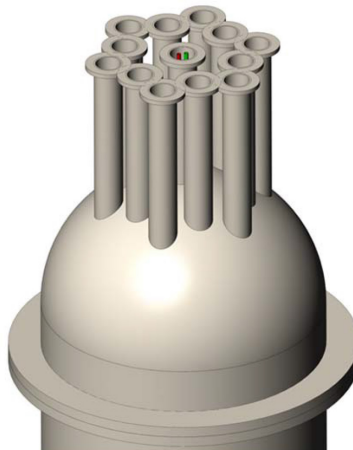


Figure 3-9. Vessel head penetrations.

## 3.6  Other Systems

The design effort thus far has been focused on the core and reactor vessel; design of most of the ex-vessel systems has not been addressed yet. Except for test-specific systems and hardware, all systems and components are prototypic of either a commercial or demonstration gas-cooled prismatic block reactor. The fuel and reflector blocks are full size. The reactor vessel and steam generator will be somewhat smaller because of the lower core power. The primary coolant system consists of the reactor vessel, a hot duct or pipe leading to a steam generator, a compressor or gas circulator, and a cold return pipe to the reactor vessel inlet. An alternate parallel path to provide high-temperature helium to a process heat application could also be included if desired.

The secondary coolant system is expected to include a turbine-generator set to generate electricity and a condenser. For licensing reasons, not all of the available steam would be used for electricity generation. The remaining steam could be used to drive the process heat test bed or could simply be sent directly to the condenser. The steam generator is expected to be used for normal decay heat removal. Alternatively, a dedicated cooling system could be included similar to those in commercial plant designs where helium is drawn from the bottom of the reactor vessel, cooled, and returned to the vessel.

Functional containment of fission products is provided by the fuel particles, compacts, and interstitial graphite. Therefore, a reactor building is preferable to a full containment structure. In the event of a large break in the primary coolant boundary, the reactor building is vented to relieve pressure while the core cools down and mitigating actions can be taken.  The levels of radiological materials that accumulate in the primary circuit during operation are low enough to be vented to the atmosphere without exceeding site boundary limits, even though much of the material released from the circuit will remain within the building. The reactor vessel is expected to be in one compartment or cavity, and the steam generator and helium circulator in another.

An RCCS will be used for passive, long-term decay heat removal. It consists of a series of cooling panels located around the reactor vessel. Water flowing on the inside of the panels removes the heat transferred to the outside of the panels by radiation and convection from the reactor vessel. A large pool

of water located higher than the reactor cavity, but not directly above it, provides water to the bottom of the cooling panels and receives the warmer water exiting the top. Flow through the panels is driven by natural convection, with no pumps required. The pool could be actively cooled during normal operation and could be designed to be cooled by air natural circulation when active cooling is not available. Given the relatively small amount of heat removed by the RCCS during steady state and the large thermal margins shown in the accident simulations in Section 4, an air-cooled system may also be a viable option.

Detailed instrumentation and control systems have not been considered yet. However, it is anticipated that the plant instrumentation and controls would only be those required to ensure safe and efficient operation of the reactor and associated systems. Instrumentation needed to control a specific experiment, such as thermocouples and flow control valves, would be provided with that experiment. Additional instrumentation that would be used strictly for computer code assessment will not be included. The most useful data for code assessment would be a detailed map of the temperatures in the core. With the blocks potentially getting moved every cycle, it would be very cumbersome to try to maintain thermocouples in all of the blocks, together with all of the wiring and patching in to the data acquisition system. Additionally, it would be helpful to know the flow rate through the various flow paths in the core. There are so many coolant holes and gaps between blocks that they could not all support measurements, and any instruments located in these small flow areas would likely perturb the flow.

# 4.   Test Reactor Safety Basis

The prismatic core design provides particle fuel radionuclide retention in a passively safe reactor that requires no energized systems for long-term decay heat removal. The large thermal capacity of the core results in long transients, on the order of days.

## 4.1   Safety Characteristics

The primary safety feature is the use of TRISO fuel. The coatings on the fuel particles have been shown to prevent fission product release both historically and during recent irradiation testing in the ATR. Use of the TRISO fuel in this reactor is within the fuel qualification envelope. Should some fission products escape the coating, the fuel matrix would be the next barrier to fission product release. The fuel compacts are sealed in graphite fuel blocks that are not structurally challenged by the temperatures achieved during the most severe accidents. The primary coolant system and reactor building provide the final barriers to fission product release to the environment.

Use of an inert gas for both the primary coolant and the gap between the irradiation loops and the experiment wells precludes any chemical interactions with the structures in the plant. It also means that there would be no adverse coolant interactions should a leak develop from an experiment irradiation loop. One challenging feature of the helium coolant is that it does not provide radiation shielding. This means that removal of irradiated experiments will require portable shielding or casks for movement of the test specimens from the reactor to a storage area.

The neutronic characteristics of the core and large graphite reflector reduce the fast neutron fluence to the core barrel and reactor vessel. The thermal neutron fluence to these components can be reduced by using borated pins in the PSR.

The steam generator is expected to be used for normal decay heat removal. Alternatively, a dedicated cooling system could be included similar to those in commercial plant designs in which helium is drawn from the bottom of the reactor vessel, cooled, and returned to the vessel. While these active systems would be used for convenience, they are not required.

Decay heat removal can be accomplished using only passive systems and physical processes. Decay heat from the core is transferred radially to the reactor vessel, primarily by radiation and conduction. From the reactor vessel, radiation and natural convection in the reactor cavity transfer energy to the water-cooled RCCS. Flow through the RCCS is provided by natural convection from a large pool located higher than the reactor cavity.

## 4.2   Safety Performance

Generally accepted criteria for TRISO fuel are peak temperatures below 1250°C during steady-state operation and temperatures within the time-at-temperature envelope established by AGR fuel testing in the ATR during an accident or transient. The peak transient temperatures are lower than those during steady state; therefore, it may be possible to increase the power and flux during steady state should further fuel testing show that operating temperatures above 1250°C result in no challenges to the fuel integrity.

The operational events and accidents for this test reactor will be mostly the same as for a commercial prismatic block reactor: increases or decreases in coolant flow, changes in the reactor inlet temperature, reactivity-initiated events, and changes in coolant system pressure. Reactivity-initiated events, such as control rod ejection or uncontrolled withdrawals, have not yet been addressed because there is no control rod design. Accidents of particular interest are water/steam ingress events (potential reactivity insertion) and total losses of forced convection cooling.

A test reactor introduces some additional accidents to be considered. Most accidents initiated in the loops, such as a loop blowdown or loss of cooling, will be seen in the reactor as a small perturbation in the reactivity that would be bounded by control rod-driven reactivity events. Failure of one of the

irradiation loops could result in the release of radioactive material to the reactor building. Liquid metal or molten salt loops would be at low pressure, making piping failure less likely. Specific transport analyses would need to be performed for the reactor building layout and systems to determine if limits on loop source terms would need to be imposed on the experiments to ensure that atmospheric releases are within established safety limits.

The most likely initiator for a water/steam ingress event is a steam generator tube rupture. Designs for commercial plants have included a steam generator feedwater dump system to depressurize the steam generator secondary side, thus reversing the break flow and minimizing the water/steam ingress; this system could be used for this reactor as well. A water loop in the core is also a potential source for this event, although failure of both the experiment pressure boundary inside the reactor vessel and the primary coolant system boundary in the same test well may fall into the beyond design basis accident realm, because it involves independent failures of two pressure boundaries.

Total losses of forced convection cooling are referred to as conduction cooldown transients, because the heat in the core is conducted (and radiated) to the reactor vessel and then to the RCCS. In a pressurized conduction cooldown (PCC), the primary coolant system pressure boundary remains intact. In a depressurized conduction cooldown (DCC), the primary coolant system is breached (usually a loss-of-coolant accident). The DCC typically produces the limiting fuel temperatures. Both DCC and PCC transient calculations were performed for nominal core configurations and for some of the steady state sensitivity cases. Some transient sensitivity calculations were also run. The calculations were performed to provide an indication of the passive safety of the design and to identify potential vulnerabilities.

## 4.2.1    Steam Ingress

The reactivity impact to the core from steam ingress was calculated by adding steam to the core coolant channels. The steam was assumed to be at the same average conditions as the helium, 500°C and 7.0 MPa, yielding a steam density of 0.0209 g/cm$^3$. The steam mass fraction was varied from 0 (pure helium) to 100% in 10% increments.

The calculated results basically showed no change in the k-effective, or no impact to the core reactivity from steam ingress. This is in contrast to typical commercial HTGR designs, where the fuel compacts are much more heavily loaded with TRISO particles in order to achieve much longer power cycles (18 months). For example, commercial HTGR designs would use particle PFs in the range of 35-45%. The relatively high PF in conjunction with a fuel block design similar to the standard FSV fuel block always results in an under-moderated core. During a steam ingress event, the hydrogen atoms provide additional neutron moderation and increase core reactivity. For this HTGTR design, the core configuration and uniform particle PF of only 15% result in a core that is near optimal moderation, such that addition of extra moderation from steam ingress produces an insignificant change in core reactivity.

## 4.2.2    Depressurized Conduction Cooldown

DCC transients were simulated for each of the nominal core configurations. At the beginning of the transient, a 1-s flow coastdown and a 1-s depressurization to atmospheric pressure were imposed; a scram signal was also assumed to be generated. Early scoping calculations showed that a longer coastdown or depressurization resulted in lower peak temperatures. Helium cooling flow on the inside of the center irradiation tube was assumed to coast down over 5 s. The reactor vessel was modeled as being open only at the outlet plenum connection to the hot duct, and the helium available to flow back into the system was at the nominal outlet temperature of 650°C. All of the figures shown are from calculations with 4-mm gaps between the blocks.

### 4.2.2.1    Base-Case Calculations

Figure 4-1 shows peak fuel temperatures from the nominal cases for each core height. The temperatures decrease quickly at the beginning of the transient, because fission power is dropping and the

large flow of helium out the break increases the heat transfer from the fuel blocks. The peak temperature is also dropping as heat is redistributed in the core. During steady state, temperatures increase steadily from the top to the bottom of the core. Once forced convection cooling is lost, axial conduction reduces the temperatures at the bottom of the core while increasing them higher up. The peak temperatures increase until heat removal through the RCCS exceeds the decay heat, after which a steady temperature decrease begins. The peak temperatures during the transient are well below the steady-state values.

Peak temperatures in the central reflector are presented in Figure 4-2. These temperatures were very close to those of the fuel during most of the transient. Figure 4-3 shows the peak temperatures in the Ring 3 reflector blocks. Peak temperatures in the inner and outer halves of Ring 4, which contain the control rod and irradiation tube holes, are presented in Figures 4-4 and 4-5, respectively. Figure 4-6 presents the peak temperatures in Ring 5, and Figure 4-7 shows the peak temperature in the PSR. While the same trend is present in all of the temperatures, the peak values get progressively lower farther away from the fuel. This trend continues through the core barrel and reactor vessel, as shown in Figures 4-8 and 4-9, respectively. The core barrel temperatures are considerably higher than the reactor vessel temperatures.

Coolant temperatures in the lower plenum are shown in Figure 4-10; Figure 4-11 presents those in the upper plenum. After the system depressurizes and forced flow stops, a natural circulation flow was established in the core region, with flow generally up in the fuel blocks and central reflector and down in the outer reflector. This downward flow from the cooler regions of the core (Ring 5 and the PSR) caused the temperature in the lower plenum to continue decreasing for about 6 hours before beginning to increase. In the upper plenum, the temperature increased immediately as hotter fluid from the core rose to mix with the cooler helium that was there initially. Peak temperatures were reached in 2 to 3 days. In the lower plenum, only the 200-MW case had temperatures higher than the steady state value.



Figure 4-1. Peak fuel temperatures for the three nominal core DCC transients.

28
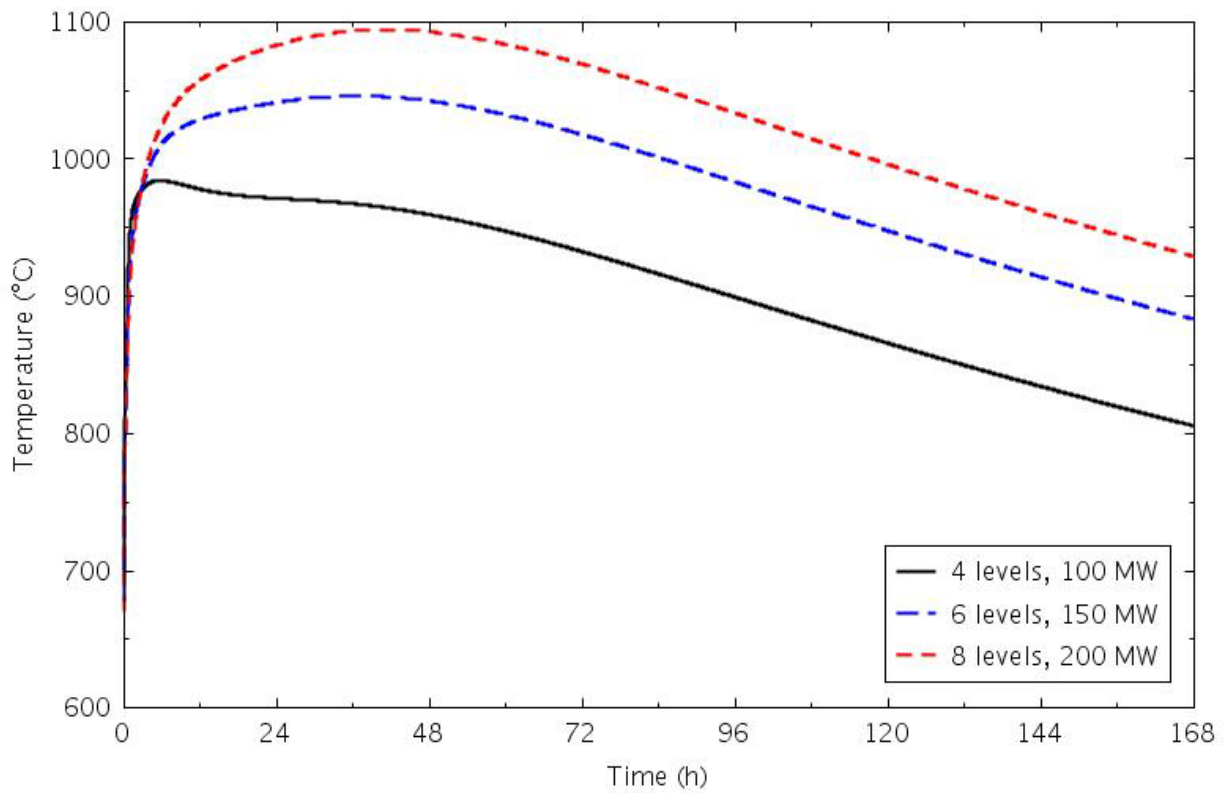
Figure 4-2. Central reflector peak temperatures for the three nominal DCC transients.



Figure 4-3. Ring 3 reflector peak temperatures for the three nominal DCC transients.

Figure 4-4. Reflector Ring 4 inner half peak temperatures for the three nominal DCC transients.



Figure 4-5. Reflector Ring 4 outer half peak temperatures for the three nominal DCC transients.

30

Figure 4-6. Reflector Ring 5 peak temperatures for the three nominal DCC transients.
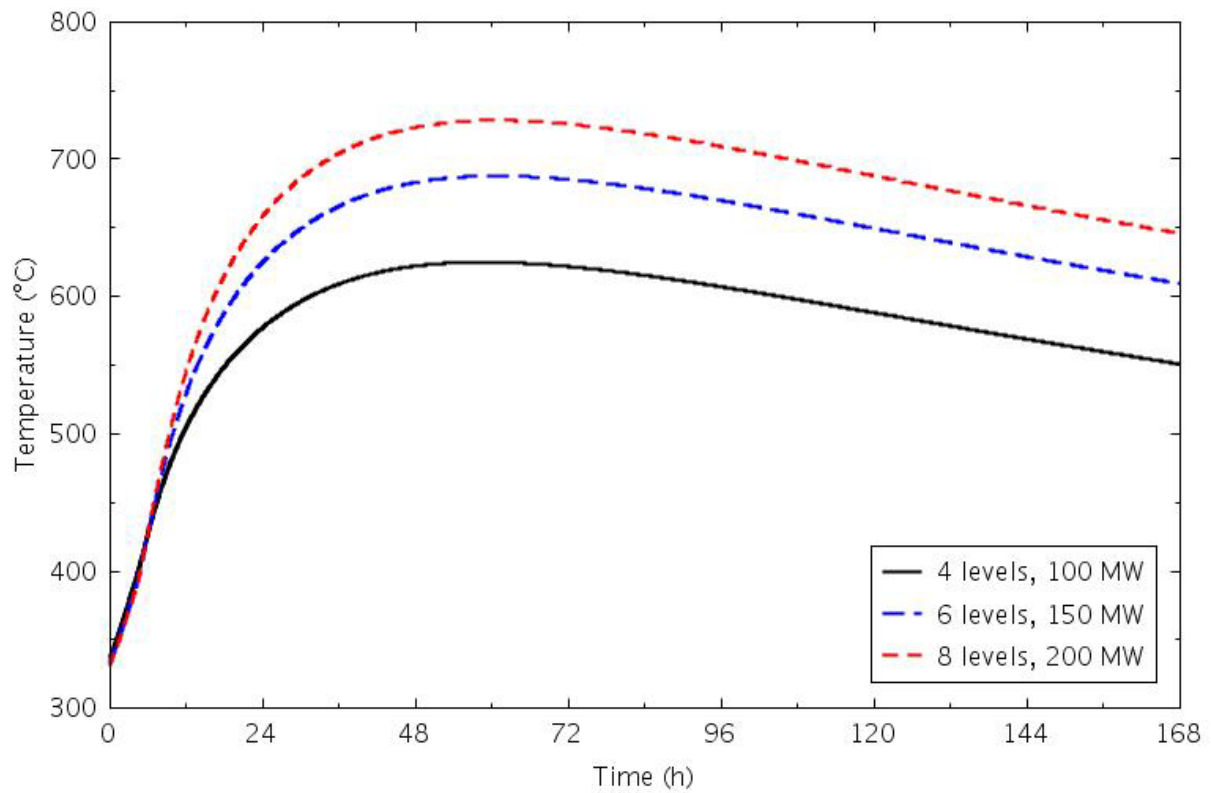

Figure 4-7. PSR peak temperatures for the three nominal DCC transients.
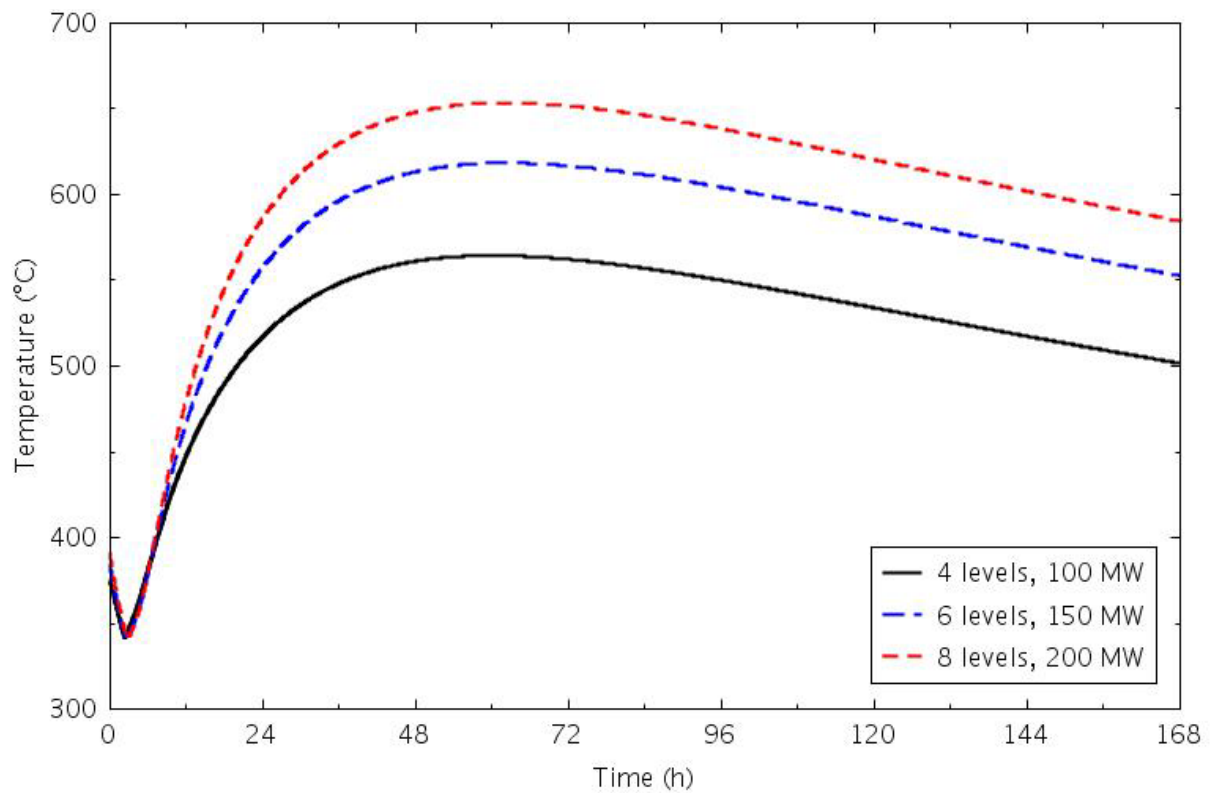
Figure 4-8. Core barrel peak temperatures for the three nominal DCC transients.



Figure 4-9. Reactor vessel wall peak temperatures for the three nominal DCC transients.
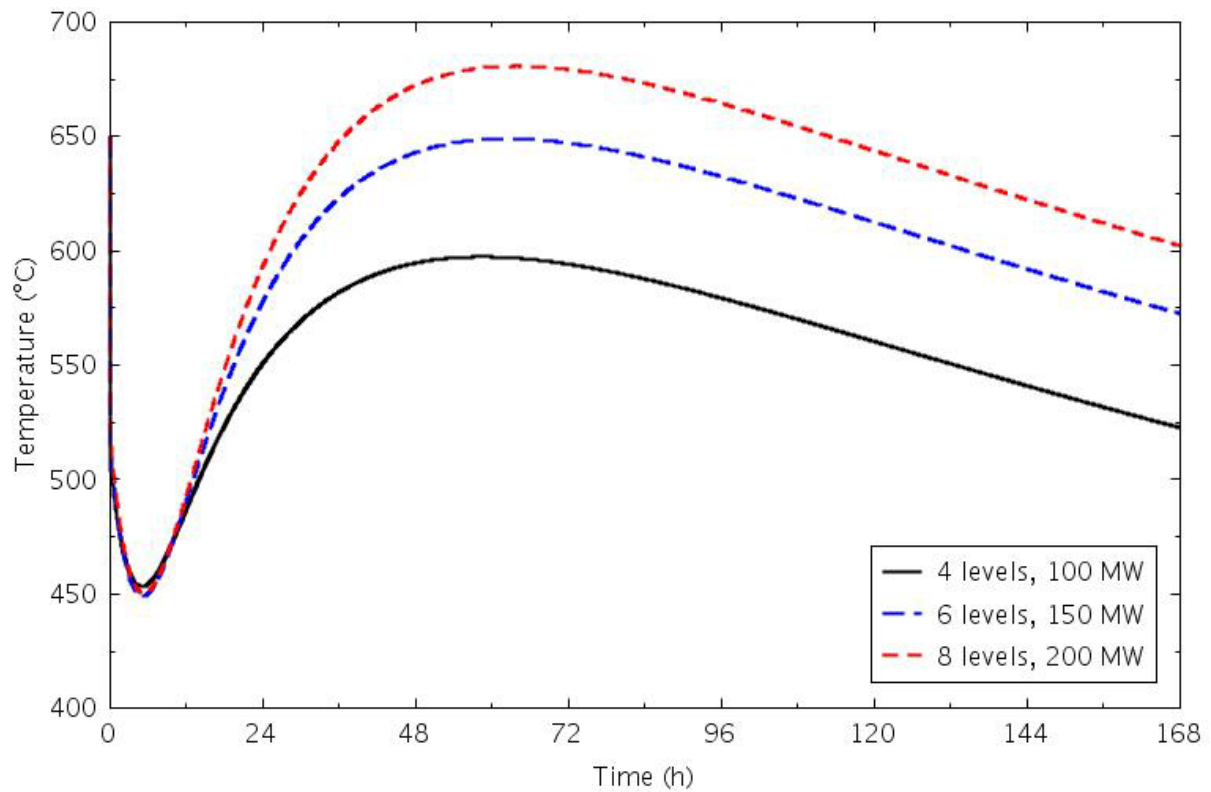
Figure 4-10. Lower plenum coolant temperatures for the three nominal DCC transients.



Figure 4-11. Upper plenum coolant temperatures for the three nominal DCC transients.

Water temperatures at the RCCS outlet are presented in Figure 4-12. The small temperature variation during the transient shows that a nearly constant boundary condition was provided.

One concern about high graphite temperatures in the core is how hot the experiment tubes may become. Figure 4-13 presents peak temperatures for the central reflector and the central irradiation tube for the 200-MW case. With no cooling on the inside of the tubes, the temperatures were about equal. While the peak temperature was well below the steel melting temperature of 1400°C, it was likely above the maximum temperature for a code-case pressure boundary. Since the irradiation tubes in the outer reflector would also be near the graphite temperatures, pressure boundary integrity following a conduction cooldown event could be a concern. For flow-through facilities cooled by the primary coolant, this should not be an issue; since these tubes do not contain pressure, a higher melting point material such as titanium or molybdenum could be used.

Figures 4-14 through 4-25 present results from the 8-level core at different power levels. The response was similar in all of the cases. Peak fuel temperatures increased 100-150°C for each 50-MW increase in core power, but also remained below the steady-state values for powers below 350 MW. The central reflector temperatures were close to the fuel temperatures, and the outer reflector temperatures decreased as they get further from the fuel. The peak temperatures occurred a little earlier as the power increased. The RCCS was still providing a nearly constant boundary temperature.

Results from the 4-level core calculations are shown in Figures 4-26 through 4-37. The peak fuel temperatures increased about 100°C for each 25-MW increase in power, but were all below the steady state values throughout the transient. There were no remarkable differences in transient behavior from those described above.
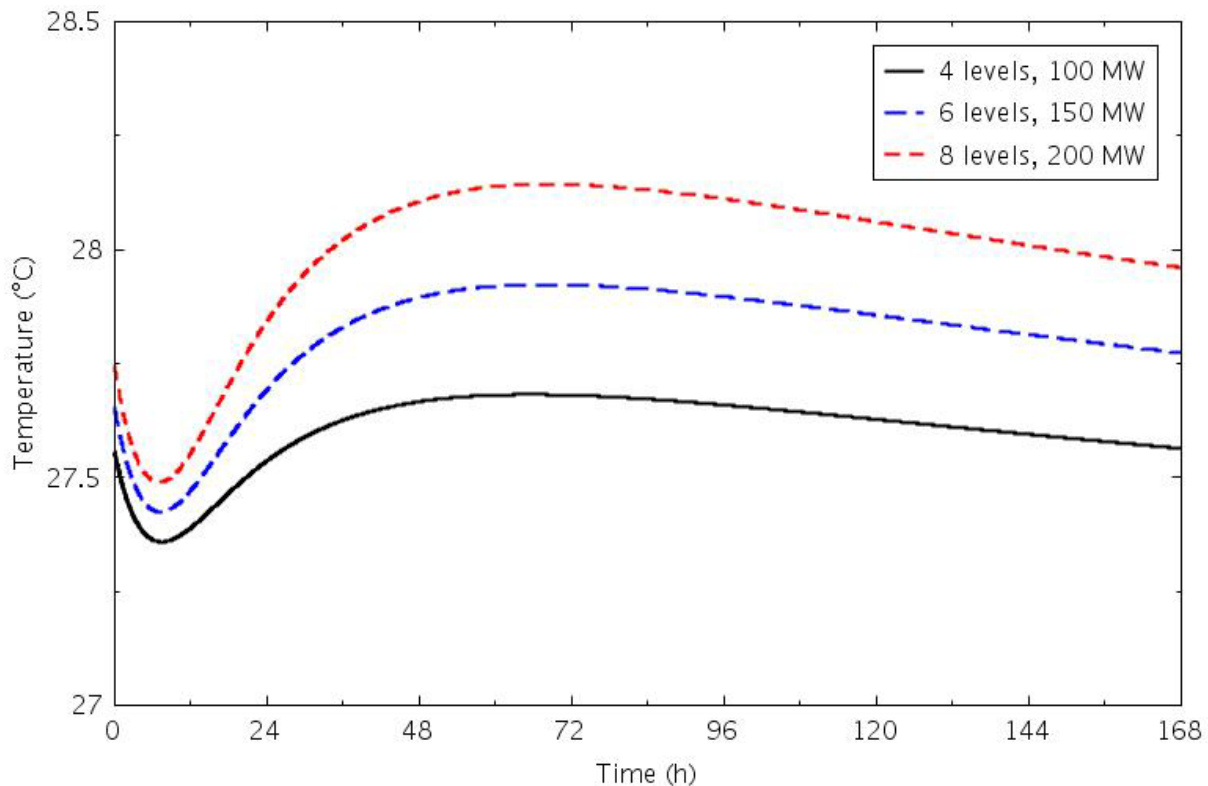


Figure 4-12. RCCS coolant outlet temperatures for the three nominal DCC transients.
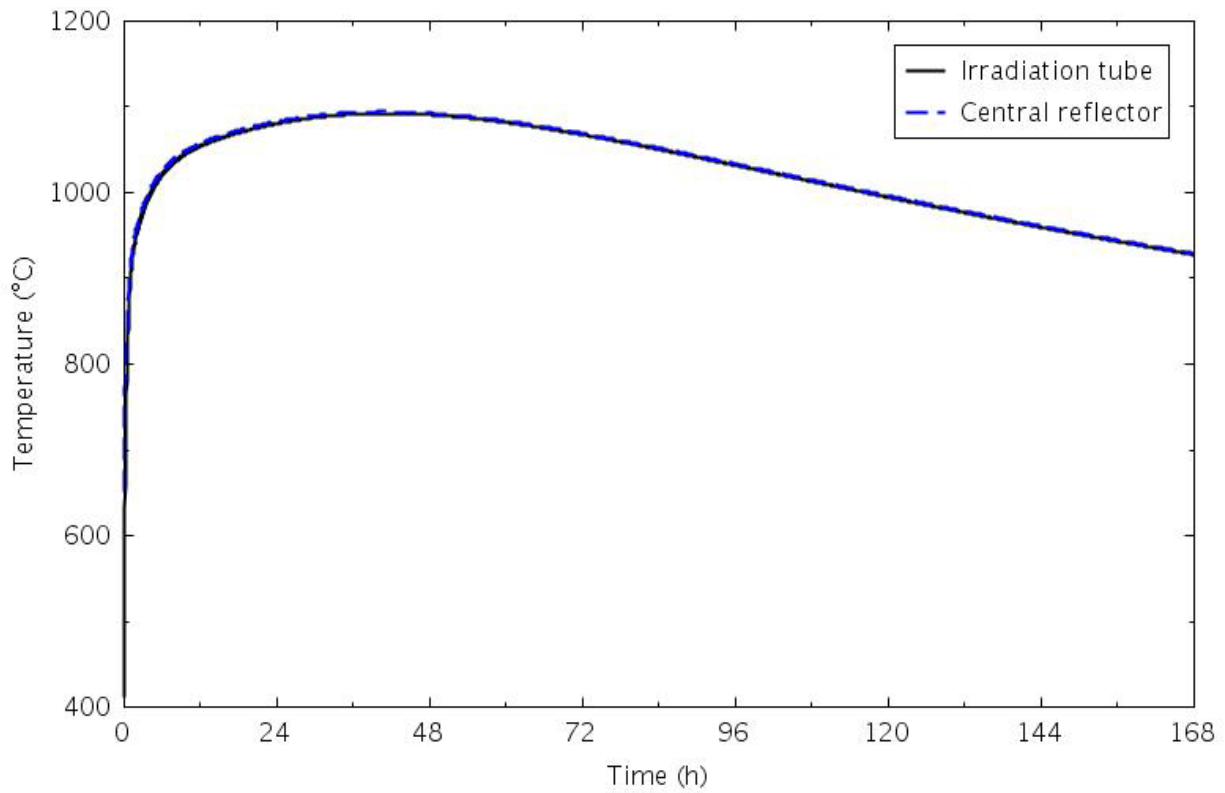
Figure 4-13. Central reflector and irradiation tube peak temperatures for the 8-level, 200-MW DCC transient.
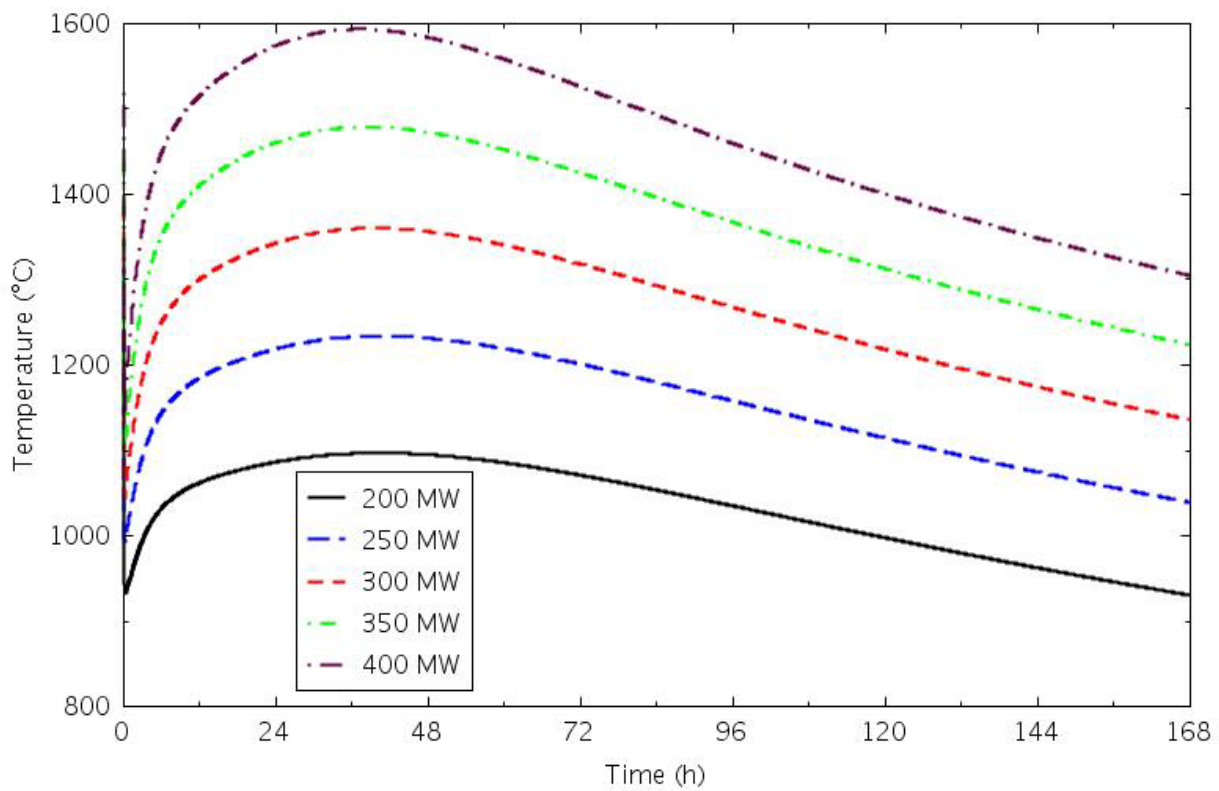


Figure 4-14. Peak fuel temperatures for the 8-level core DCC transients.
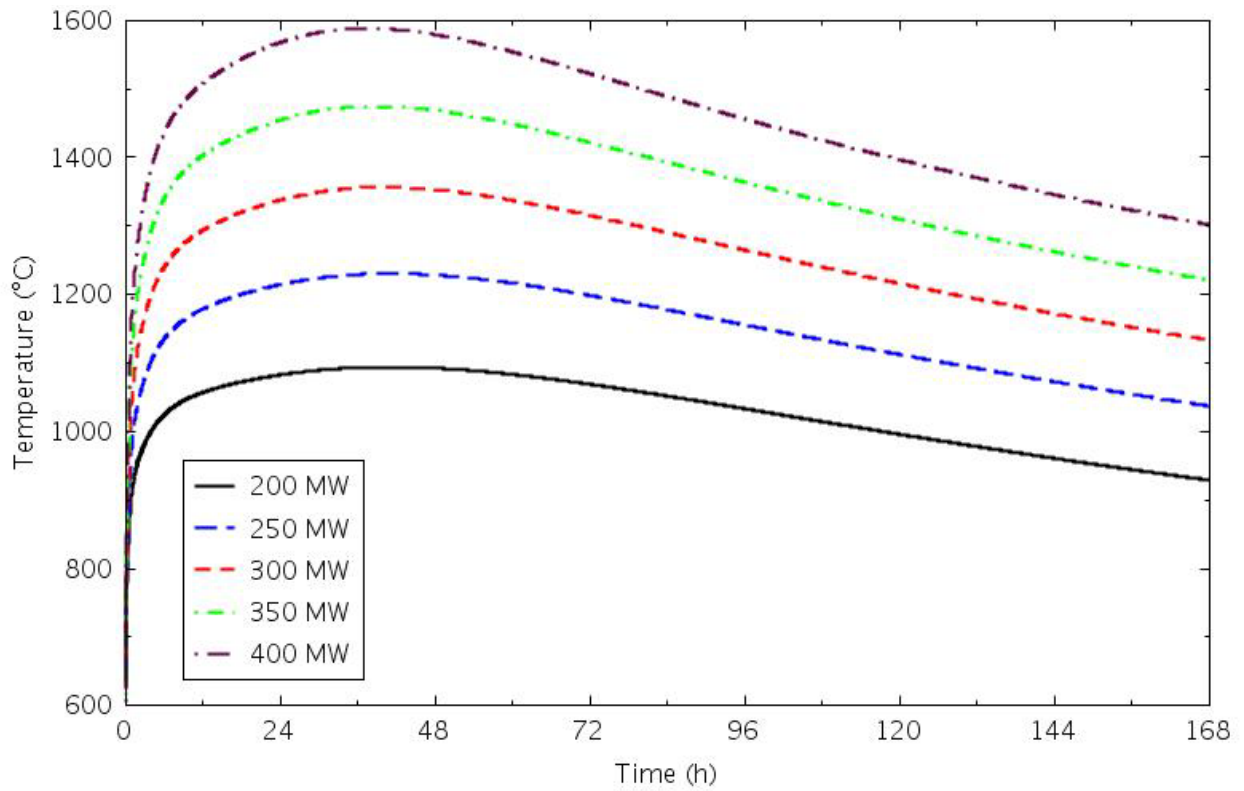
Figure 4-15. Central reflector peak temperatures for the 8-level core DCC transients.
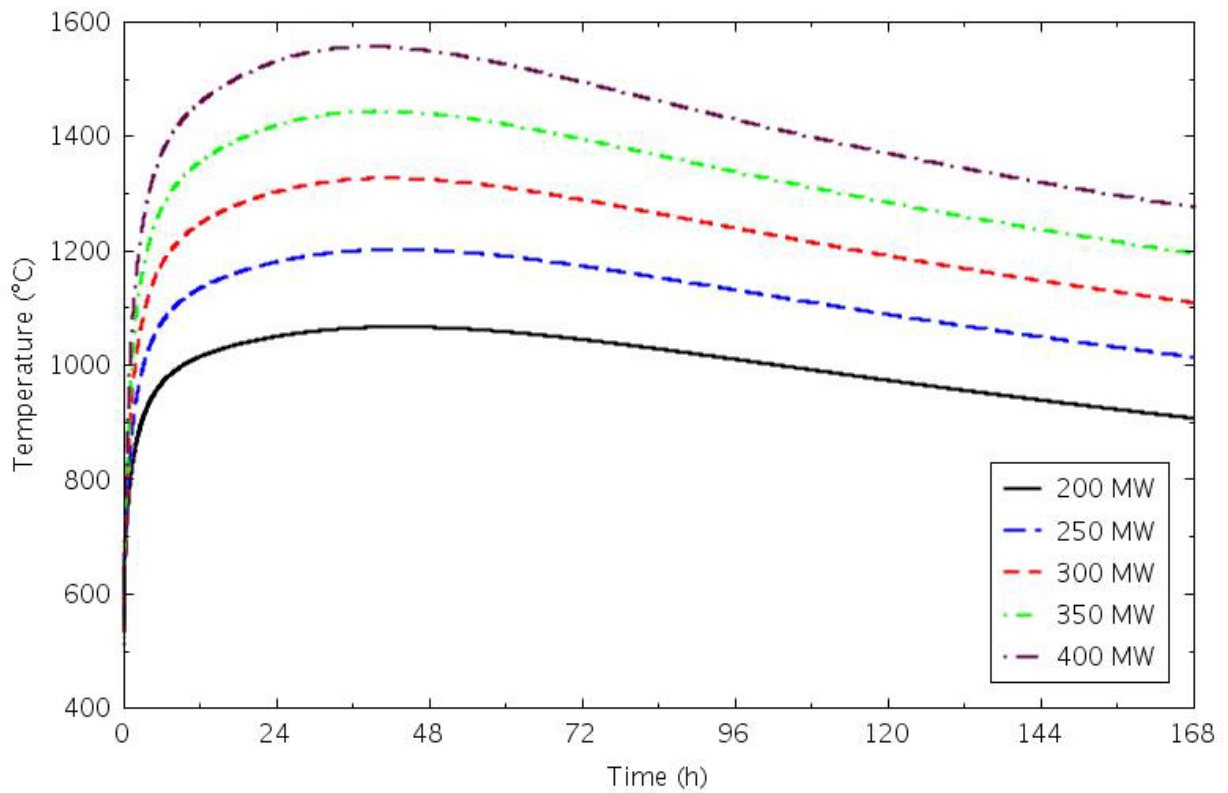


Figure 4-16. Ring 3 reflector peak temperatures for the 8-level core DCC transients.
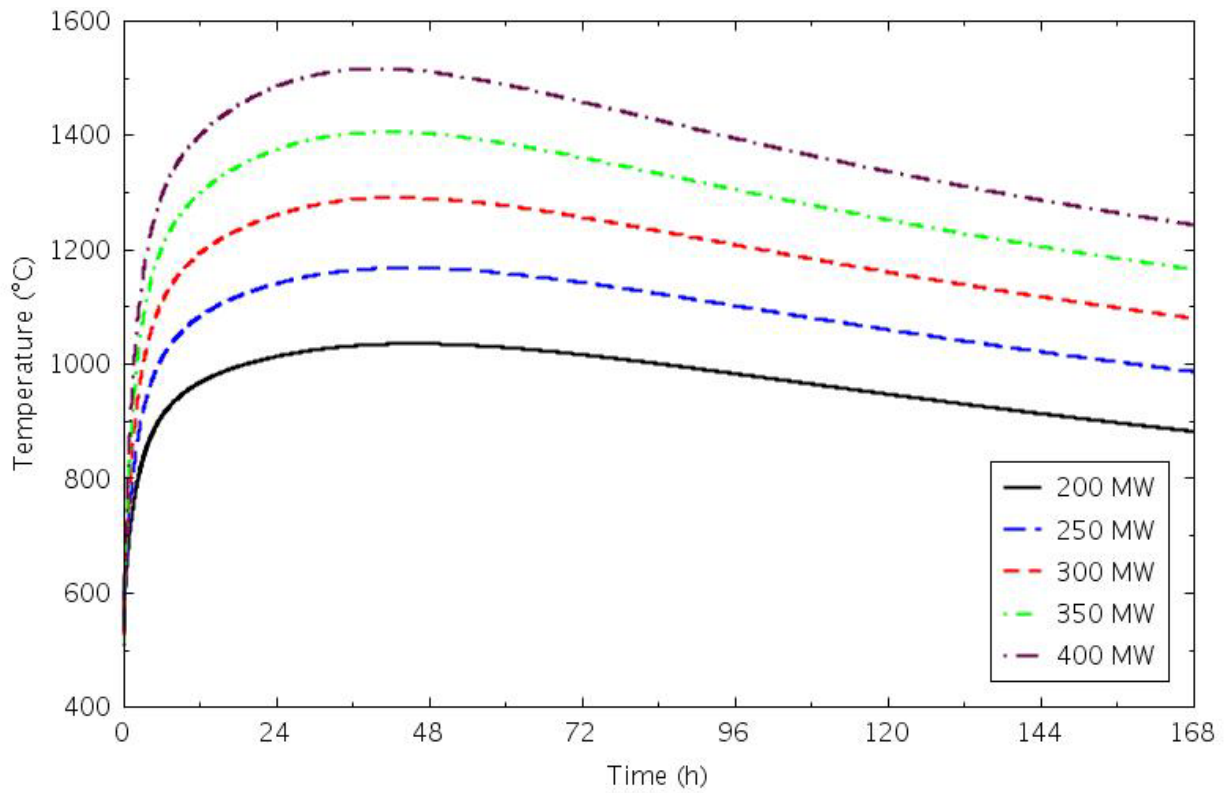
Figure 4-17. Reflector Ring 4 inner half peak temperatures for the 8-level core DCC transients.
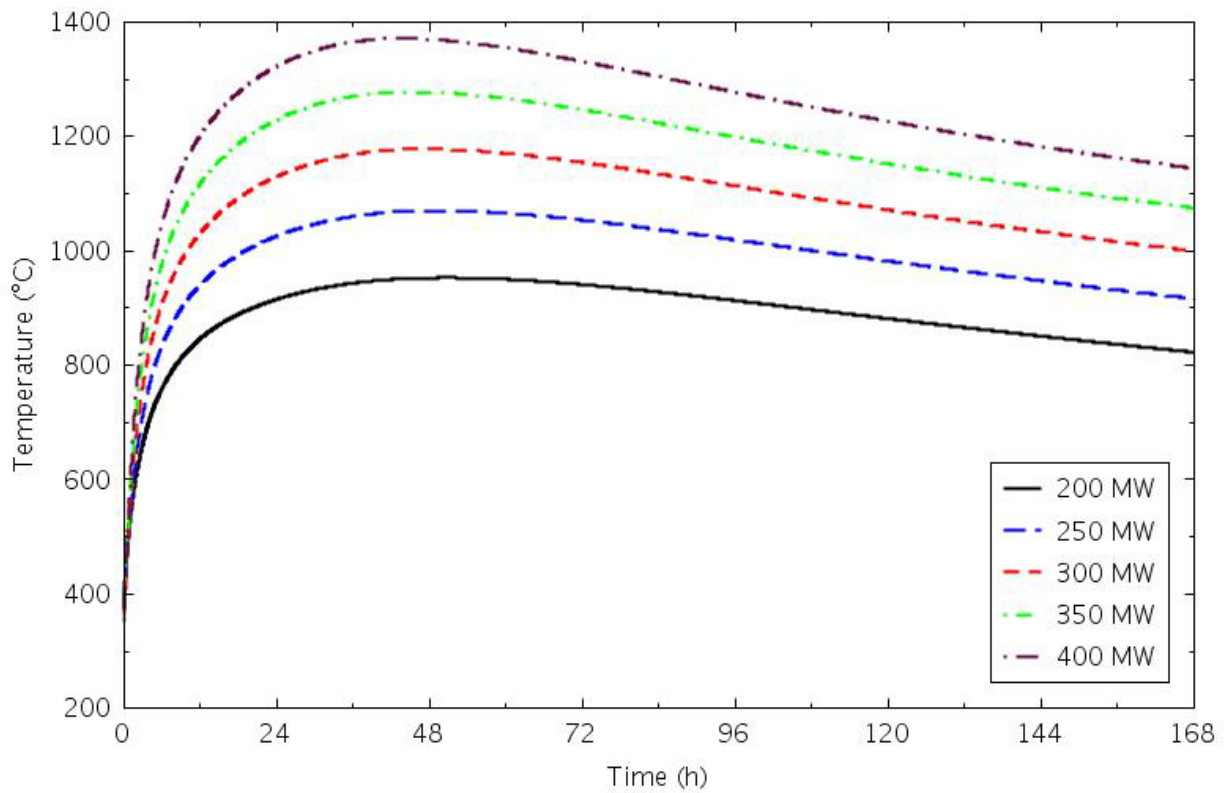


Figure 4-18. Reflector Ring 4 outer half peak temperatures for the 8-level core DCC transients.
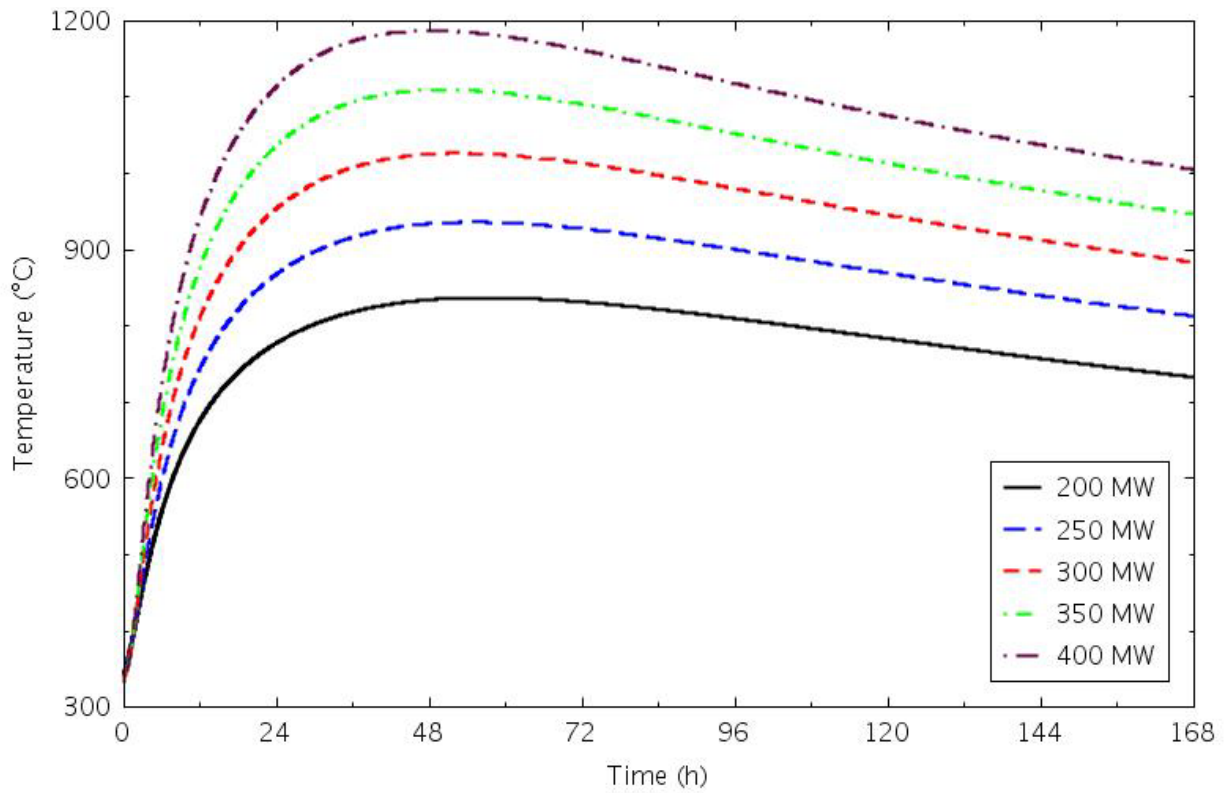
Figure 4-19. Reflector Ring 5 peak temperatures for the 8-level core DCC transients.
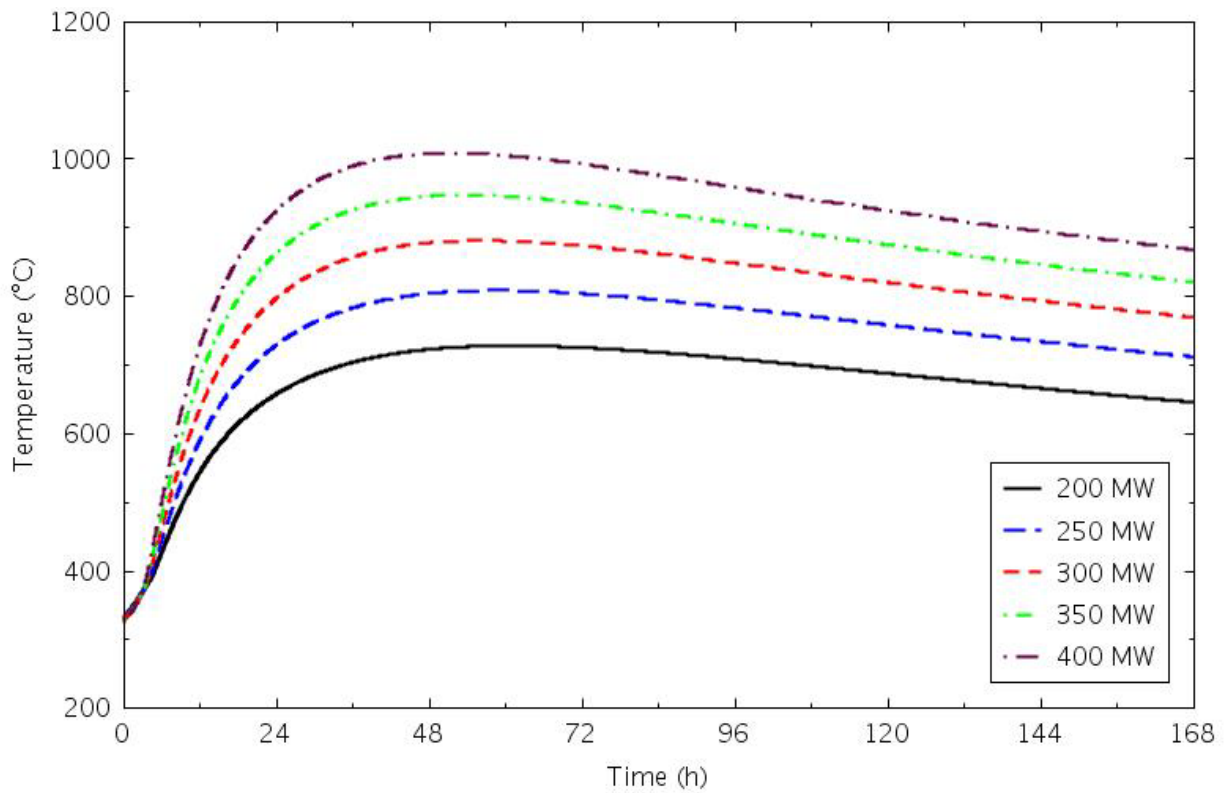


Figure 4-20. PSR peak temperatures for the 8-level core DCC transients.
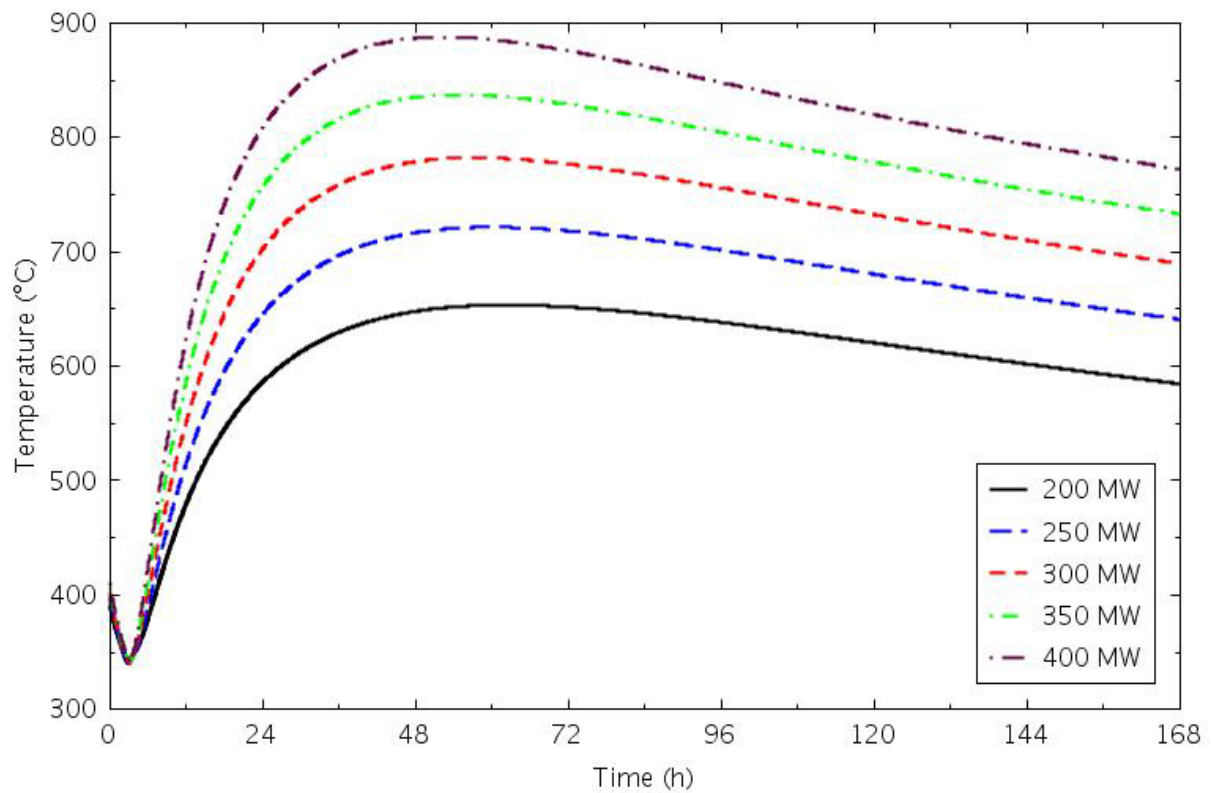
Figure 4-21. Core barrel peak temperatures for the 8-level core DCC transients.
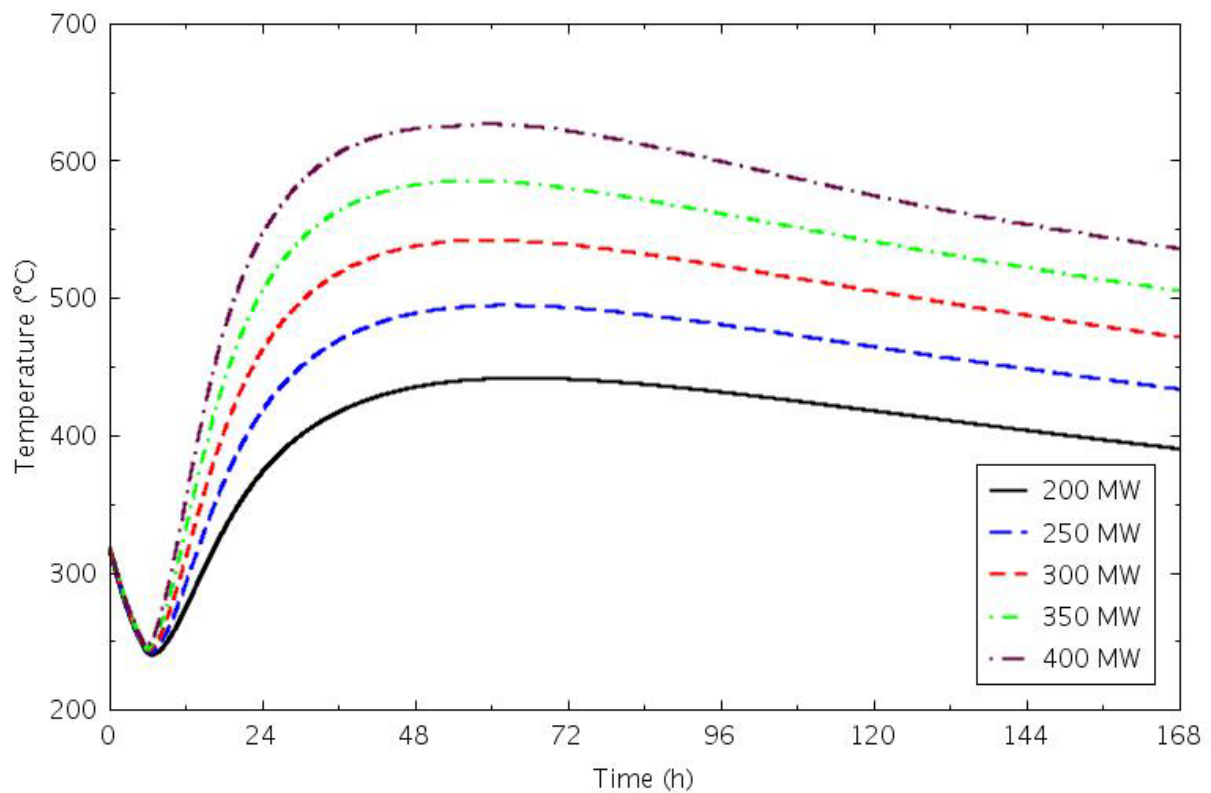


Figure 4-22. Reactor vessel wall peak temperatures for the 8-level core DCC transients.
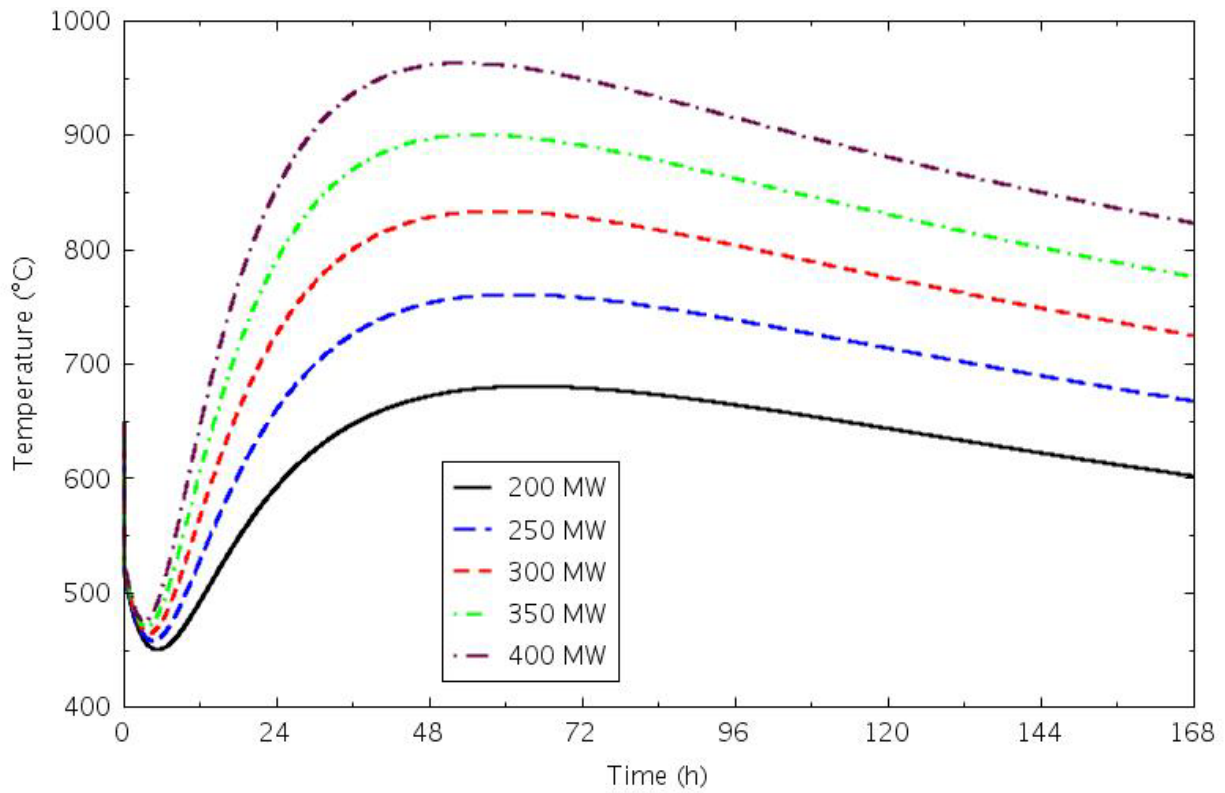
Figure 4-23. Lower plenum coolant temperatures for the 8-level core DCC transients.
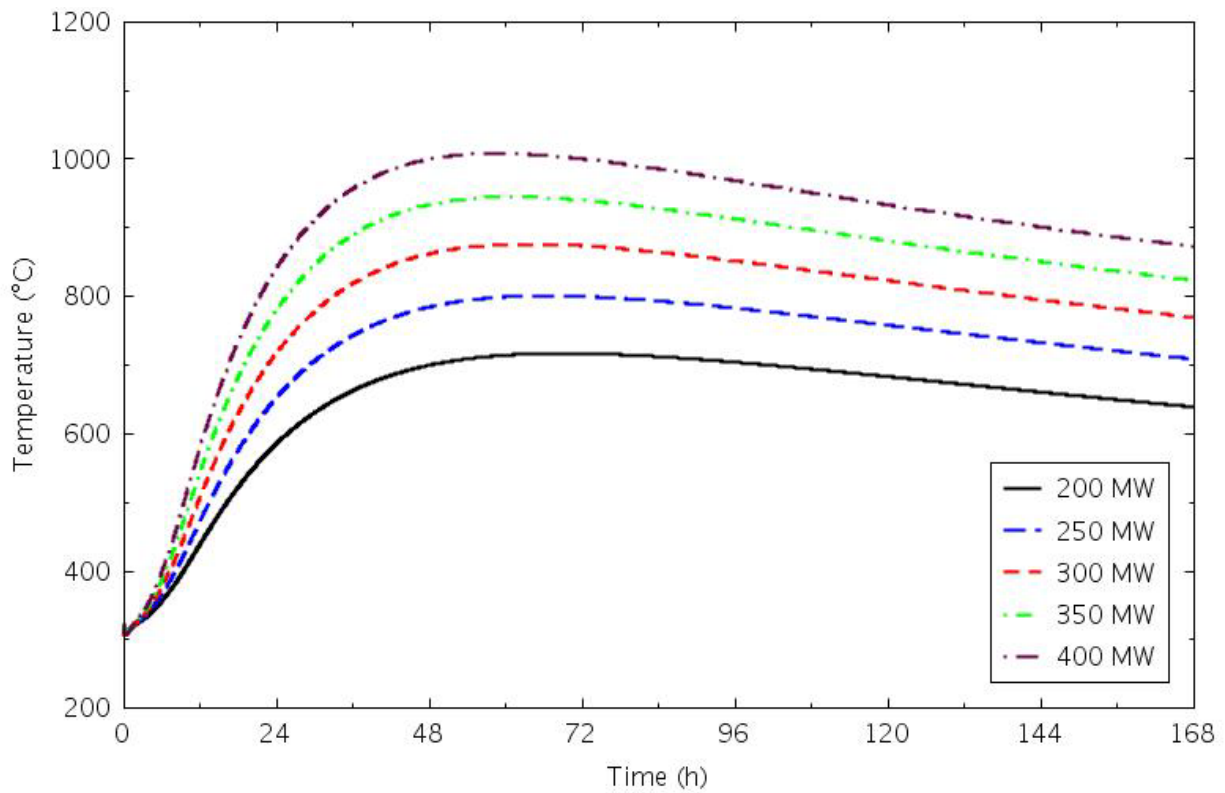


Figure 4-24. Upper plenum coolant temperatures for the 8-level core DCC transients.
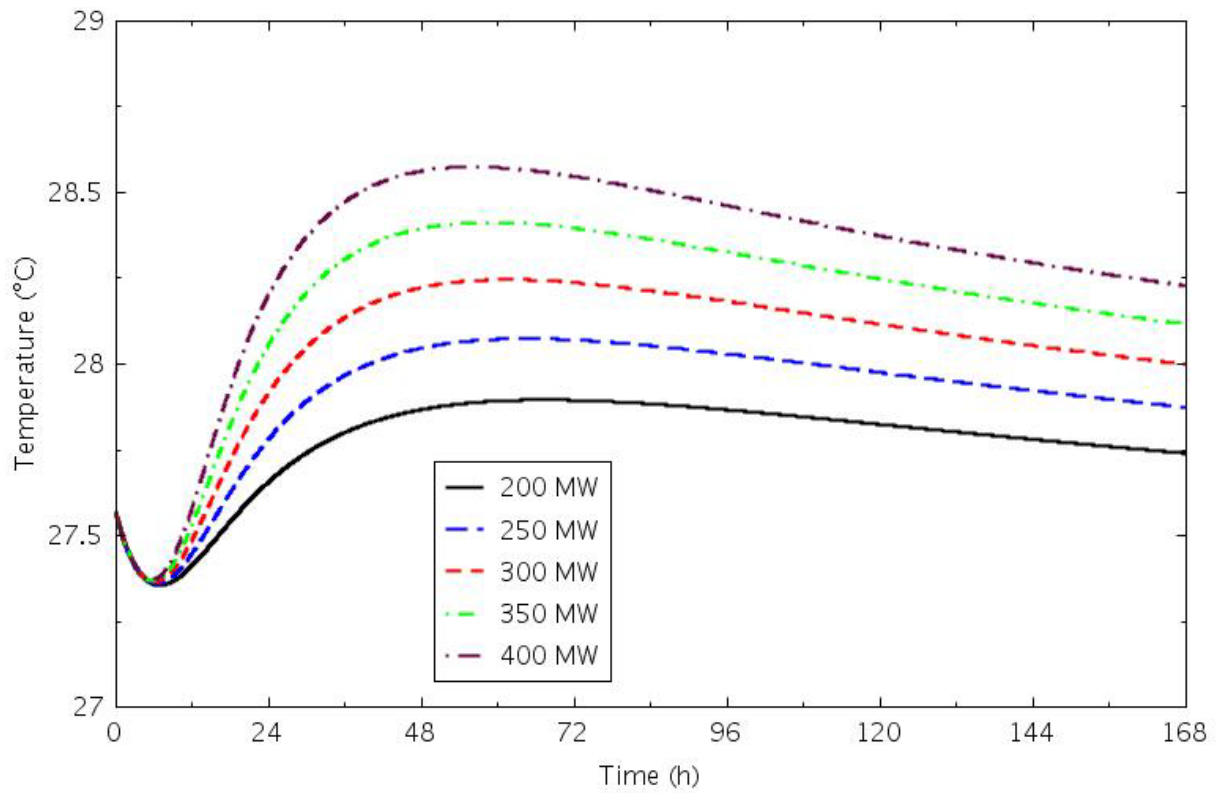
Figure 4-25. RCCS coolant outlet temperatures for the 8-level core DCC transients.
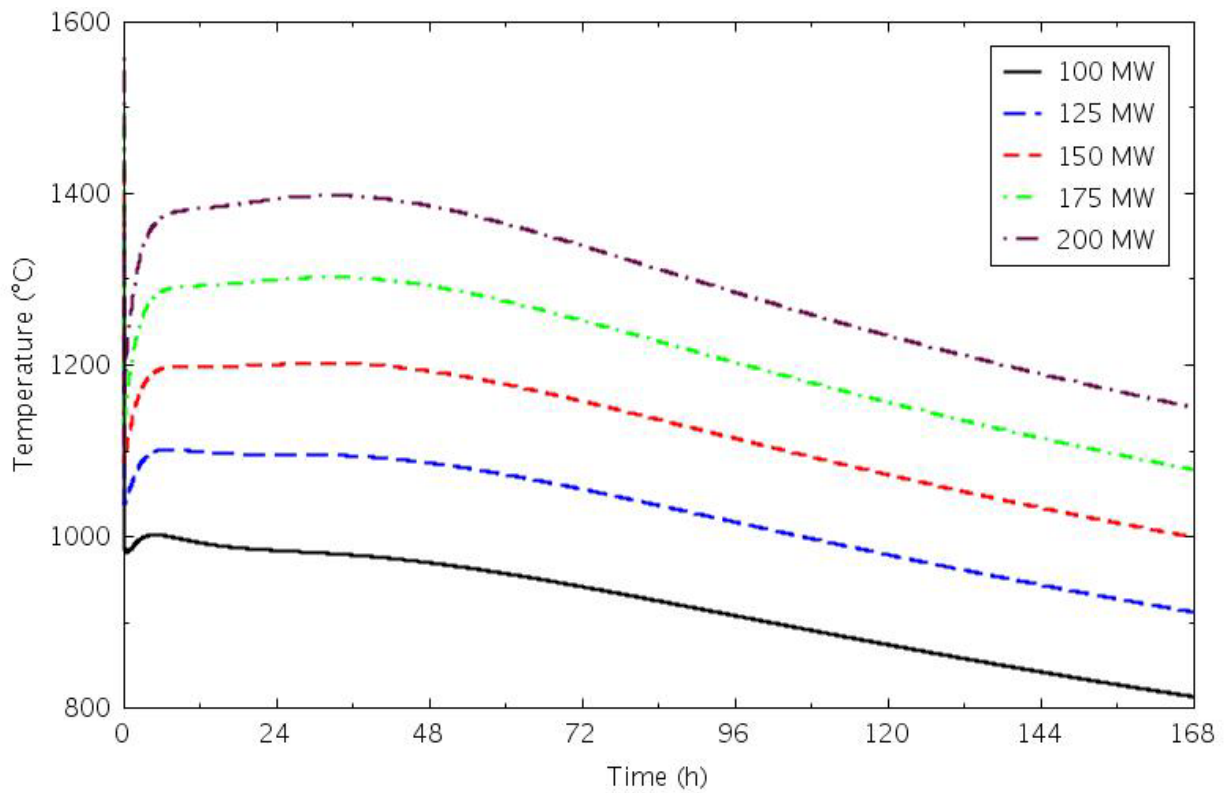


Figure 4-26. Peak fuel temperatures for the 4-level core DCC transients.
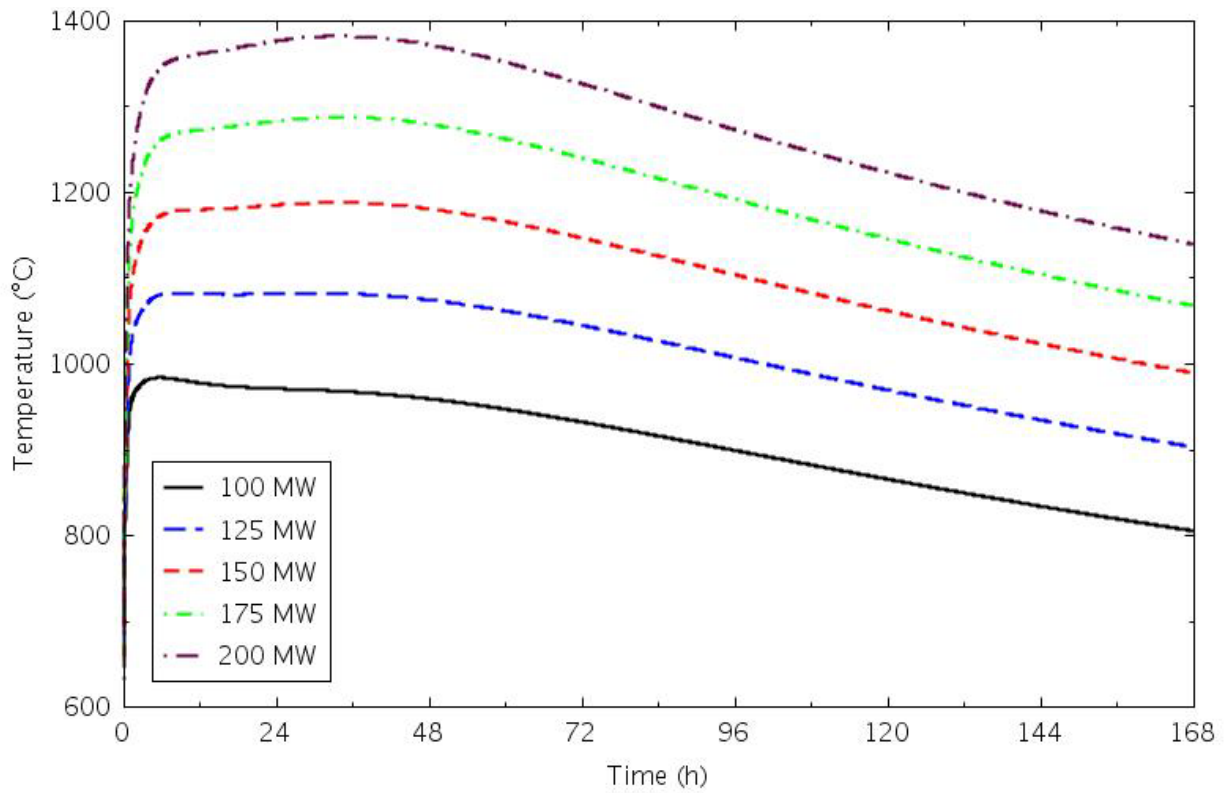
Figure 4-27. Central reflector peak temperatures for the 4-level core DCC transients.
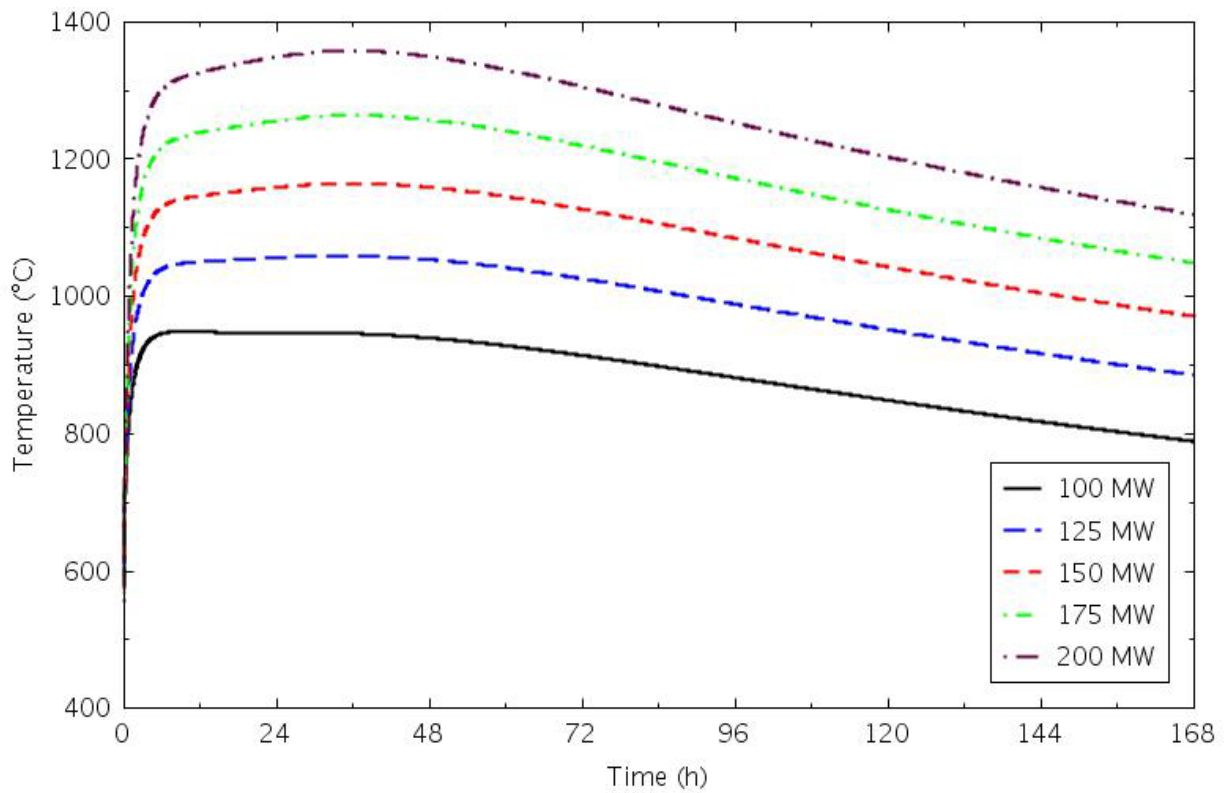


Figure 4-28. Ring 3 reflector peak temperatures for the 4-level core DCC transients.
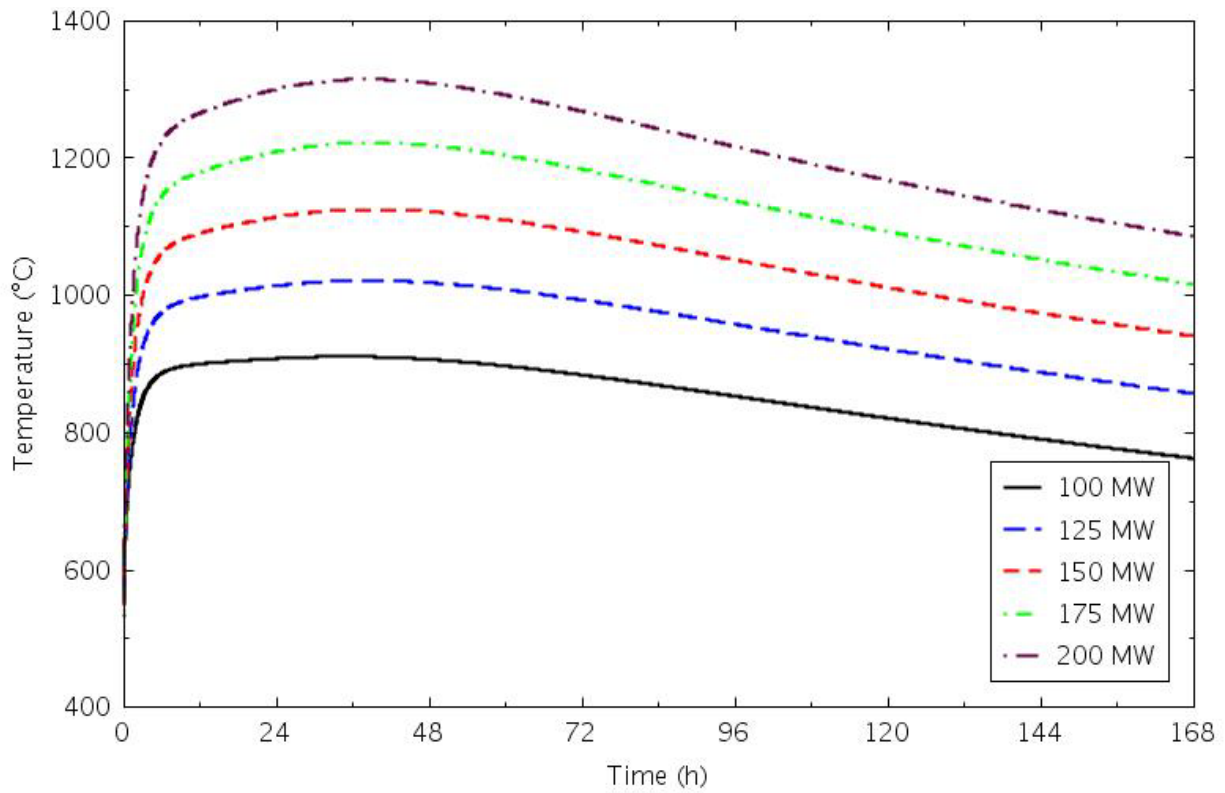
Figure 4-29. Reflector Ring 4 inner half peak temperatures for the 4-level core DCC transients.
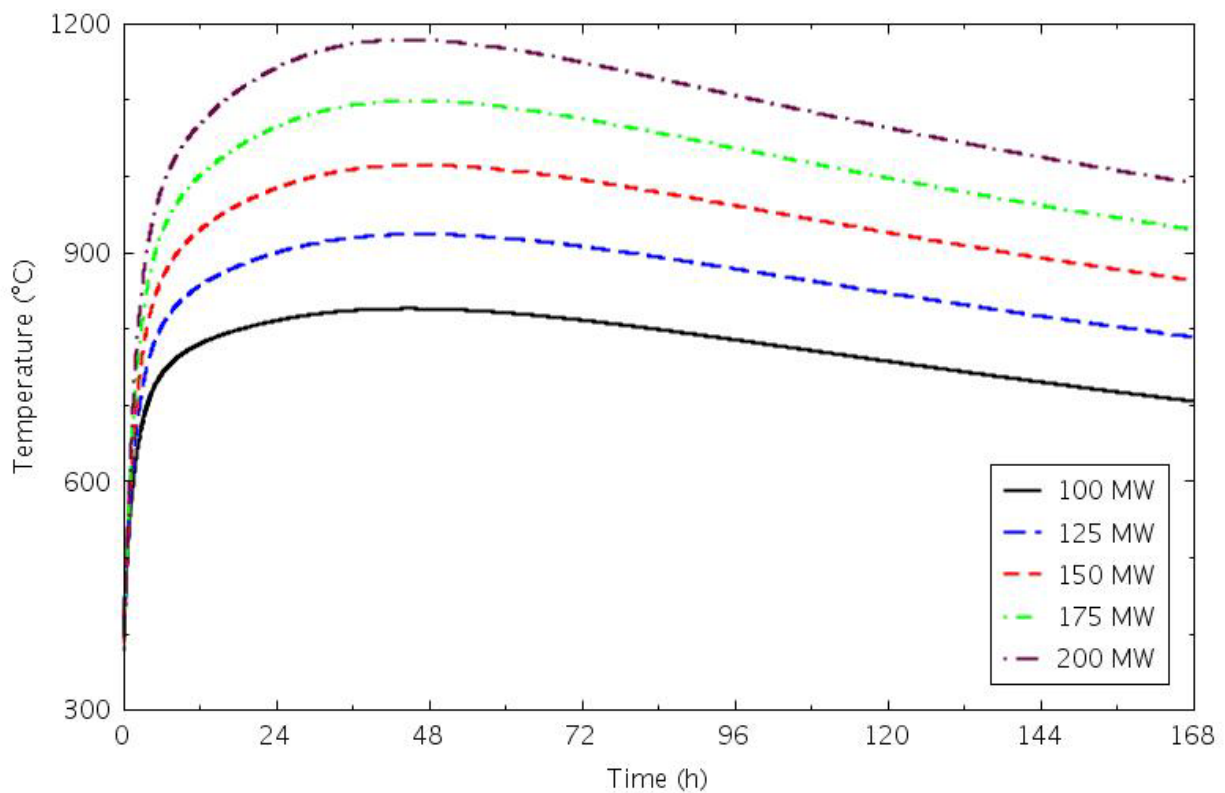


Figure 4-30. Reflector Ring 4 outer half peak temperatures for the 4-level core DCC transients.
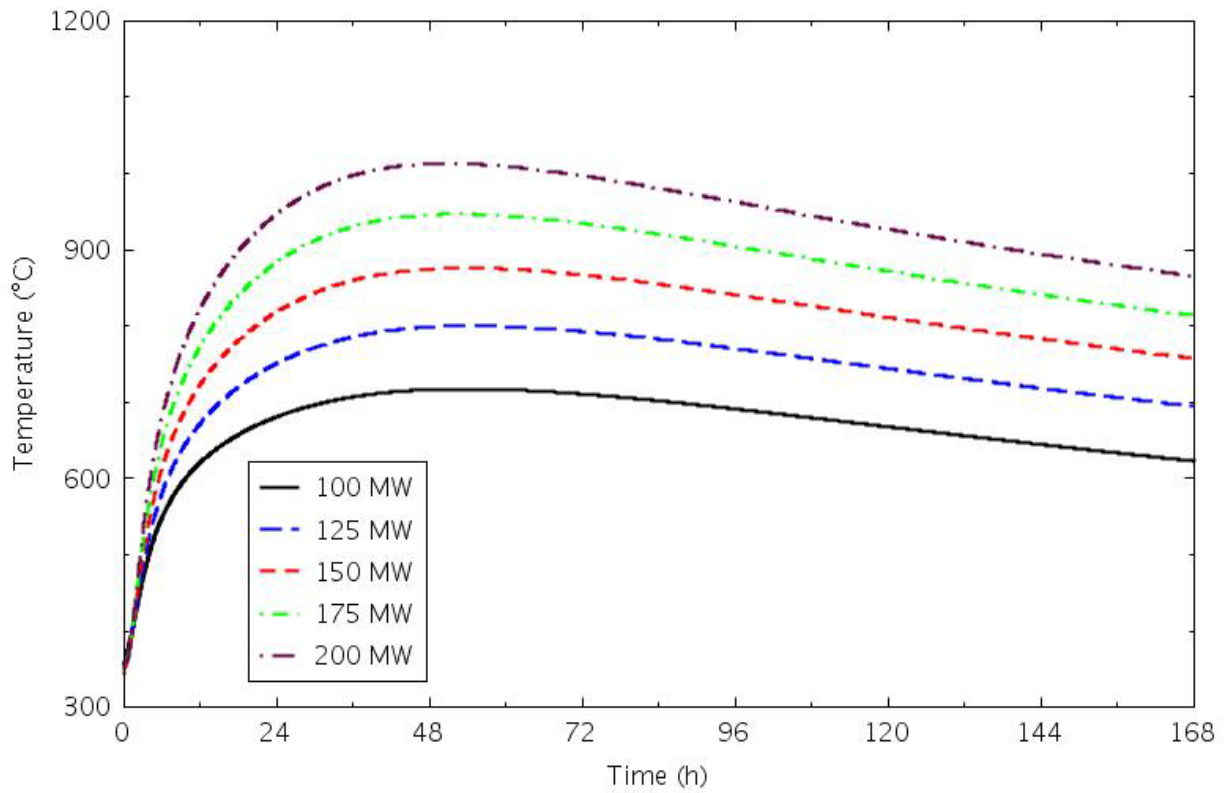
Figure 4-31. Reflector Ring 5 peak temperatures for the 4-level core DCC transients.
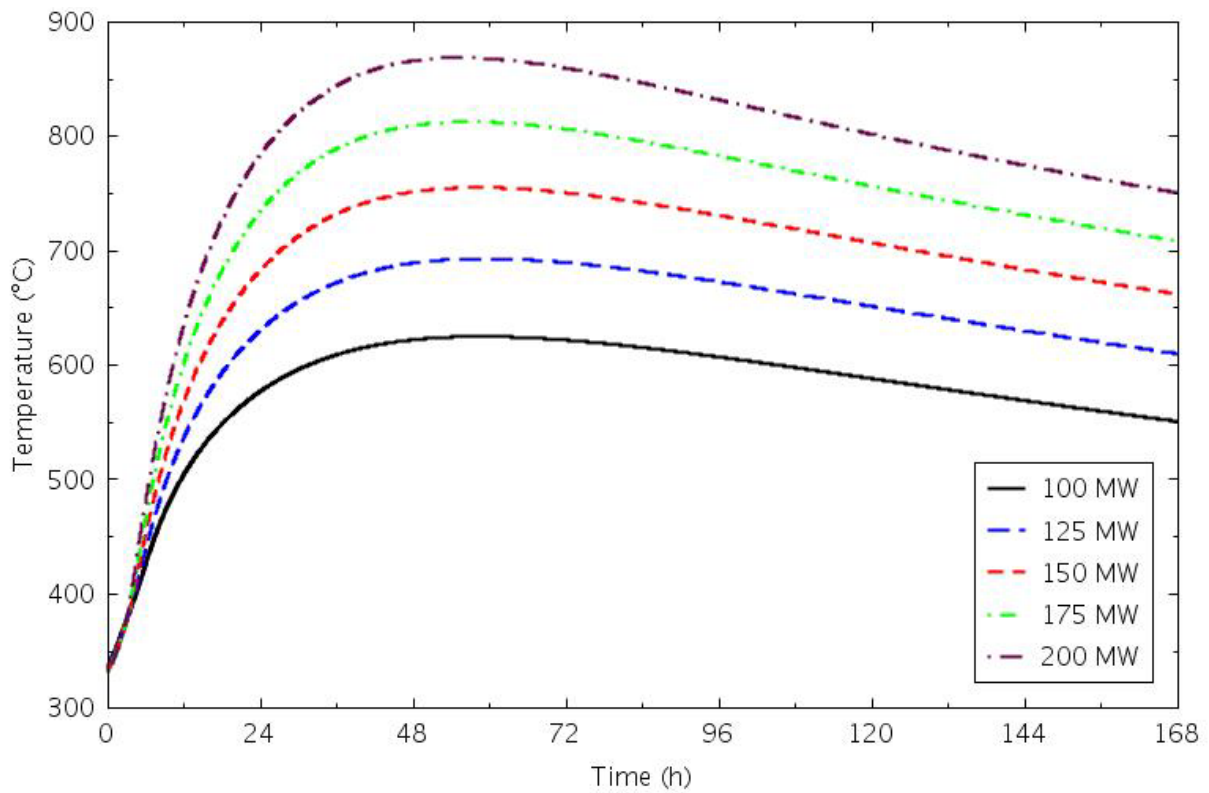


Figure 4-32. PSR peak temperatures for the 4-level core DCC transients.
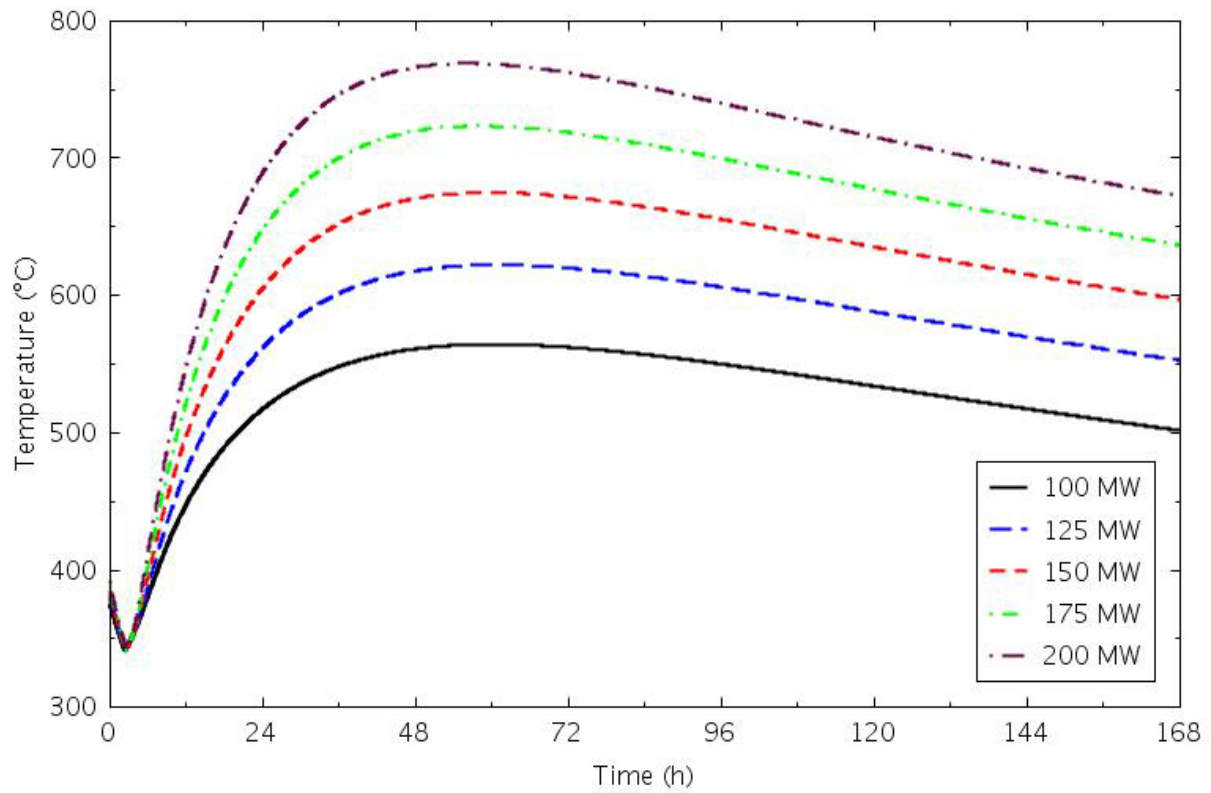
Figure 4-33. Core barrel peak temperatures for the 4-level core DCC transients.
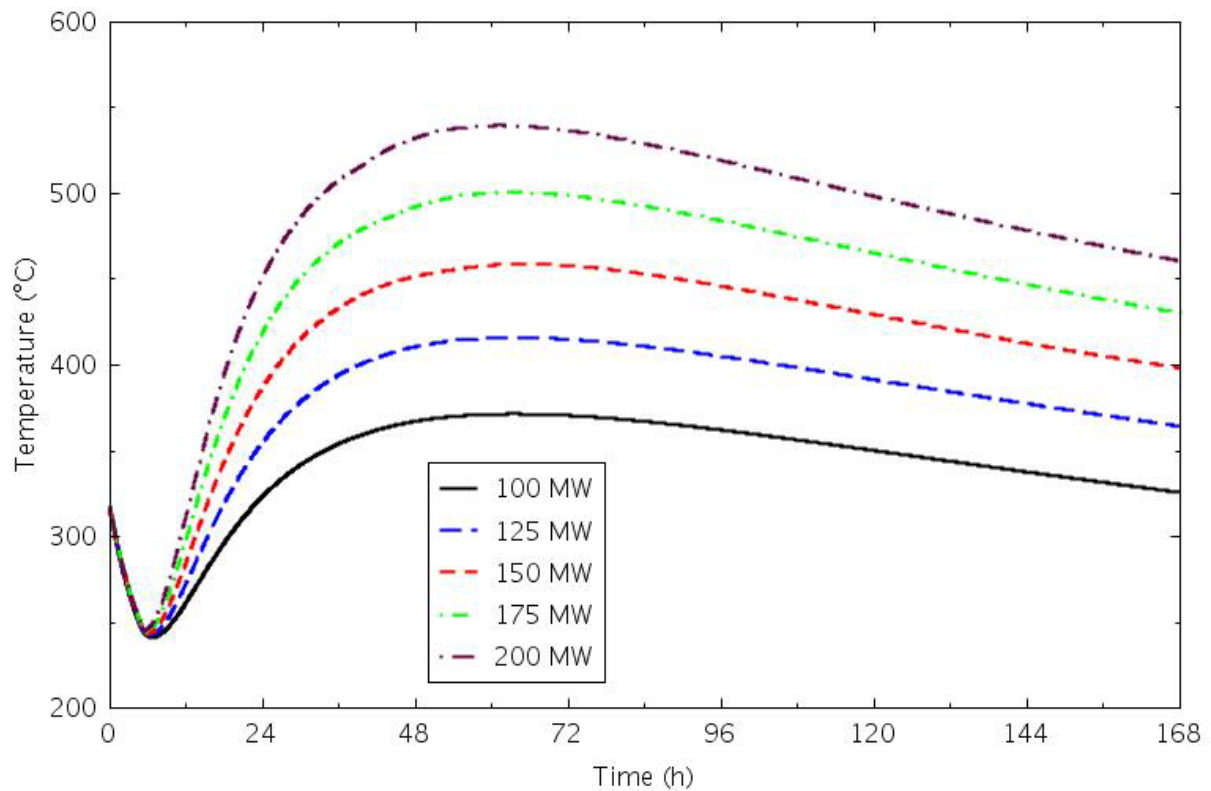


Figure 4-34. Reactor vessel wall peak temperatures for the 4-level core DCC transients.
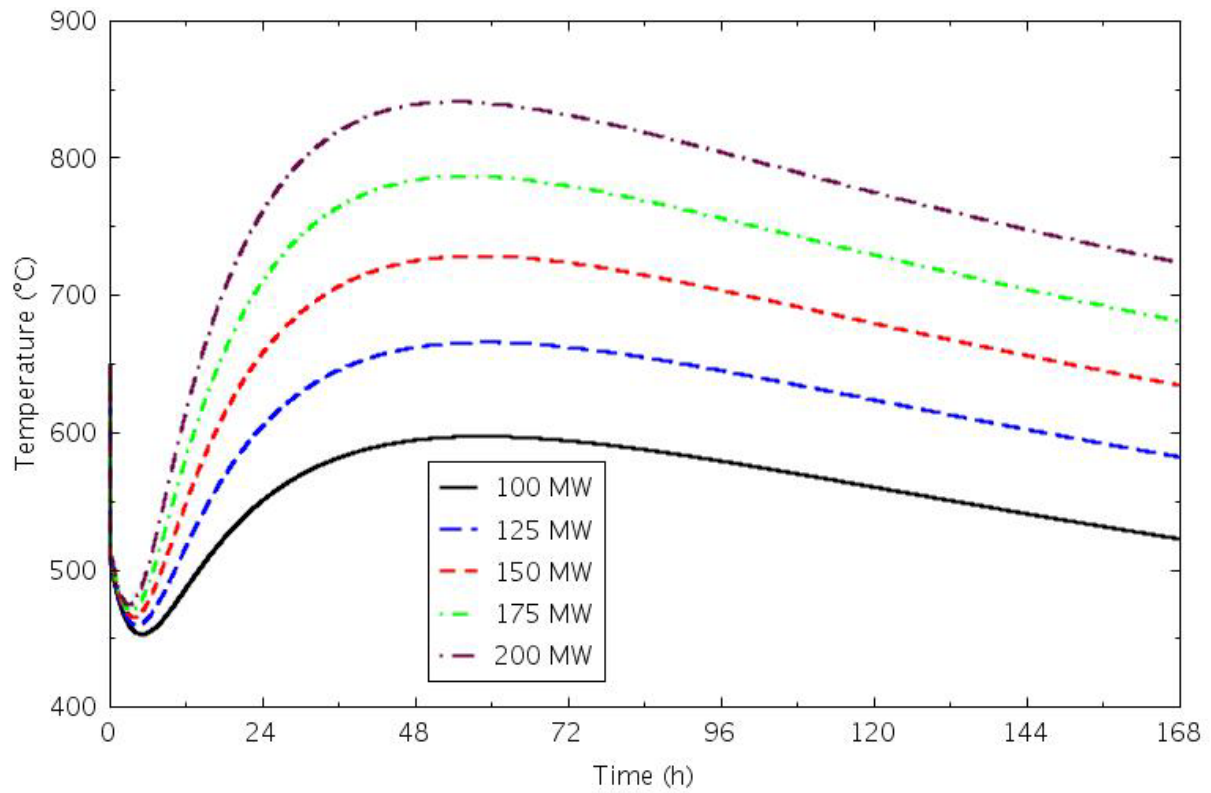
Figure 4-35. Lower plenum coolant temperatures for the 4-level core DCC transients.
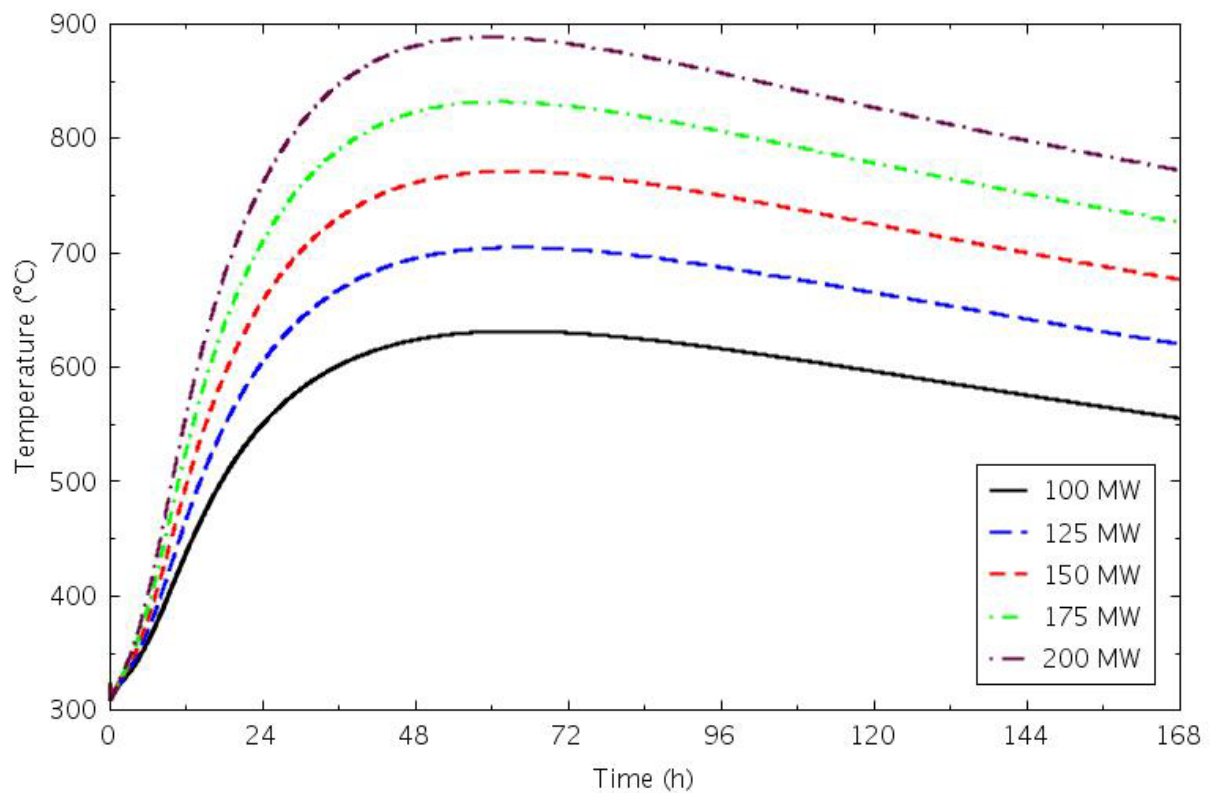


Figure 4-36. Upper plenum coolant temperatures for the 4-level core DCC transients.
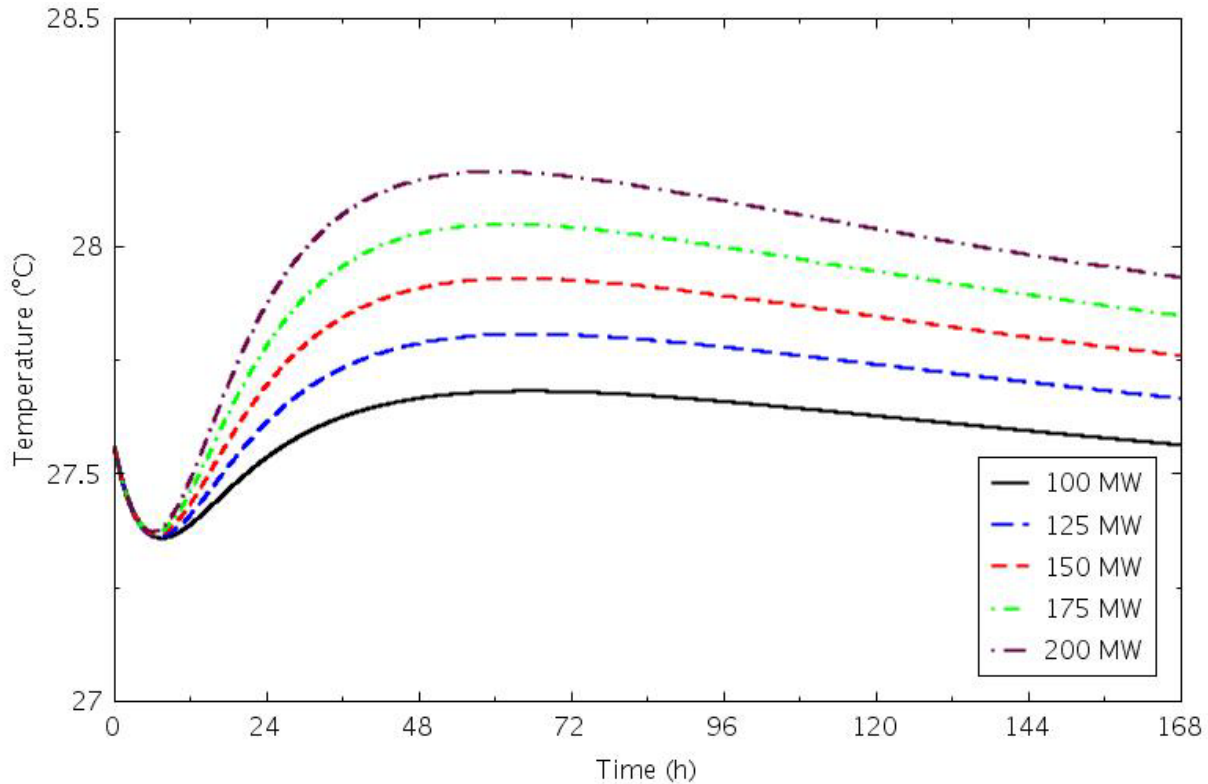
Figure 4-37. RCCS coolant outlet temperatures for the 4-level core DCC transients.

Figures 4-38 through 4-49 show results from the 6-level core calculations. The peak fuel temperatures increased about 150°C for every 50-MW power increase, but remained below the steady-state values. No notable differences from the transient response described above were observed.

### 4.2.2.2    *Sensitivity Calculations*

Transient calculations were performed that addressed the steady state sensitivity cases. Additional studies addressed delaying the reactor scram, adding a break at the vessel inlet, varying the temperature of the helium available to flow back into the primary coolant system through the break, and maintaining some cooling flow in the central irradiation tube. All calculations were performed for the 200-MW 8-level core, which is the base case in the figures.

Figure 4-50 presents peak fuel temperatures from calculations with flat and cosine axial power shapes. The cosine power shape peak temperature was 1°C higher.

Peak fuel temperatures from the cases with the outer reflector gaps blocked are shown in Figure 4-51. Diverting flow around the blocked top and/or bottom changed the peak fuel temperature by only about 1°C. Axial average temperatures over the fuel length are presented in Figure 4-52 for the outer half of the reflector in Ring 4, in Figure 4-53 for reflector Ring 5, and in Figure 4-54 for the PSR. Blocking flow into or out of the gaps around the Ring 5 blocks had an insignificant effect on the temperatures.

Calculations were also performed with the higher steady-state coolant temperatures, 350°C at the inlet and 750°C at the vessel outlet. Both 150 and 200-MW cases were simulated; the 150-MW case was simulated because its steady state peak fuel temperature was near 1300°C. Peak fuel temperatures for these two cases are compared with the base case in Figure 4-55. The 100°C higher initial coolant temperature for the 200 MW case resulted in a 17°C higher peak temperature during the transient that occurred about 10 hours earlier. Figure 4-56 shows that the change in coolant temperature also resulted in

47
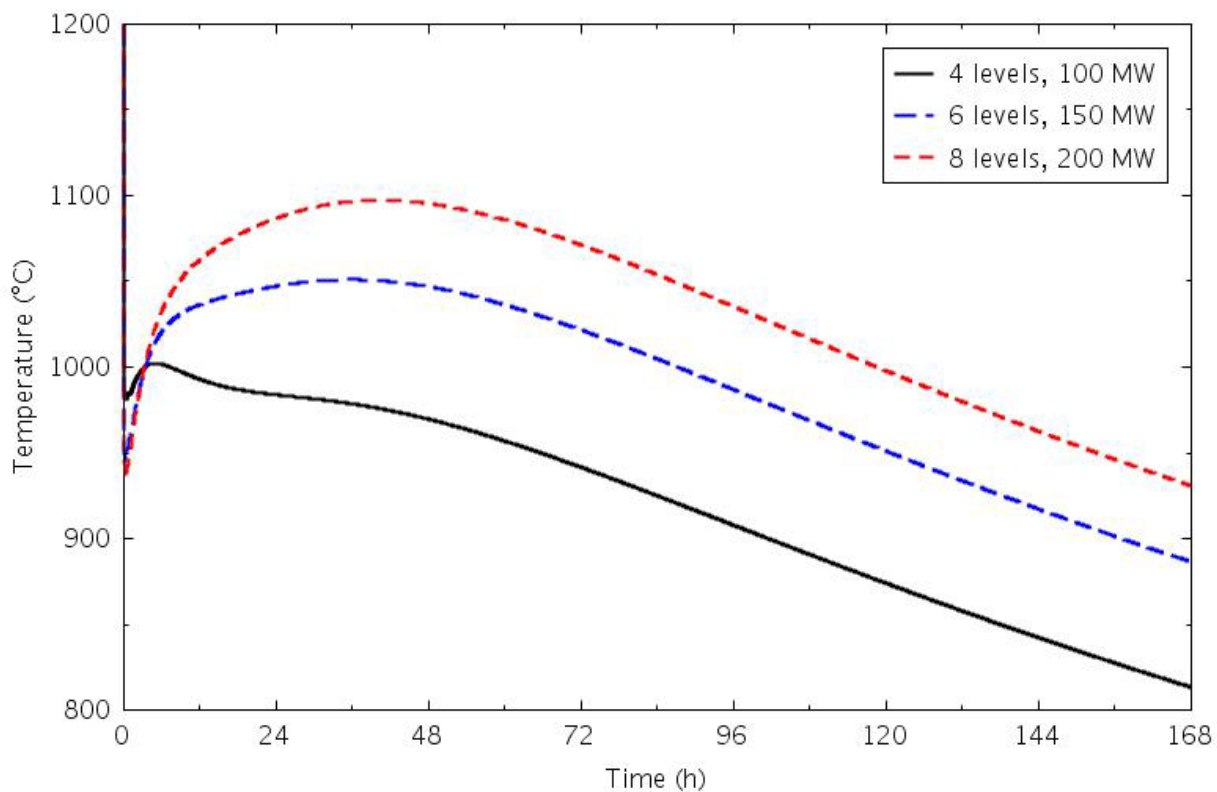
Figure 4-38. Peak fuel temperatures for the 6-level core DCC transients.



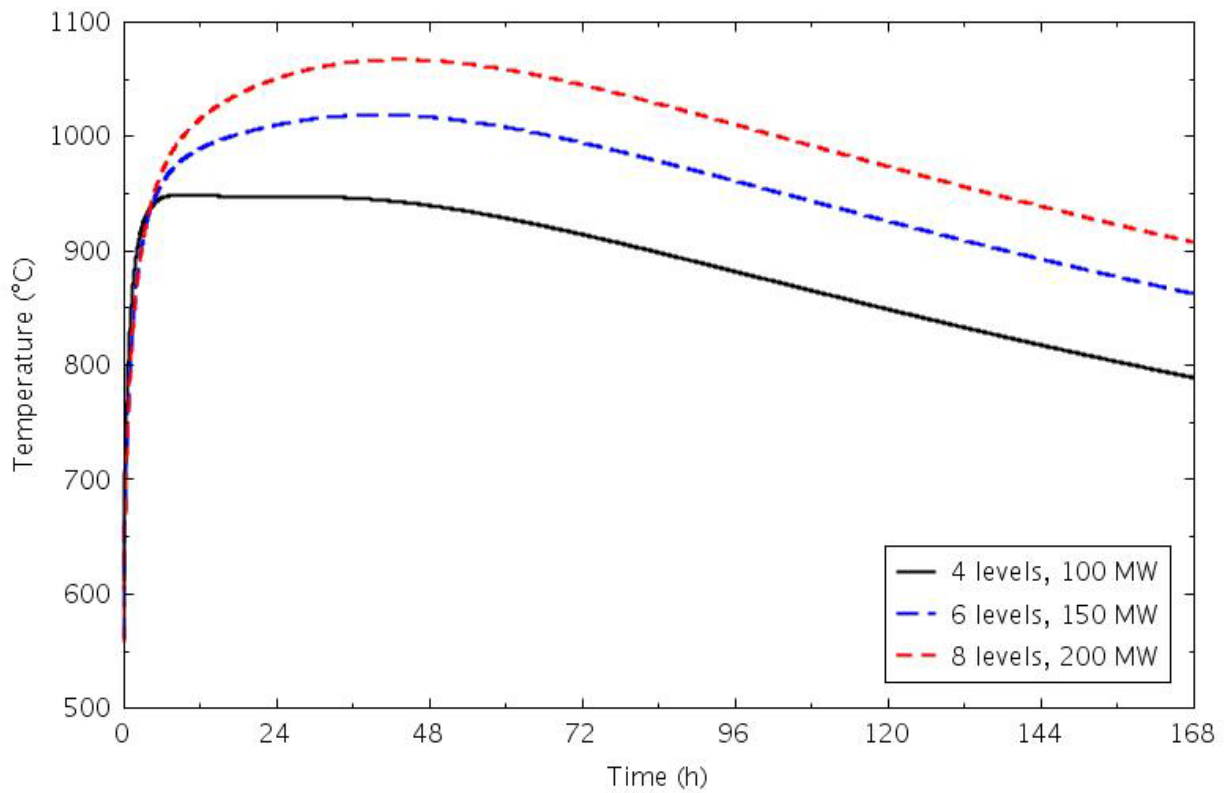Figure 4-39. Central reflector peak temperatures for the 6-level core DCC transients.

48
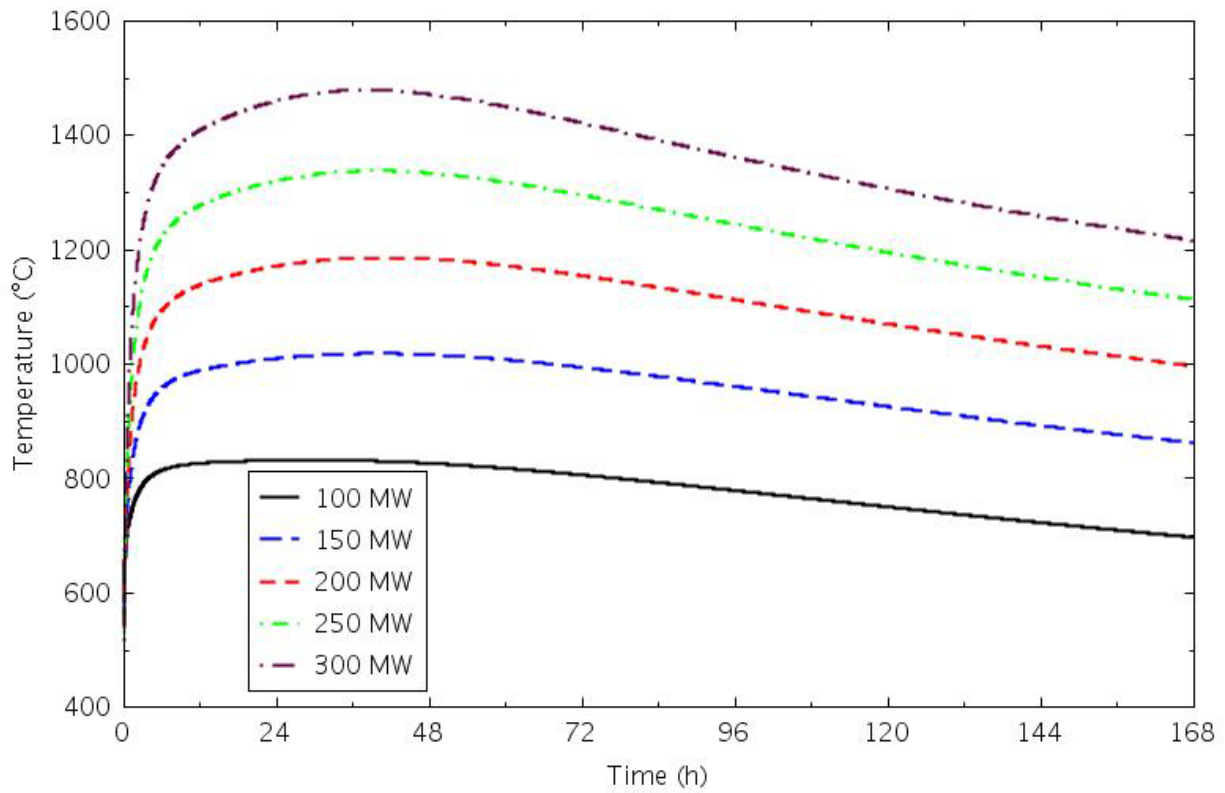
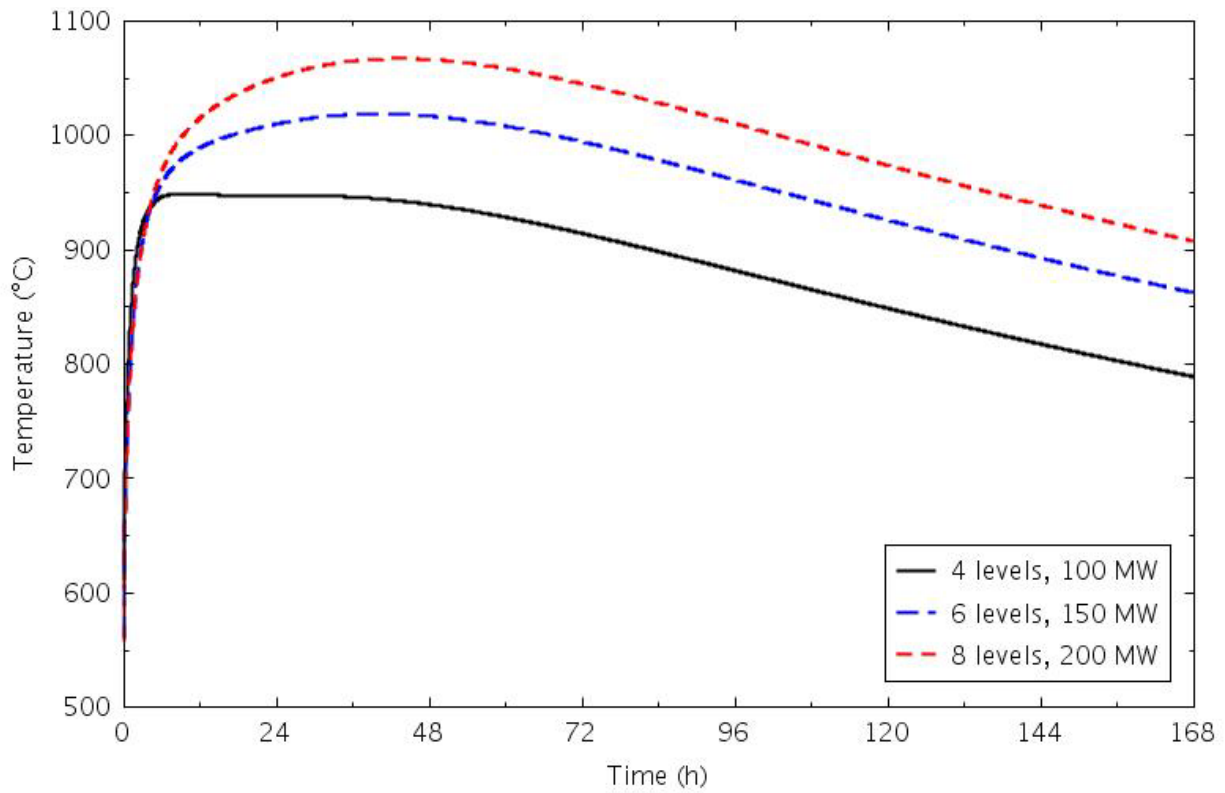Figure 4-40. Ring 3 reflector peak temperatures for the 6-level core DCC transients.



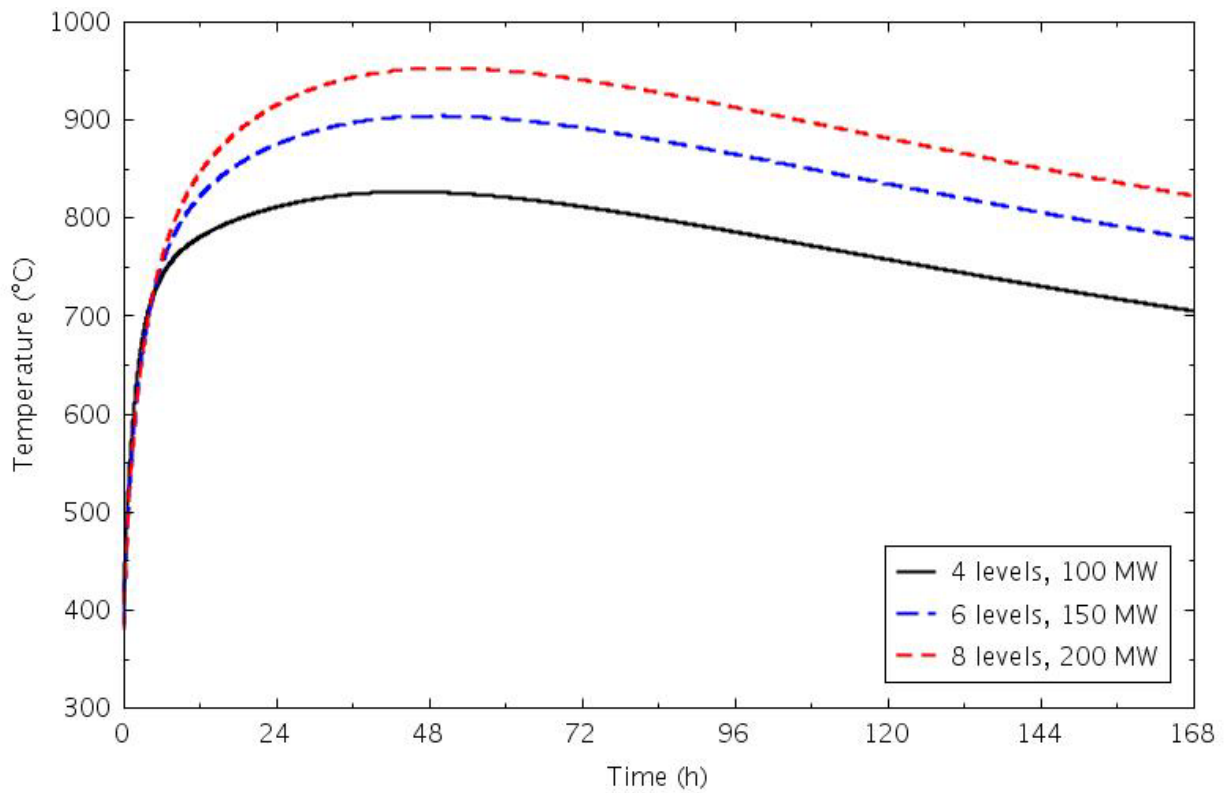Figure 4-41. Reflector Ring 4 inner half peak temperatures for the 6-level core DCC transients.

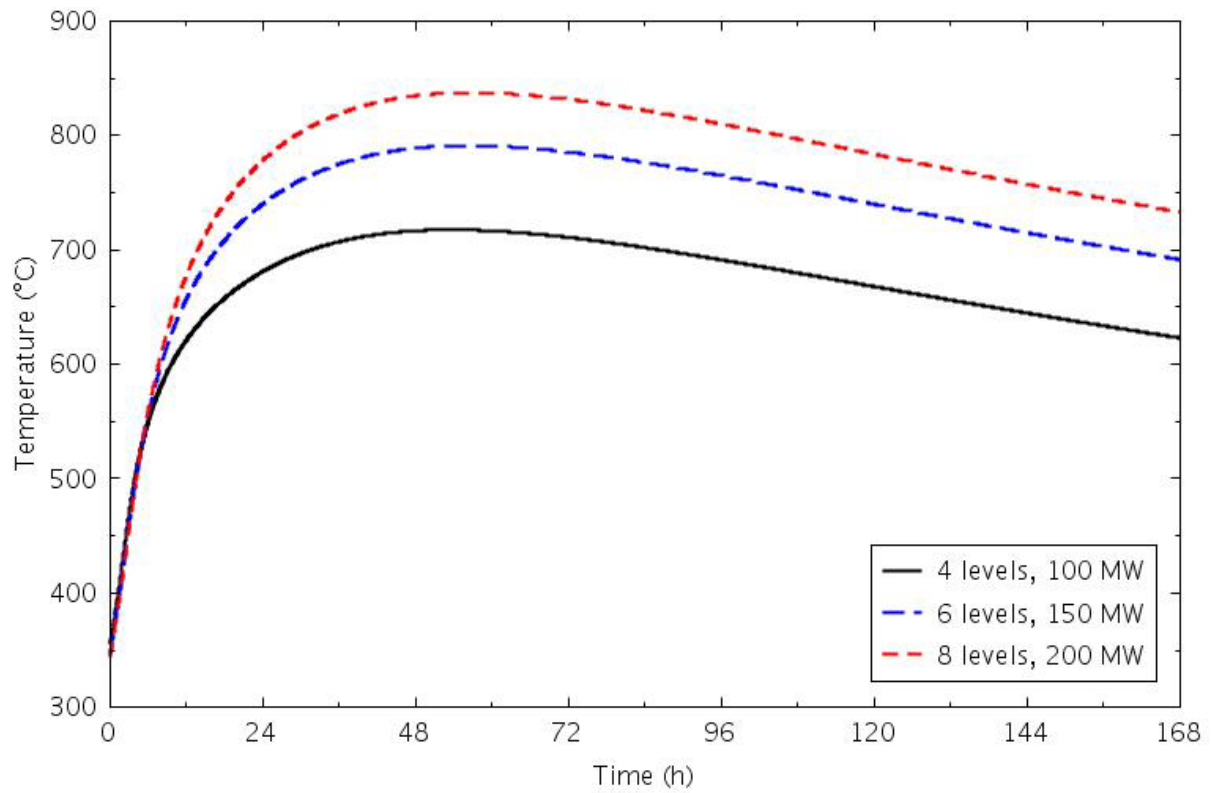Figure 4-42. Reflector Ring 4 outer half peak temperatures for the 6-level core DCC transients.
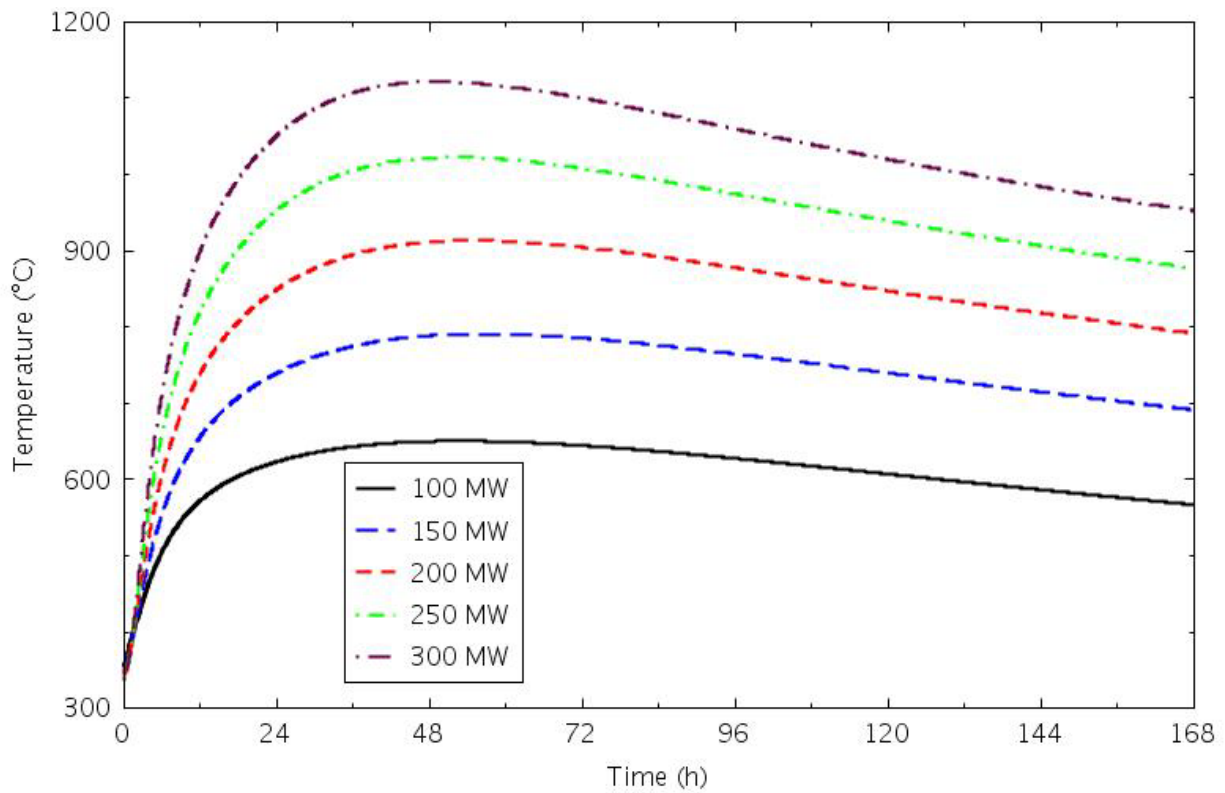


Figure 4-43. Reflector Ring 5 peak temperatures for the 6-level core DCC transients.
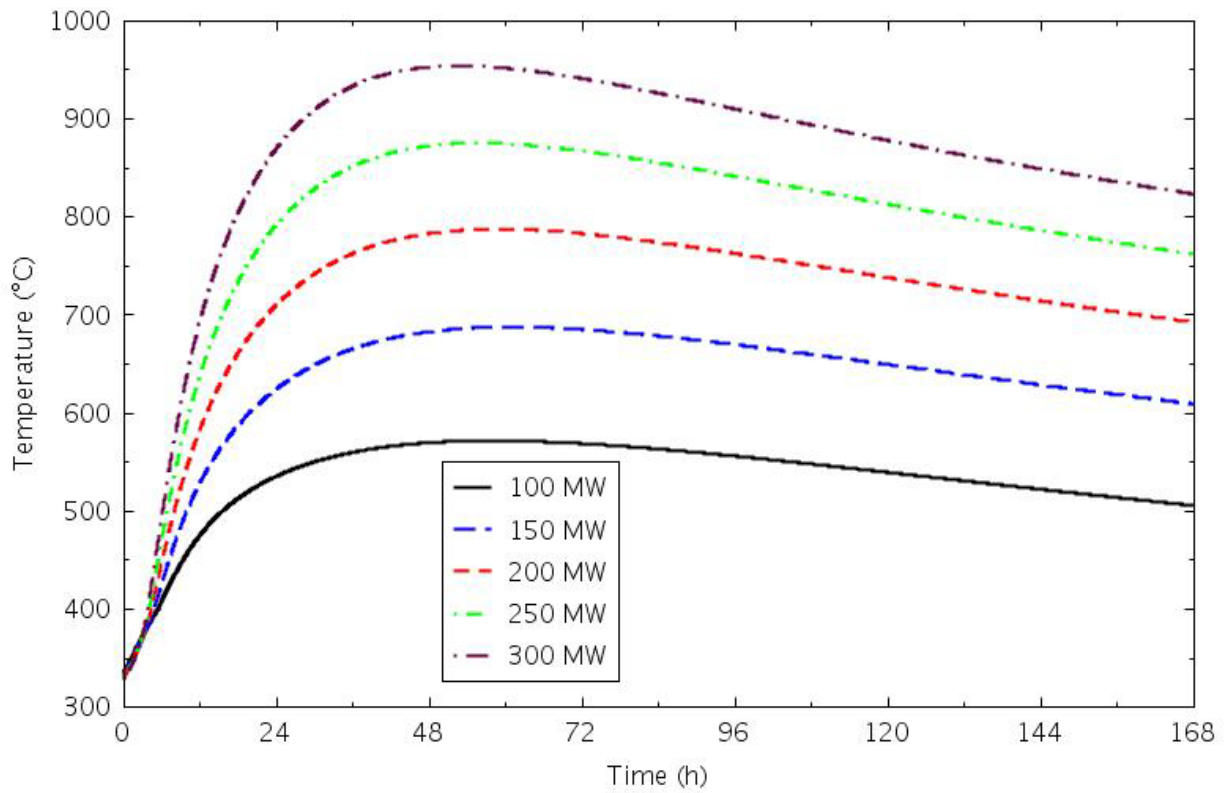
Figure 4-44. PSR peak temperatures for the 6-level core DCC transients.
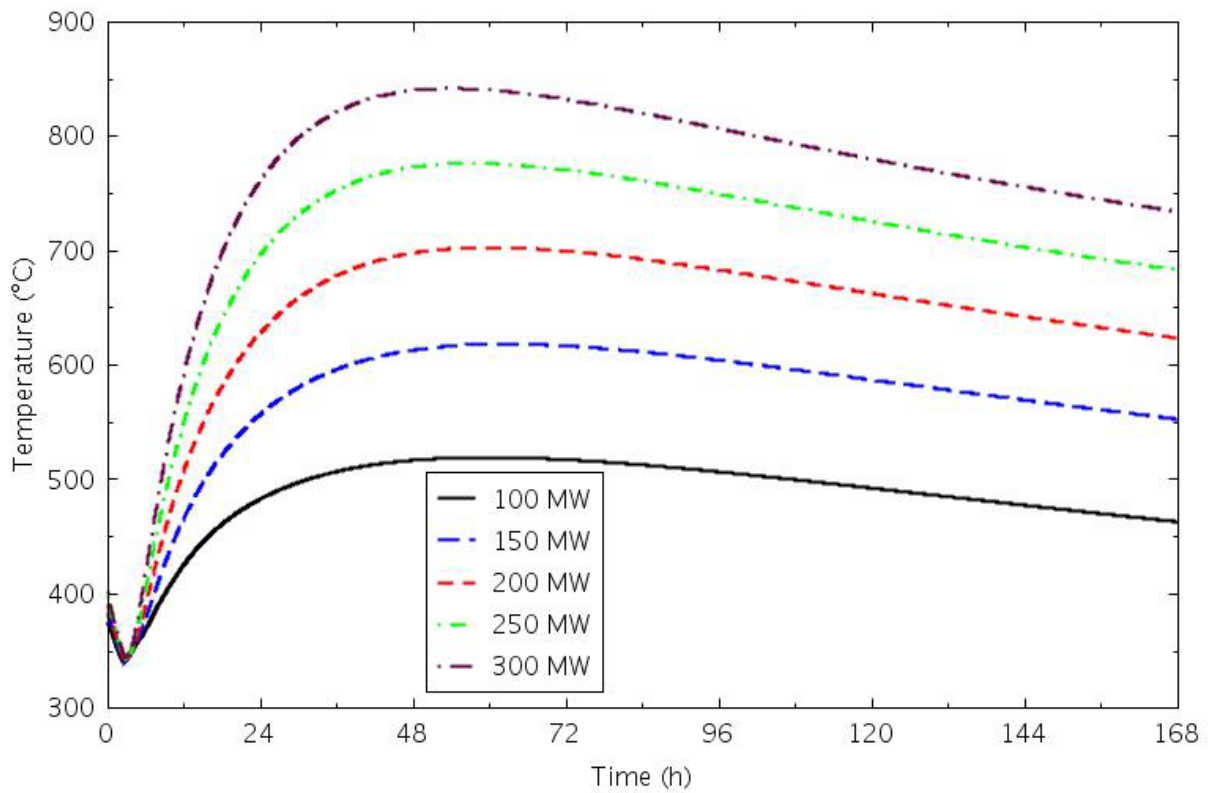


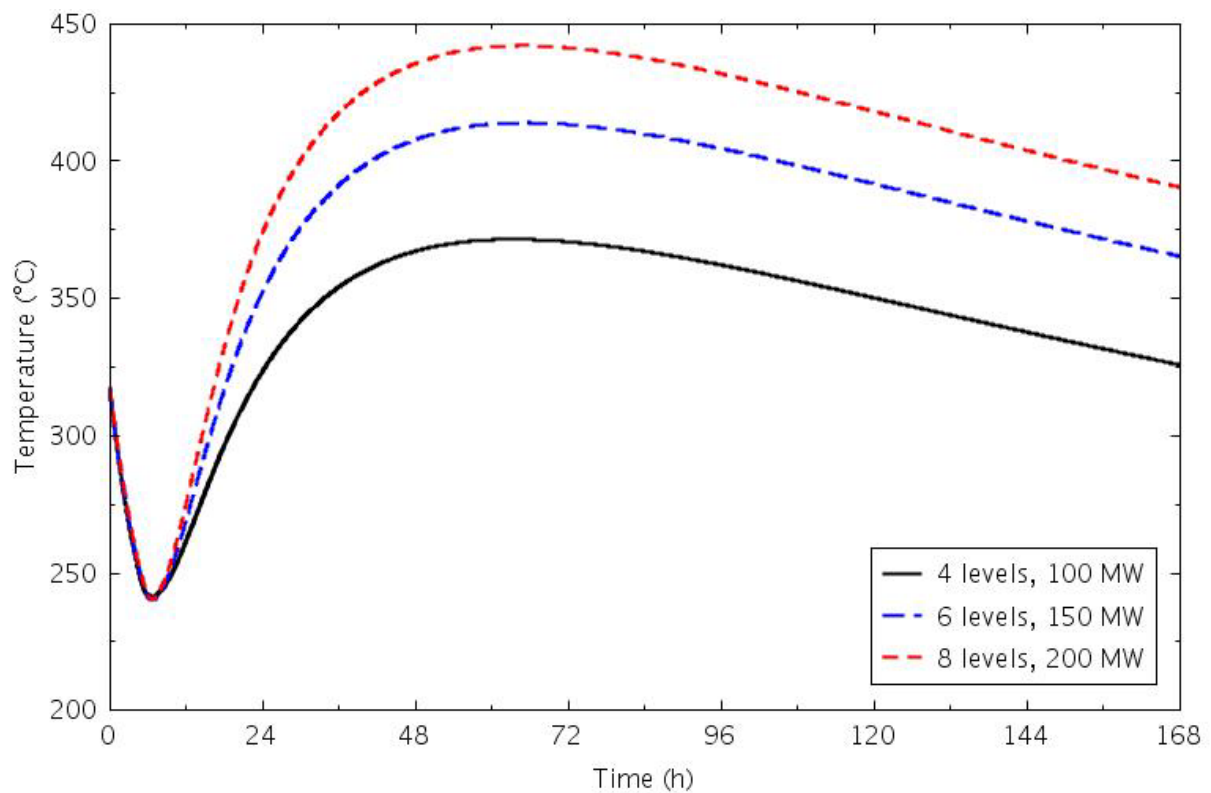Figure 4-45. Core barrel peak temperatures for the 6-level core DCC transients.
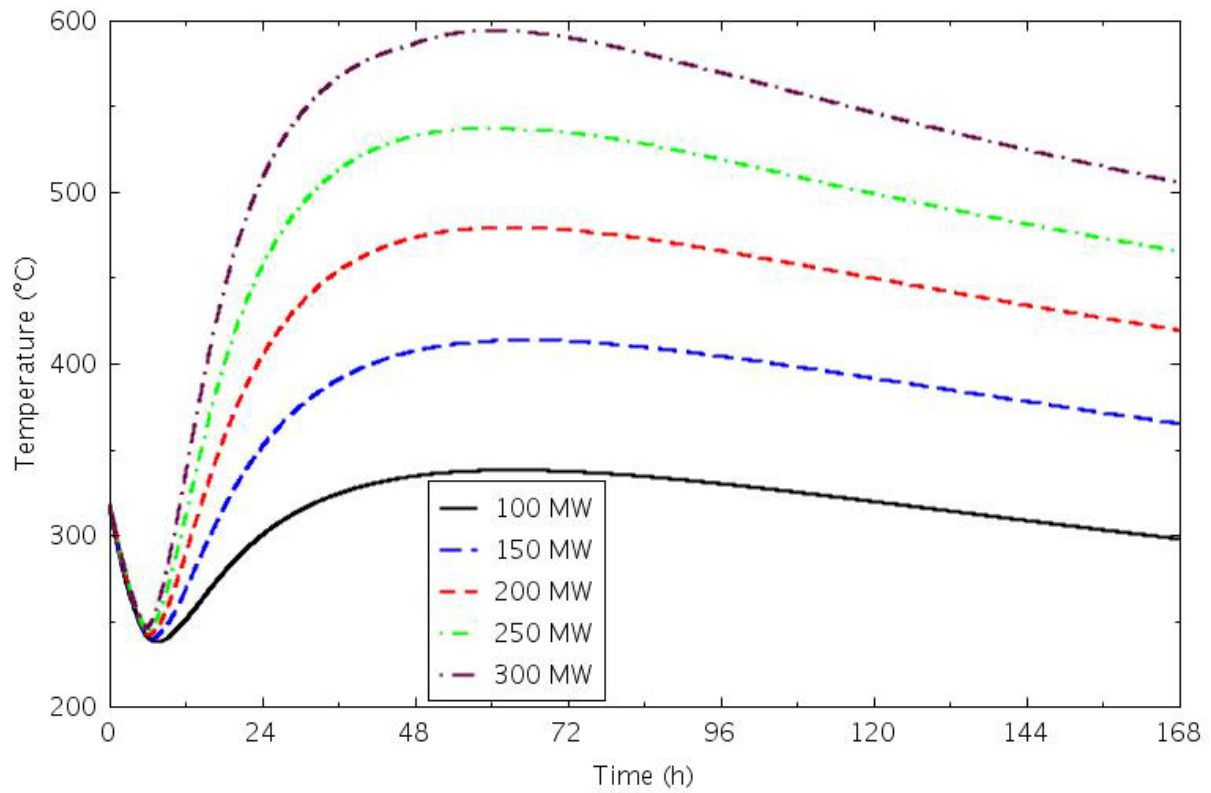
Figure 4-46. Reactor vessel wall peak temperatures for the 6-level core DCC transients.
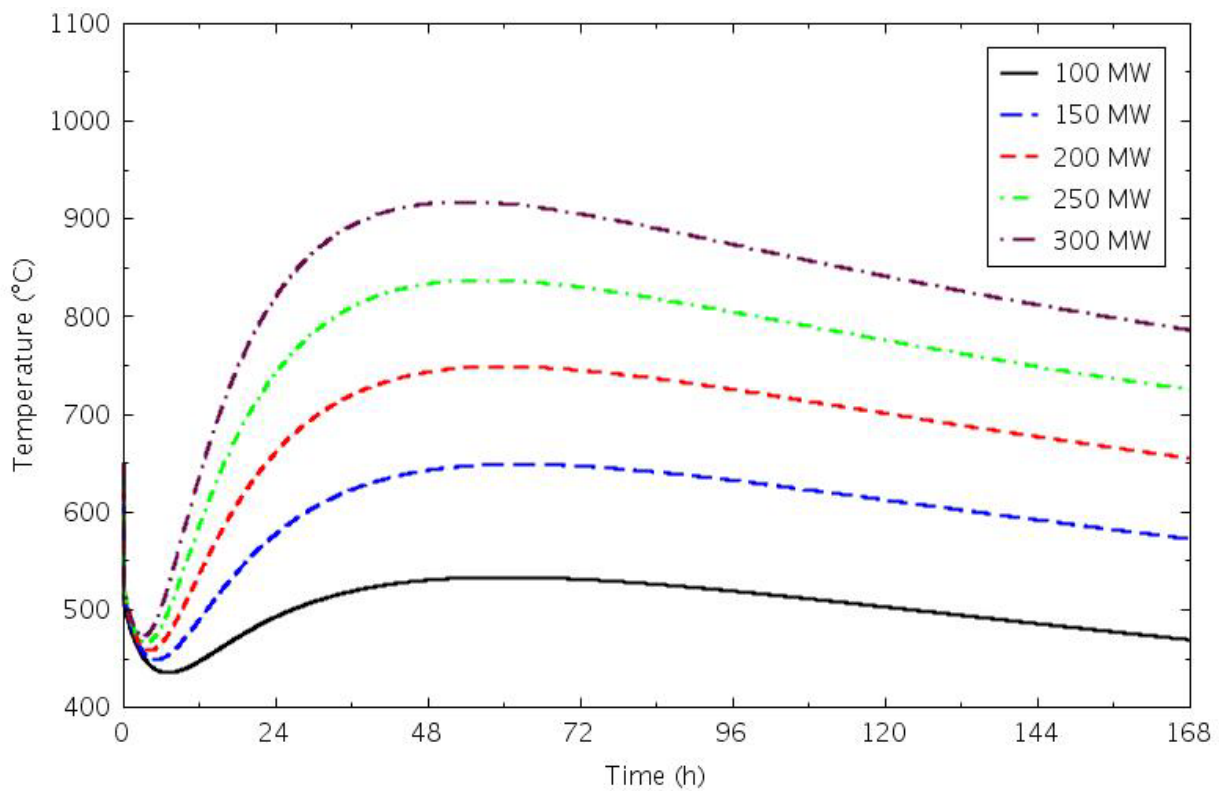


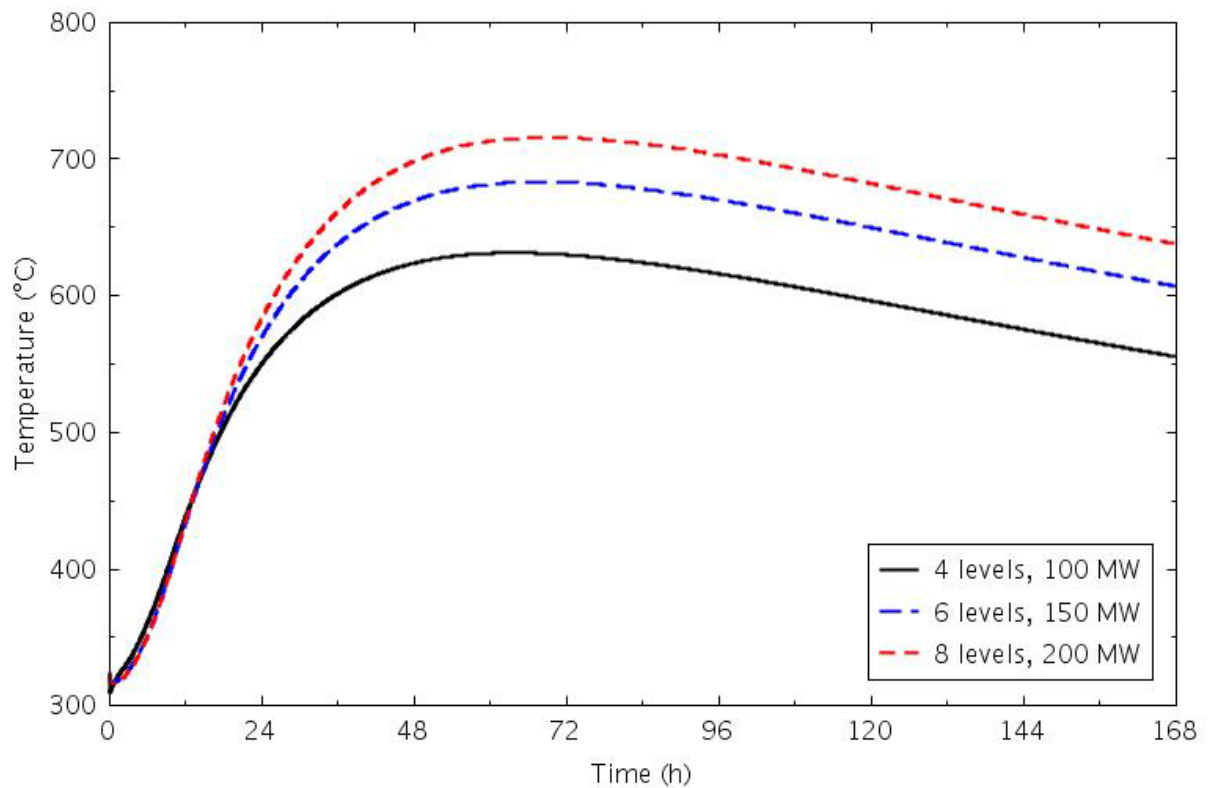Figure 4-47. Lower plenum coolant temperatures for the 6-level core DCC transients.
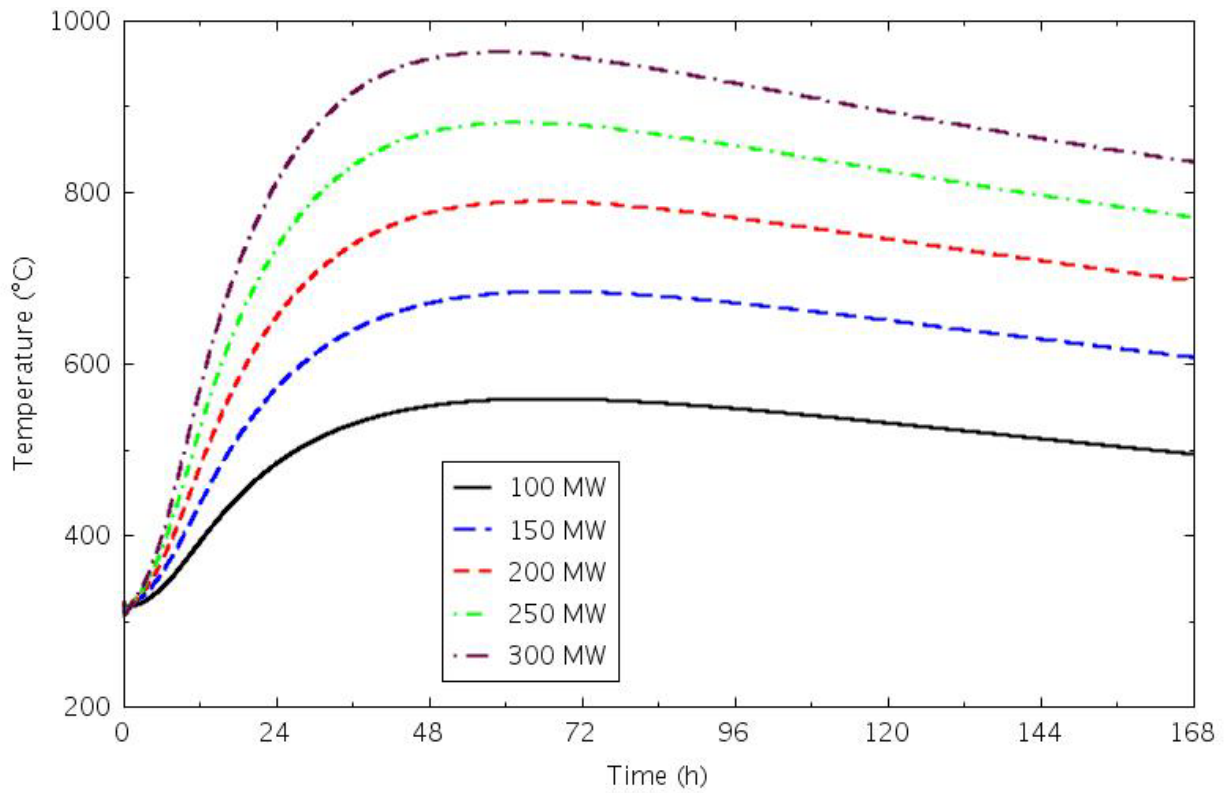
Figure 4-48. Upper plenum coolant temperatures for the 6-level core DCC transients.
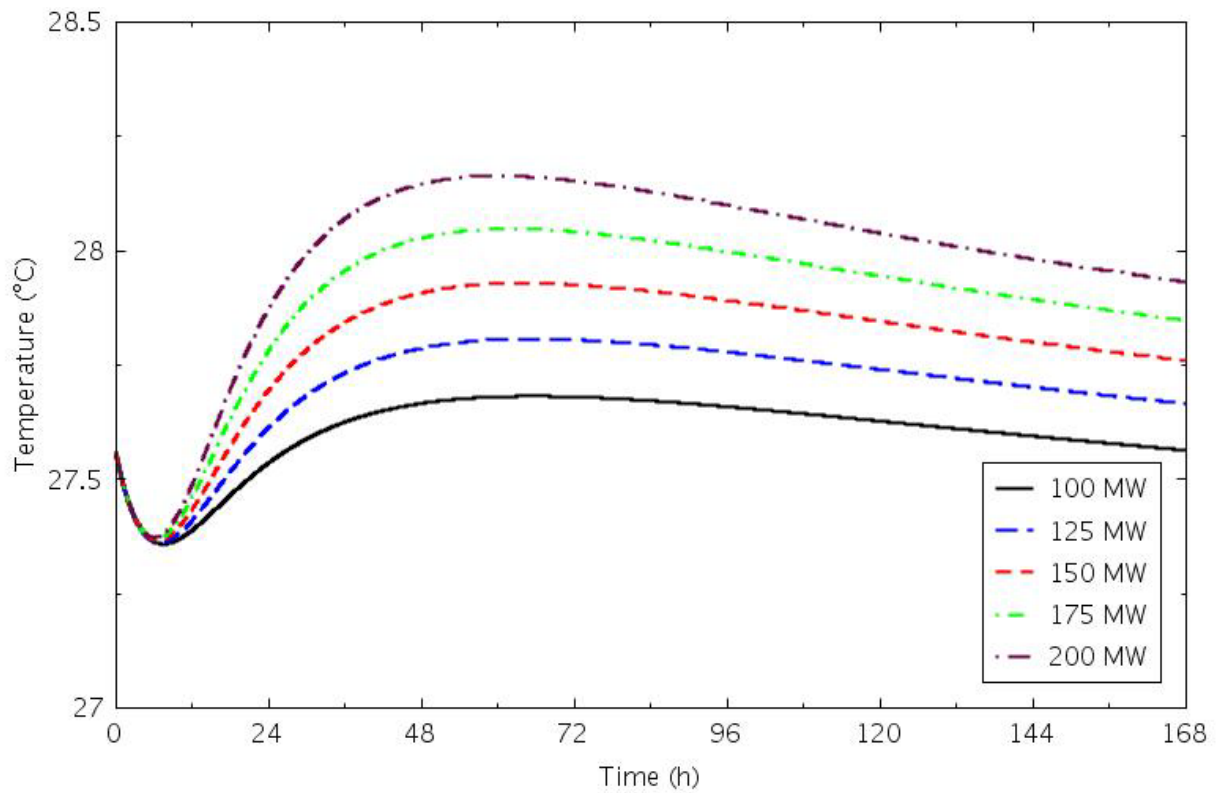


Figure 4-49. RCCS coolant outlet temperatures for the 6-level core DCC transients.
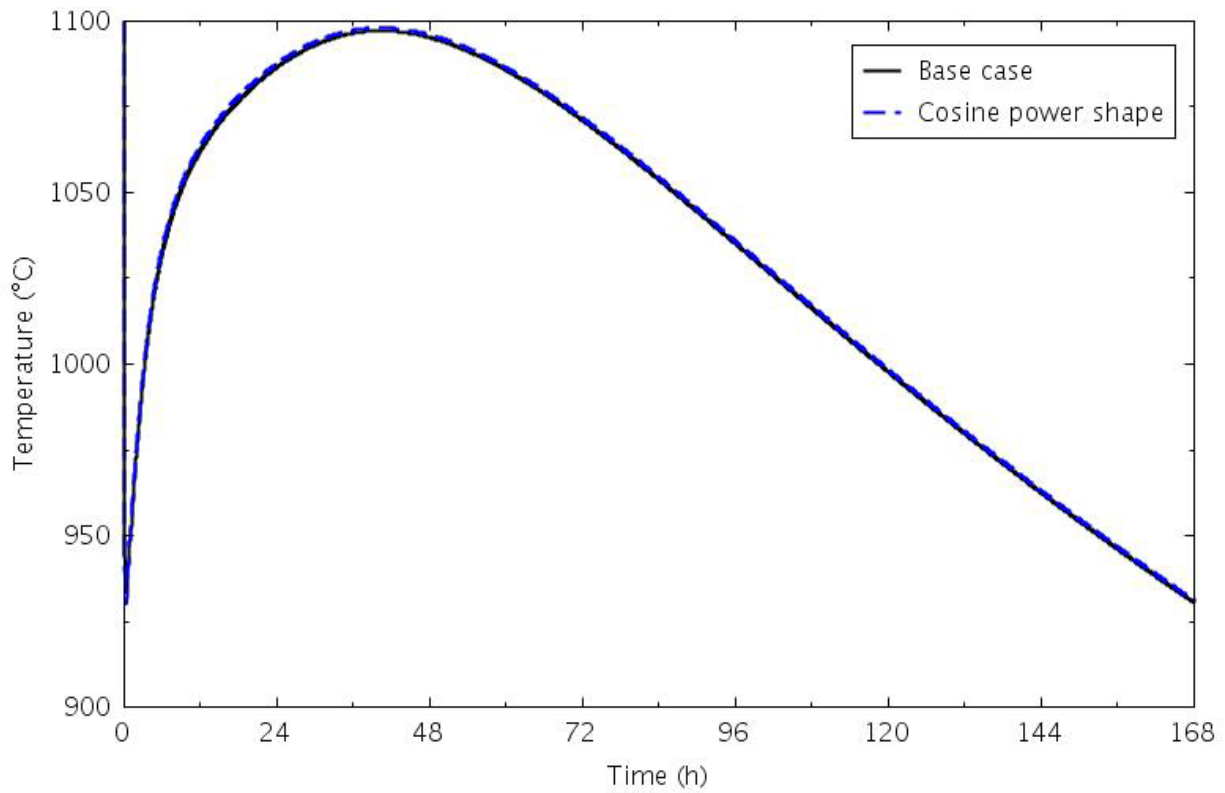
Figure 4-50. Peak fuel temperatures from the cosine power shape and base-case DCC transients.
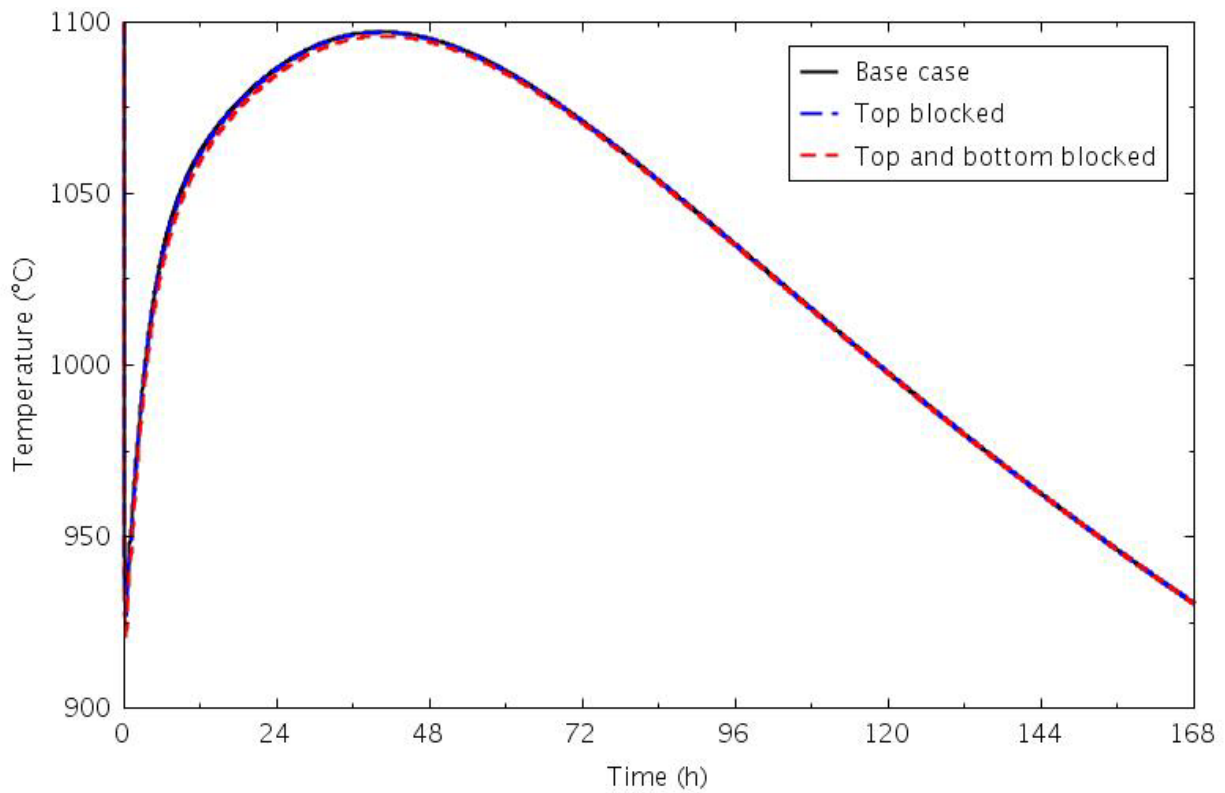


Figure 4-51. Peak fuel temperatures for the bypass blockage and base-case DCC transients.
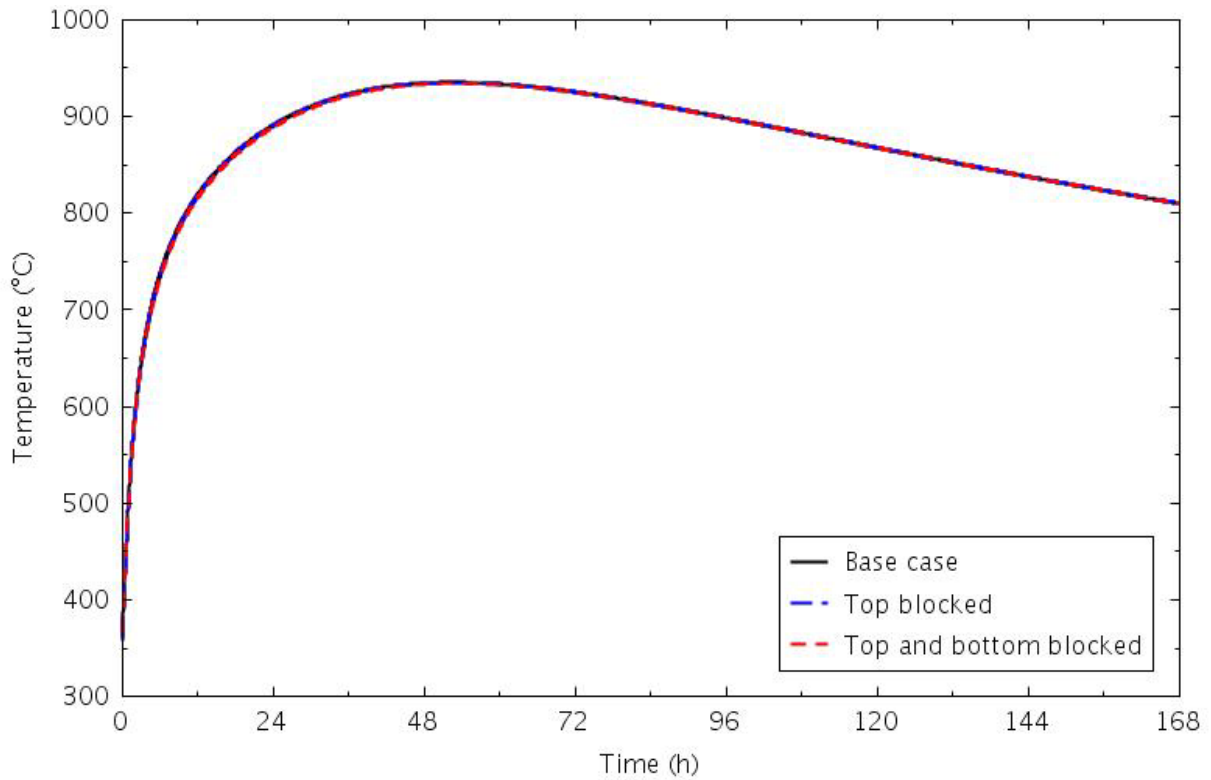
Figure 4-52. Reflector Ring 4 outer half axial average temperatures for the bypass flow blockage and base-case DCC transients.
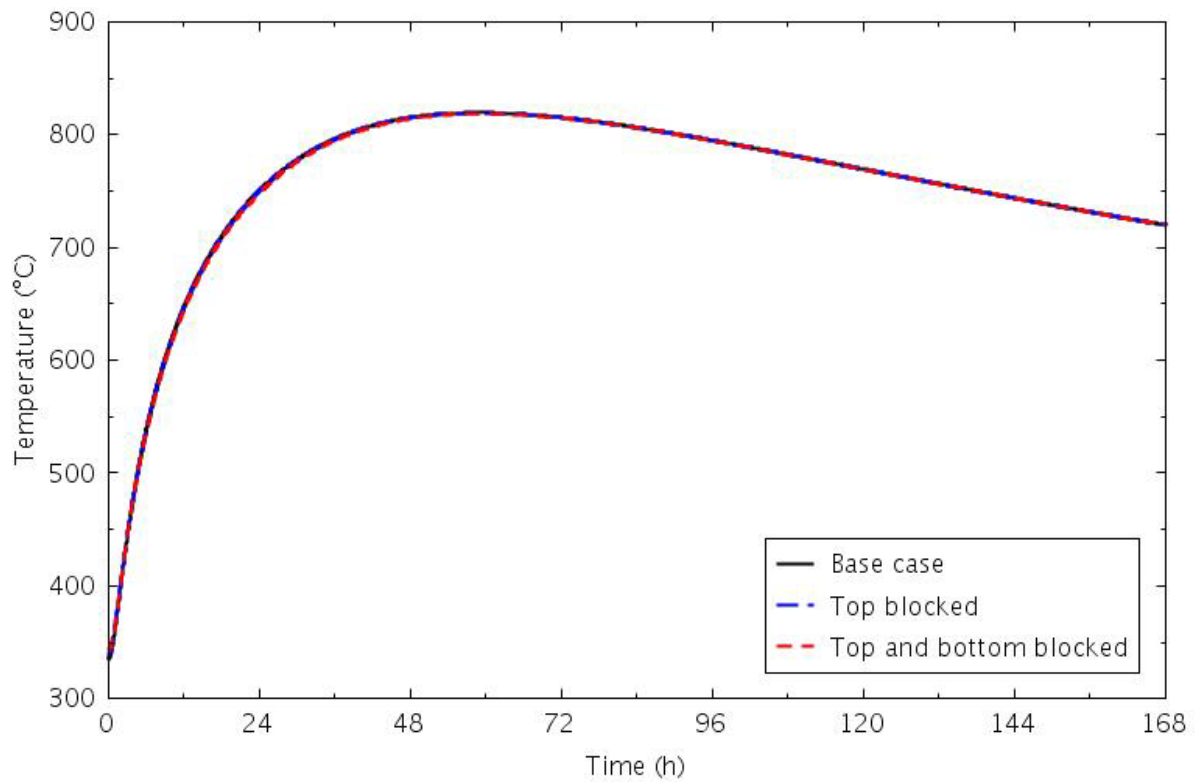


Figure 4-53. Reflector Ring 5 axial average temperatures for the bypass blockage and base-case DCC transients.
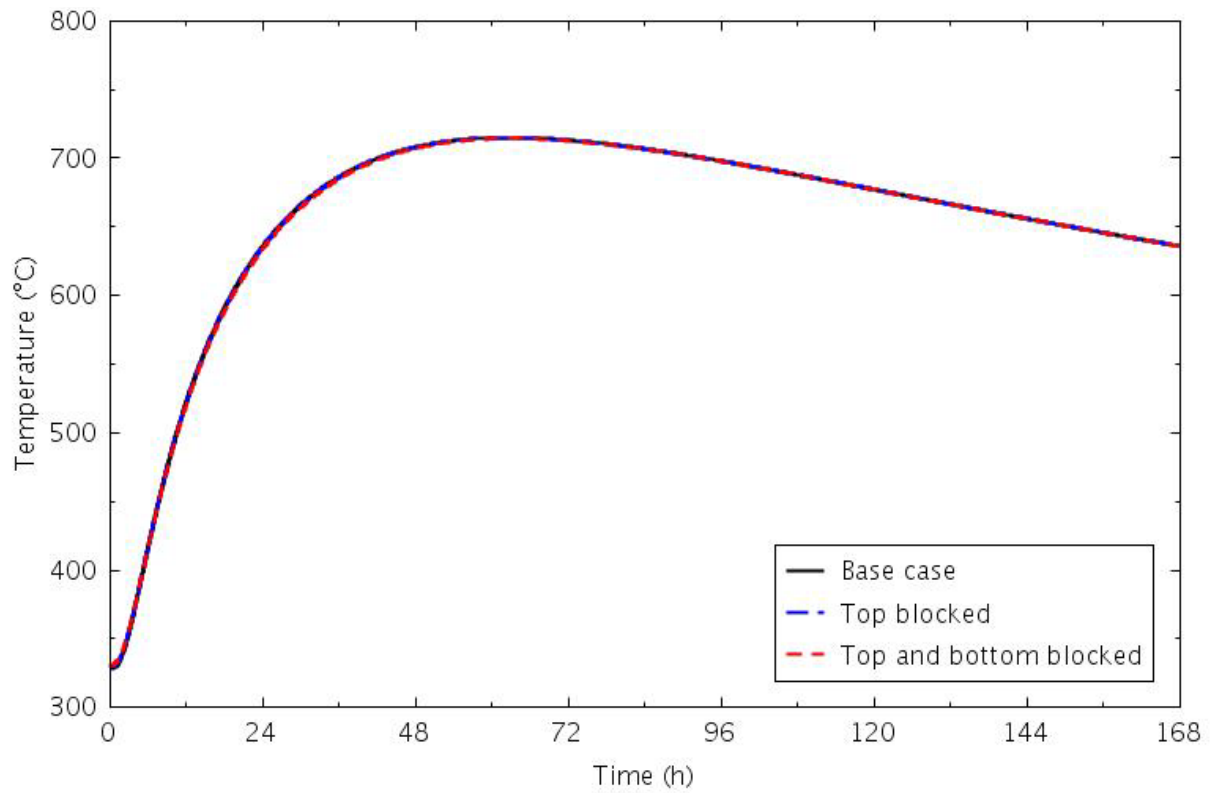
Figure 4-54. PSR axial average temperatures for the bypass blockage and base-case DCC transients.
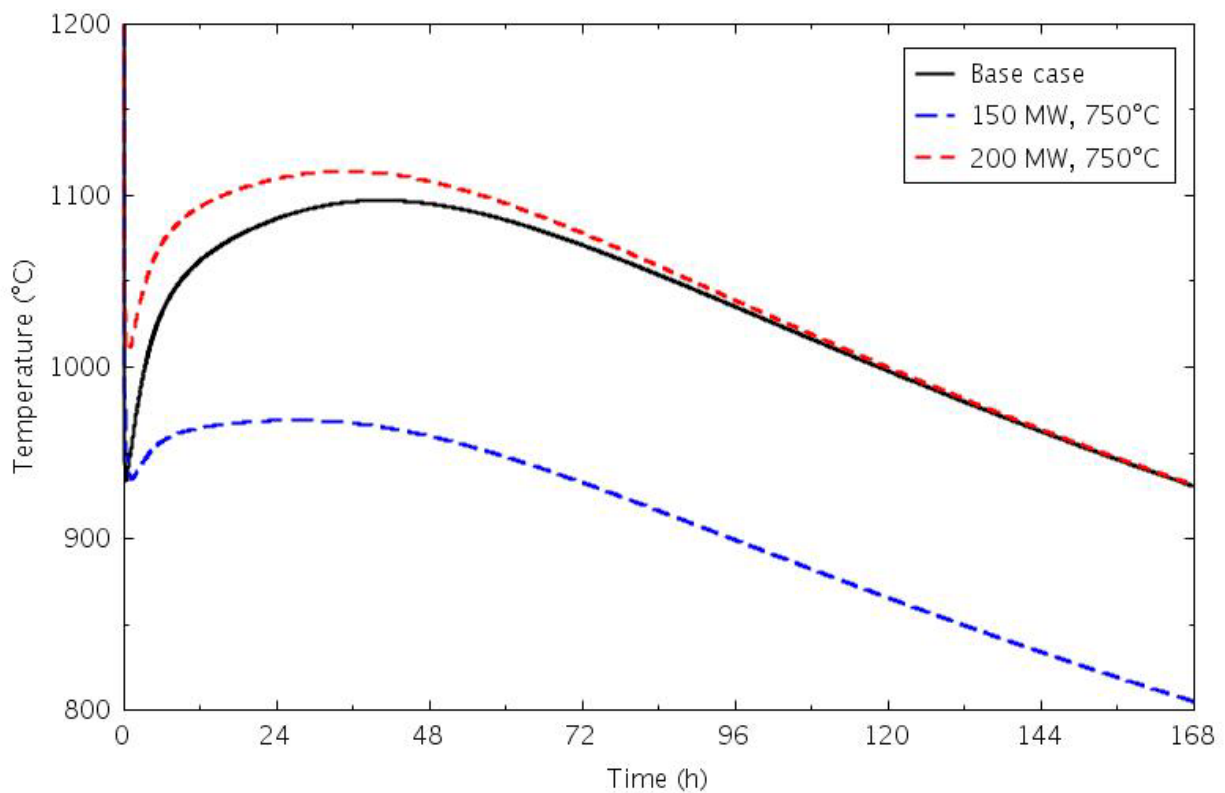


Figure 4-55. Peak fuel temperatures for the higher coolant temperature and base-case DCC transients.
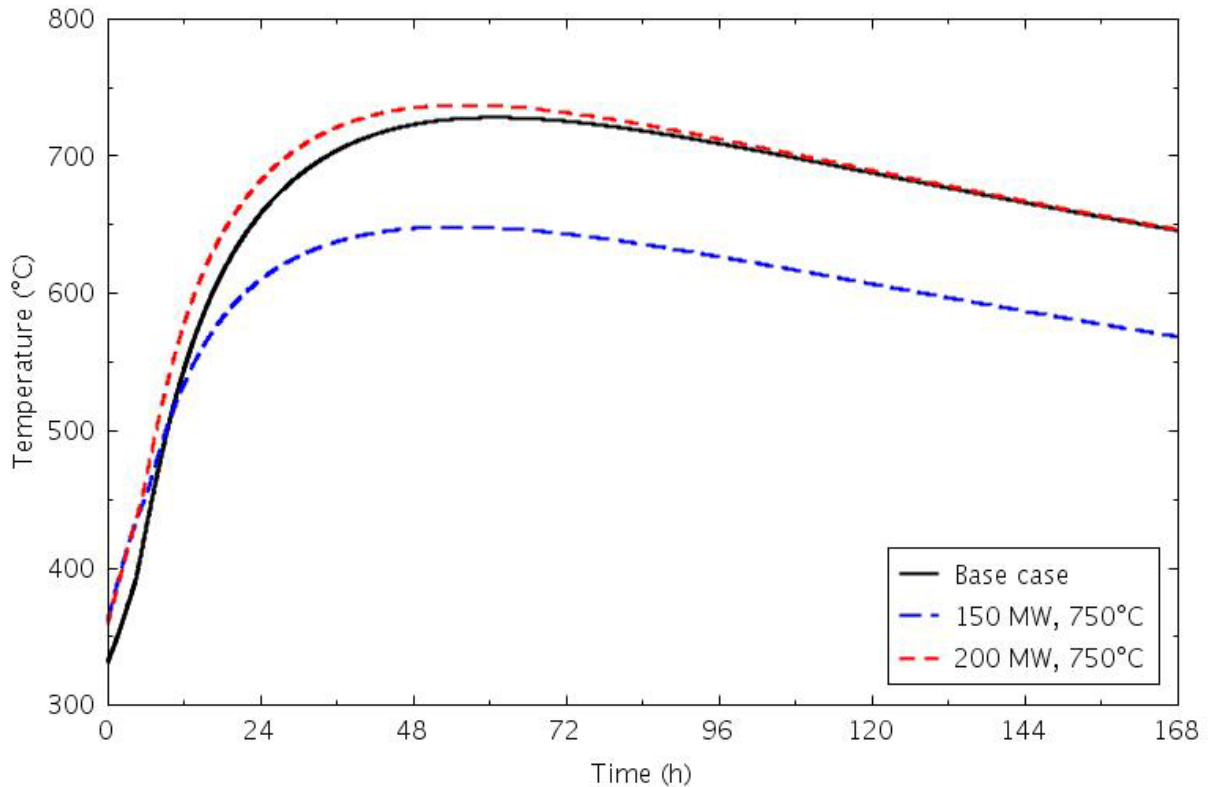
Figure 4-56. PSR peak temperatures for the higher coolant temperature and base-case DCC transients.

a small increase in the PSR peak temperature. The reactor vessel wall peak temperature, shown in Figure 4-57, was much smaller than the 25°C difference in the initial temperature.

The next sensitivity calculation modeled a double-ended break, such that both the reactor inlet and outlet were open to atmospheric pressure. This allows once-through flow through the core, from the outlet up through the core then back down the annulus between the core barrel and reactor vessel to the inlet side of the break. Figure 4-58 shows there is a small continuous flow back into the lower plenum from the vessel outlet. Figure 4-59 compares the peak fuel temperature from this case with that from the base case; there is essentially no difference between the two calculations. This is also the case for the peak temperatures in reflector Ring 5, shown in Figure 4-60, and the reactor vessel wall, presented in Figure 4-61.

The base-case calculation assumed that any helium returning from the break was at the nominal outlet temperature of 650°C in order to maximize peak fuel temperatures during the transient. Calculations were also performed with that temperature reduced to 127, 177, and 227°C. Figure 4-62 shows the peak fuel temperatures for these calculations along with the base case; differences in the temperatures were insignificant. This was also the case for the peak temperatures in the PSR (Figure 4-63) and the reactor vessel wall (Figure 4-64).

One analysis uncertainty is the timing of the reactor scram. In the base case, a scram signal was modeled at the beginning of the transient. Sensitivity calculations were performed with scram signals generated at 1 s (at the end of the blowdown) and at 10 s after the transient began. Peak fuel temperatures from these cases are presented in Figure 4-65 for the full transient and in Figure 4-66 for the first 40 s. The 1-s delay had no impact on the peak temperature, while the 10-s delay resulted in an increase of a few degrees near 36 hours. The peak fuel temperature for the 10-s delay case occurred at 10 s. The impact on the reflector temperatures was smaller, as shown in Figure 4-67 for reflector Ring 5.

57
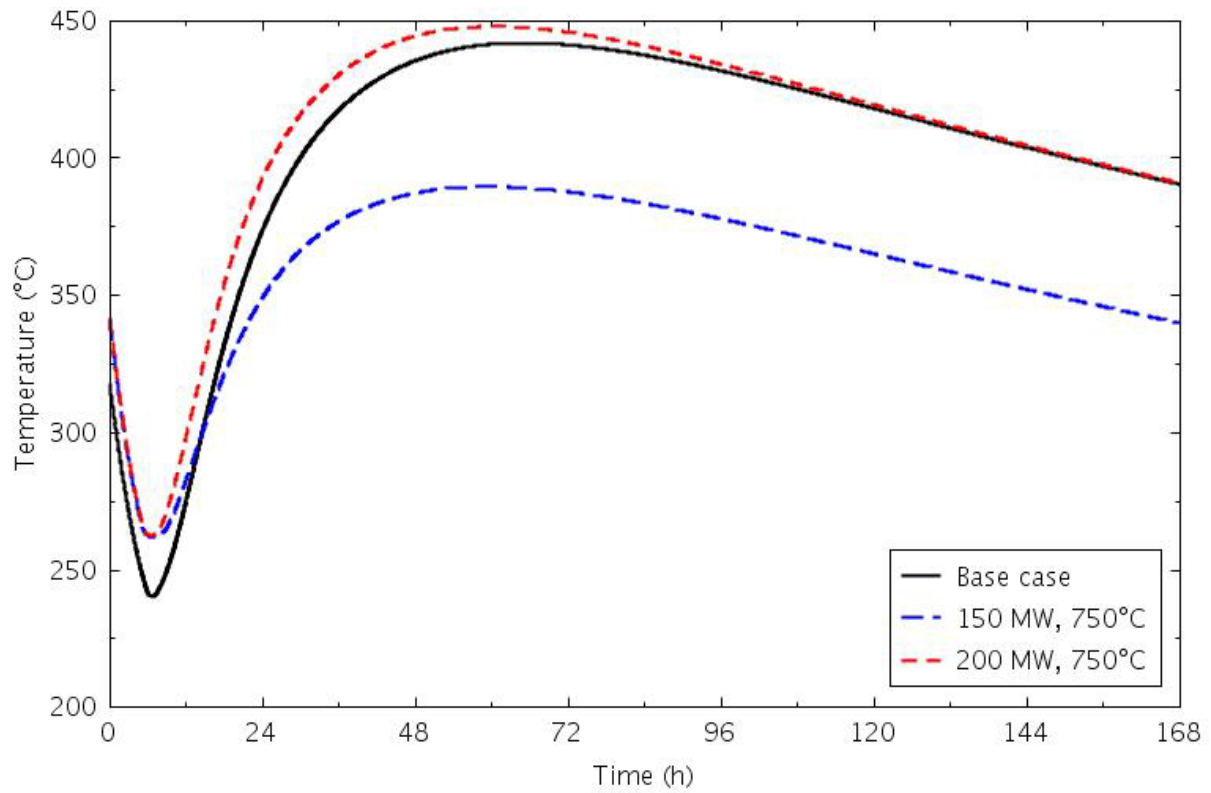
Figure 4-57. Reactor vessel wall peak temperatures for the higher coolant temperature and bas- case DCC transients.
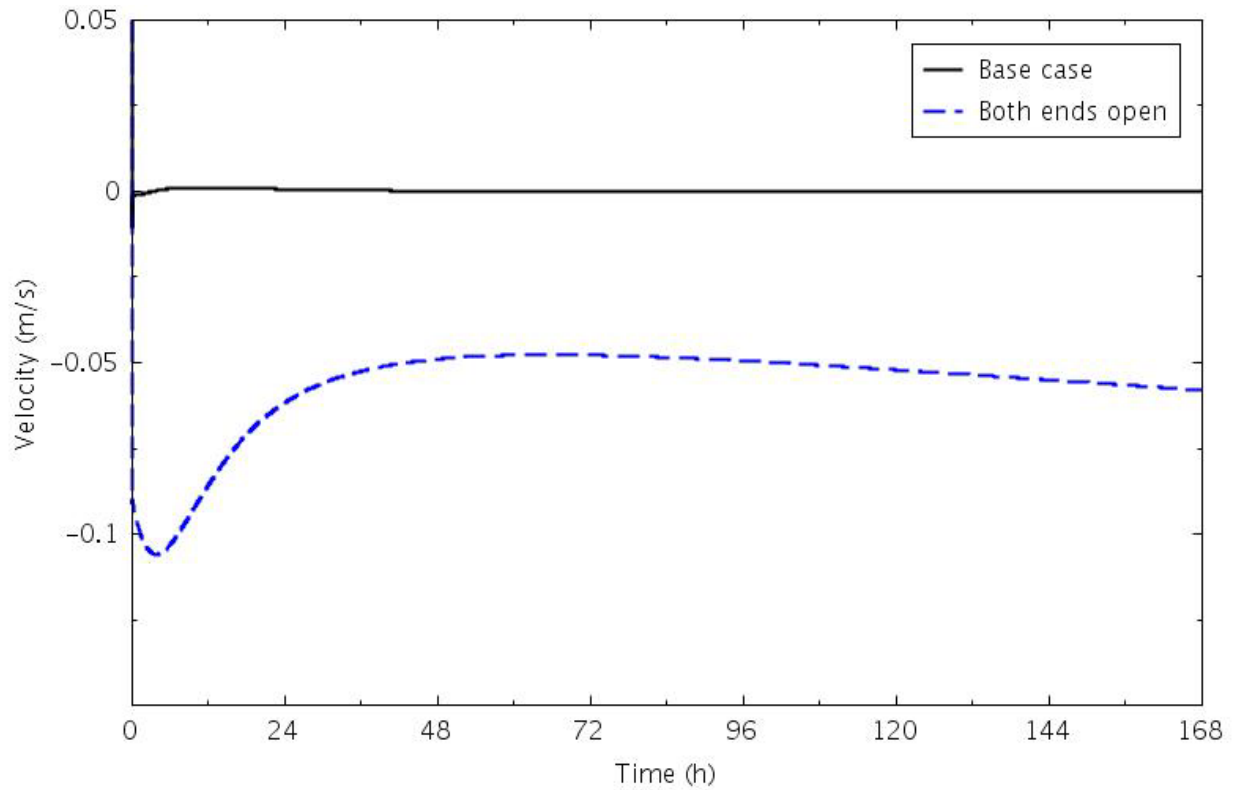


Figure 4-58. Reactor vessel outlet coolant velocities for the double-ended break and base-case DCC transients.

Figure 4-59. Peak fuel temperatures for the double-ended break and base-case DCC transients.
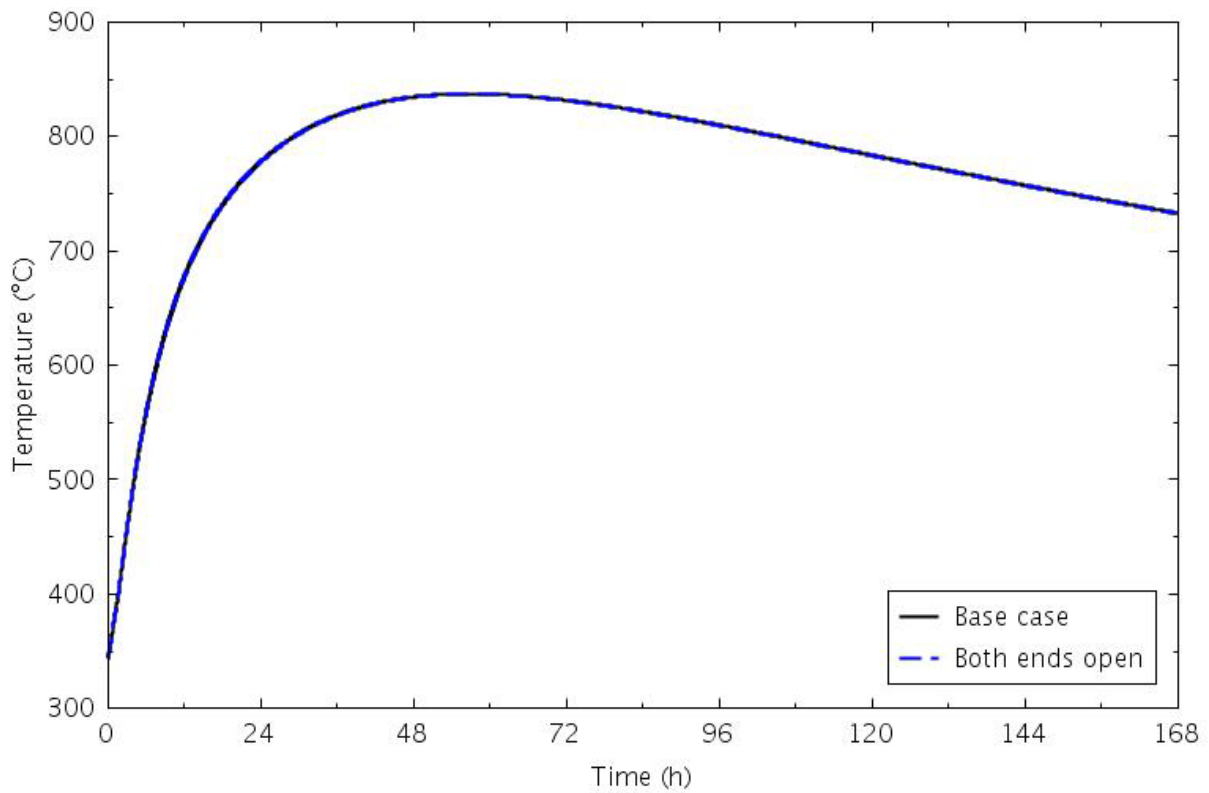


Figure 4-60. Reflector Ring 5 peak temperatures for the double-ended break and base-case DCC transients.
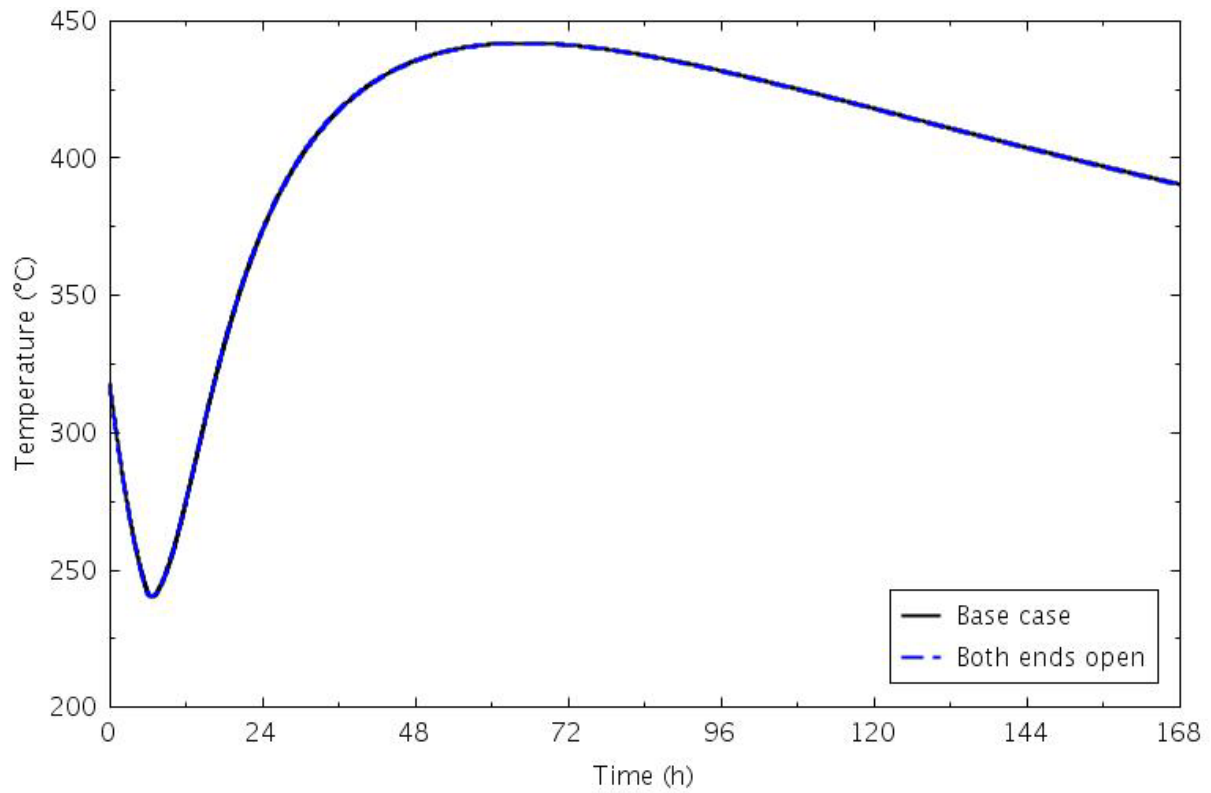
Figure 4-61. Reactor vessel peak temperatures for the double-ended break and base-case DCC transients.



Figure 4-62. Peak fuel temperatures for the cavity temperature sensitivity and base-case DCC transients.

60

Figure 4-63. PSR peak temperatures for the cavity temperature sensitivity and base-case DCC transients.



Figure 4-64. Reactor vessel wall peak temperatures for the cavity temperature sensitivity and base-case DCC transients.
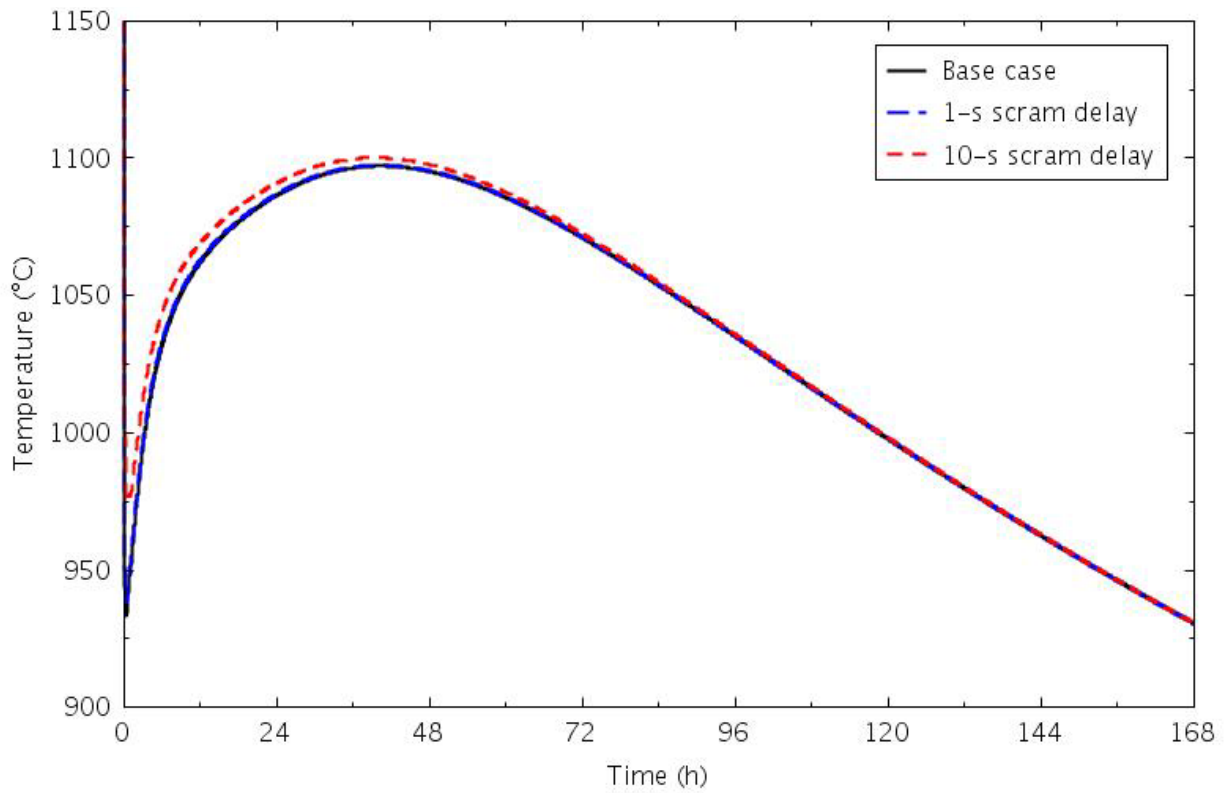
Figure 4-65. Peak fuel temperatures for the delayed scram and base-case DCC transients (long term).
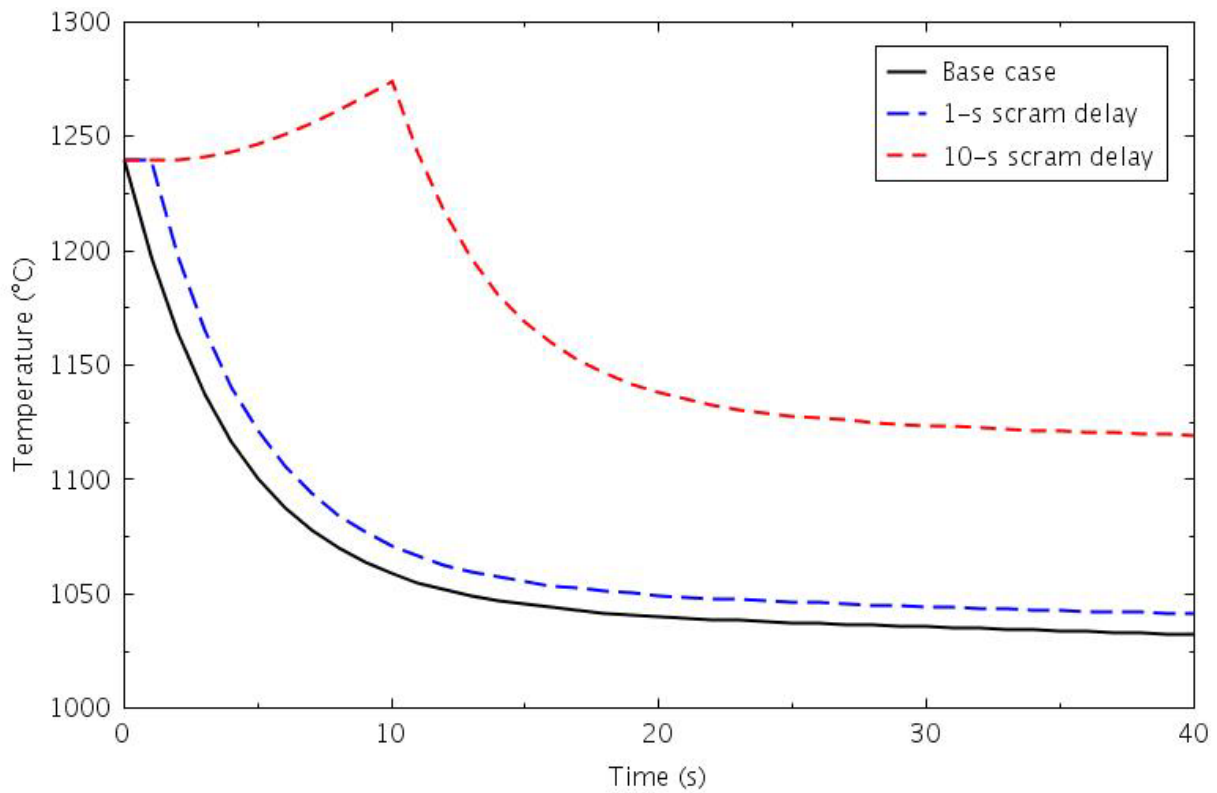


Figure 4-66. Peak fuel temperatures for the delayed scram and base-case DCC transients (short term).
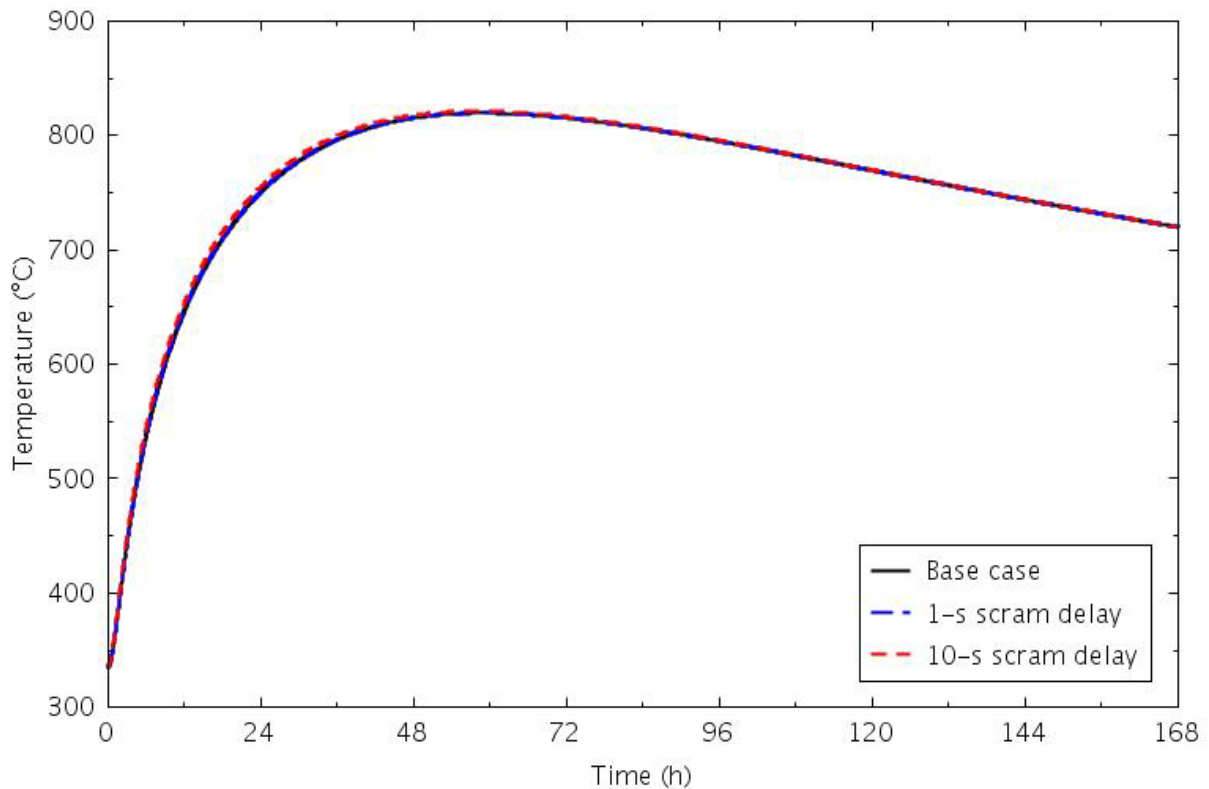
Figure 4-67. Reflector Ring 5 axial average temperatures for the delayed scram and base-case DCC transients.

The final sensitivity addressed cooling flow inside the center irradiation tube. The base transients were run without any cooling to conservatively maximize the temperatures in the core. The results showed that although the steel would not melt, the structural integrity of pressurized loops would be questionable following a DCC transient. Calculations were performed with helium flows ranging from 0.01 to 0.1 kg/s being maintained inside the tube throughout the transient; 0.1 kg/s was the flow assumed during steady state operation. Peak irradiation tube temperatures are shown in Figure 4-68 for the entire transient, and in Figure 4-69 for the first 3 hours. The amount of flow had a significant impact on the peak temperatures, and a fairly high flow rate would be needed to ensure the tube integrity.

The flow rate also had a significant impact on the peak fuel temperatures, which are presented in Figure 4-70. The additional cooling reduced the peak temperatures and shifted them earlier. The same change in response was seen in the peak temperatures for reflector Ring 5, shown in Figure 4-71. Peak temperatures in the reflector occurred later than in the fuel. Figure 4-72 compares the total heat removal through the tube cooling flow and the RCCS with the core power. The timing of the crossover, where the heat removal exceeded the core power, corresponded to the timing of the reflector peak temperatures. The core peak temperature was more influenced by the tube cooling in the center reflector, while the RCCS was the primary influence on the reflector cooling. The implication is that additional coolant loops in the outer reflector would further reduce the fuel temperatures, but might have an even greater impact on reducing the reflector temperatures.
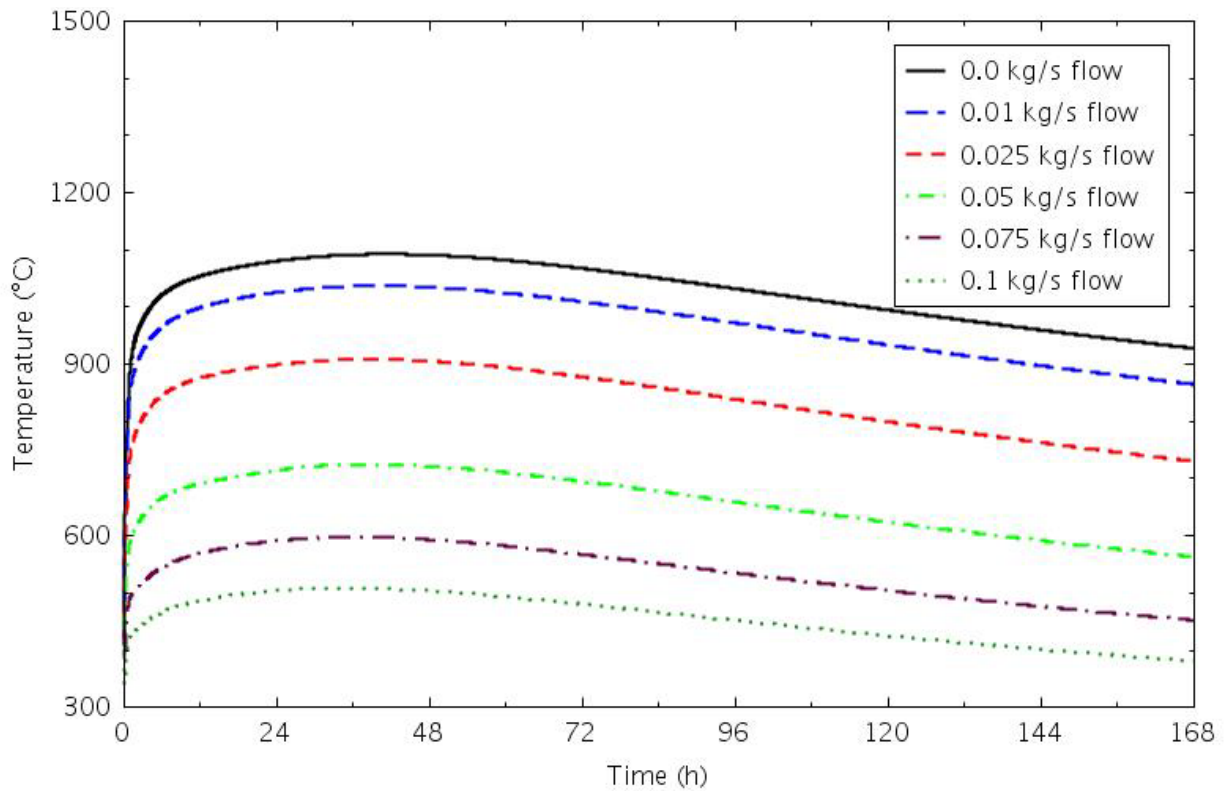
Figure 4-68. Central irradiation tube peak temperatures for the tube cooling flow sensitivity and base-case DCC transients (long term).
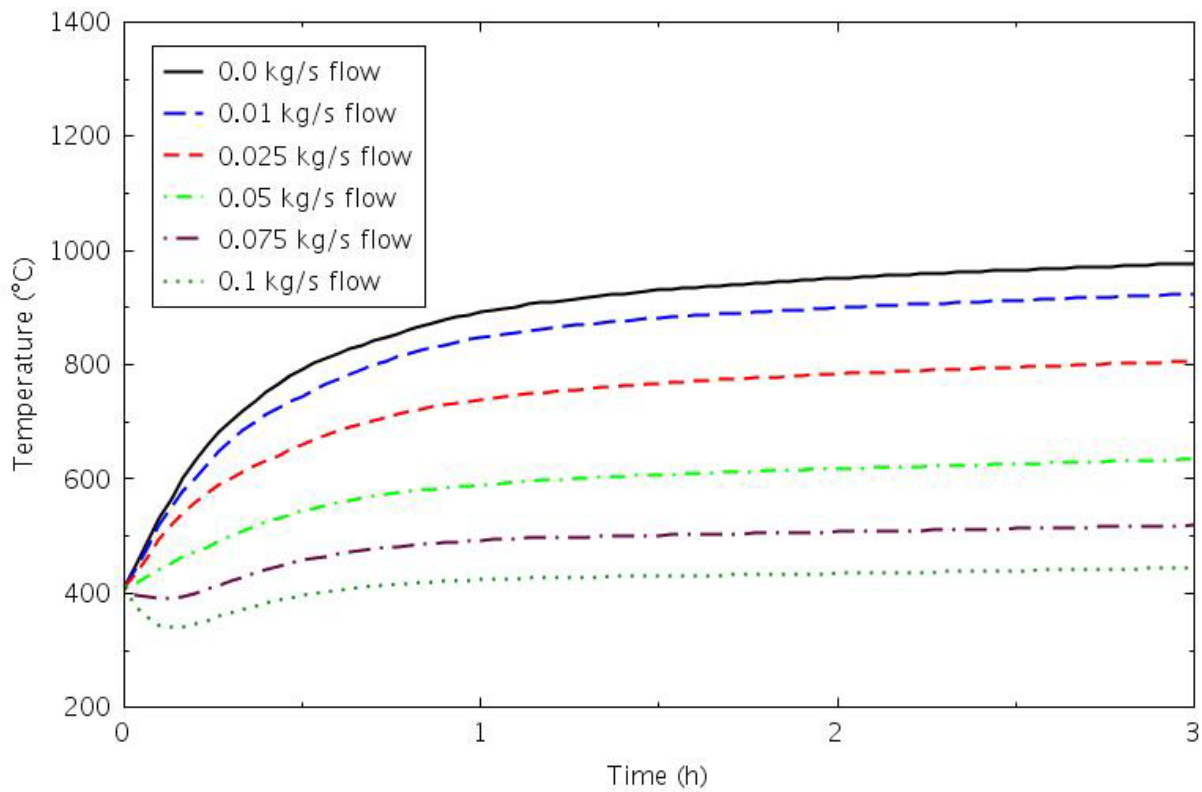


Figure 4-69. Central irradiation tube peak temperatures for the tube cooling flow sensitivity and base-case DCC transients (short term).
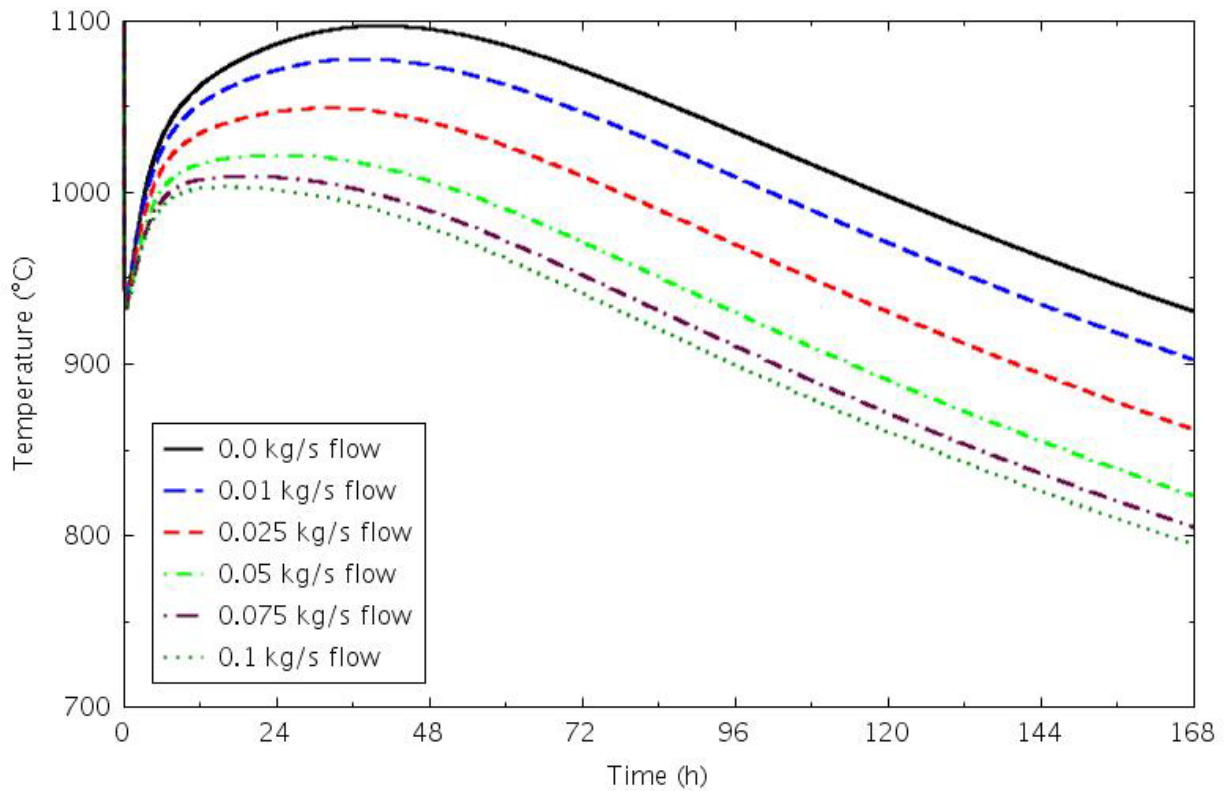
Figure 4-70. Peak fuel temperatures for the tube cooling sensitivity and base-case DCC transients.
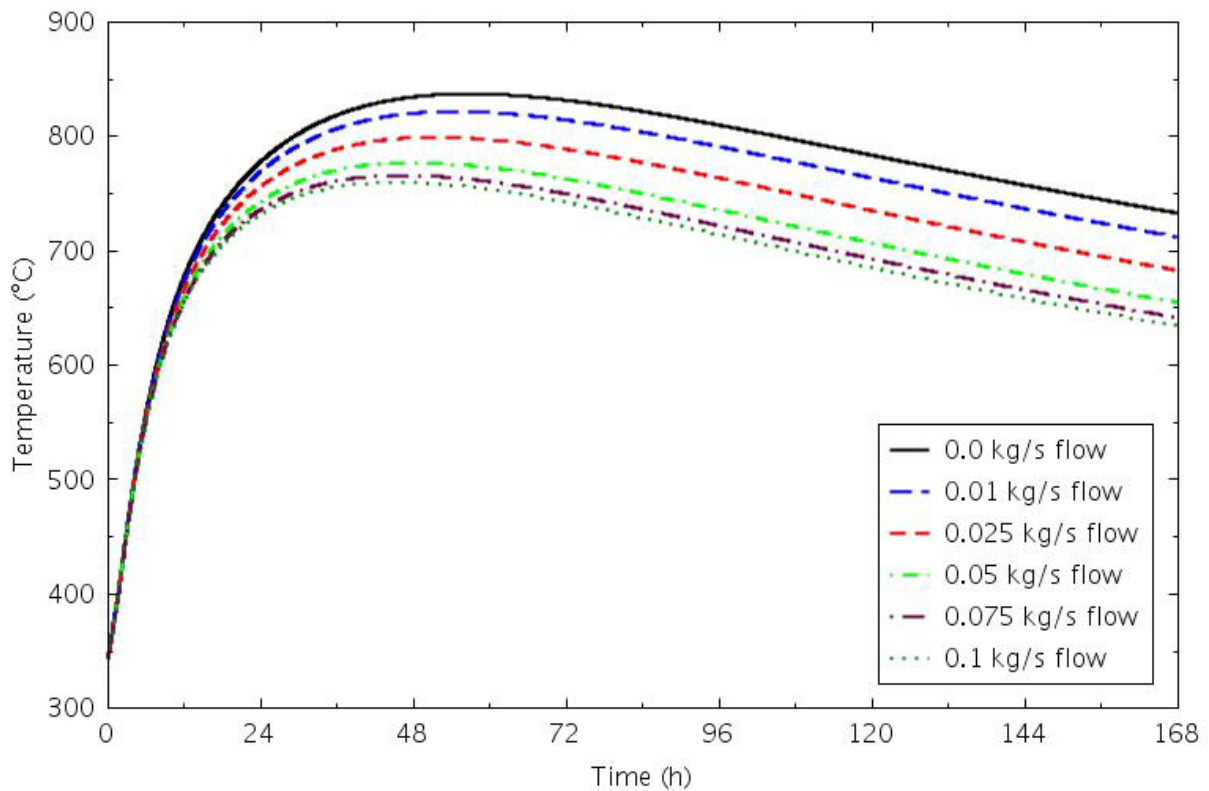


Figure 4-71. Reflector Ring 5 peak temperatures for the tube cooling sensitivity and base-case DCC transients.
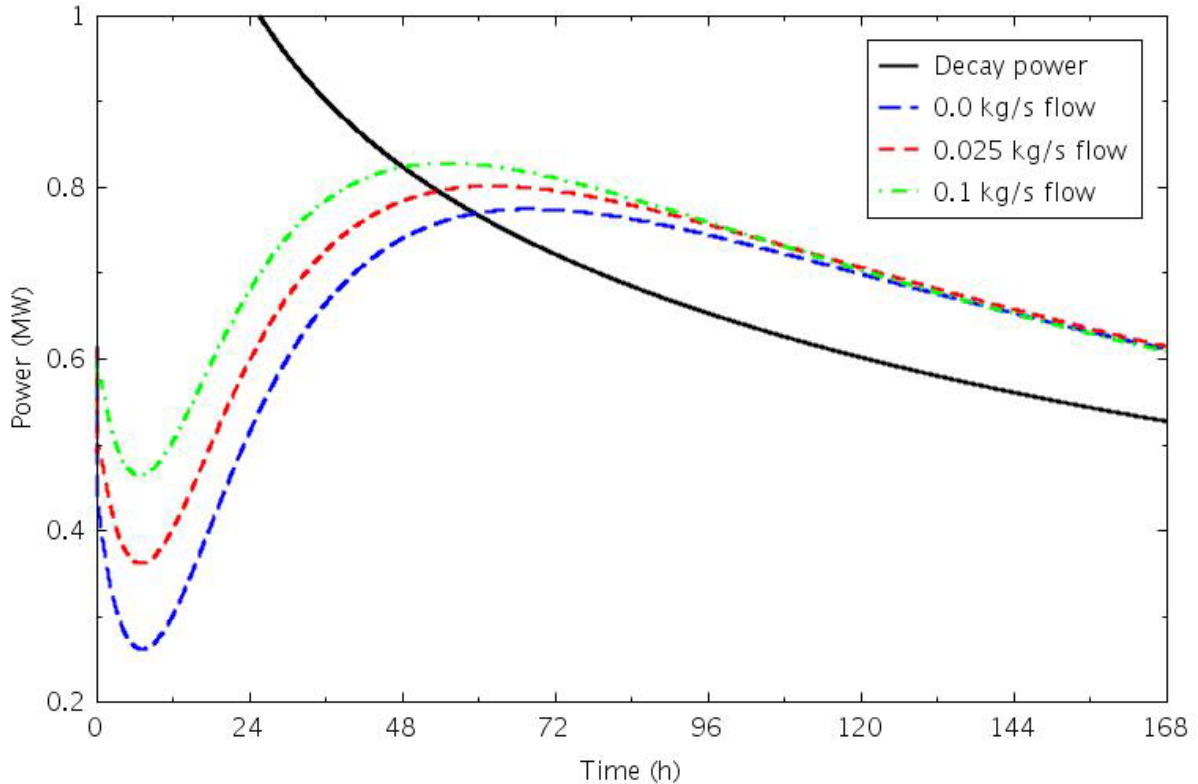
Figure 4-72. Core power and heat removal for the tube cooling flow sensitivity and base-case DCC transients.

## 4.2.3 Pressurized Conduction Cooldown

PCC transients were simulated at different power levels for the 4, 6, and 8-level cores. Most of the calculations were performed with 4-mm gaps between the blocks. At the beginning of the transient, a 5-s linear flow coastdown was imposed on both the primary coolant and the irradiation tube coolant, and the reactor was scrammed. The reactor outlet pressure and temperature were maintained at the steady-state values throughout the transient. Both base-case and sensitivity calculations were performed.

### 4.2.3.1 Base Case Calculations

Figure 4-73 presents the peak fuel temperatures for the three nominal cases. As the core power and height increased, the peak temperatures increased and the time to reach the peak lengthened. The temperatures dropped at the beginning of the transient as heat was redistributed from the bottom of the core to the middle and top. The peak temperatures were about 100-170°C lower than the values from the corresponding DCC transients.

Peak temperatures in the central reflector are shown in Figure 4-74. With no cooling flow in the center irradiation tube, the reflector temperatures were nearly the same as the fuel temperatures. The peak graphite temperatures decreased moving radially outward from the fuel. Figures 4-75 through 4-79 show peak temperatures from the outer reflector rings and the PSR; the peak temperatures decreased about 100°C for each full ring. This rate of peak temperature decrease was maintained through the core barrel and reactor vessel wall as well, as shown in Figures 4-80 and 4-81.

Coolant temperatures in the lower and upper plenums are presented in Figures 4-82 and 4-83, respectively. After the forced flow stopped, a natural circulation flow was established in the core region, with flow generally up in the fuel blocks and central reflector and down in the outer reflector. This downward flow from the cooler regions of the core (Ring 5 and the PSR) caused the temperature in the
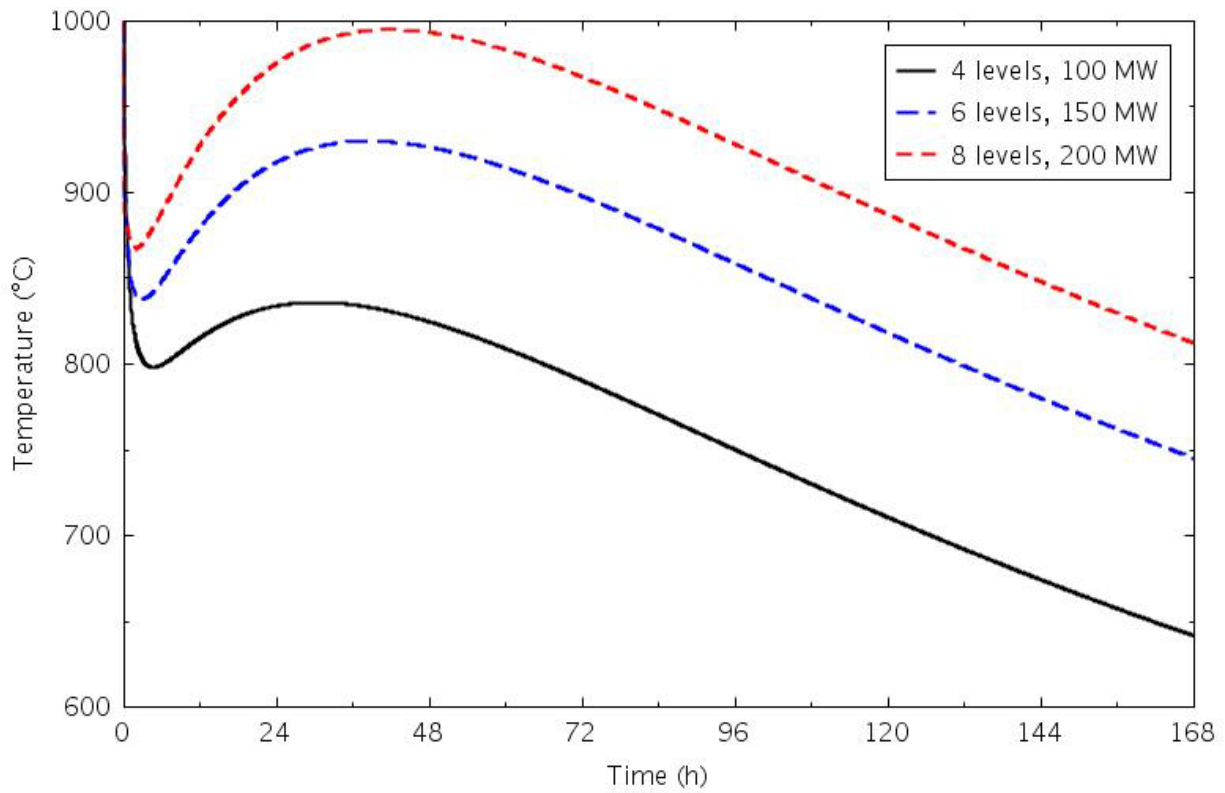
Figure 4-73. Peak fuel temperatures for the three nominal core PCC transients.
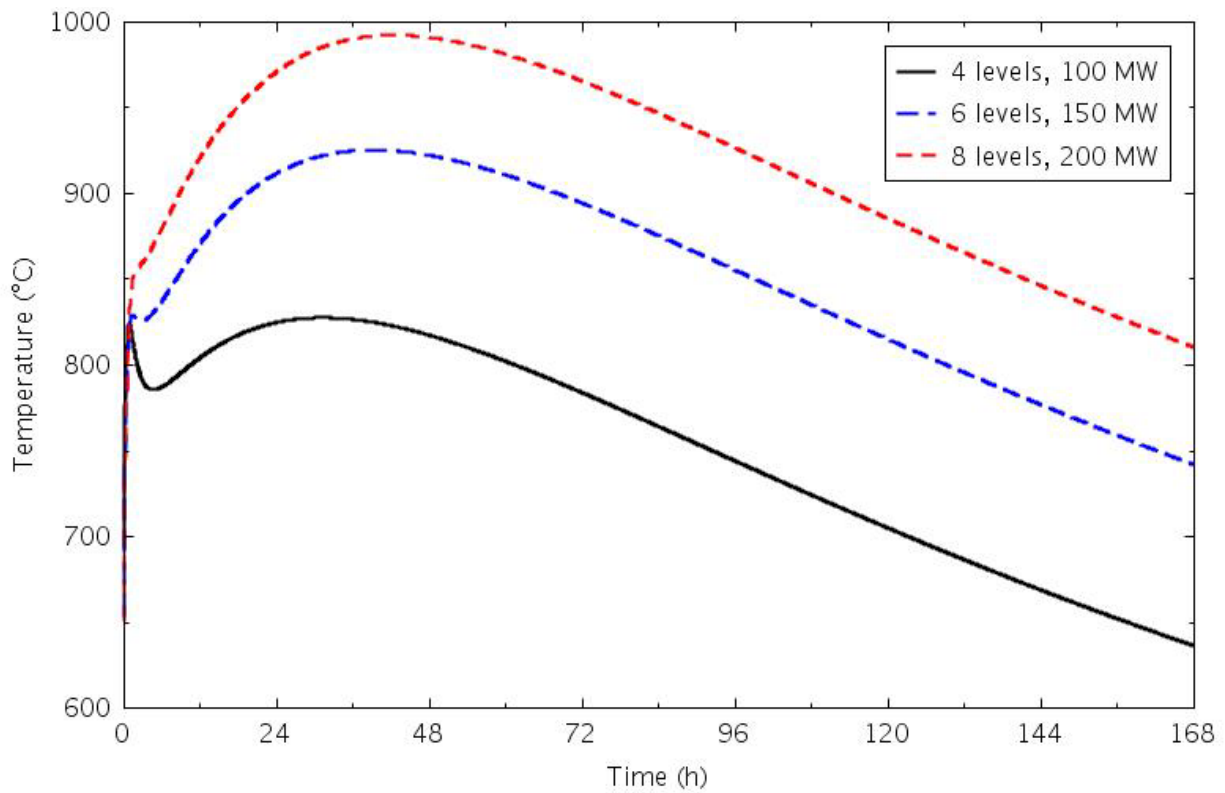


Figure 4-74. Central reflector peak temperatures for the three nominal core PCC transients.
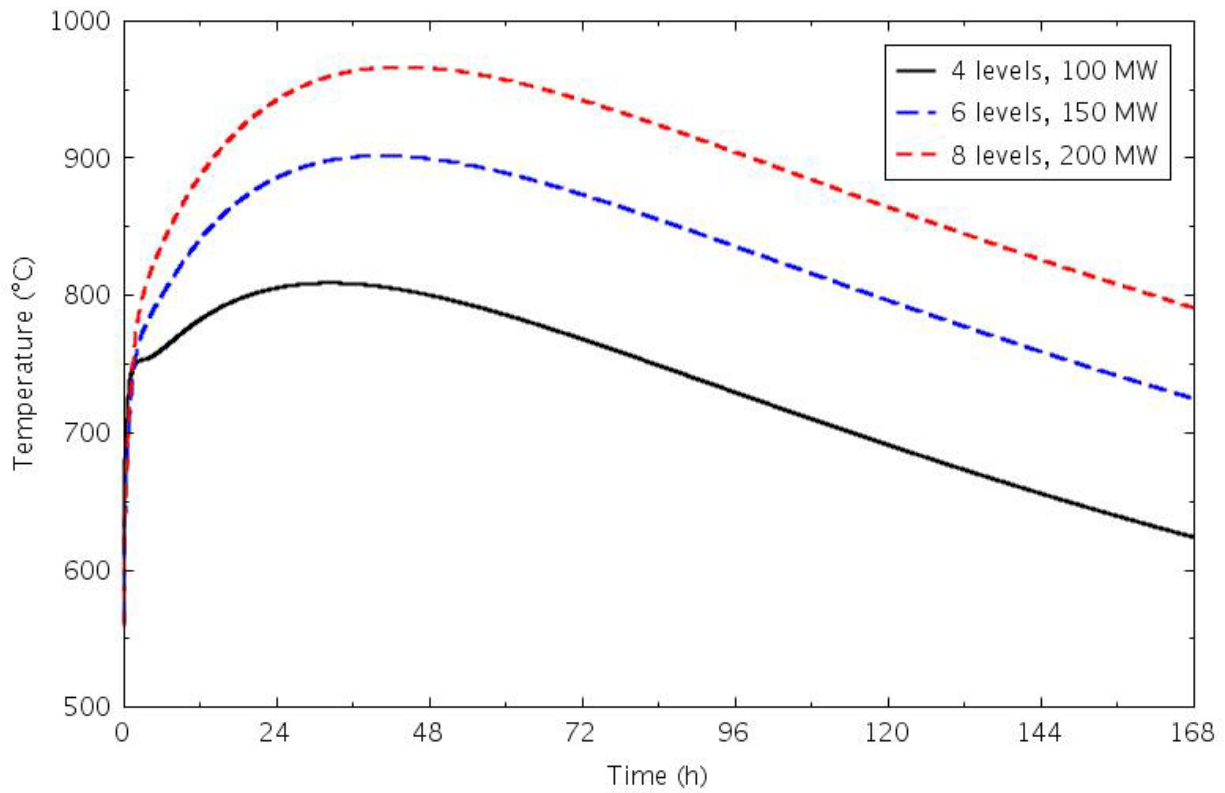
Figure 4-75. Ring 3 reflector peak temperatures for the three nominal core PCC transients.
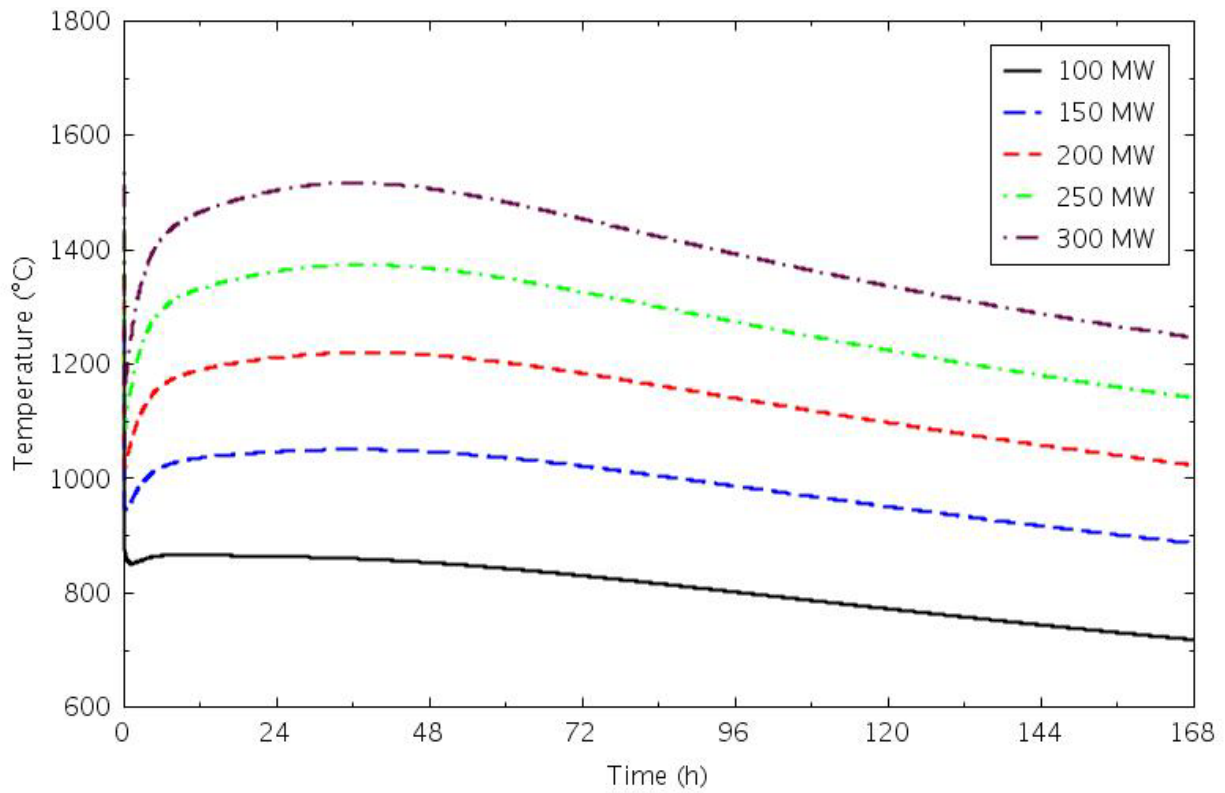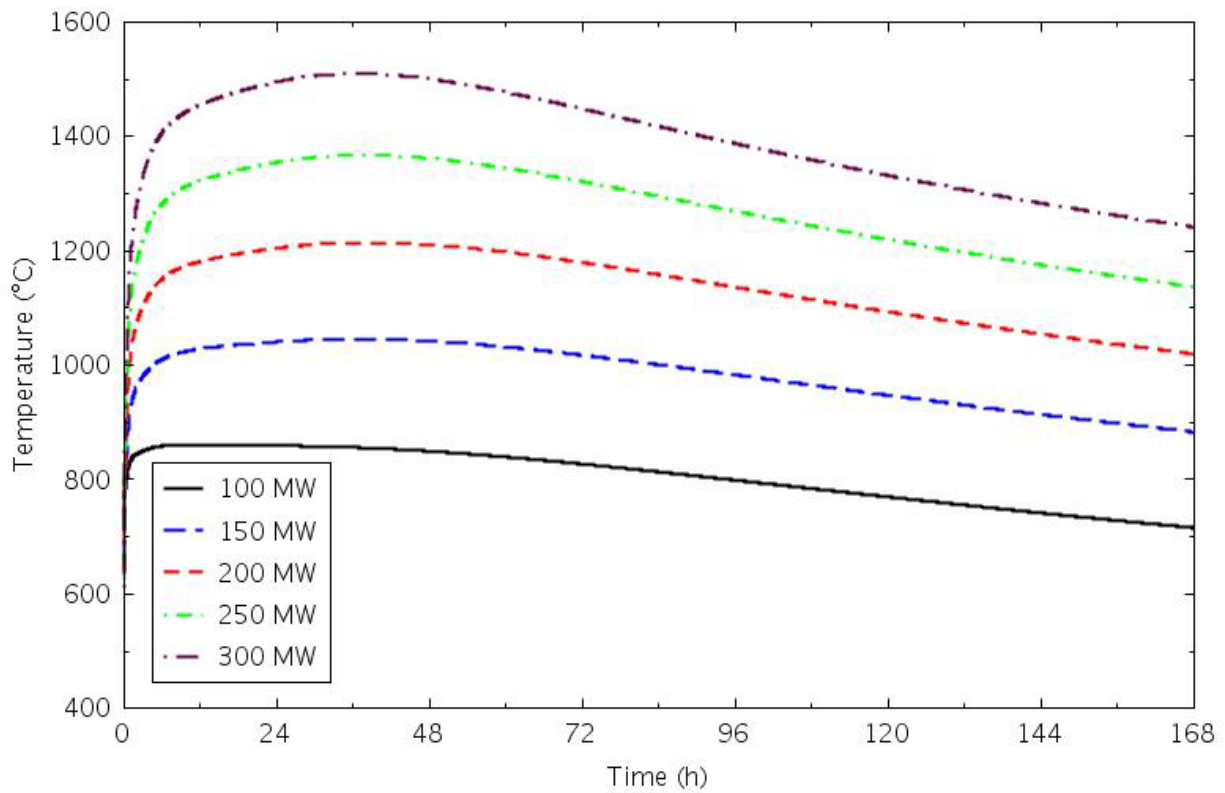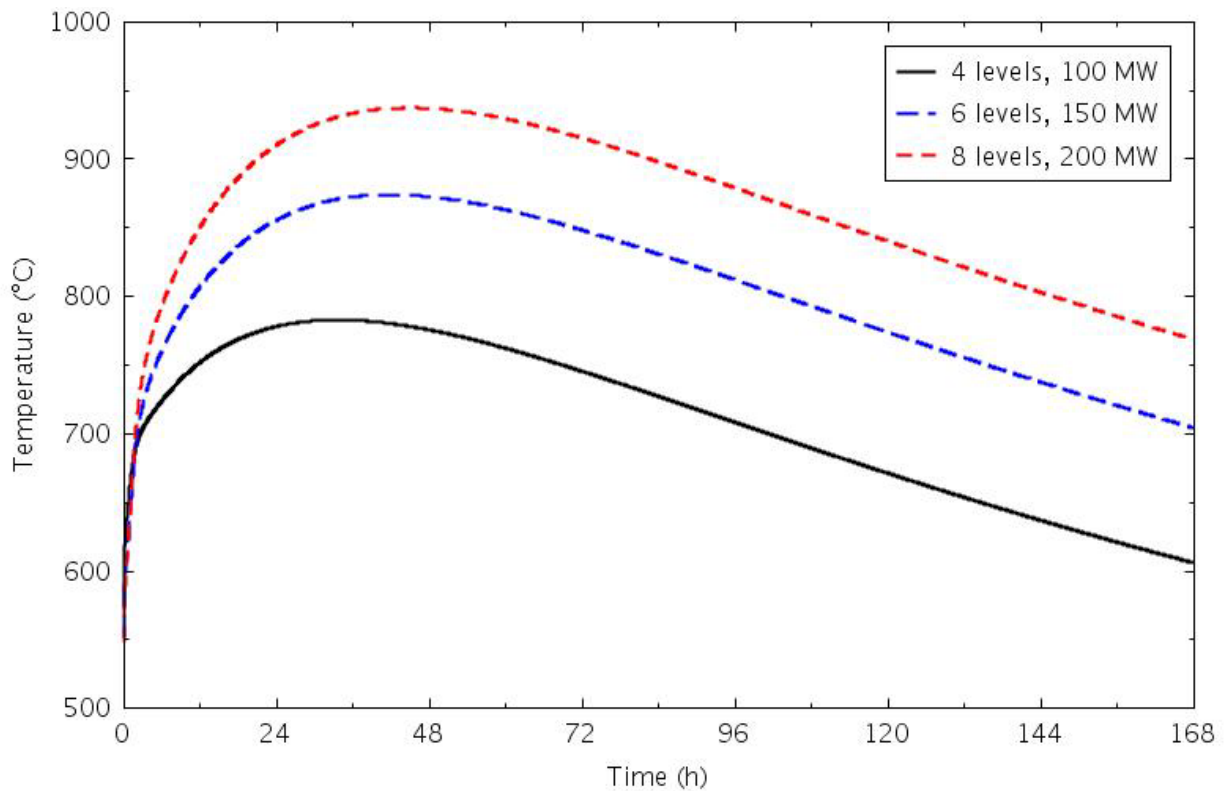


Figure 4-76. Reflector Ring 4 inner half peak temperatures for the three nominal core PCC transients.
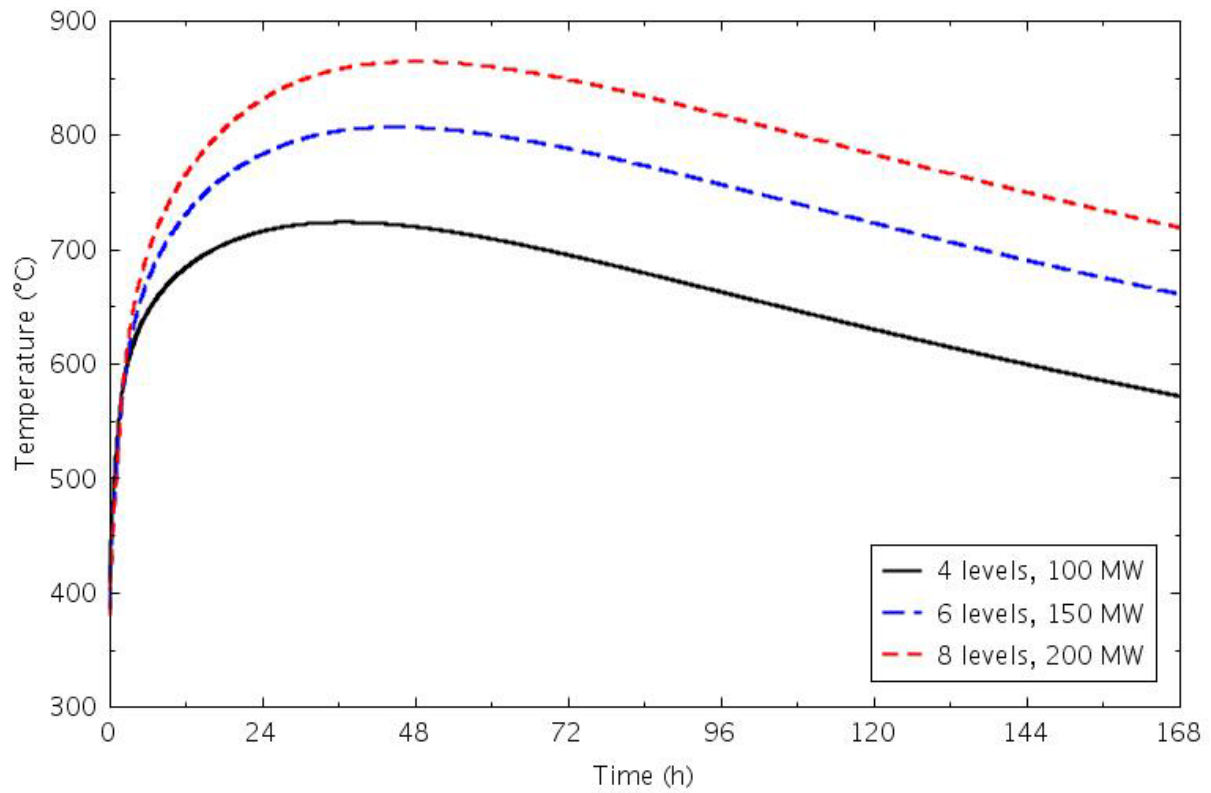
Figure 4-77. Reflector Ring 4 outer half peak temperatures for the three nominal core PCC transients.
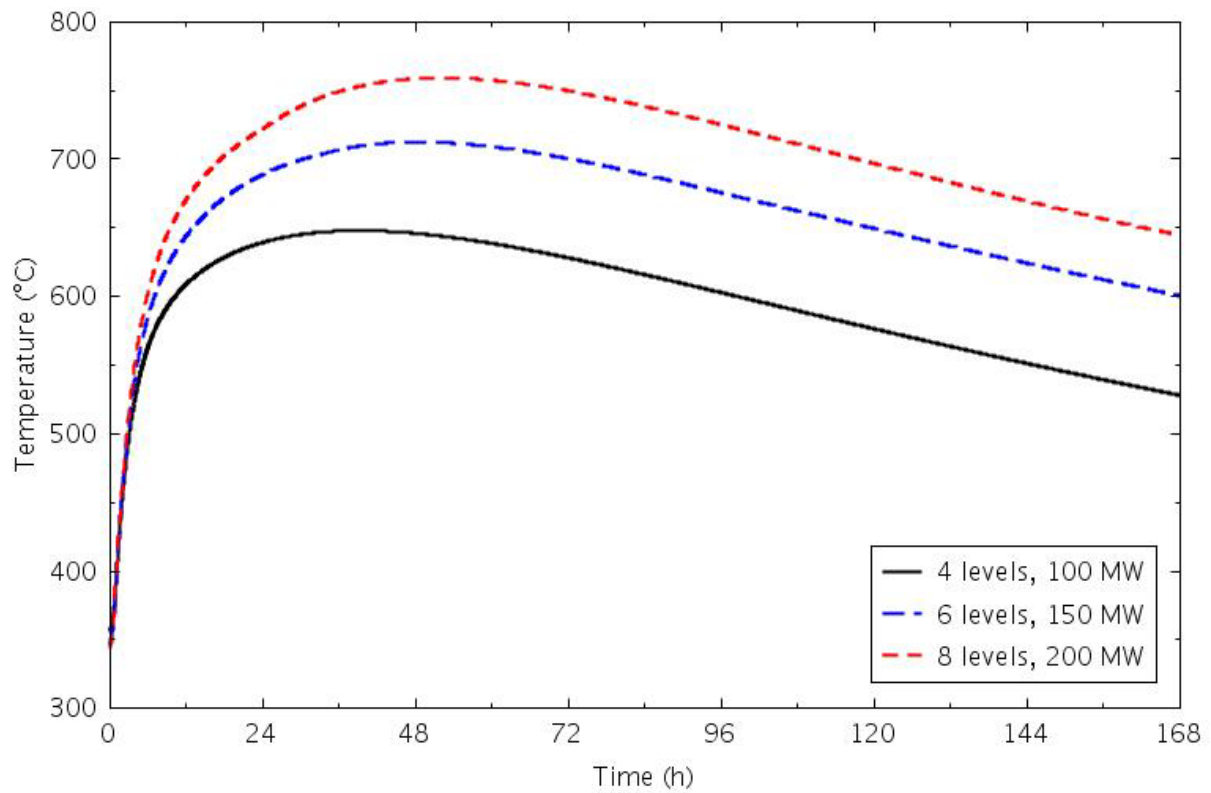


Figure 4-78. Reflector Ring 5 peak temperatures for the three nominal core PCC transients.
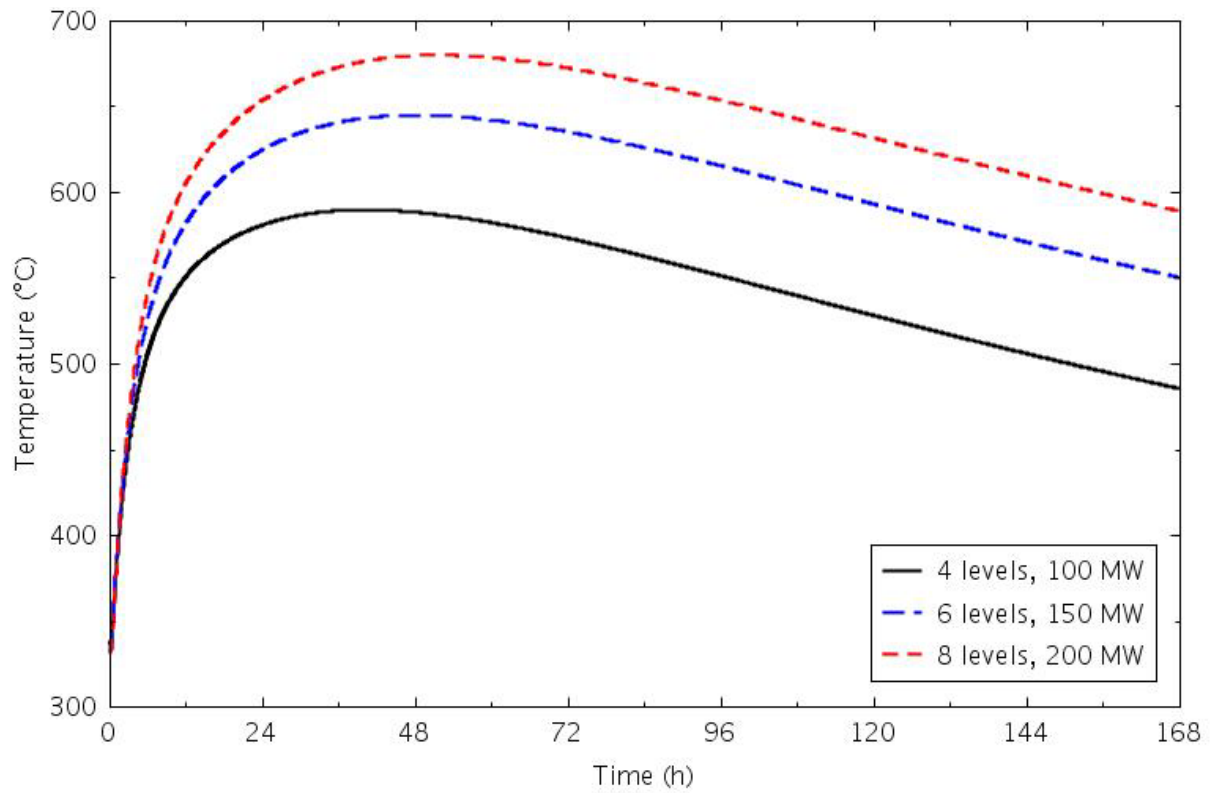
Figure 4-79. PSR peak temperatures for the three nominal core PCC transients.
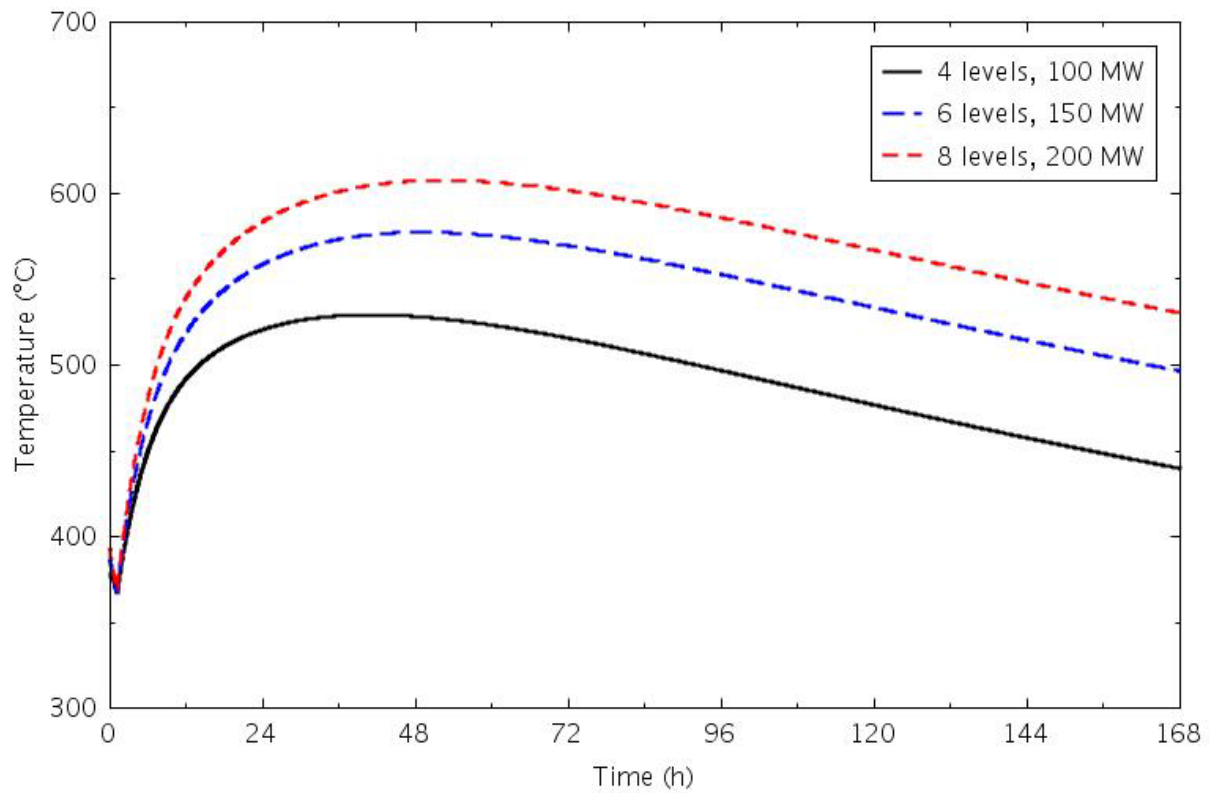


Figure 4-80. Core barrel peak temperatures for the three nominal core PCC transients.
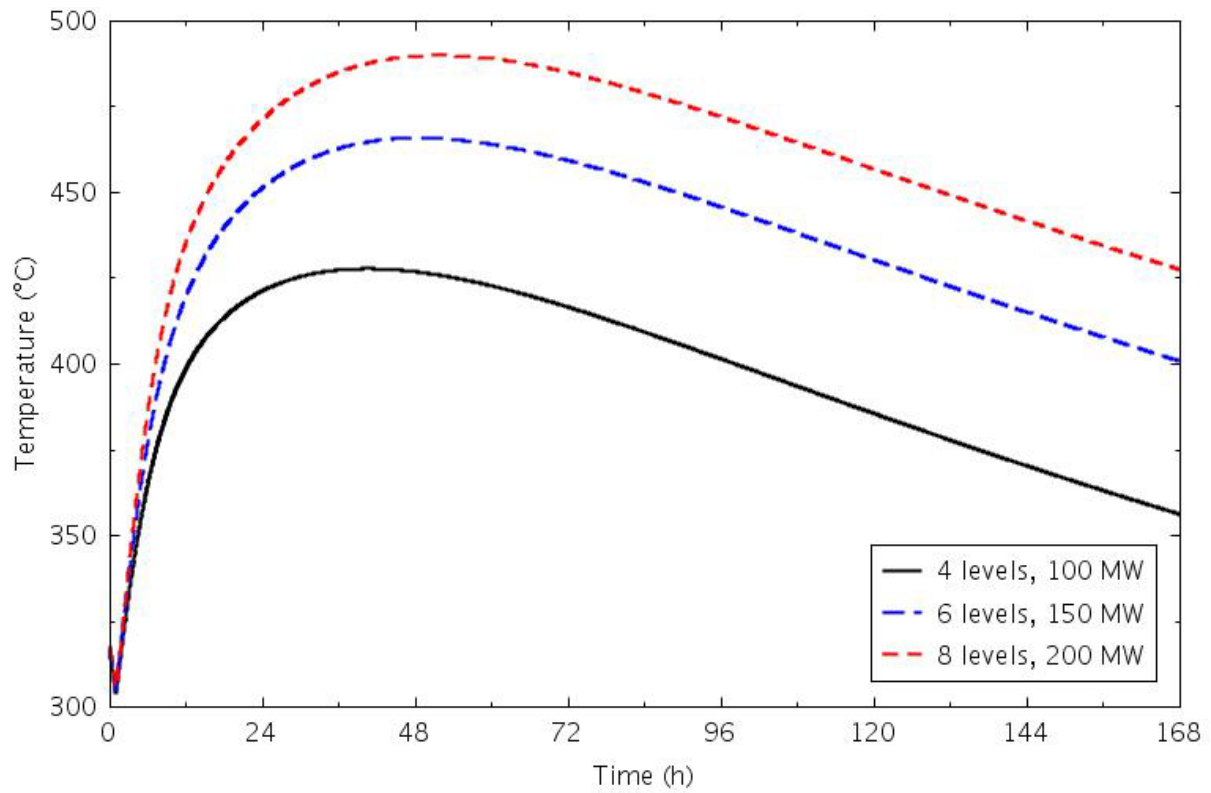
Figure 4-81. Reactor vessel wall peak temperatures for the three nominal core PCC transients.
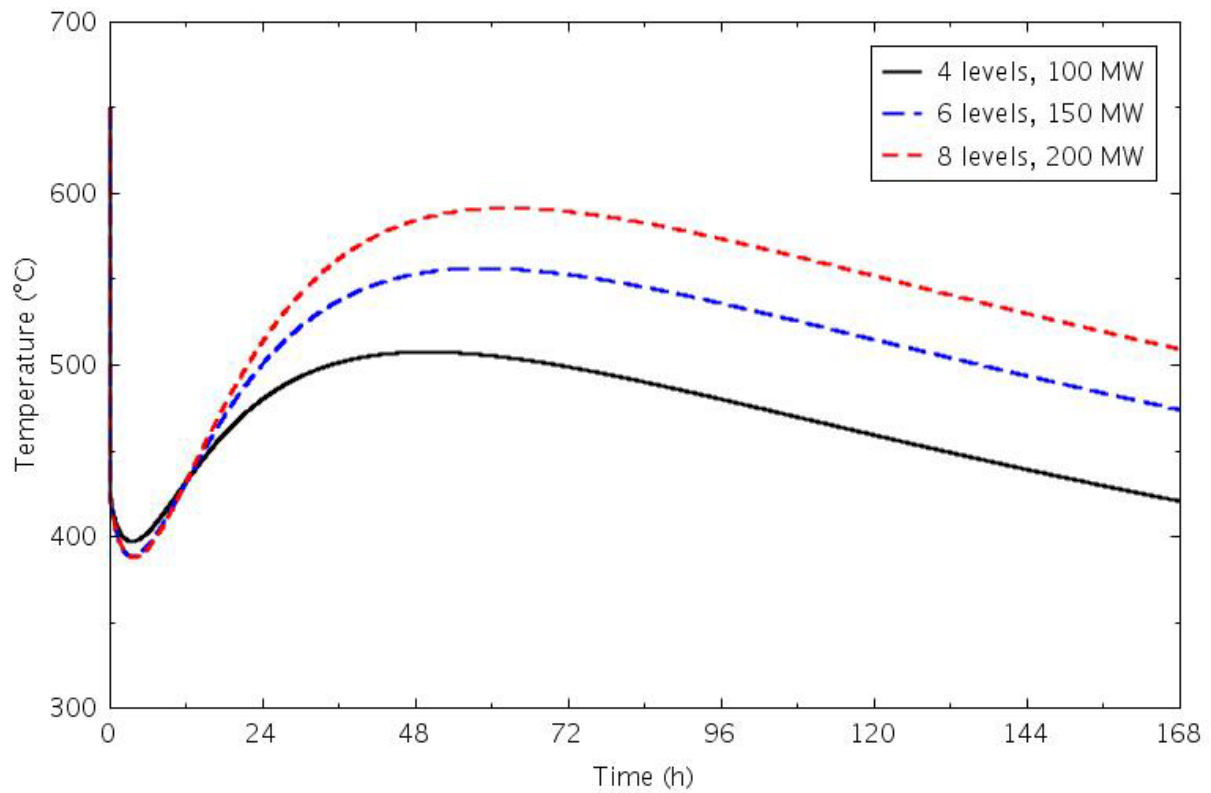


Figure 4-82. Lower plenum coolant temperatures for the three nominal core PCC transients.
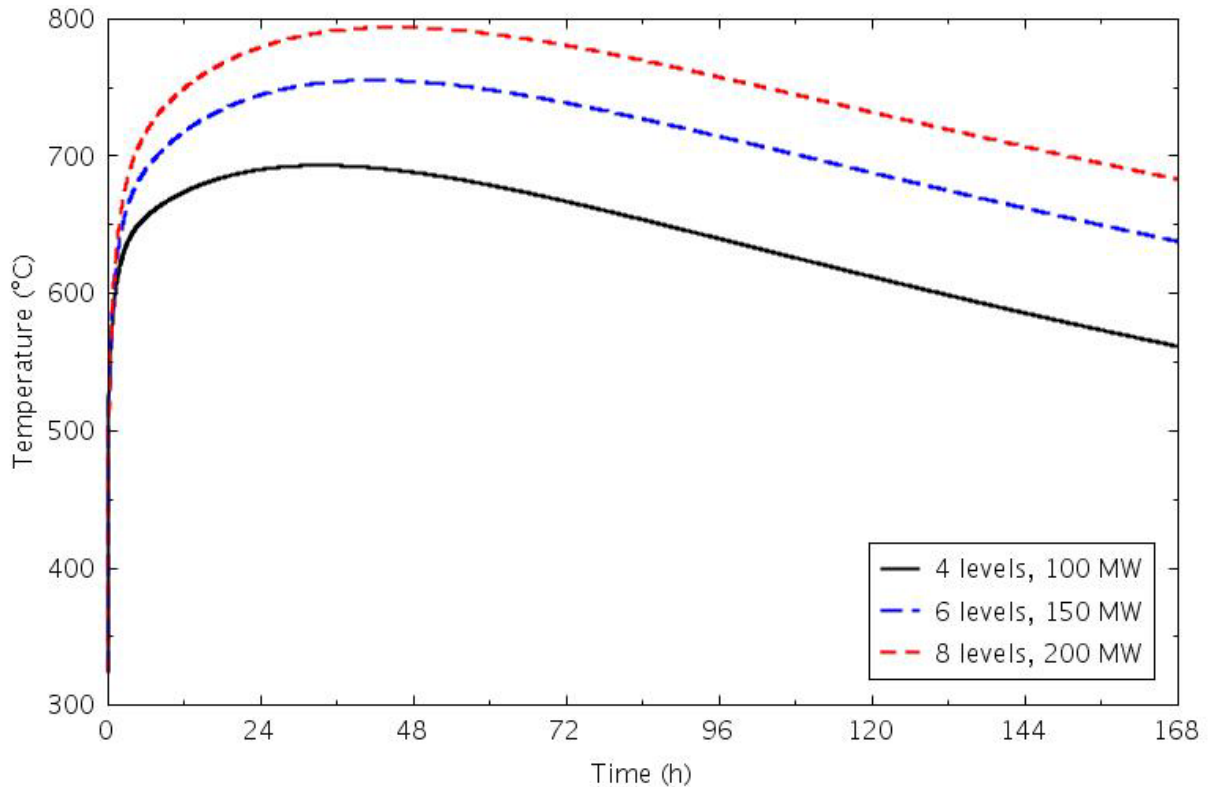
Figure 4-83. Upper plenum coolant temperatures for the three nominal core PCC transients.

lower plenum to continue decreasing for about 4 hours before beginning to increase. In the upper plenum, the temperature increased immediately as hotter fluid from the core rose to mix with the cooler helium that was there initially. Peak temperatures were reached in 48 to 60 hours; in the lower plenum, none of the cases had temperatures higher than the steady-state value.

Coolant temperatures at the RCCS outlet are presented in Figure 4-84. There was little variation in the temperature, indicating that the RCCS panels were providing a nearly constant boundary condition for radiation from the reactor vessel.

Figures 4-85 through 4-96 present the results from 4-level core simulations at powers ranging from 100 to 200 MW. Figures 4-97 through 4-108 present results from 6-level core calculations at powers from 100 to 300 MW. Results from the 8-level core simulations at powers ranging from 200 to 400 MW are presented in Figures 4-109 through 4-120. All of these calculations were performed with 4-mm gaps between the blocks. The behavior in each of the transients was similar to that described above for the nominal cases. No unexpected phenomena were encountered; the structure and coolant temperatures increased with increasing power, the time peak temperatures were reached lengthened with increasing power, and the RCCS temperature changed very little.
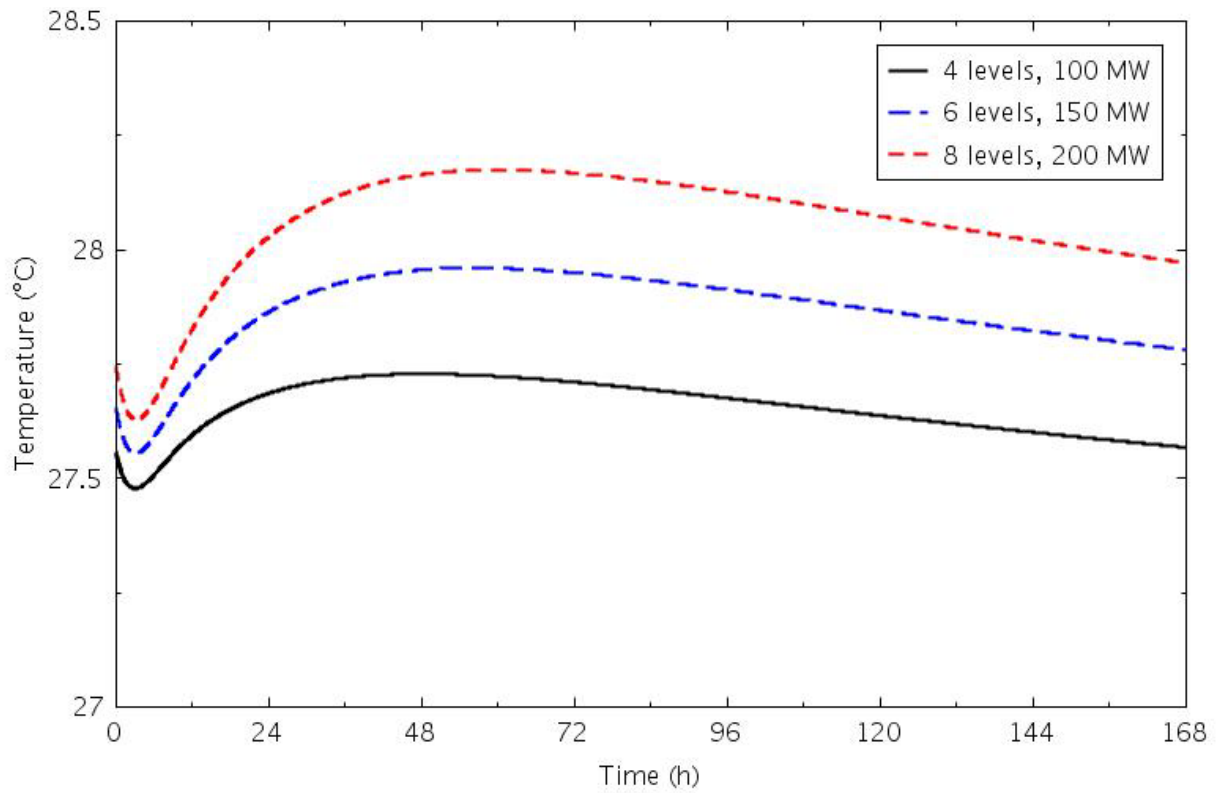
Figure 4-84. RCCS coolant outlet temperatures for the three nominal core PCC transients.
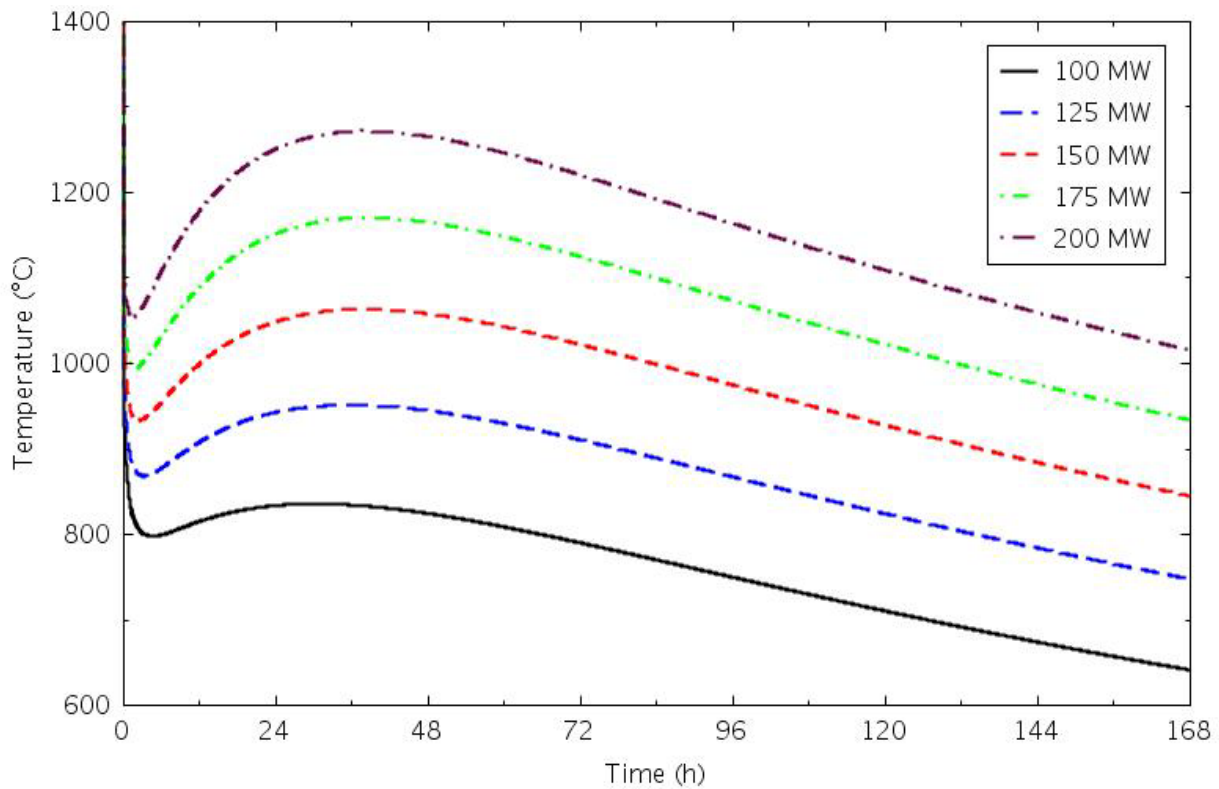


Figure 4-85. Peak fuel temperatures for the 4-level core PCC transients.
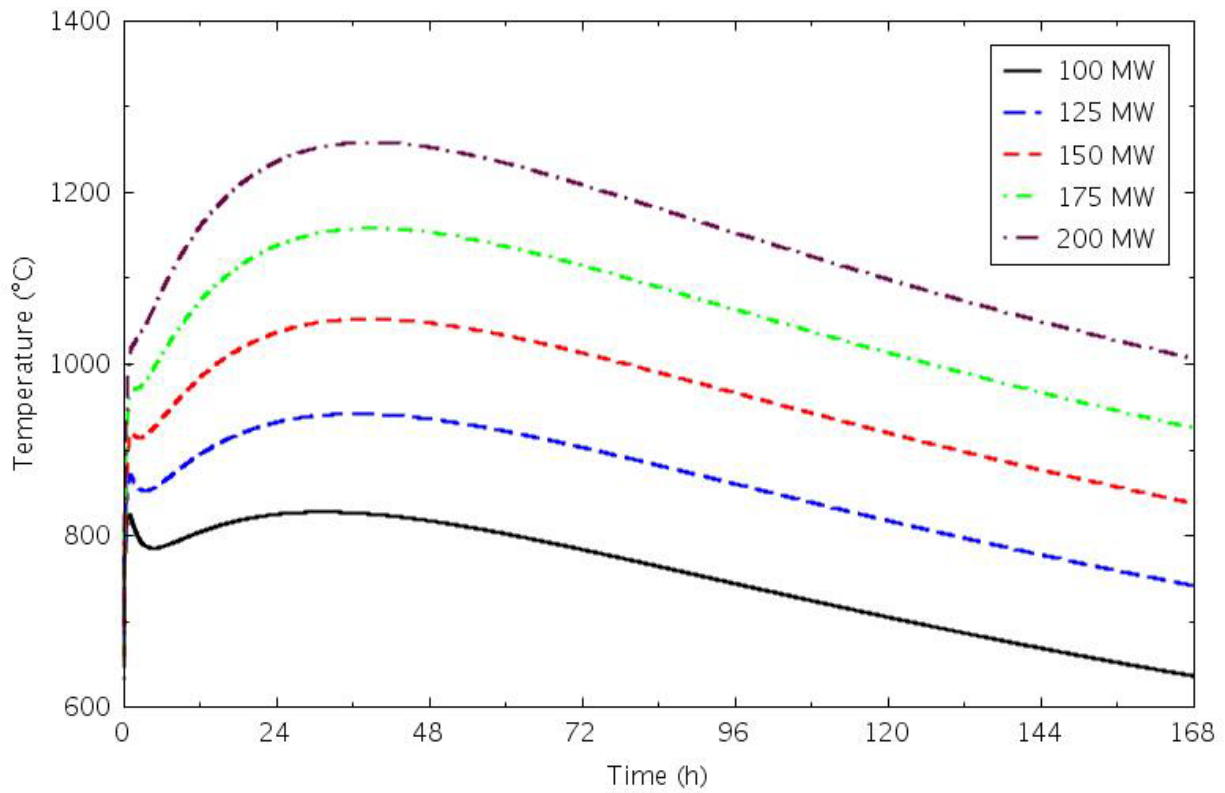
Figure 4-86. Central reflector peak temperatures for the 4-level core PCC transients.
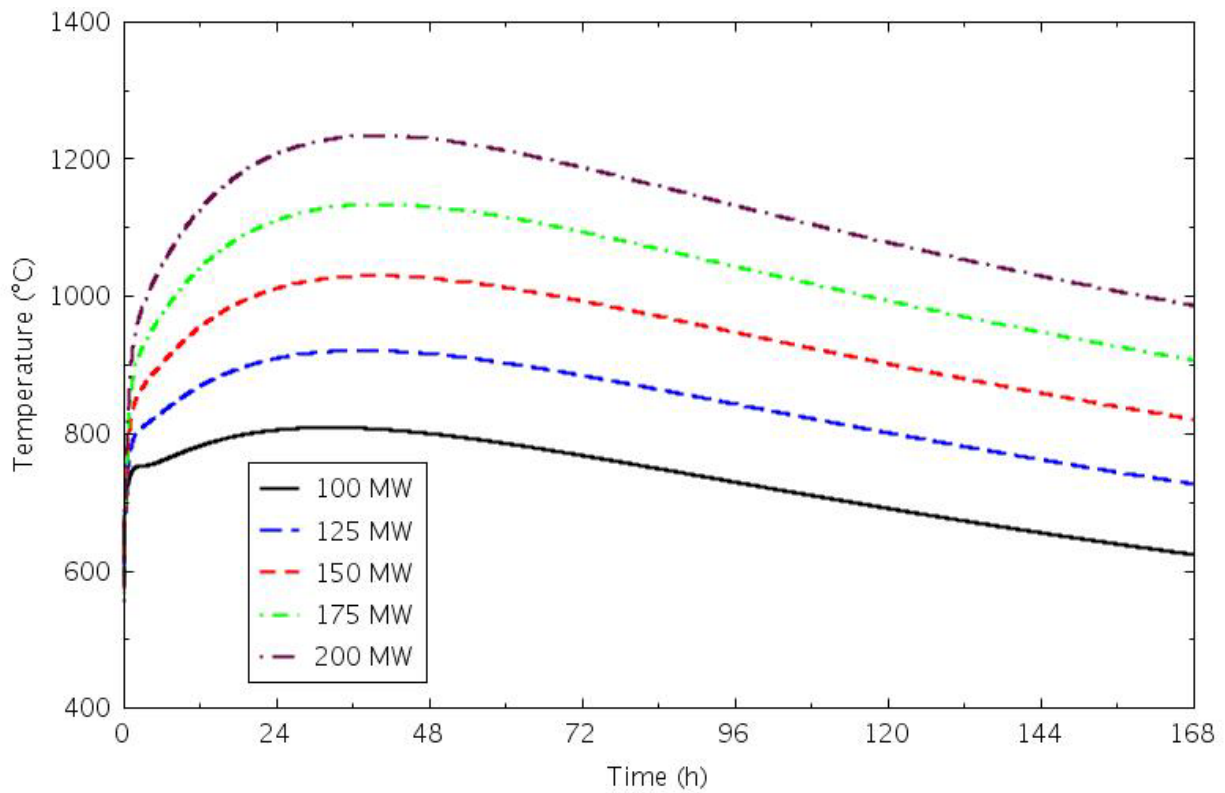


Figure 4-87. Ring 3 reflector peak temperatures for the 4-level core PCC transients.
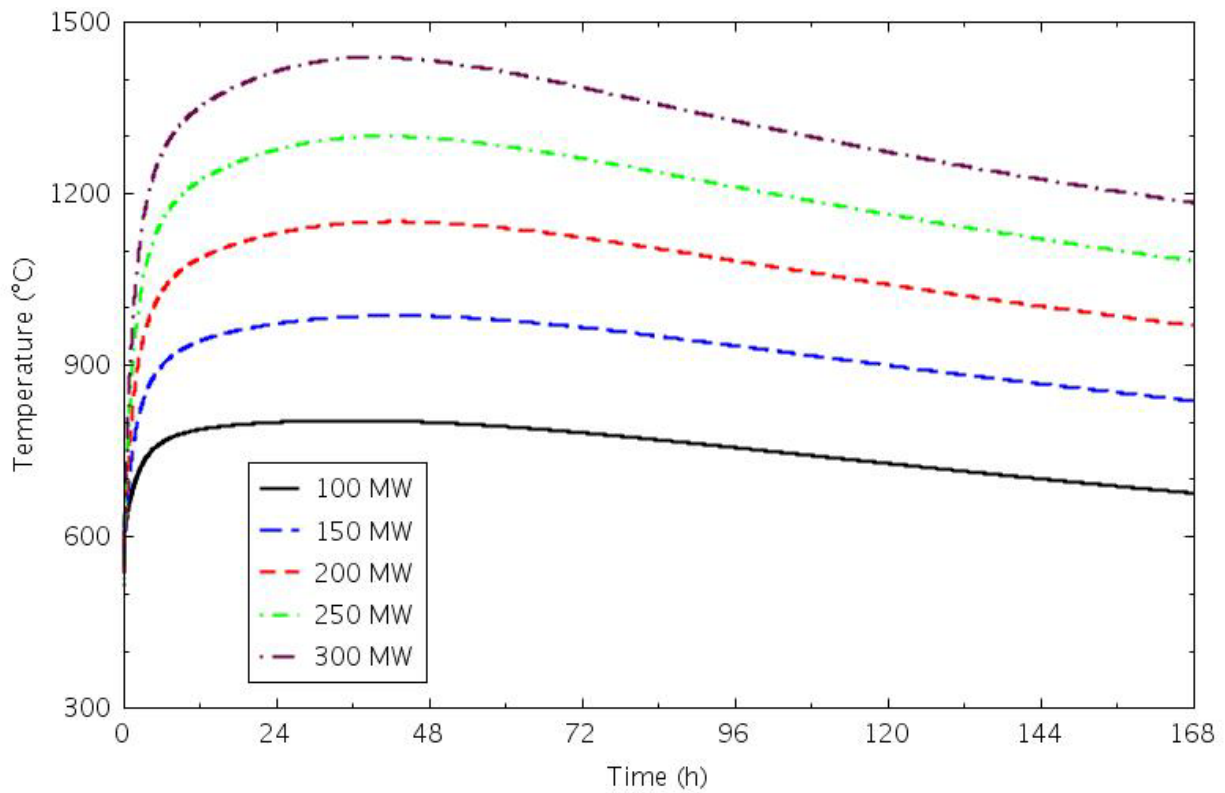
74
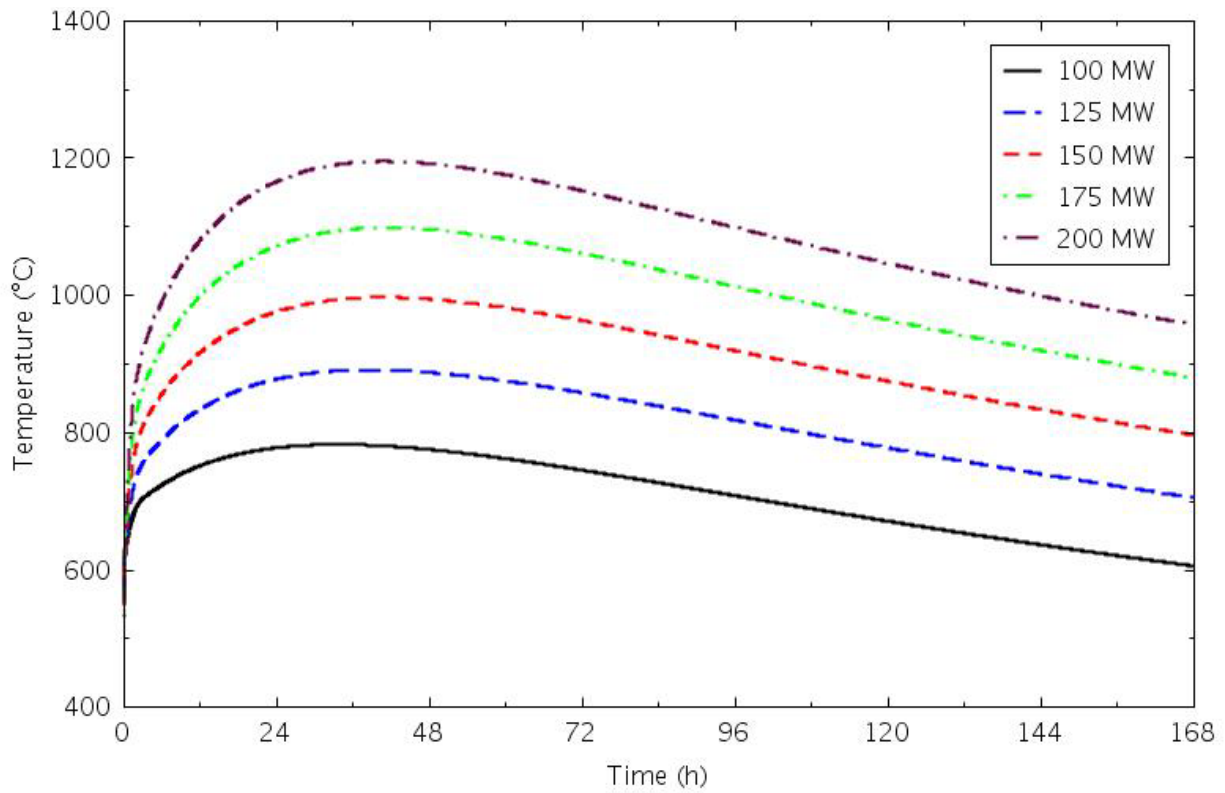
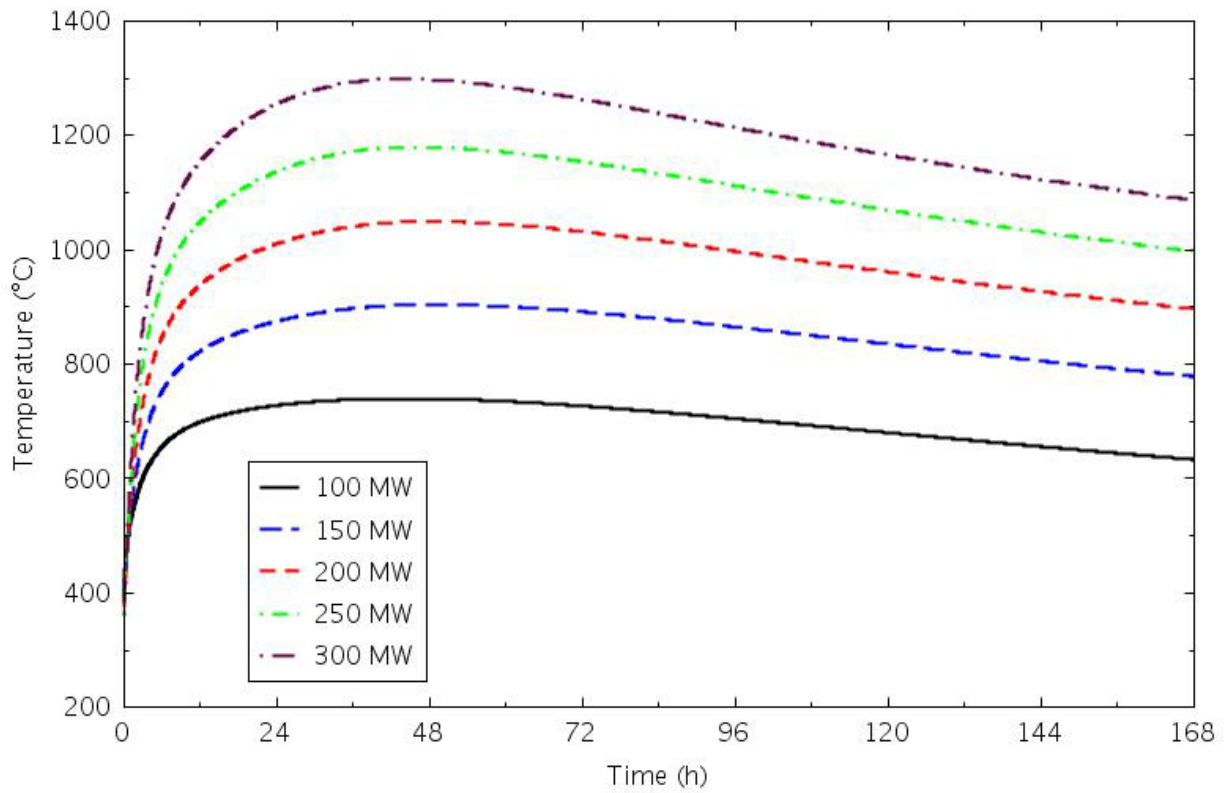Figure 4-88. Reflector Ring 4 inner half peak temperatures for the 4-level core PCC transients.
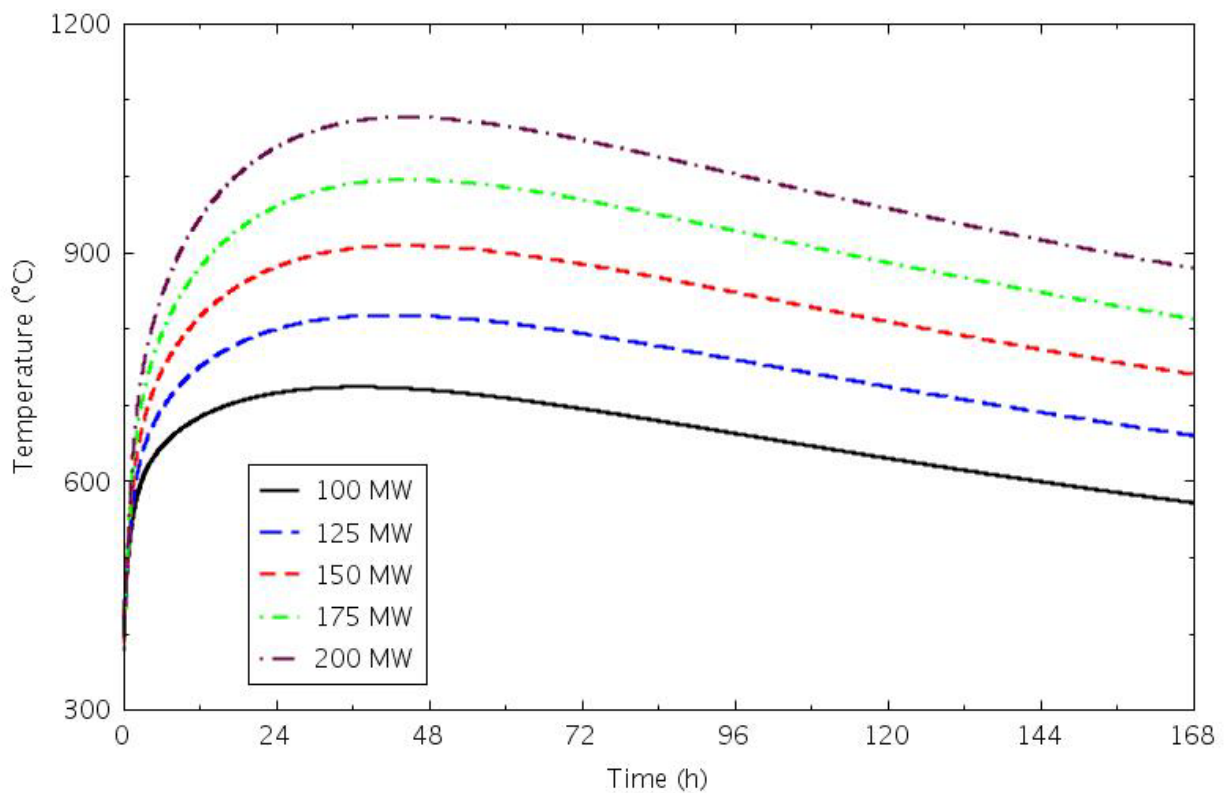


Figure 4-89. Reflector Ring 4 outer half peak temperatures for the 4-level core PCC transients.

75
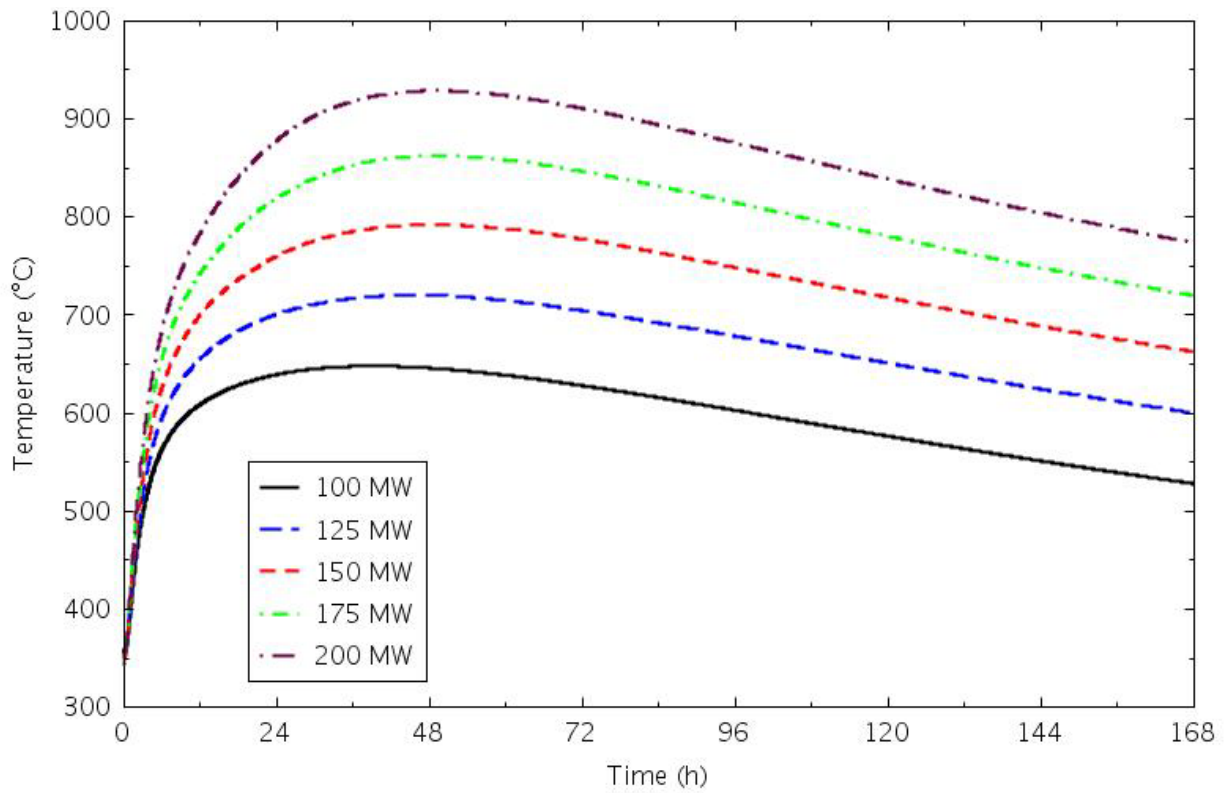
Figure 4-90. Reflector Ring 5 peak temperatures for the 4-level core PCC transients.
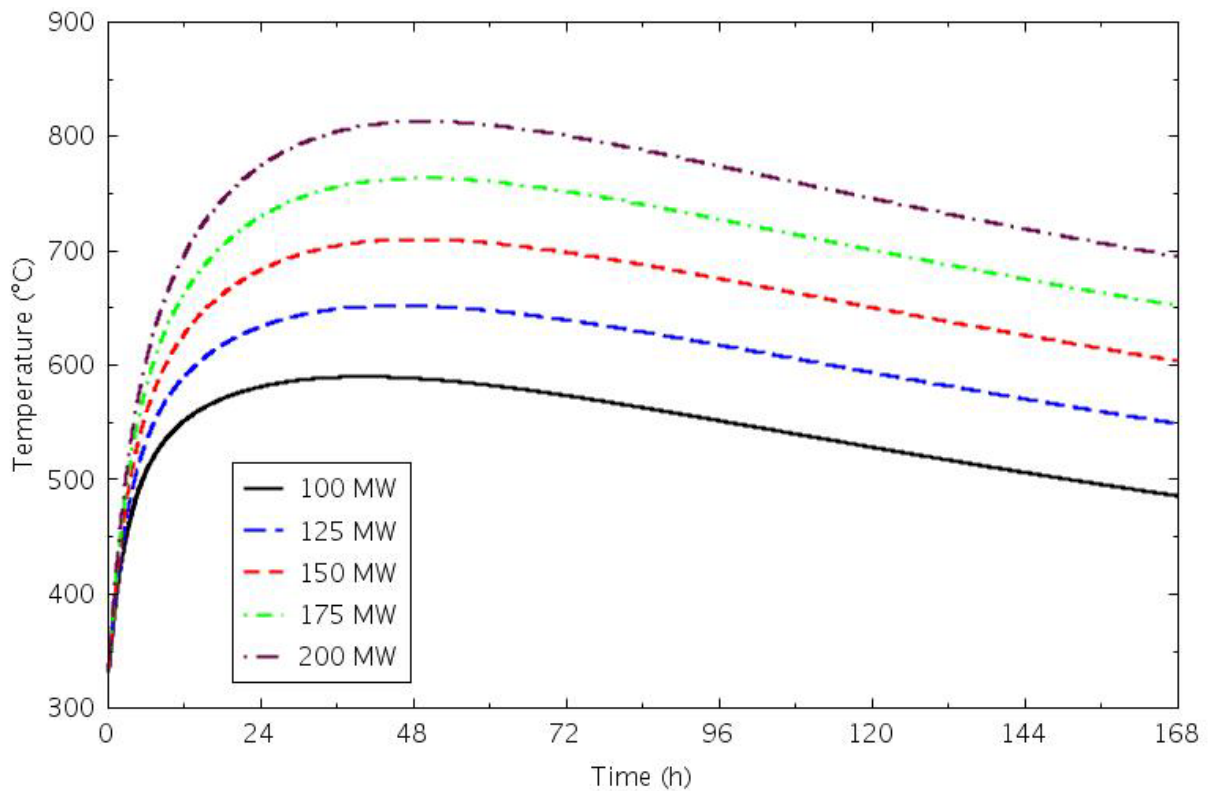


Figure 4-91. PSR peak temperatures for the 4-level core PCC transients.
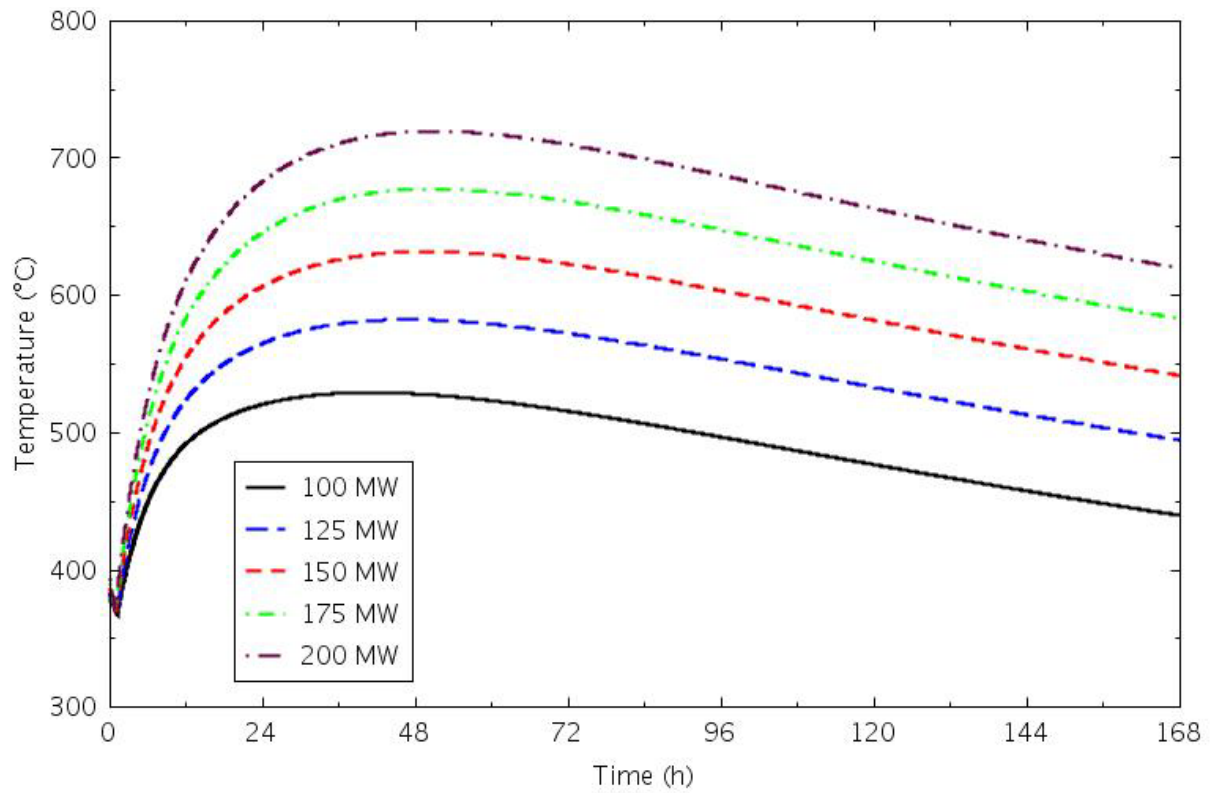
Figure 4-92. Core barrel peak temperatures for the 4-level core PCC transients.
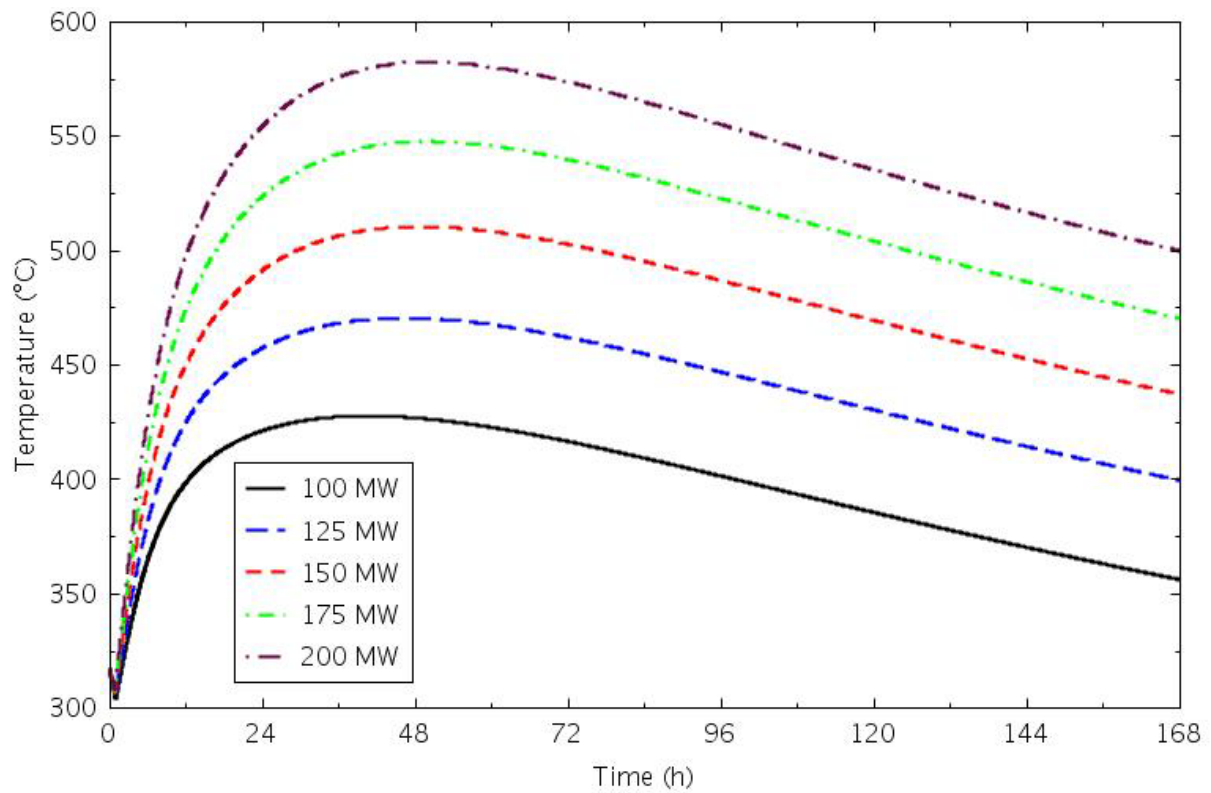


Figure 4-93. Reactor vessel wall peak temperatures for the 4-level core PCC transients.
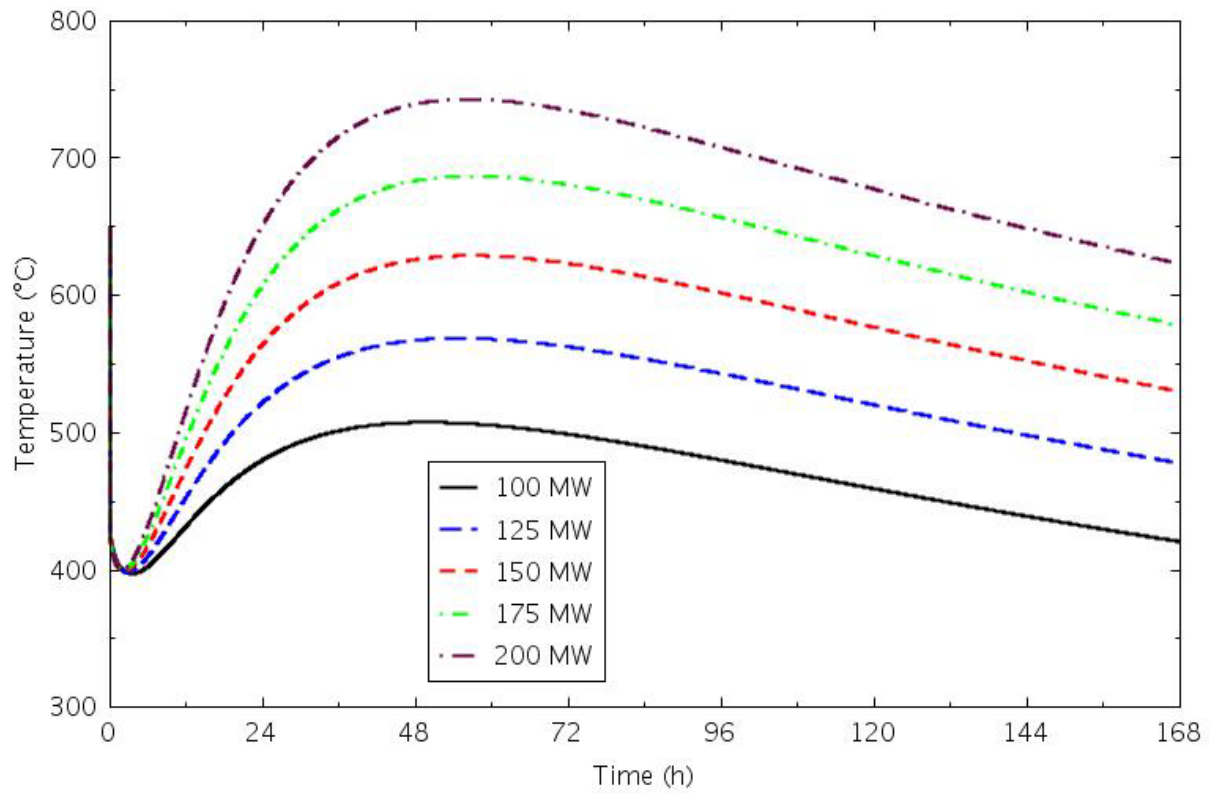
Figure 4-94. Lower plenum coolant temperatures for the 4-level core PCC transients.
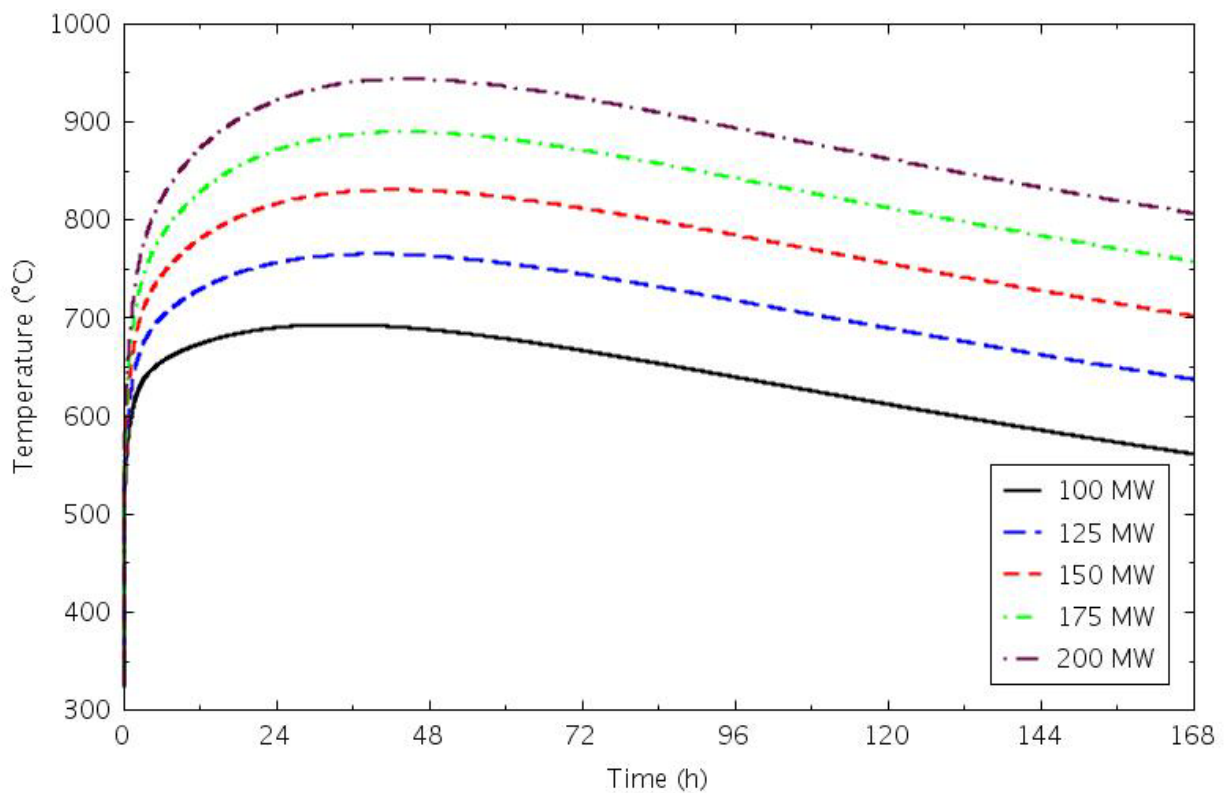


Figure 4-95. Upper plenum coolant temperatures for the 4-level core PCC transients.
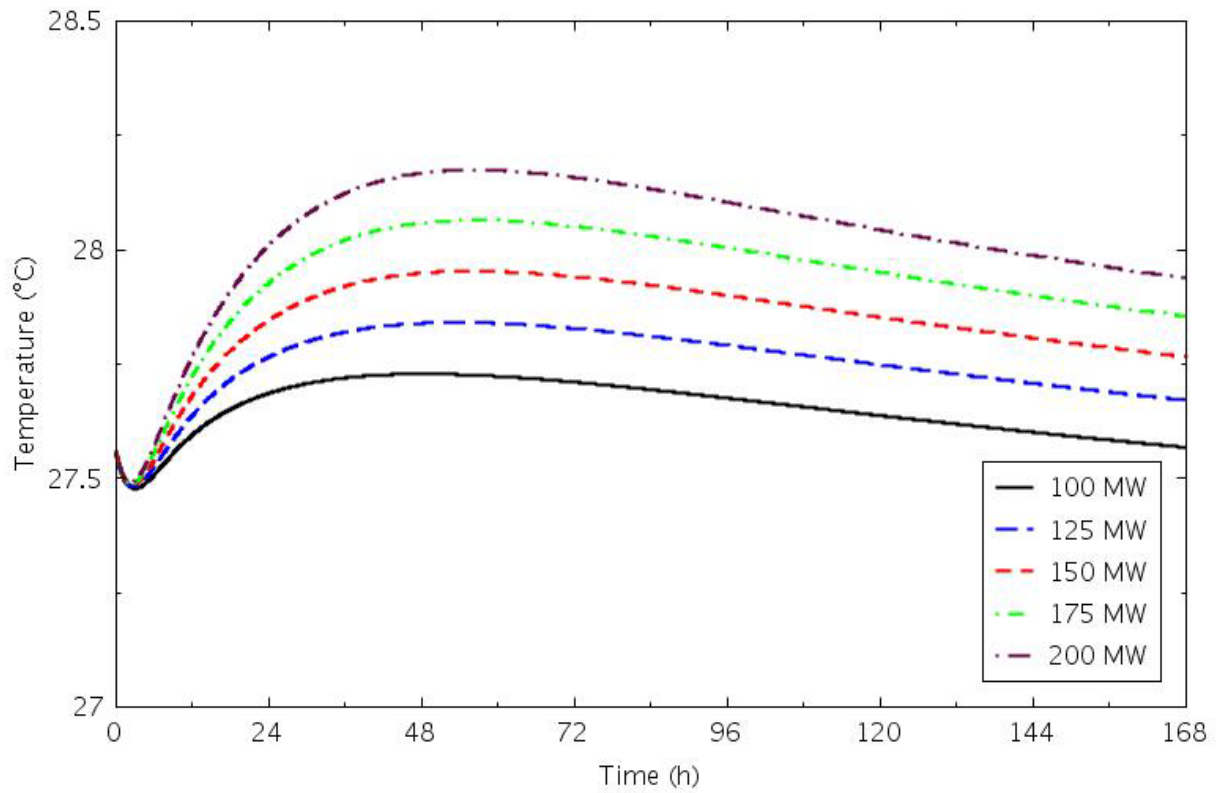
Figure 4-96. RCCS coolant outlet temperatures for the 4-level core PCC transients.
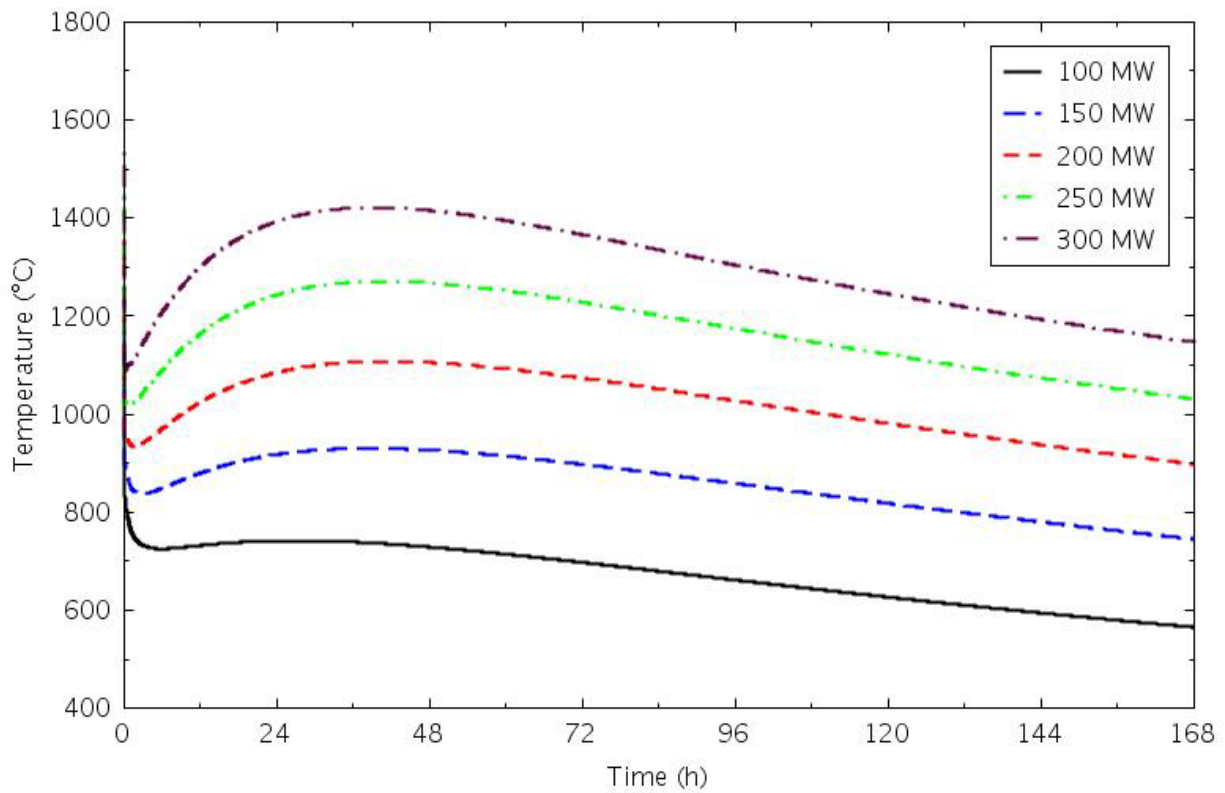


Figure 4-97. Peak fuel temperatures for the 6-level core PCC transients.

79
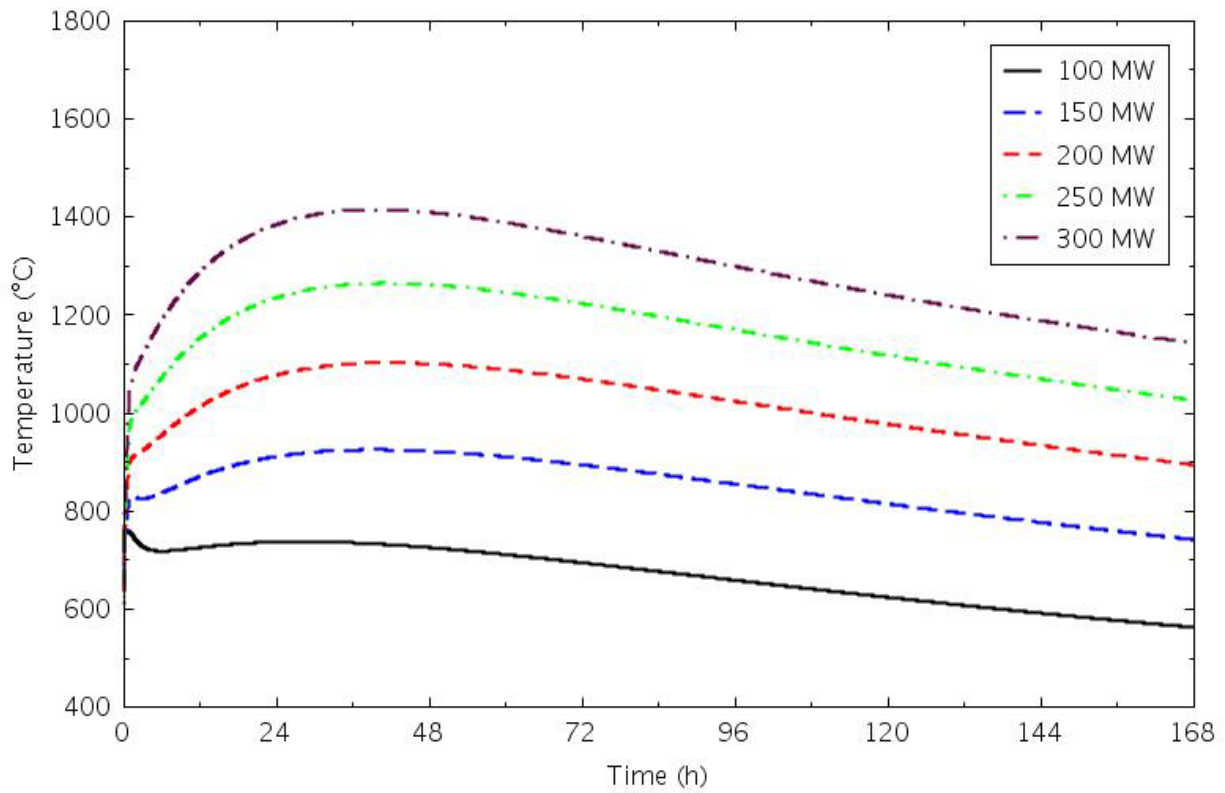
Figure 4-98. Central reflector peak temperatures for the 6-level core PCC transients.
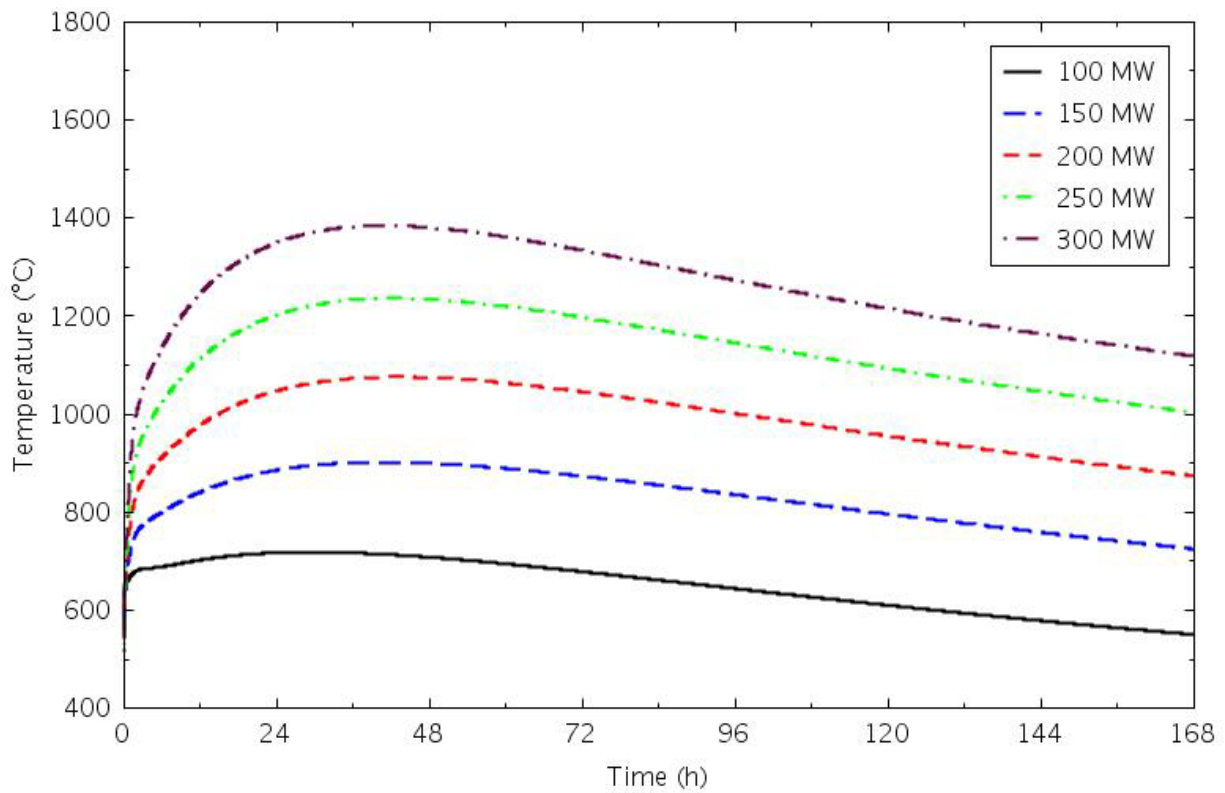


Figure 4-99. Ring 3 reflector peak temperatures for the 6-level core PCC transients.
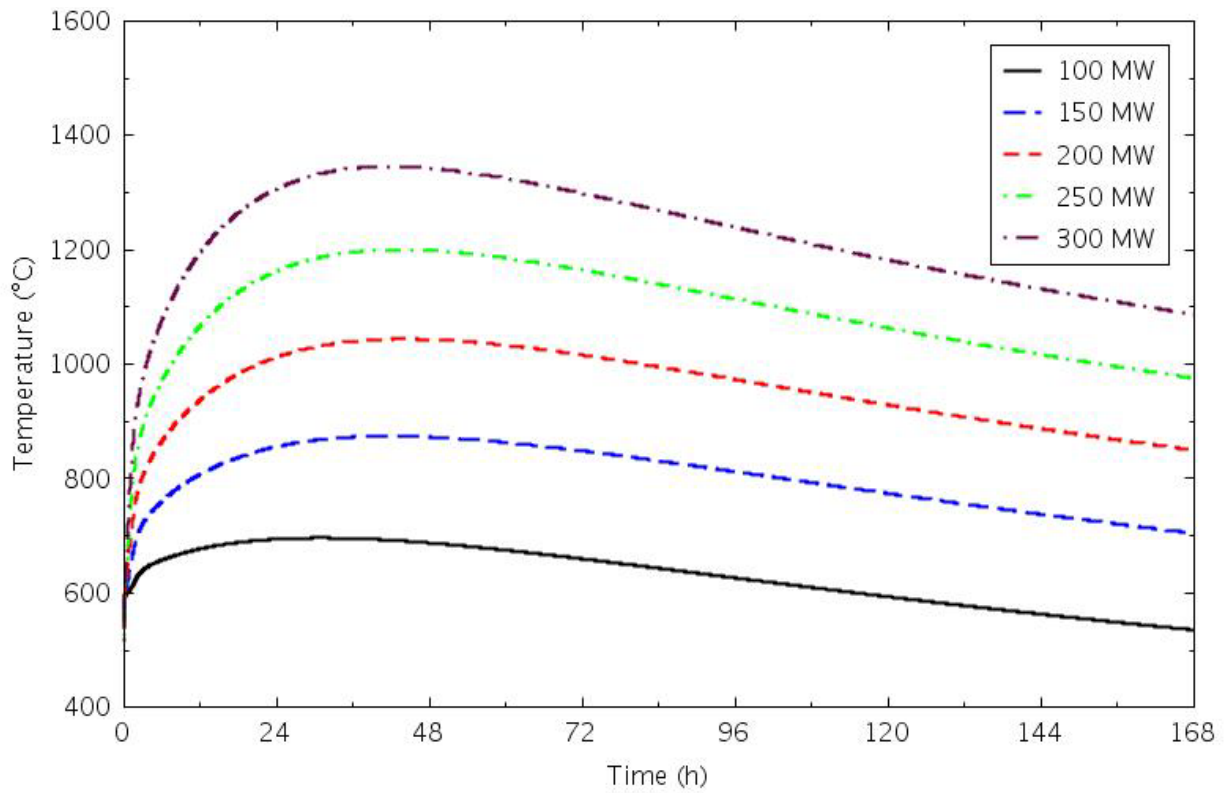
Figure 4-100. Reflector Ring 4 inner half peak temperatures for the 6-level core PCC transients.
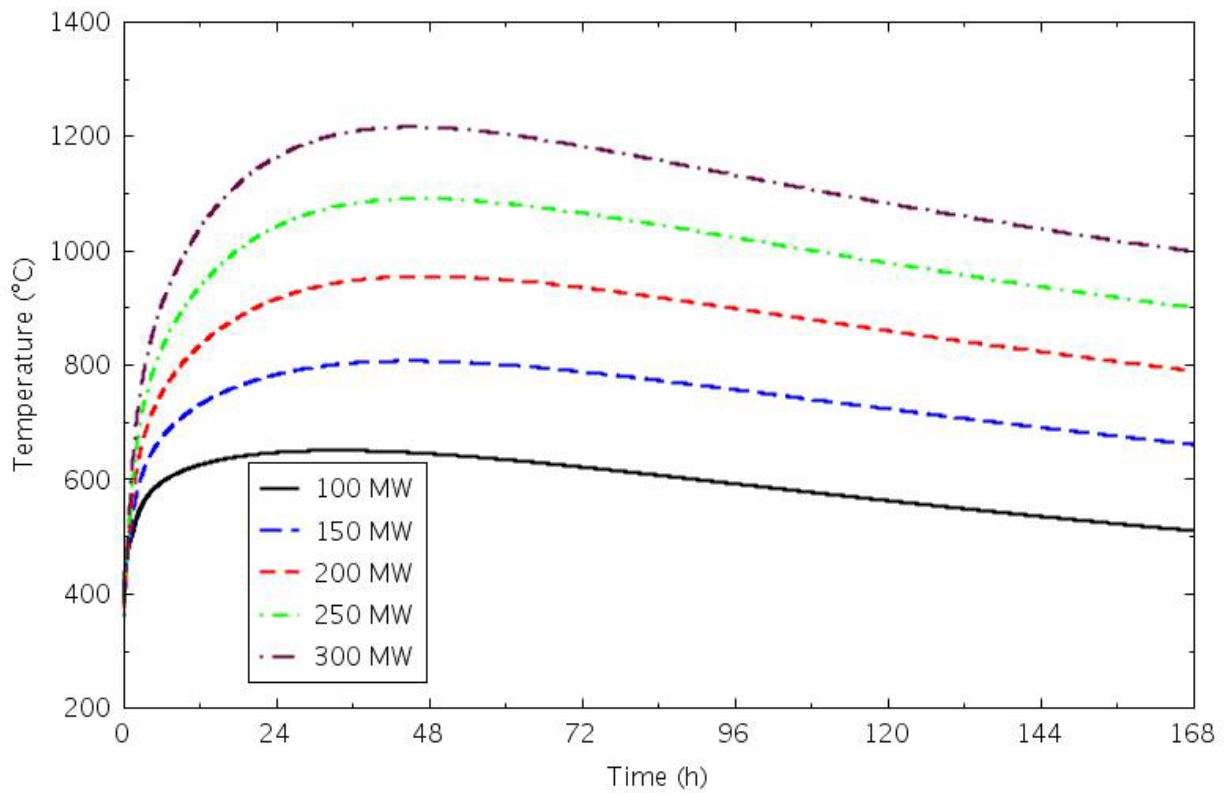


Figure 4-101. Reflector Ring 4 outer half peak temperatures for the 6-level core PCC transients.
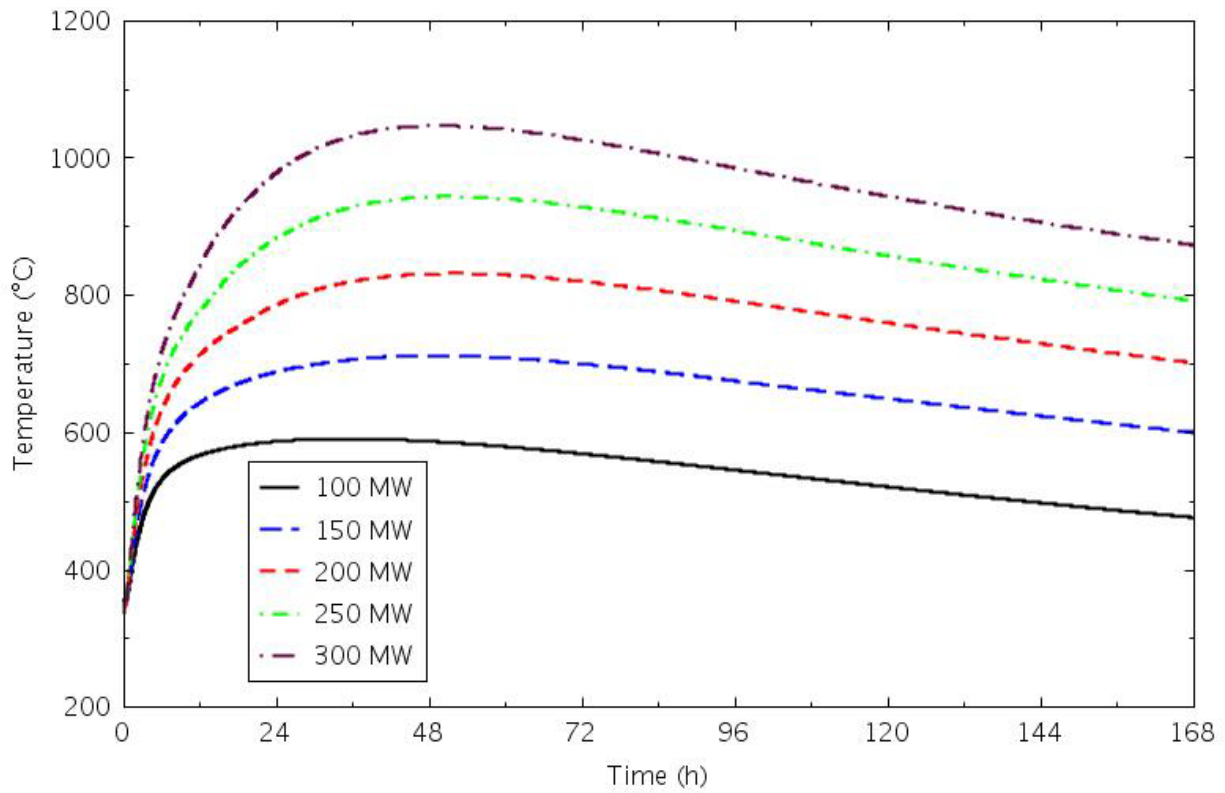
Figure 4-102. Reflector Ring 5 peak temperatures for the 6-level core PCC transients.
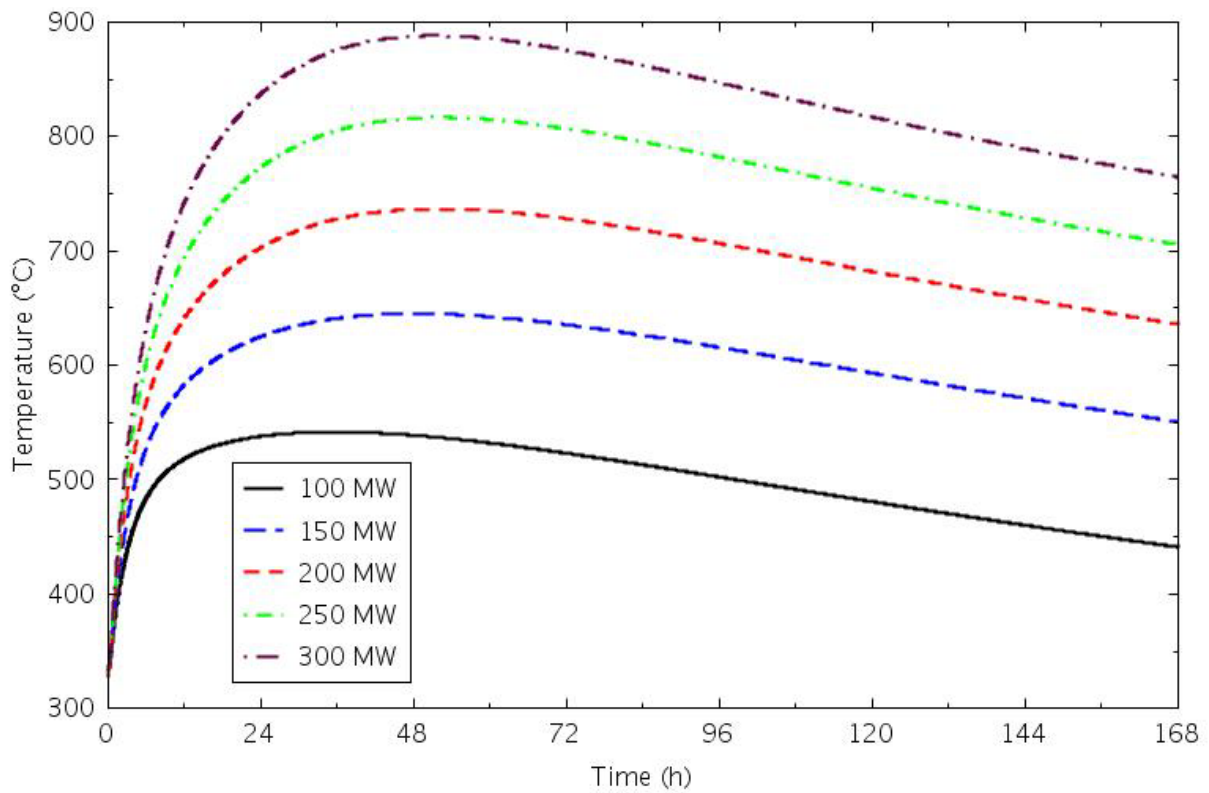


Figure 4-103. PSR peak temperatures for the 6-level core PCC transients.
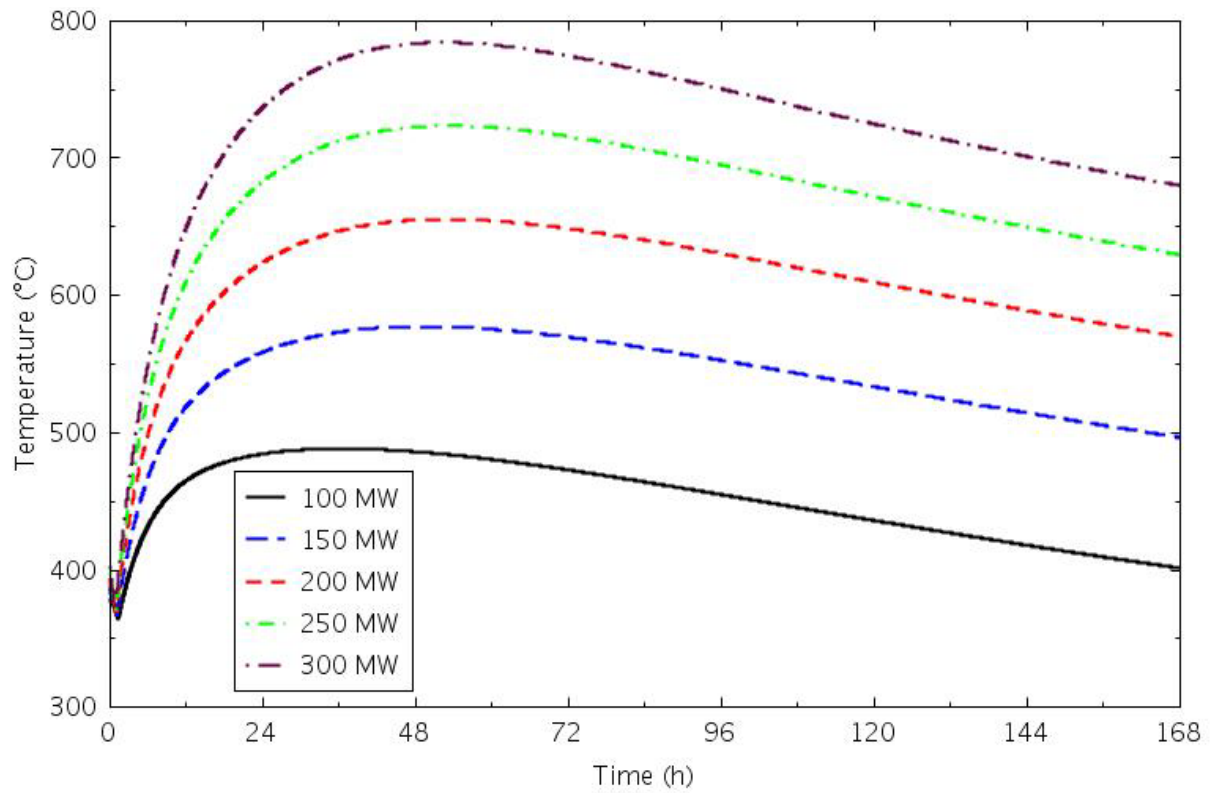
Figure 4-104. Core barrel peak temperatures for the 6-level core PCC transients.
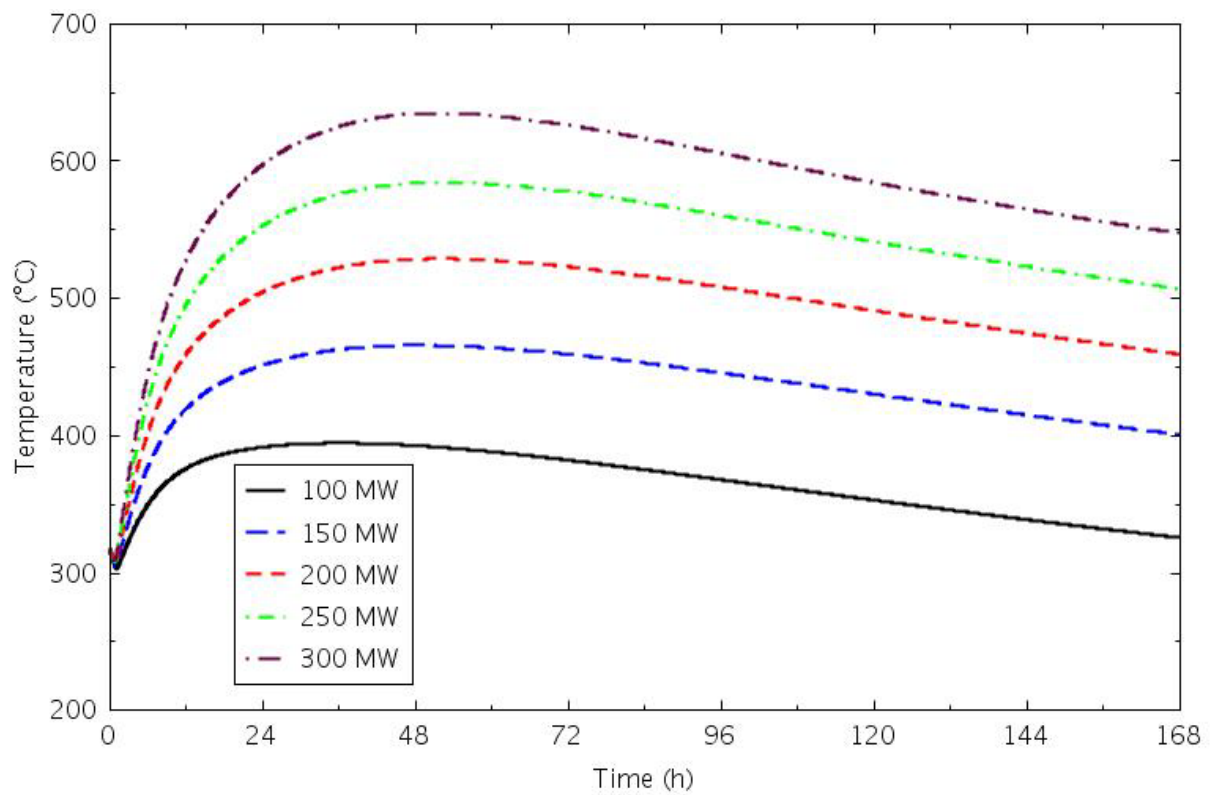


Figure 4-105. Reactor vessel wall peak temperatures for the 6-level core PCC transients.
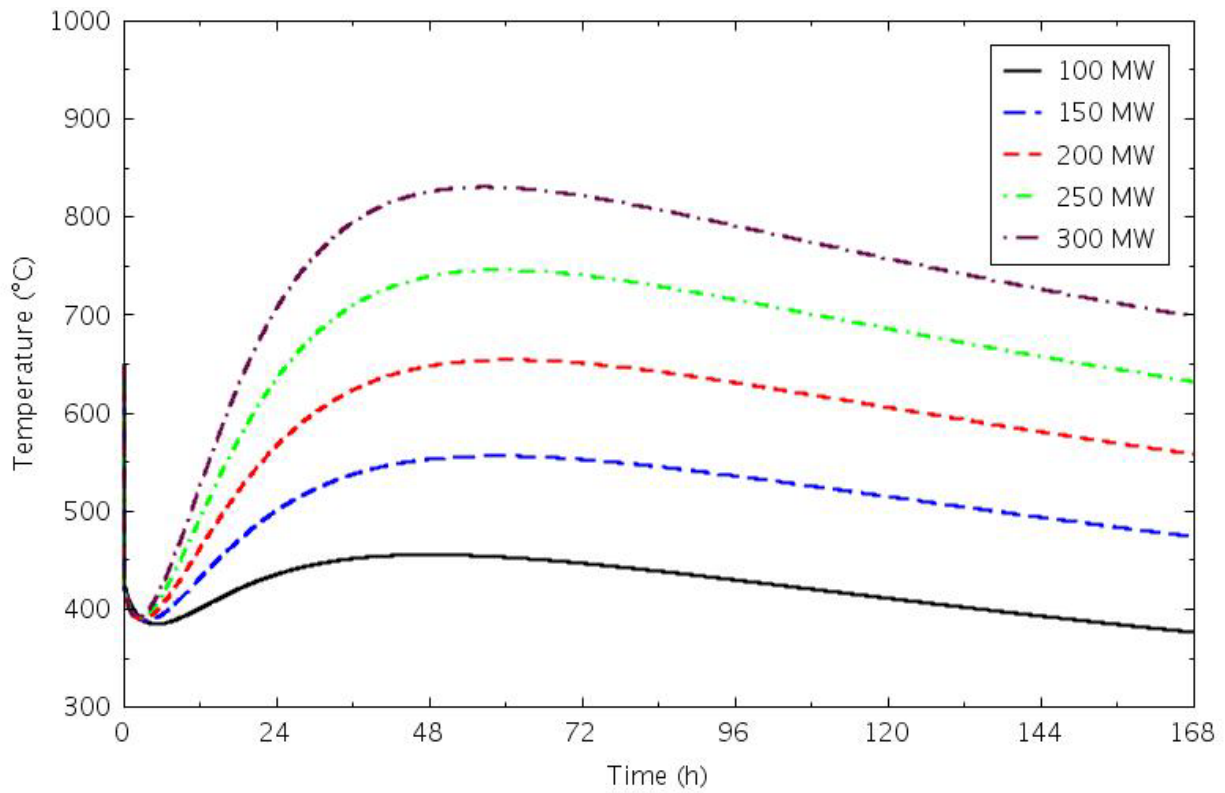
Figure 4-106. Lower plenum coolant temperatures for the 6-level core PCC transients.
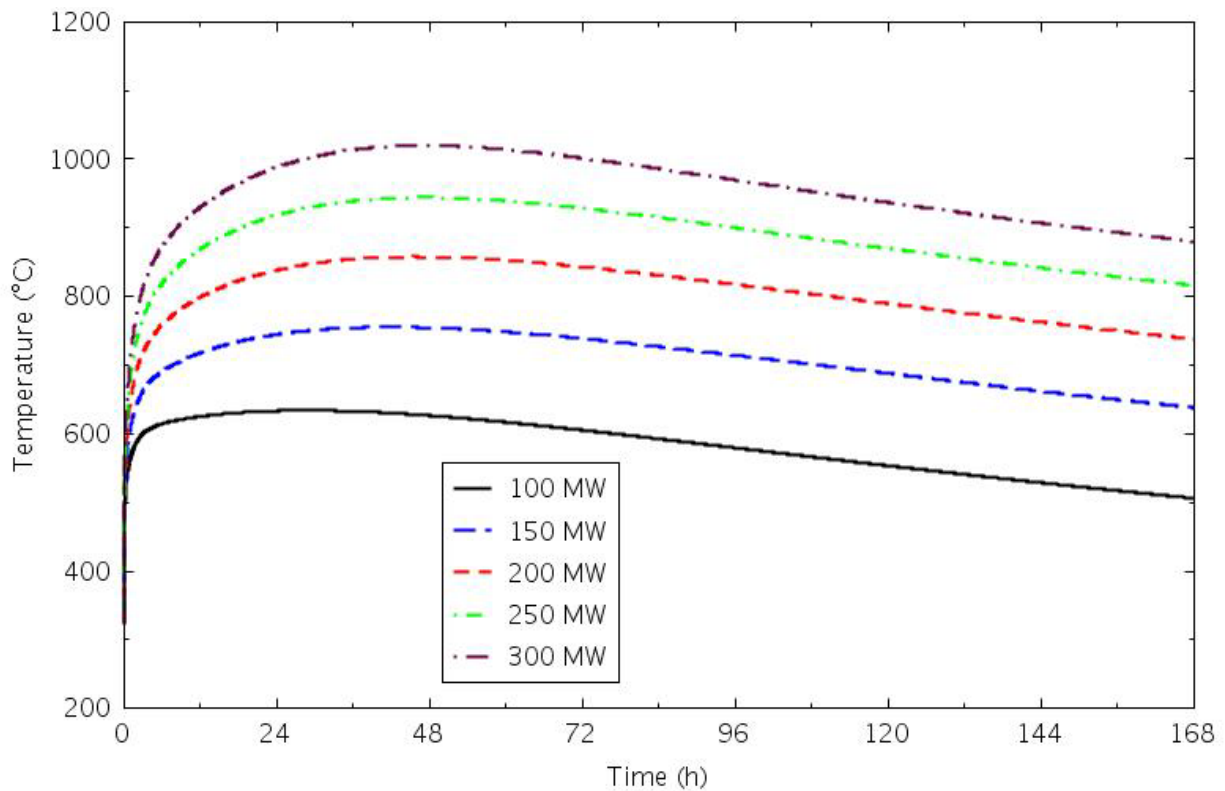


Figure 4-107. Upper plenum coolant temperatures for the 6-level core PCC transients.
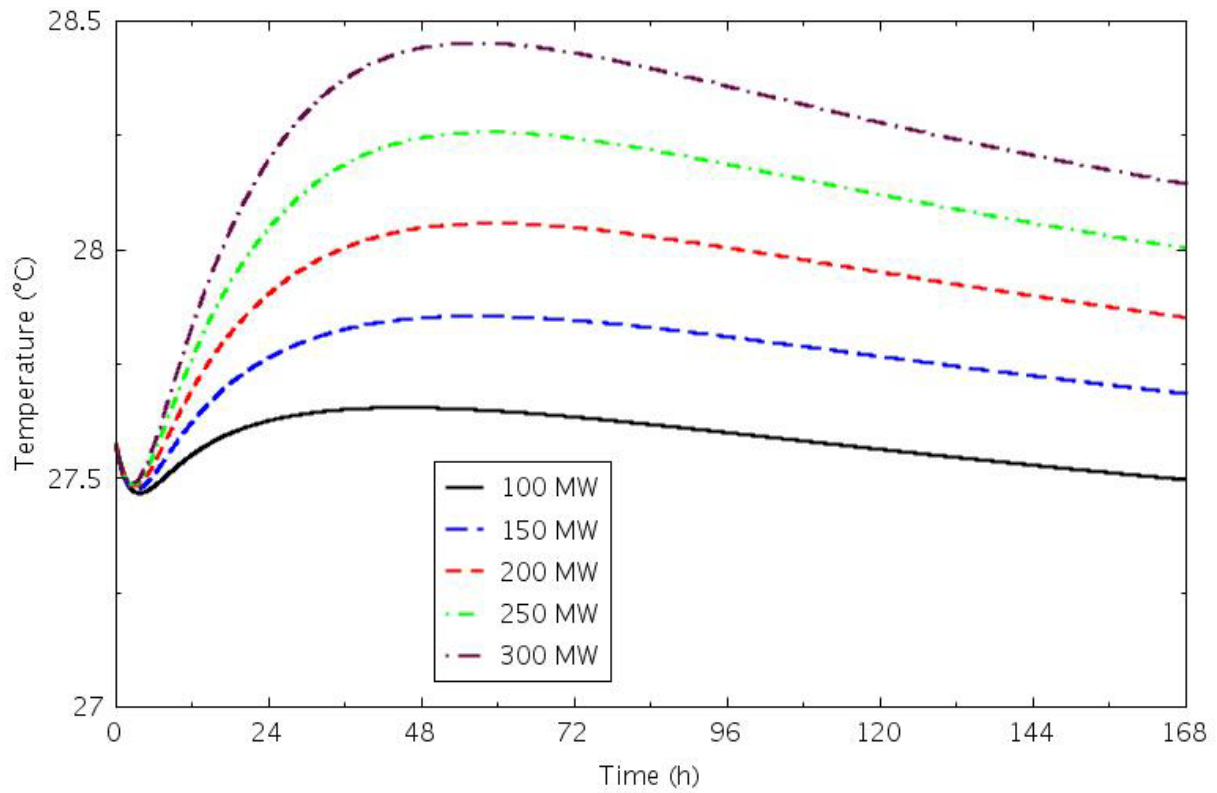
Figure 4-108. RCCS coolant outlet temperatures for the 6-level core PCC transients.
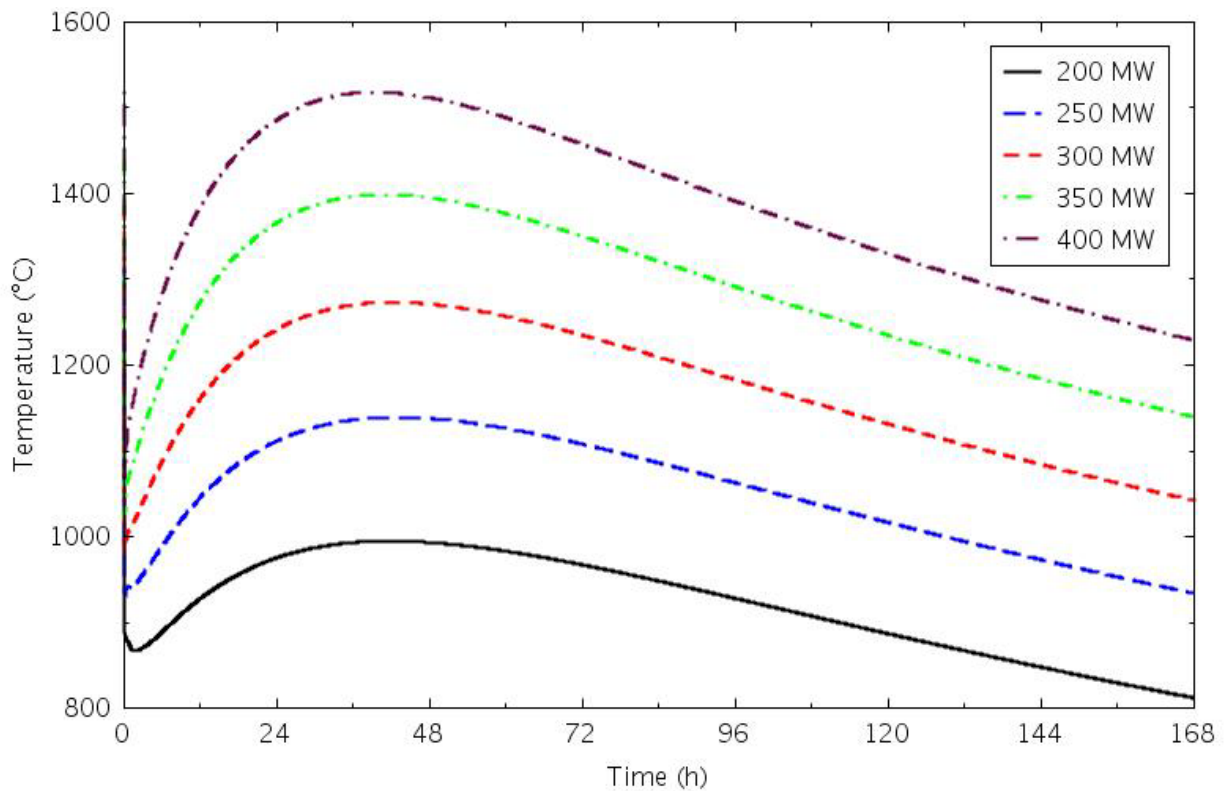


Figure 4-109. Peak fuel temperatures for the 8-level core PCC transients.
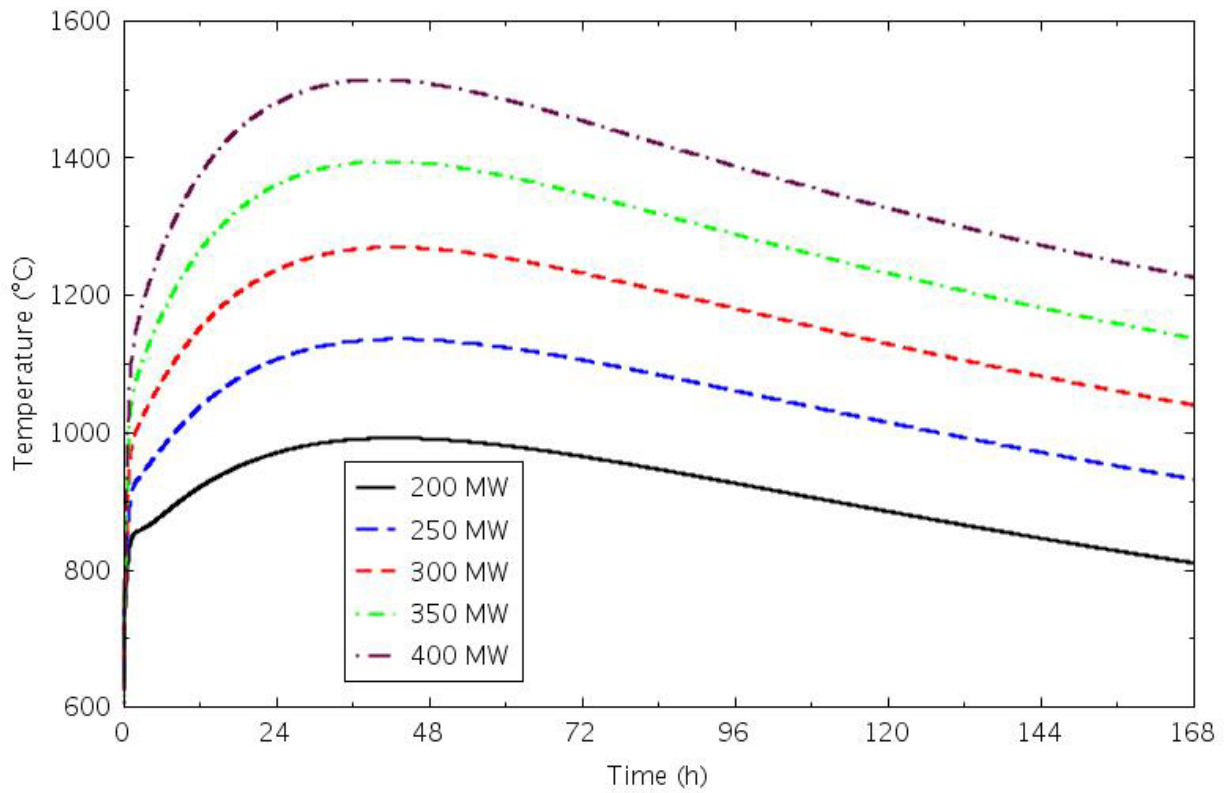
Figure 4-110. Central reflector peak temperatures for the 8-level core PCC transients.
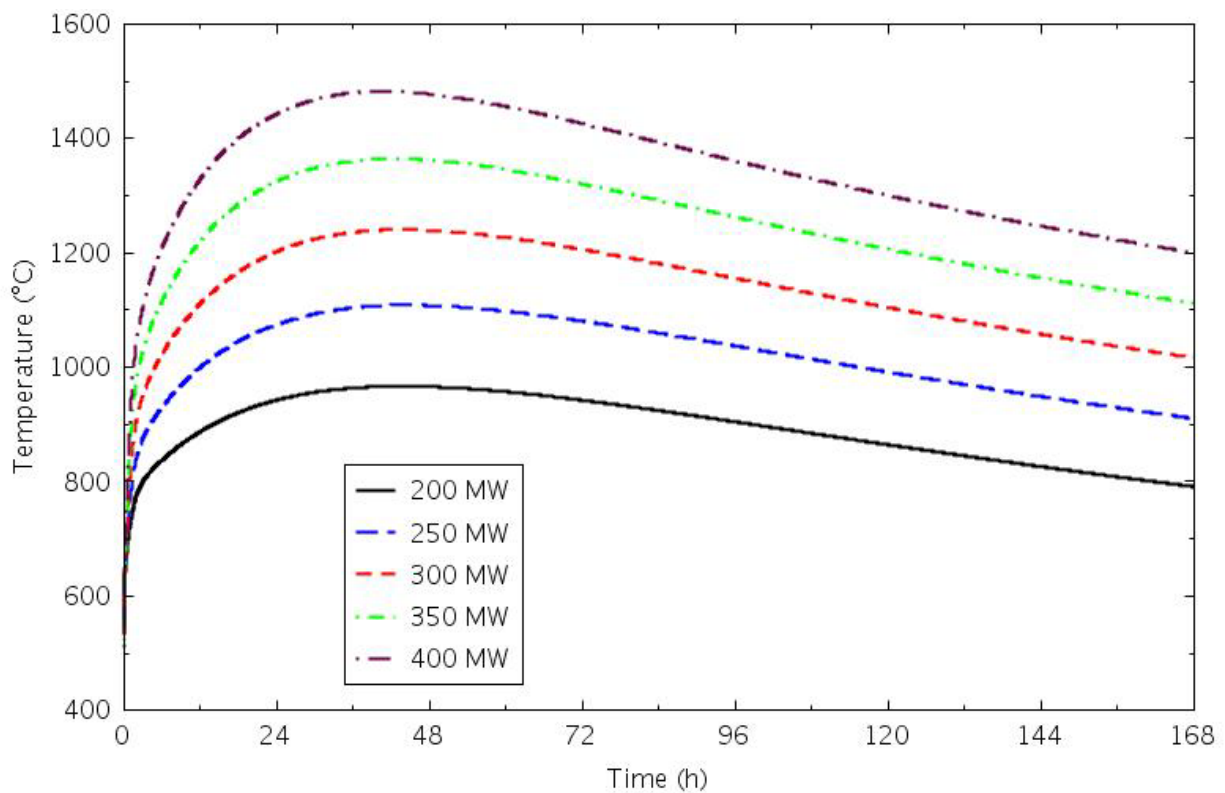


Figure 4-111. Ring 3 reflector peak temperatures for the 8-level core PCC transients.
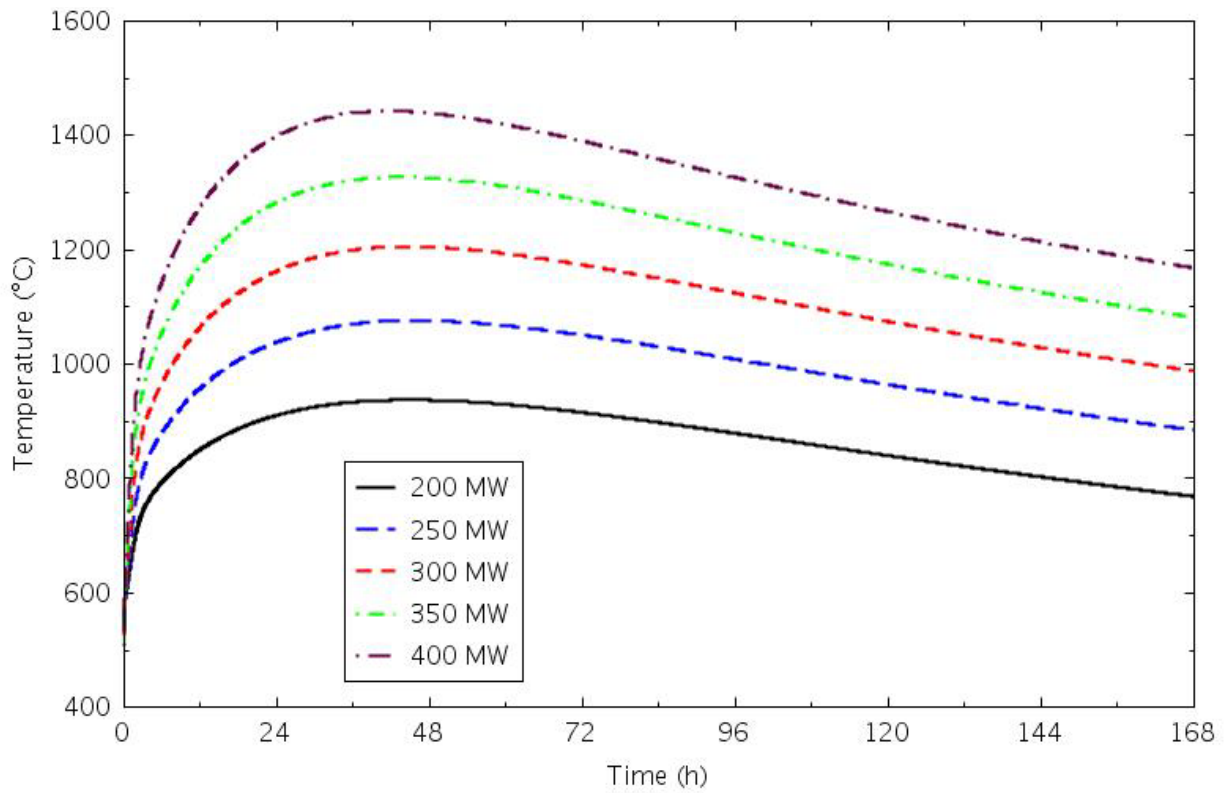
Figure 4-112. Reflector Ring 4 inner half peak temperatures for the 8-level core PCC transients.
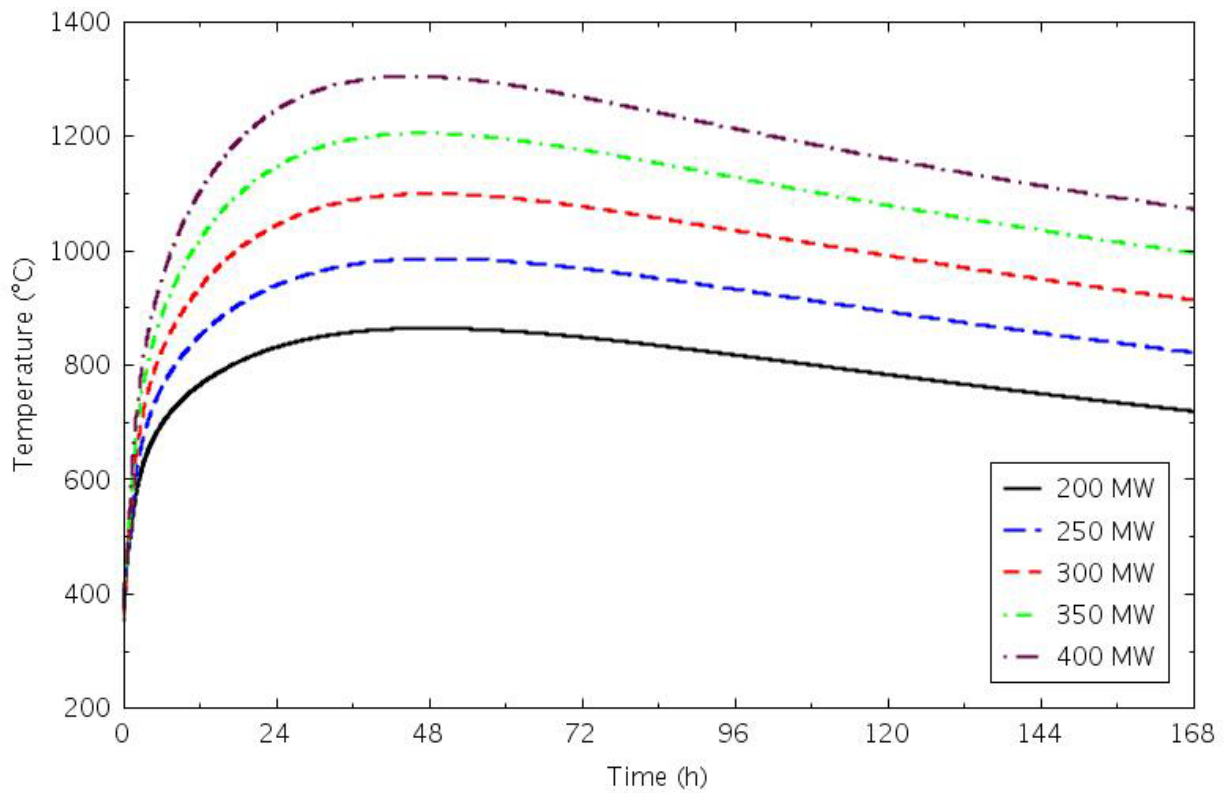


Figure 4-113. Reflector Ring 4 outer half peak temperatures for the 8-level core PCC transients.
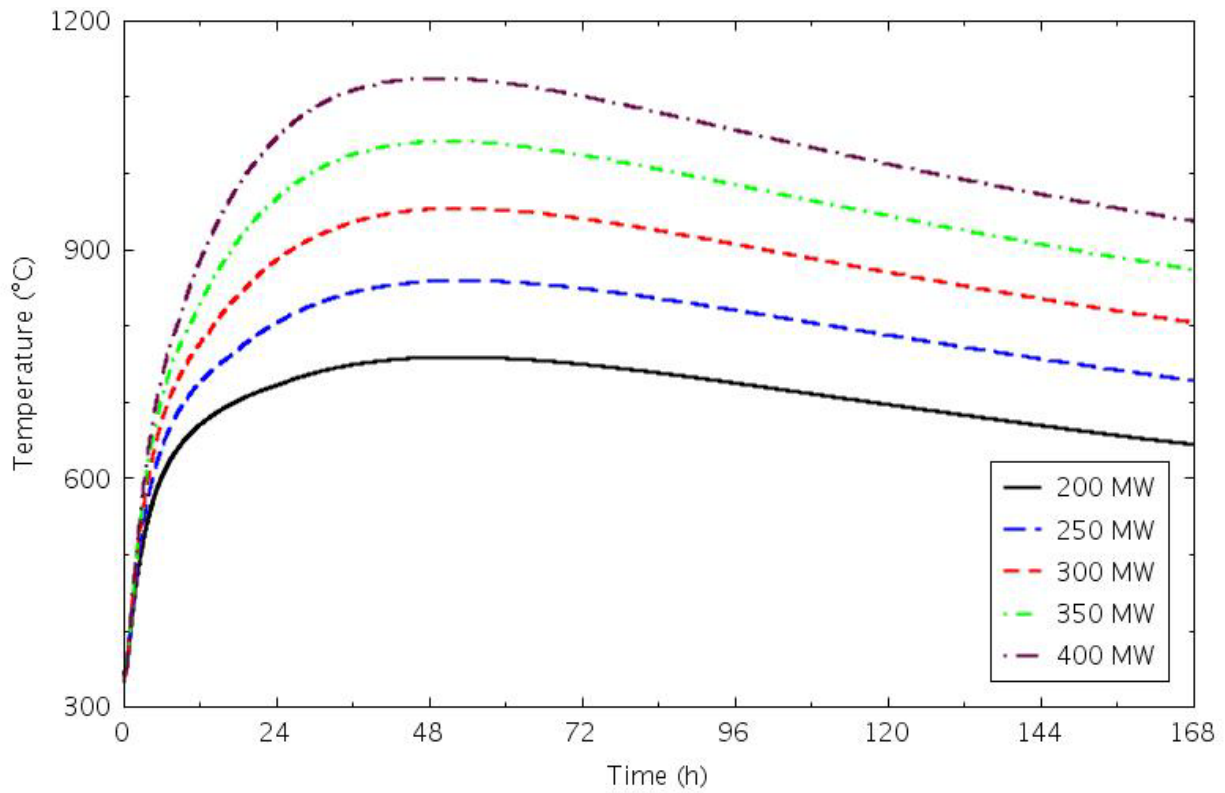
Figure 4-114. Reflector Ring 5 peak temperatures for the 8-level core PCC transients.
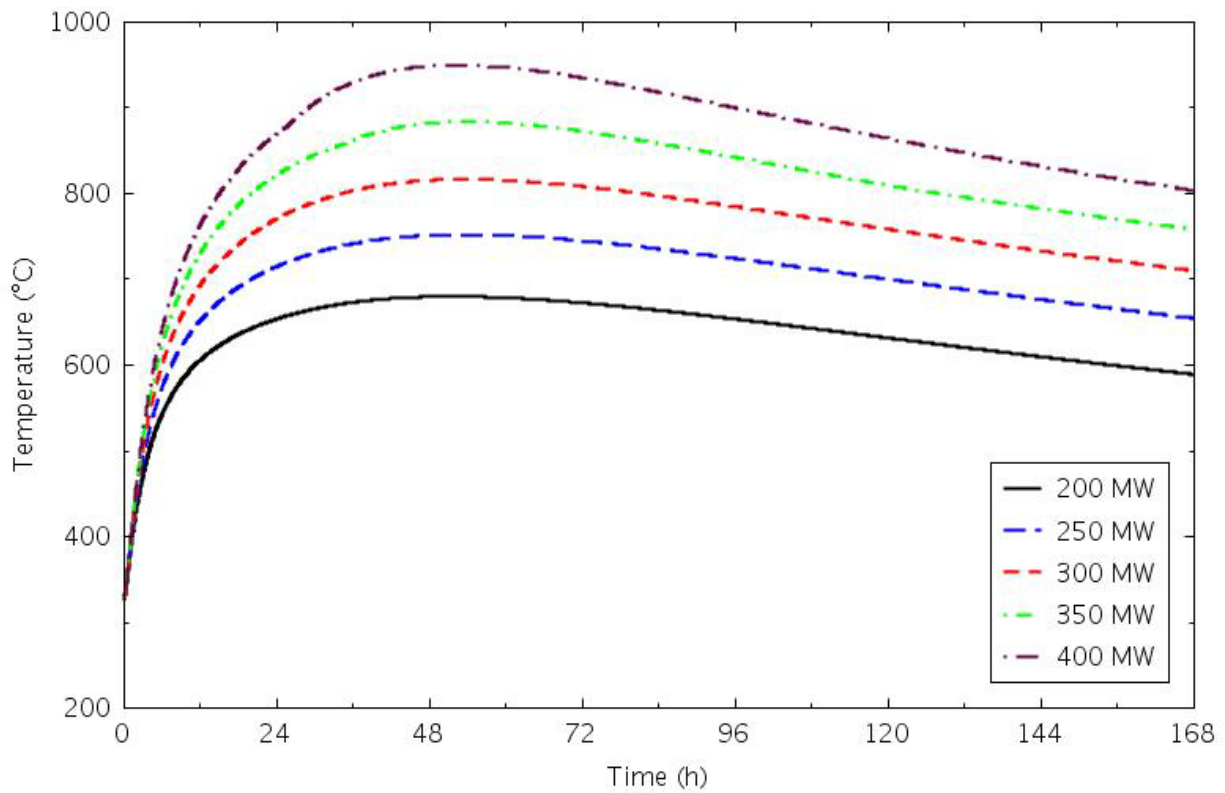


Figure 4-115. PSR peak temperatures for the 8-level core PCC transients.
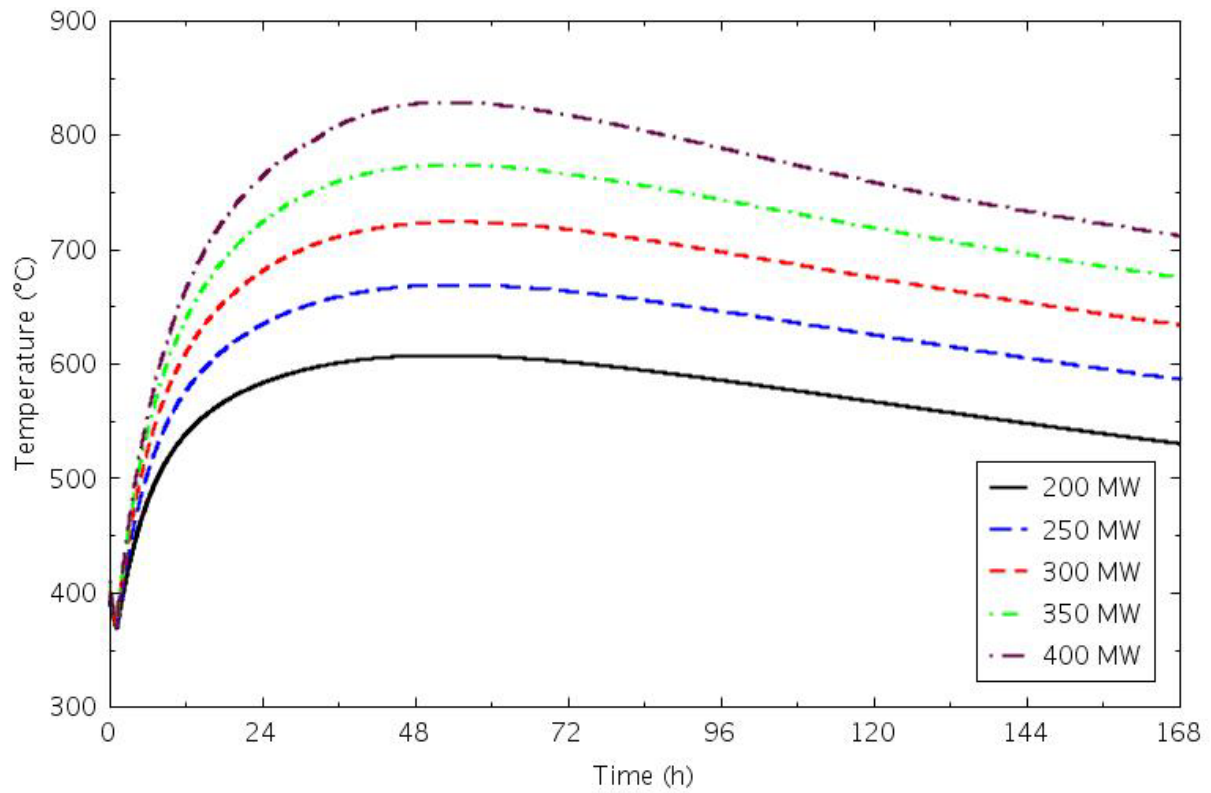
Figure 4-116. Core barrel peak temperatures for the 8-level core PCC transients.
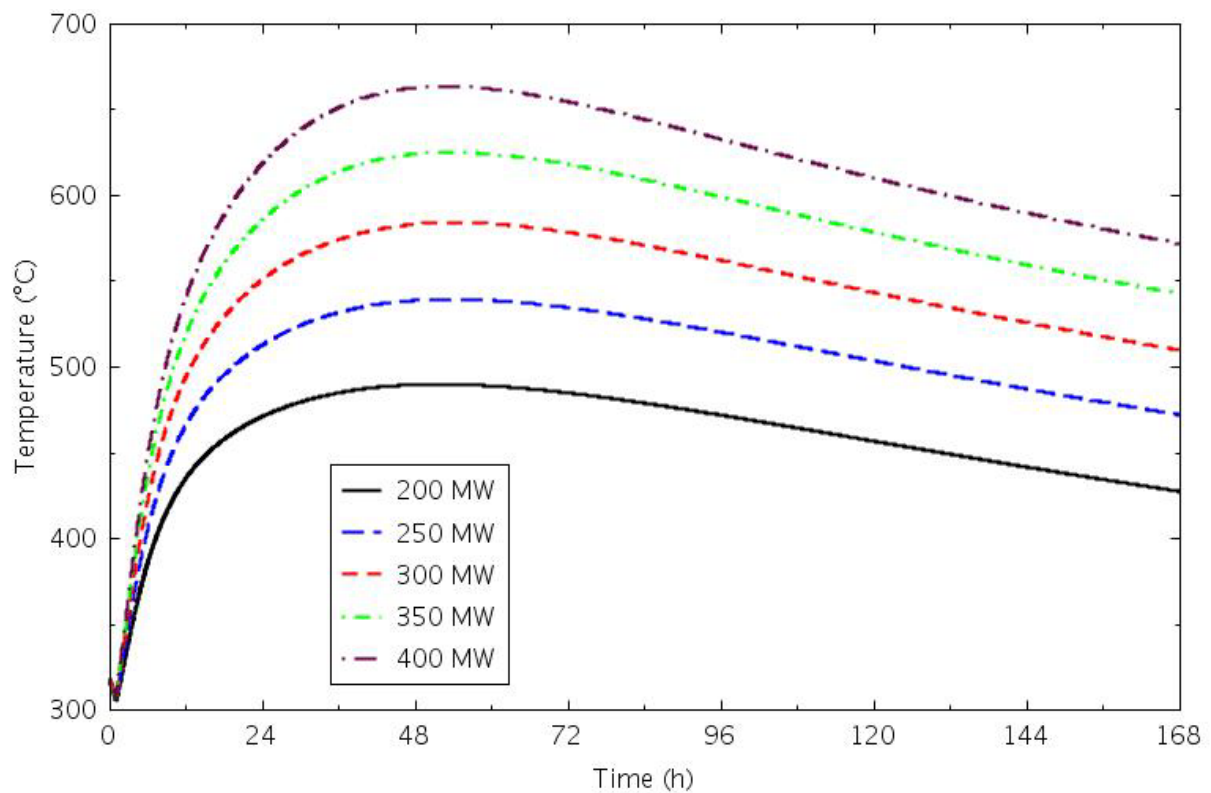


Figure 4-117. Reactor vessel wall peak temperatures for the 8-level core PCC transients.
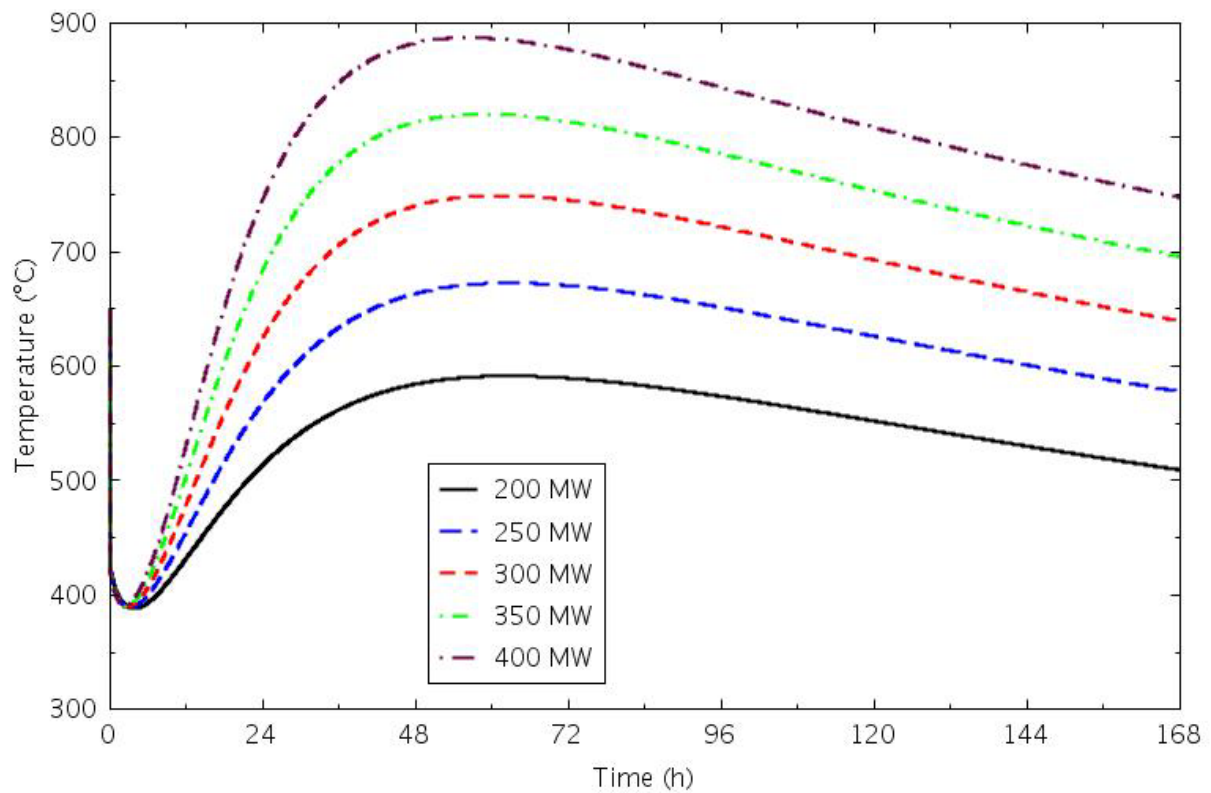
Figure 4-118. Lower plenum coolant temperatures for the 8-level core PCC transients.
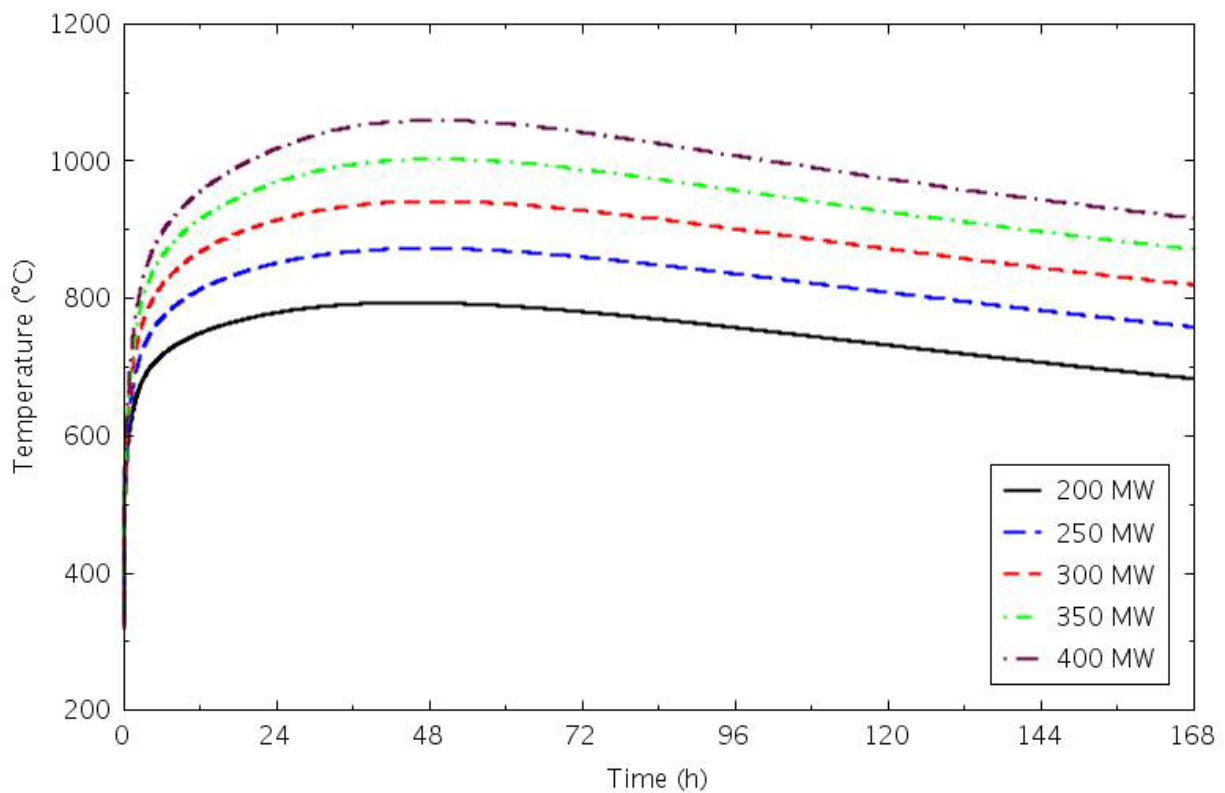


Figure 4-119. Upper plenum coolant temperatures for the 8-level core PCC transients.
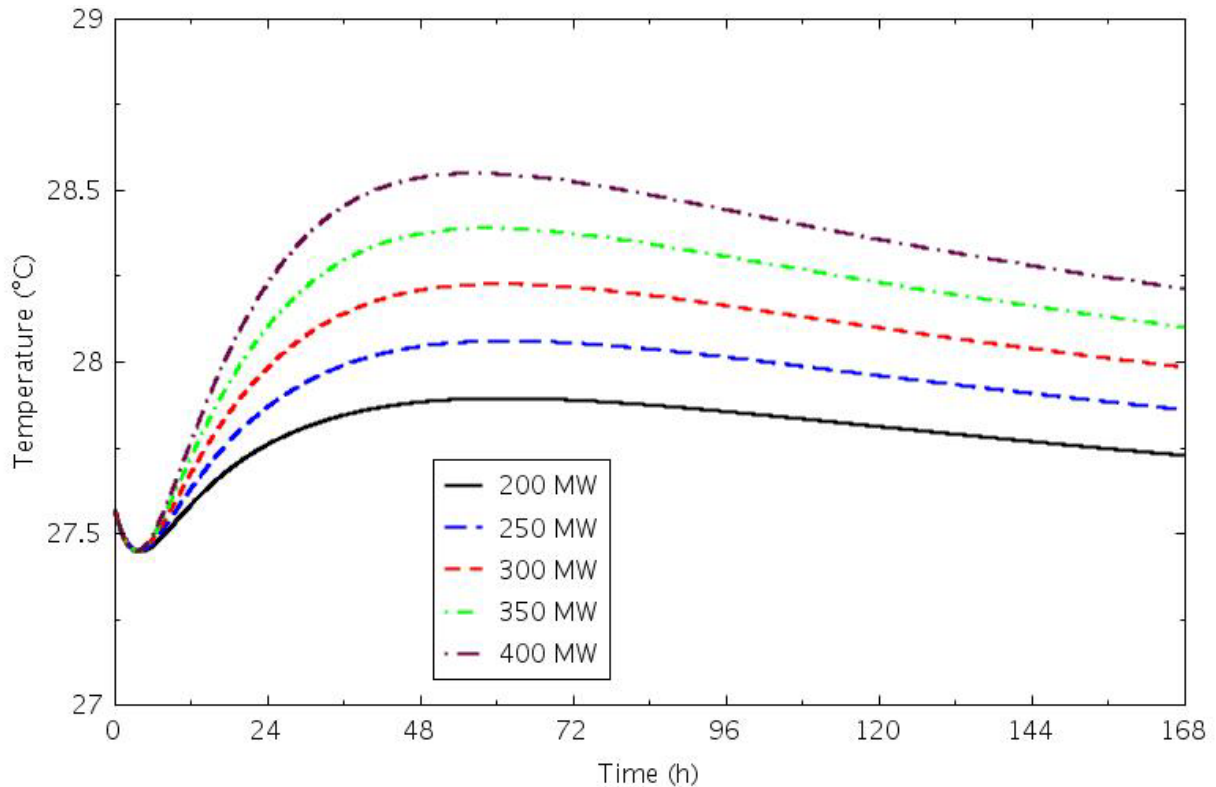
Figure 4-120. RCCS coolant outlet temperatures for the 8-level core PCC transients.

### *4.2.3.2 Sensitivity Calculations*

Sensitivity calculations addressed the core axial power shape and the steady-state coolant temperatures. All of the calculations used the 8-level core model and assumed 4-mm gaps between the blocks.

The effect of a chopped cosine axial power profile on the peak fuel temperatures is shown in Figure 4-121. The cosine shape had a slightly higher peak temperature during the transient. There was essentially no change in temperature in reflector Ring 5 (Figure 4-122) or in the PSR (Figure 4-123).

The coolant temperature sensitivity calculations were PCC transients initiated from the higher temperature steady-state calculations, which had coolant inlet and outlet temperatures of 350 and 750°C. The impact on the peak fuel temperature is shown in Figure 4-124, where the peak temperature during the transient increased by about 20°C for the 200-MW case but was still more than 350°C below the steady-state temperatures. Similar increases in peak temperature were observed in the PSR (Figure 4-125) and the reactor vessel wall (Figure 4-126).

## 4.2.4 Summary

Both DCC and PCC transients were run for the three nominal core configurations at a range of powers. Seven sensitivity studies were performed for the DCC transients and two were performed for the PCC transients. Temperatures were higher for the DCC transients than for the PCC transients.

Peak fuel temperatures during the DCC transients for the three nominal core cases were 150-250°C below the steady-state temperatures. Transient peak temperatures exceeded the steady-state values only for the 8-level core with powers of at least 350 MW. With no cooling flow on the inside of the center irradiation tube, the central reflector temperature was very close to the fuel temperature. Reflector temperatures decreased steadily in moving radially from the fuel blocks out toward the core barrel, but

91
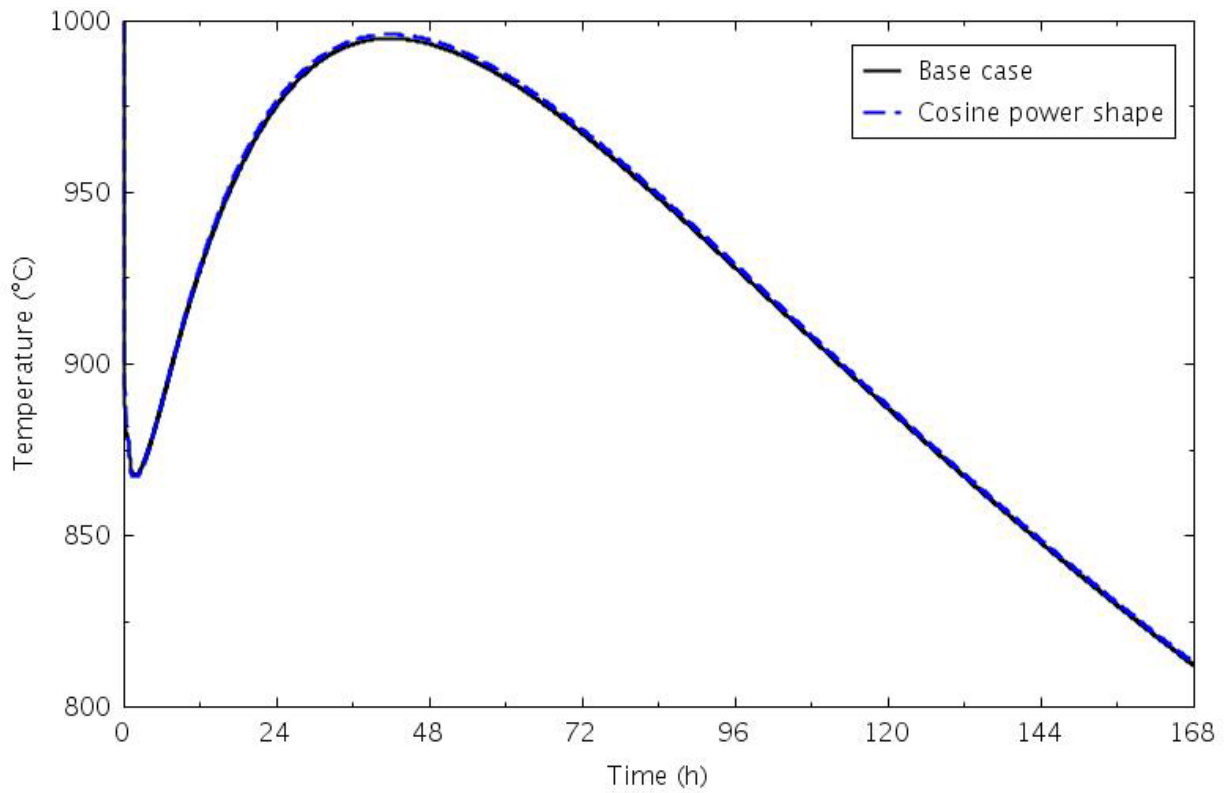
Figure 4-121. Peak fuel temperatures for the cosine power shape and base-case PCC transients.
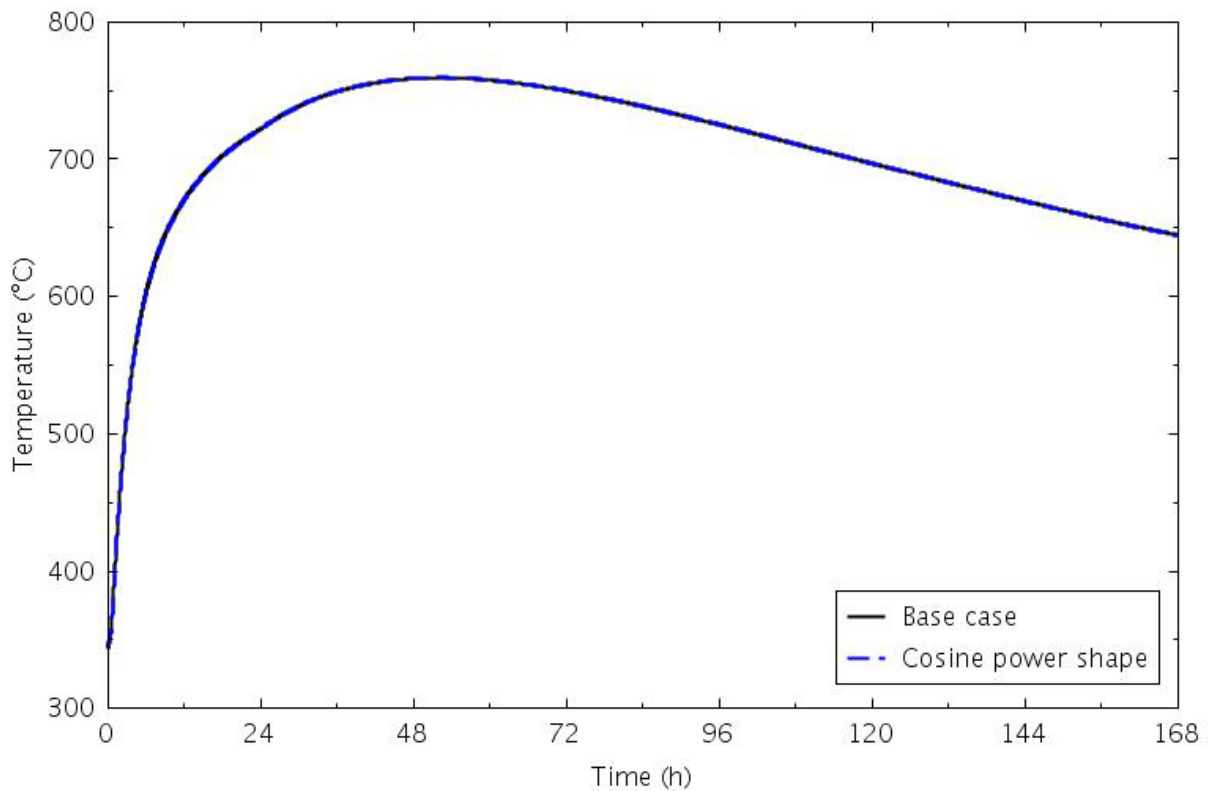


Figure 4-122. Reflector Ring 5 peak temperatures for the cosine power shape and base-case PCC transients.
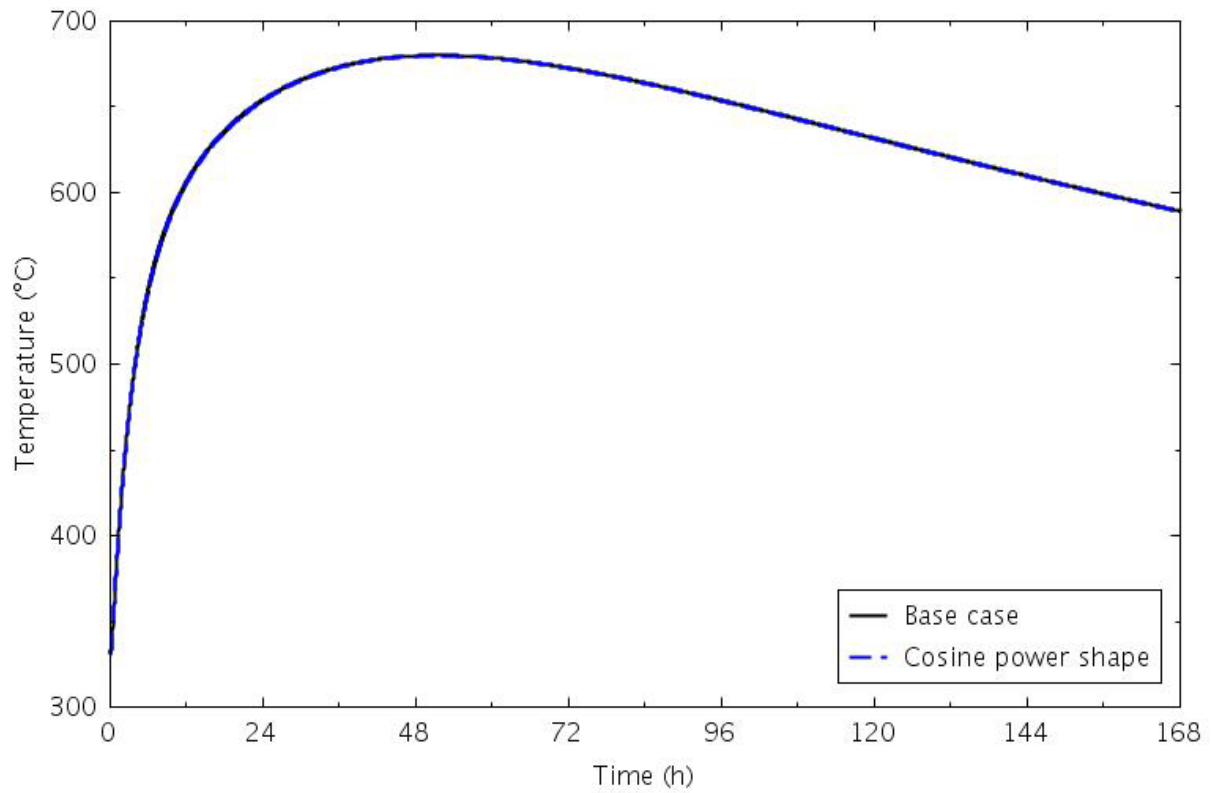
Figure 4-123. PSR peak temperatures for the cosine power shape and base-case PCC transients.
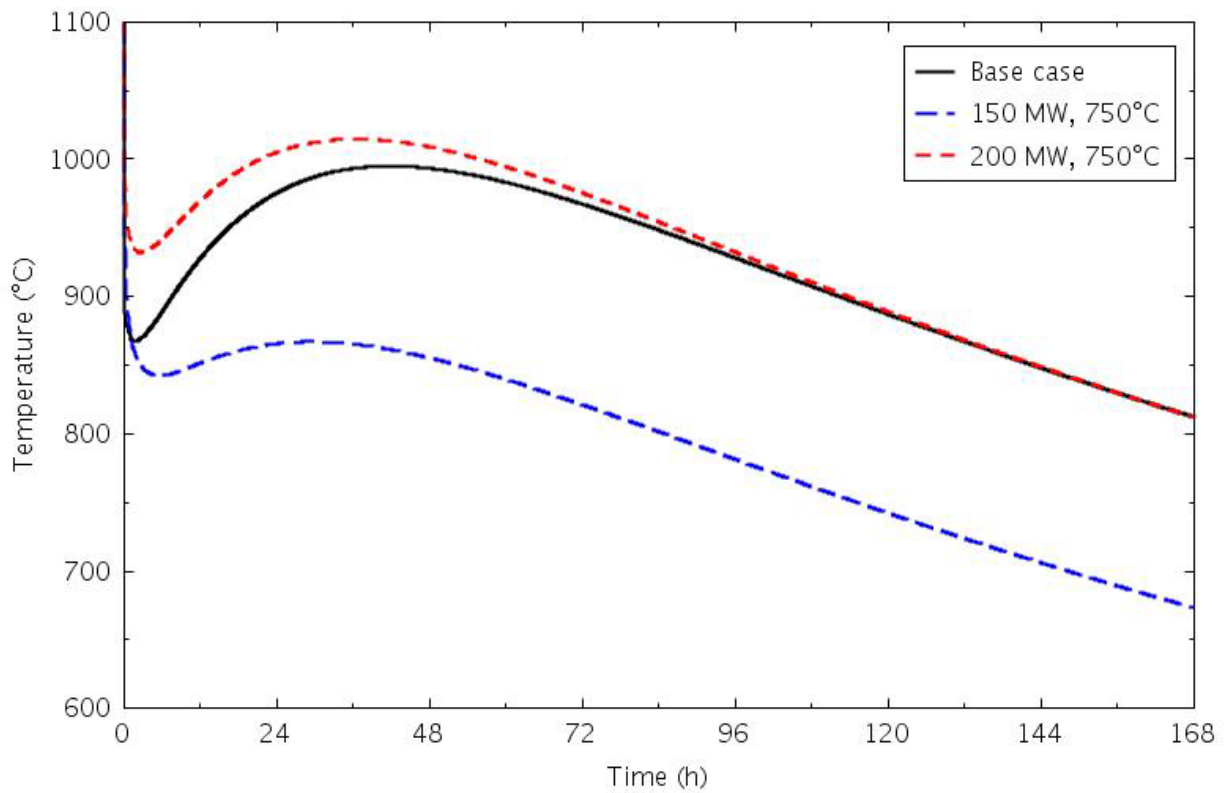


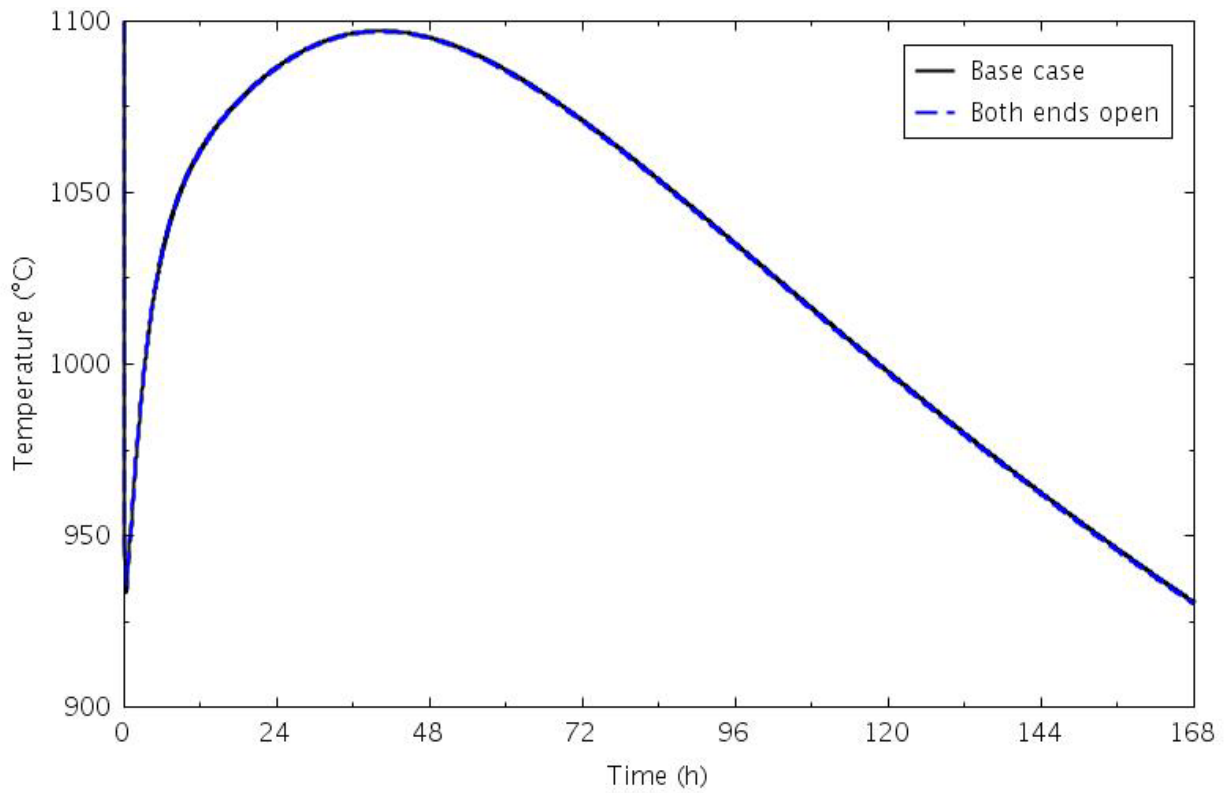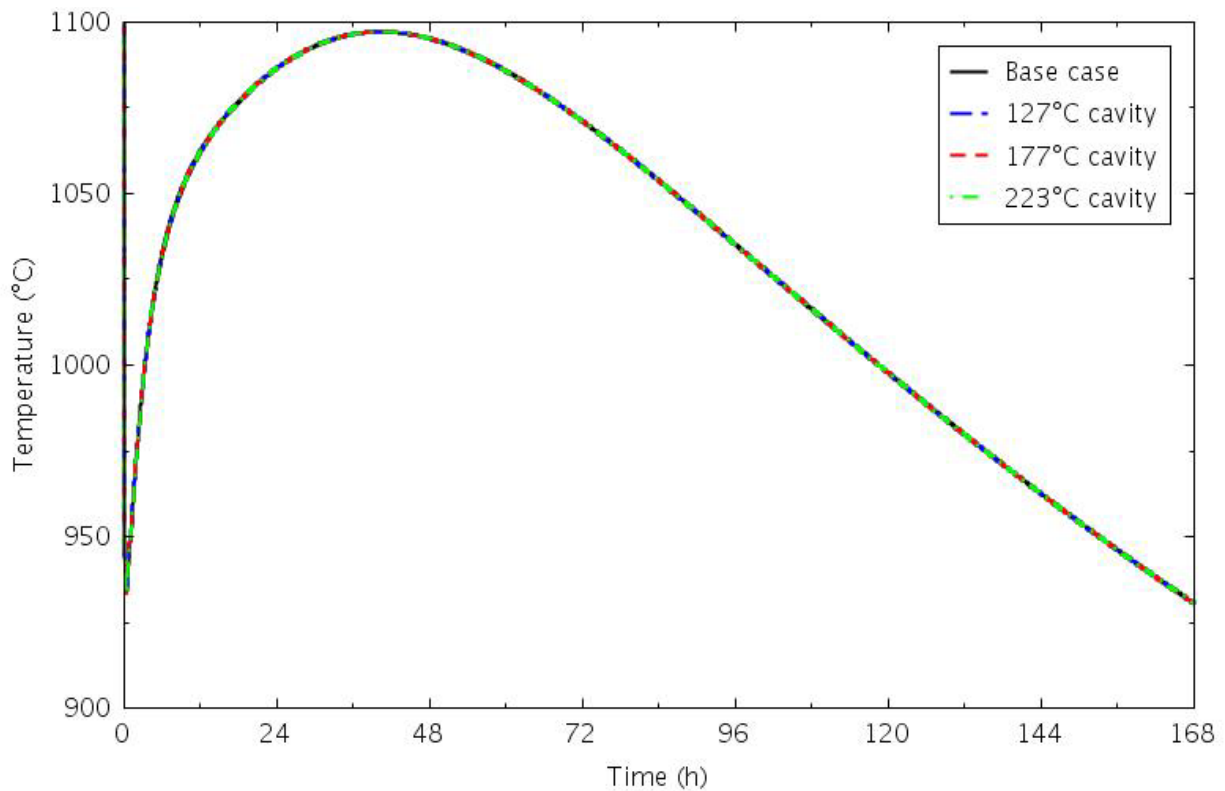Figure 4-124. Peak fuel temperatures for the coolant temperature and base-case PCC transients.
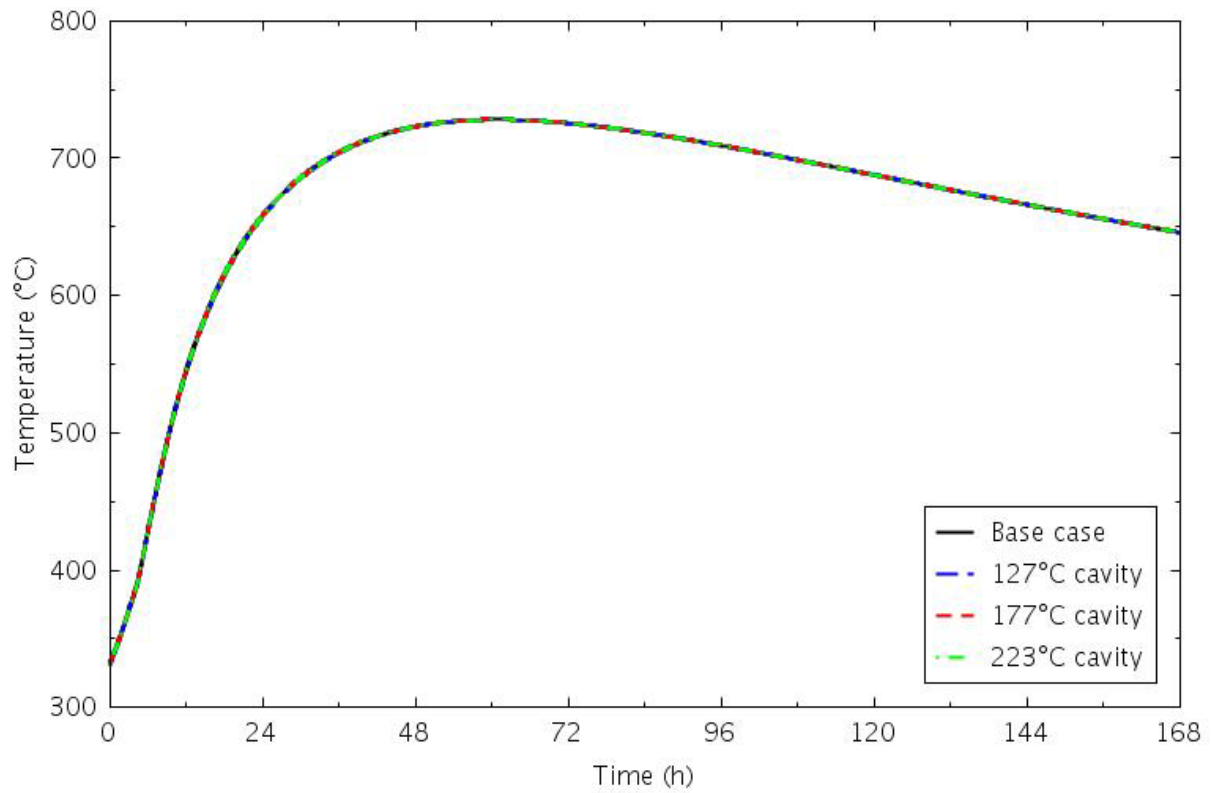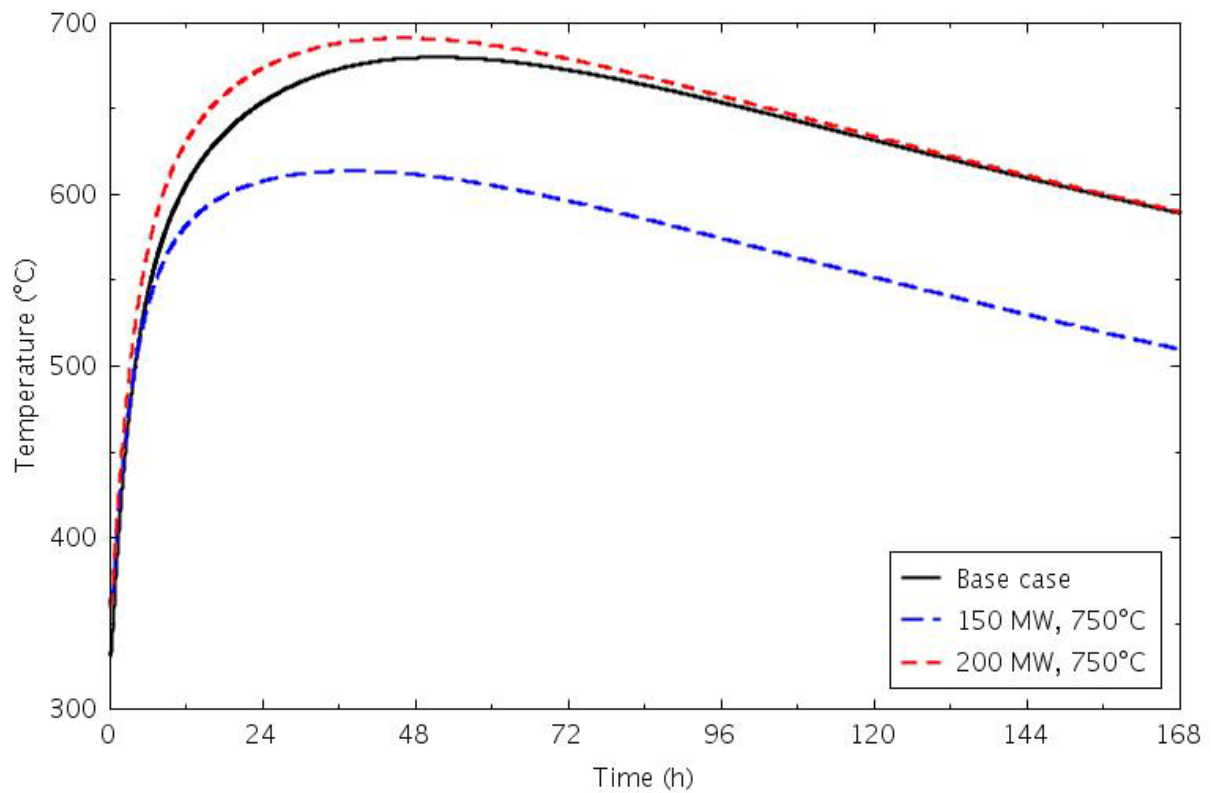
Figure 4-125. PSR peak temperatures for the coolant temperature and base-case PCC transients.
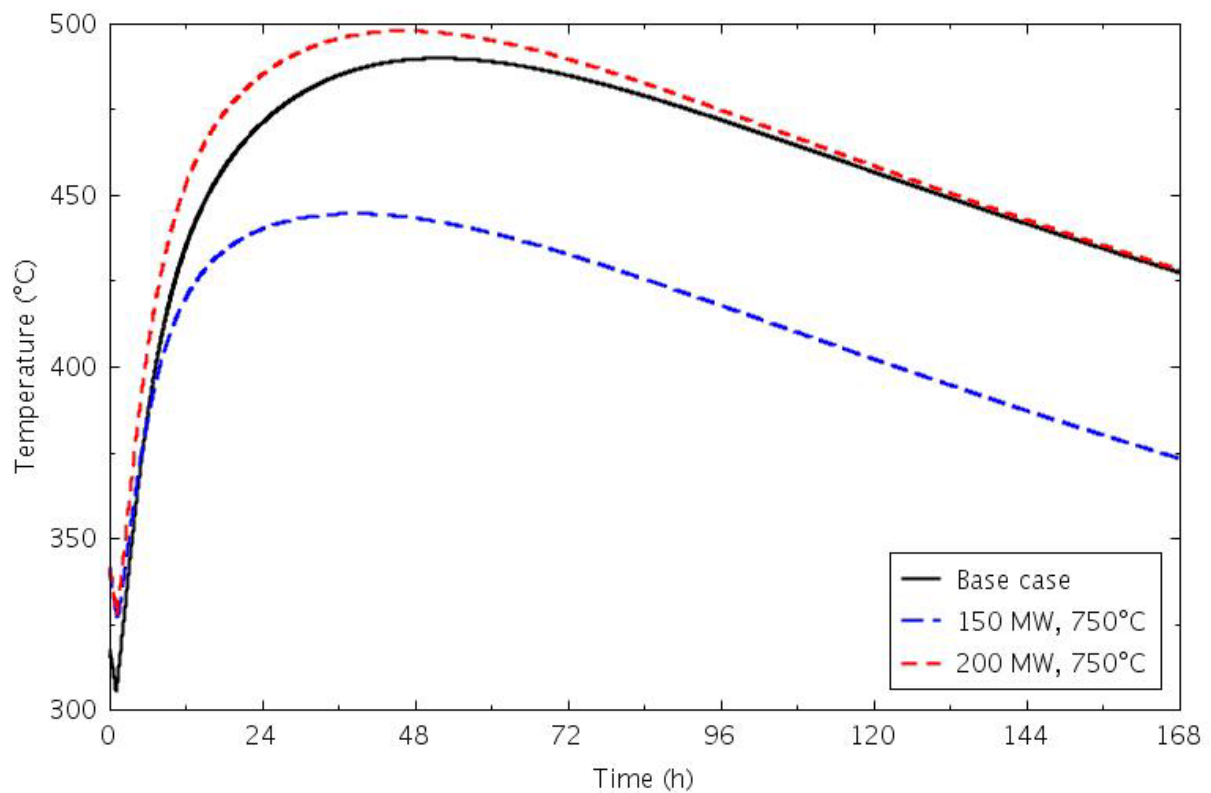


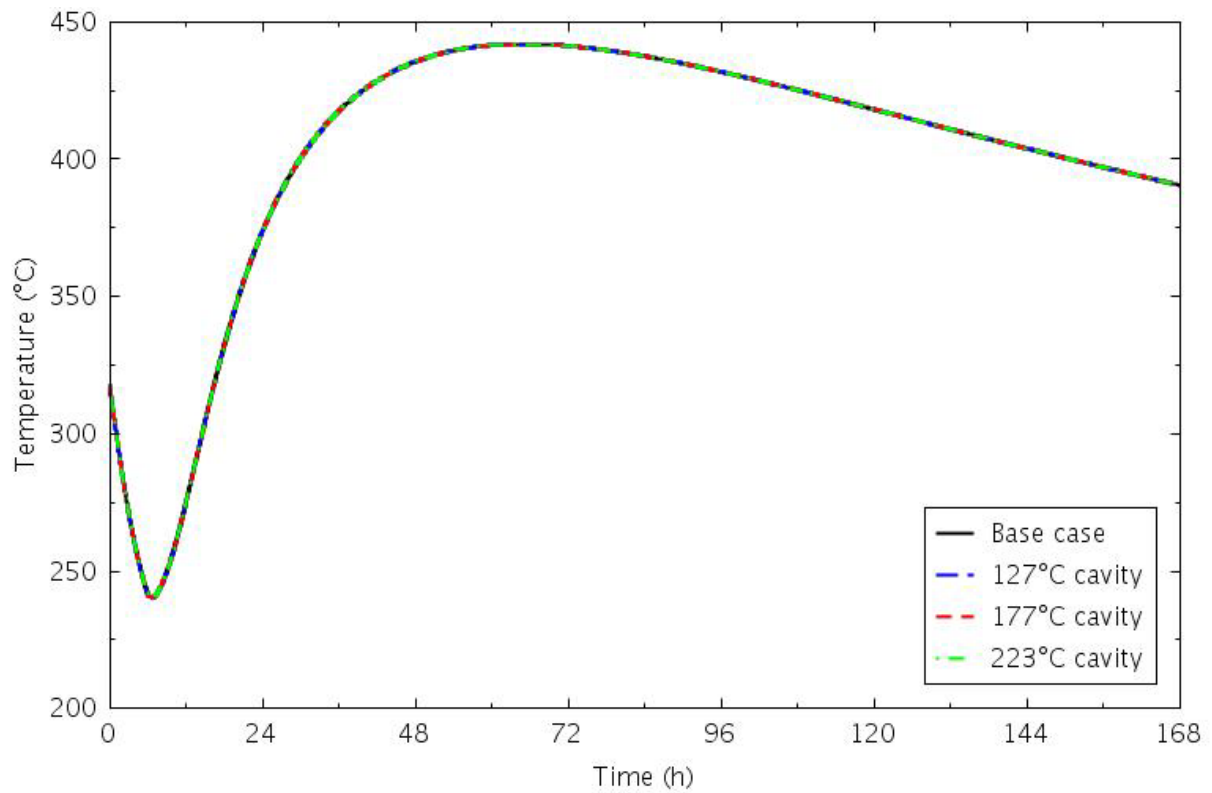Figure 4-126. Reactor vessel wall temperature for the coolant temperature and base-case PCC transients.

were high enough that the structural integrity of any pressure-containing irradiation tubes might be questionable. The RCCS was effective in maintaining a nearly constant temperature boundary condition for radiation from the reactor vessel.

The transient behavior was insensitive to many of the parameters varied in the sensitivity studies: changing the axial power shape from flat to a chopped cosine, modeling a double-ended break instead of a single-ended break, changing the temperature of the helium re-entering the lower plenum from the break, blocking some of the core bypass paths, and delaying reactor scram by 1 or 10 s. Starting the transients with coolant inlet and outlet temperatures of 350 and 750°C instead of the nominal 325 and 650°C caused peak temperatures in the fuel, reflectors, and metal structures to increase by about 20°C. The largest impact was providing some cooling flow to the inside of the center irradiation tube, which reduced the temperature of the central reflector and fuel while not affecting the outer reflector temperatures.

The PCC transients exhibited the same behavior as the DCC transients, but with lower peak temperatures. Changing to a cosine axial power shape had no material effect on the structure and coolant temperatures. Starting with higher steady-state coolant temperatures resulted again in about a 20°C increase in the peak temperatures for the vessel structures.

The primary concern identified was the temperature of the irradiation tubes. With no inside cooling flow, the tube temperatures would be close to those of the reflector blocks around them. This would not be a problem for flow-through tubes cooled by the primary coolant, as they can be made of higher-melting temperature materials such as titanium or molybdenum. However, tubes that must contain an internal pressure will likely have to be made of steel to meet American Society of Mechanical Engineers code. The temperatures reached during the transients will probably exceed the maximum values allowed by the code, meaning that either a method to maintain sufficient cooling during these accidents is needed or the tubes may need to be replaced should such an event occur.

# 5. Technology Readiness of Test Reactor Concept

The timeline (and cost) for design and deployment of a test reactor is strongly dependent on the technical maturity of the reactor technology. Of all of the non-LWR concepts proposed in recent decades for power and other applications, the HTGR is among the most technically mature. Indeed HTGRs supplied power to the electric grid in the U.S. (FSV) and in Germany (Thorium Hochtemperatur Reaktor) in the 1980s. More modern engineering-scale HTGRs employing passive decay heat removal are operating in Japan (High-Temperature Engineering Test Reactor) and China (HTR-10).

As with General Electric's Power Reactor Innovative Small Module reactor, the U.S. Government collaborated with industry to develop a small, modular version of the high temperature reactor (HTR) in the 1980s. The GA MHTGR was subjected to pre-application safety review by the NRC. (Fuel development by the federal government continued under the New Production Reactor Program, whose mission was the production of tritium for the weapons program.) An important difference between the MHTGR and the FSV plant was the lower core power density that enabled the ability to reject decay heat passively to the environment, even in the most severe loss-of-coolant accident. This is achieved by limiting the core power (about 600 MW) and building a tall core with a relatively small diameter, thus providing a short conduction path from the core to the vessel. All HTRs designed since then have adopted this inherent safety feature. The detailed technical status of the MHTGR and its pebble-bed counterpart developed in Germany, the HTR Modul, are described by Gougar (2014). The HTR Modul design was submitted to the German regulator in the late 1980s, but was never built. A two-unit pebble-bed modular HTR power plant based on the German design is under construction in China.

As part of the overall Advanced Test/Demonstration Reactor Options Study, an assessment of the maturity of Generation IV reactor technologies was conducted by a multi-laboratory panel of experts and documented by Gougar et al. (2015). The panel's assessment results of the HTGR are summarized in this section.

A technology readiness scale developed by DOE was used to evaluate the HTGR and other systems. Numerical scores for the different systems and subsystems of the HTGR are tabulated in Table 5-1. The scale, using the DOE-defined readiness levels described by Gougar (2014), ranges from 9 for technologies with operational experience down to 1 where the technology's basic principles have been observed and reported. The overall technology readiness level (TRL) was obtained by taking the minimum value of the TRLs of the key subsystems shown in the shaded cells in Table 5-1. Key subsystems are those that were determined by the panel to be critical to safe operation and performance of the concept. A more detailed explanation of the scoring process and rationale for the score is provided by Gougar et al. (2015).

Table 5-1. TRLs for each HTGTR system and subsystem for test reactor deployment (key subsystems are shaded).

| System | HTGTR |
|---|:---:|
| Nuclear Heat Supply | 5 |
| Fuel element (fuel, cladding, assembly) | 6 |
| Reactor internals | 6 |
| Reactivity control | 6 |
| Reactor enclosure | 5 |
| Operations/inspection/maintenance | 5 |
| Core instrumentation | 6, 3 |
| Heat Transport | 5, 3 |
| Coolant chemistry control/purification | 6 |

Table 5-1. (continued).

| System | HTGTR |
|---|---|
| Primary heat transport system (hot duct) | 6 |
| Intermediate heat exchanger (if applicable) | NA[a]/3 |
| Pumps/valves/piping | 5 |
| Auxiliary cooling | 6 |
| Residual heat removal | 5 |
| Power Conversion | 6 |
| Turbine | 7 |
| Compressor/recuperator (Brayton) | NA |
| Reheater/superheater/condenser (Rankine) | 7 |
| Steam generator | 7 |
| Pumps/valves/piping | 6 |
| Process heat plant (e.g., $H_2$) | NA/3 |
| Balance of Plant | 6 |
| Fuel handling and interim storage | 6 |
| Waste heat rejection | 7 |
| Instrumentation and control | 6 |
| Radioactive waste management | 6 |
| Safety | 6 |
| Inherent (passive) safety features | 6 |
| Active safety system | 6 |
| Licensing | 3, 6[b] |
| Safety design criteria | 3 |
| Applicability of previous licensing experience | 3 |
| Safety and analysis tools | 4 |
| Fuel Cycle | NA |
| Recycled fuel fabrication technology | |
| Used fuel separation technology | |
| Safeguards | 3 |
| Proliferation resistance—intrinsic design features (e.g., special nuclear material accountability) | 3 |
| Plant protection—intrinsic design features | 3 |
| **Overall Technology Readiness Level** | **5** |
| a.  NA = not applicable. | |
| b.  The safety design criteria have recently been updated based on a broad set of industry and DOE inputs and comments (NRC feedback on this is due out later in 2016). A TRL of 6 is suggested as a more accurate reflection of this status, but the TRL of 3 is retained to be consistent with the detailed TRL assessment that is reported in (Gougar et al. 2015). | |

For the HTGR design, the lowest technical maturity scores were assigned to certain metallic components inside the pressure vessel. When exposed to core conditions during accidents, these may be subject to failure. If coolant temperatures are limited to 850°C, SA508/533 (the steel alloy used in LWRs) is adequate for the pressure vessel. For the most severe loss-of-forced cooling events, significant fuel particle degradation is not expected, although some metallic components in the core region (such as control rod guide tubes) may need to be replaced. Qualification of new alloys or even use of carbon or silicon carbide composites for the guide tubes may be beneficial. The control elements are not anticipated to reach failure temperatures. For these reasons, the reactor enclosure subsystem for the demonstration plant was assigned a TRL of 5.

The overall conclusion of the panel was that the HTGR, with outlet temperatures limited to 850°C, is suitable for near-term deployment as either a test or demonstration reactor.

# 6.  Test Reactor Licensing, Development and Deployment Plans

The HTGTR aligns with the NRC's definition of a Test Facility (10 CFR 50.2):

> *A thermal power level in excess of 1 megawatt, if the reactor is to contain a circulating loop through the core in which the applicant proposes to conduct fuel experiments. Subsection 104c of the Atomic Energy Act, and are therefore issued "Class 104c" licenses. An additional restriction regarding this class of reactor license is that the facility must be used so that no more than*

Test reactors are one type of non-power reactors that the NRC licenses under the authority of Subsection 104c of the Atomic Energy Act, and are therefore issued "Class 104c" licenses. An additional restriction regarding this class of reactor license is that the facility must be used so that no more than 50% of the annual cost of owning and operating the facility is devoted to the production of materials, products, or energy for sale or commercial distribution, or to the sale of services, other than R&D or education or training.

Congress directed the NRC to impose the minimum amount of regulation on Subsection 104(c) research reactor and test reactor licensees. In keeping with this direction, the NRC staff utilizes NUREG-1537 (NRC 1996) as the primary guidance for review of research reactors and test reactor technologies and license applications. NUREG-1537 is based on the key constituents from 10 CFR 50; use of the historically-applied "two-step" NRC licensing is summarized in Section 6.3.

NRC's research reactor and test reactor reviews are typically performed using a "performance-based" approach, rather than the more prescriptive-review approach that is used when licensing commercial power reactors under the NRC's Standard Review Plan for LWRs (NRC 2007). This approach is expected to be characterized by the establishment and implementation of flexible and tailored technical requirements specific to the advanced technologies being developed.

## 6.1  Test Reactor Dose Limits

The occupational and public dose limits for test reactors are found in 10 CFR 20.1201 and 10 CFR 20.1301; accident doses for workers should be compared with the limits found in 10 CFR 100. These limits are summarized in Table 6-1.

Table 6-1. Dose limits applicable to the HTGTR.

| Test Reactors—Occupational, Public, and Accident Dose Limits | | | |
|---|---|---|---|
| Applicability | Requirement Document | Dose Limit | |
| Occupational Dose—Annual Limit | 10 CFR 20.1201 | TEDE | ≤5 rem |
| | | Organ dose | ≤50 rem |
| Public Dose Limit | 10 CFR 20.1301 | Annual TEDE | ≤100 mrem |
| | | Hourly external dose | ≤2 mrem |
| Accident Dose Limit—Worker | 10 CFR 100.11 | Whole body | ≤25 rem |
| | | Thyroid dose | ≤300 rem |

TEDE = total effective dose equivalent.

## 6.2 Design Criteria for Modular High-Temperature Gas-Cooled Reactors

DOE and NRC established a joint initiative in July 2013 to develop guidance for advanced reactor developers and other stakeholders on how the existing general design criteria reflected in 10 CFR 50, Appendix A, can be adapted to non-LWRs. A proposed set of general design criteria adaptations specific to modular HTGRs was developed by a DOE/national laboratory team and submitted to NRC for review in December 2014 (Kinsey and Holbrook 2014).

Initial NRC feedback on those adaptations is pending, and expected to ultimately be reflected in an NRC Regulatory Guide that will be formally issued in late 2016. These adapted criteria provide guidance and direction to be considered by both test reactor developers and the NRC staff reviewing the related license application(s).

## 6.3 Research and Development Needed for Licensing

The Advanced Reactor Technologies (ART) Program team has recently reviewed and discussed the R&D needed to support commercial licensing for the modular HTGR and sodium fast reactor advanced reactor design types. Results from those efforts are reflected in the ART Regulatory Technology Development Plan (Kinsey 2015). The Regulatory Technology Development Plan identifies, assesses, and prioritizes key ART research opportunities with respect to their associated regulatory impact, and recommends research priorities that specifically consider the needs of the NRC independent safety review process. Although this plan focused on supporting development and deployment of commercial facilities, it can be used as a resource for identifying key R&D needed to support test reactor licensing, since many of the issues to be addressed are largely the same. Key R&D topical areas identified include:

- Accident progression modeling
- Primary system and containment performance
- Fission product behavior modeling
- Core heat removal
- Thermal-fluid dynamics
- Nuclear analysis
- Fission product transport
- Event sequence frequency.

In addition to the above key R&D topical areas, it will be necessary to identify and assess any adverse effects that may result from interactions between the test reactor and associated test mediums (e.g., molten salt), and from feedback/interaction from "over-the-fence" test reactor output end-users.

## 6.4 Deployment Schedule

NRC's license application review process for research reactors and test reactors is built around the 10 CFR 50 ("two-step") licensing process, which consists of a series of applications for a construction permit (CP), followed by an operating license. Although no NRC regulations apply specifically to the submittal of a safety analysis report (SAR) for non-power reactors, the SAR format historically has been used in direct support of this process and is expected to provide the most efficient and effective method for facilitating NRC's review of the HTGTR discussed in this report.

The application for a CP must contain the following three types of information:

1. Preliminary safety analyses

2. An environmental review

3. Financial and anti-trust statements.

NRC also conducts an environmental review, in accordance with the National Environmental Policy Act, to evaluate the potential environmental impacts and benefits of the proposed test reactor facility.

Final design information and plans for operation are developed during construction of the facility. The applicant then submits an application to NRC for an operating license. The application contains a final SAR, an updated environmental report, and a description of the plans for operation, including technical specifications. The review process is similar to that applied to the CP application (Figure 6-1), but may exclude certain steps (e.g., hearing) depending on the petitions received.
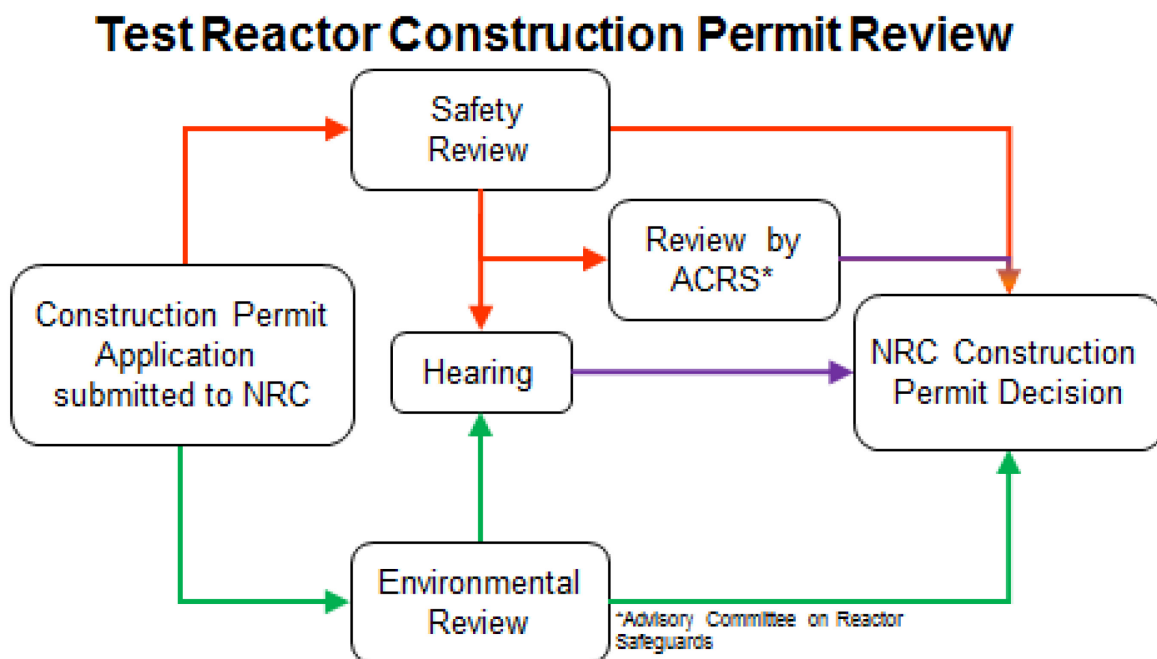


Figure 6-1. NRC test reactor construction permit review process.

The design, procurement, and construction processes follow a system engineering philosophy of progression. This includes conceptual design (2 years), preliminary design (2 years), and final (detailed) design (3 years). Key activities in these areas are summarized as follows and a representative schedule is reflected in Figure 6-2:

- **Conceptual Design.** The purpose of conceptual design is to fully define the selected concept. Feasibility questions have been adequately addressed (sometimes subject to future ongoing development activities with known fallback options), and key design decisions have been made. The product of conceptual design is a moderately detailed plant design concept for which all main features have been identified and key analyses have been performed. This information is used to support pre-application discussions with NRC, including establishment of the licensing technical requirements that will be applied to NRC's review of the license application.

- ***Preliminary Design.*** The purpose of preliminary design is to advance the design process to the point of project commitment to manufacture/construction. Any adjustments needed as a result of conceptual design work are made and the second design iteration is performed. In general, the design activity during preliminary design is more complete and thorough, using more complete design information and more mature analysis tools and models. The preliminary design would form the basis for the bulk of the content of the SAR submitted to NRC in support of the CP application.

- ***Construction and Startup Testing.*** Construction activities can begin once a plant CP has been obtained. A CP is granted based on NRC review of the preliminary SAR. In accordance with our schedule, this review is to last a maximum of 3 years and conclude as the plant final design phase comes to completion.

The reference HTGTR plant construction schedule is 6 years. At the end of the 6th year, the HTGTR is installed and ready for fuel loading and shake-down phase operation. Initial operating license conditions or restrictions (e.g., reduced power level) are addressed during this shake-down phase. The HTGTR is operational after 13 years, with some initial restrictions on the operating power level.

| HTGR Test Reactor Schedule | 1 | 2 | 3 | 4 | 5 | 6 | 7 | 8 | 9 | 10 | 11 | 12 | 13 | 14 | 15 | 16 |
|---|---|---|---|---|---|---|---|---|---|---|---|---|---|---|---|---|
| **Research and Development** | ▓ | ▓ | ▓ | ▓ | ▓ | ▓ | ▓ | ▓ | | | | | | | | |
| **Test Reactor Licensing** | | | | | | | | | | | | | | | | |
| Pre-application Review | | ▓ | ▓ | ▓ | | | | | | | | | | | | |
| CP Application and Review | | | | | ▓ | ▓ | ▓ | | | | | | | | | |
| CP Issued | | | | | | | ◇ | | | | | | | | | |
| OL Application and Review | | | | | | | | | | | ▓ | ▓ | ▓ | | | |
| OL ssued and fuel load authorized | | | | | | | | | | | | | | ◇ | | |
| Test and verification of safety features | | | | | | | | | | | | ▓ | ▓ | ▓ | ▓ | |
| OL restrictions satisfied and removed | | | | | | | | | | | | | | | | ◇ |
| **Test Reactor Design and Deployment** | | | | | | | | | | | | | | | | |
| Conceptual Design | ▓ | ▓ | | | | | | | | | | | | | | |
| Preliminary Design | | | ▓ | ▓ | | | | | | | | | | | | |
| Final Design | | | | | ▓ | ▓ | ▓ | ▓ | | | | | | | | |
| Procurement | | | | | | | | | | | | | | | | |
| Construction and Startup Testing | | | | | | | | ▓ | ▓ | ▓ | ▓ | ▓ | ▓ | | | |
| Test Reactor Operational - with restrictions | | | | | | | | | | | | | | ◇ | | |
| Test Reactor Fully Operational | | | | | | | | | | | | | | | | ◇ |

Figure 6-2. HTGTR design, licensing, and deployment timeline.

# 7. Economics and Schedule

The capital, operating, and decommissioning costs for the HTGTR are based on information presented in the NGNP pre-conceptual design report (INL 2007) for a 350-MW first-of-a-kind (FOAK) reactor with a single reactor module. The detailed cost model utilized for this cost estimate was developed as part of the NGNP Project using data from three vendors (Gandrik 2012). Unless otherwise stated, all costs are presented in 2015 dollars and are scaled using the Chemical Engineering Plant Cost Index. The total capital cost for an HTGR includes preconstruction costs, direct costs, indirect costs, and project contingency. Operating costs include staffing requirements, annual fees, insurance, taxes, material supplies, outage costs, and administration and general cost overhead.

The AREVA Steam Cycle-HTGR Demonstration Reactor Report estimated a total overnight cost of $3,963 million for the 625-MW design, while the NGNP cost model produces an estimate of $3,669 million, based on a 600-MW Rankine-cycle FOAK design (Mayer, Lommers and Shahrikhi 2016). The two estimates are based on two slightly different designs, but are still within 8% of each other, which is well within the uncertainty range of both estimates. Therefore, it can be concluded that the NGNP cost model for the large (600 MW) design still represents a valid benchmark point for the estimates that are presented in this section.

The cost estimate for the 200-MW HTGTR is based on the 350-MW NGNP demonstration reactor data, because this was the closest match to the selected power level. The NGNP cost model included several complex scaling factors for calculating the cost of a scaled 350-MW design from the larger 600-MW design that was considered as the reference NGNP design. Further scaling down to 200 MW was not recommended by the AREVA review team or INL personnel involved in the NGNP cost model, because the uncertainties related to the cost trade-offs of the higher complexity of the test reactor design versus a simpler power reactor design are significant. Extrapolation of the NGNP correlations developed for the 600- to 350-MW costs also cannot be measured using existing vendor data. The 350-MW costs were therefore applied "as-is" for the estimate for the 200-MW HTGTR costs.

The best-estimate (point) cost of the 200-MW HTGTR design is summarized in Table 7-1, along with the cost estimate uncertainties of −50% and +50%, which are consistent with the level of project definition of 0 to 2% (an American Association of Cost Engineers International Class 5 estimate). The total capital investment is calculated by summing preconstruction costs, direct costs, indirect costs, and project contingency. The total capital investment required to build a 200-MW HTGTR is estimated at $3,942 million, within an uncertainty range of $1,972–5,913 million.

The following assumptions were used to determine these cost estimates:

- **Reactor outlet temperature.** The reactor outlet temperature of the HTGTR is selected at 650°C, but correlations available in the NGNP cost model are only specified between 750 and 950°C. An extrapolation down to 650°C was not recommended due to possible non-linear variances in material costs when the lower temperatures are utilized. Therefore, the lowest available model point, 750°C, was selected for the 200-MW HTGTR estimate and provides justification for decreasing the lower bound of the cost-estimate uncertainty range.

- **Non-scaling factors.** The NGNP cost model (INL, 2007) shows that building, support facilities, licensing and design cost components do not scale with a change in reactor power, because the activities and durations required for a large or small reactor design are comparable. These components make up $1,325 million of the total cost (34%).

- **Cost of additional test features and increased complexity.** The 200-MW HTGTR includes several features that are not present in the 350-MW demonstration reactor: test loops, irradiation positions and the peripheral supporting elements (e.g., pumps, vessel head penetrations, and extraction and sample storage space). The cost of these features cannot be assessed within the scope of this point design study; however, an estimate of $200 million has been added to account for this increase in

design complexity. This is roughly based on data available from INL's ATR Program, where the addition of a single gas test loop to the current design has been estimated at approximately $80 million. If it is assumed that the addition of four test loops would achieve some economy of scale, $200 million could be an approximate estimate of this factor, possibly within the same −50% and +50% uncertainty band as the rest of this estimate.

Table 7-1. Summary of lower, best-estimate, and upper cost estimates for 200-MW FOAK HTGTR.

| Item | −50% | Best Estimate | 50% |
|---|---|---|---|
| Capital Cost summary (Million 2015$) | | | |
| Preconstruction costs | | | |
| Land and land rights | 0 | 0 | 0 |
| Licensing and application costs | 122 | 244 | 366 |
| Total preconstruction costs | 122 | 244 | 366 |
| Direct cost | | | |
| Selected configuration direct cost total | 447 | 894 | 1,341 |
| Balance of equipment adder | 112 | 224 | 336 |
| Test loops/facilities | 100 | 200 | 300 |
| Total direct cost | 659 | 1,318 | 1,977 |
| Indirect costs | | | |
| Total design cost | 540 | 1,081 | 1,621 |
| Construction services | 112 | 224 | 336 |
| Home office and engineering services | 90 | 180 | 270 |
| Field office and engineering services | 55 | 109 | 164 |
| Owner's costs | 64 | 129 | 193 |
| Total indirect cost | 861 | 1,723 | 2,585 |
| Construction cost | 1,642 | 3,285 | 4,927 |
| Project contingency | 328 | 657 | 985 |
| **Total Capital Investment** | **1,971** | **3,942** | **5,913** |
| Yearly Operations and Maintenance (O&M) Summary (Million 2015$) | | | |
| Total yearly O&M cost | 18 | 36 | 54 |
| Fuel Cost Summary (Million 2015$) | | | |
| Refueling cost per core | 30 | 60 | 90 |
| Total average yearly fuel cost | 20 | 40 | 60 |
| Decommissioning Cost Summary (Million 2015$) | | | |
| Total decommissioning cost | 39 | 78 | 117 |

For each of the major cost categories, a short summary of the major contributors is provided in the following subsections.

## 7.1   Capital Costs

The total capital cost is comprised of the cost categories addressed in the following subsections.

### 7.1.1 Preconstruction Costs

The main contributor to the preconstruction cost category is NRC licensing and application. Design certification costs are included in the licensing costs for the test plant. Costs for land and land rights are normally included in this cost category, but have been assumed to be zero for this analysis because the proposed reactor would be constructed on government land. Generally, it may be assumed that a single HTGR requires 50 acres of land.

### 7.1.2 Direct Costs

Direct costs for the reactor plant are associated with the cost of materials and installation for the equipment items that make up the reactor plant. Given the nascent stage of the HTGR design, previous reactor cost estimates provided by selected reactor design suppliers were assessed to determine the reactor plant equipment items that make up the majority of the direct costs. The following equipment items make up approximately 80% of the installed equipment costs: reactor building, vessel, initial core, metallic and graphite internals, reactor cavity cooling system, core refueling equipment, heat rejection system, intermediate heat exchanger, and the power generation equipment (Rankine cycle assumed). (The HTGTR will most likely not include an intermediate heat exchanger; therefore, an estimate of the cost for this component is beyond the scope of this work.) To account for the balance of equipment costs not included in the direct cost estimate, the total cost of the items above was multiplied by a factor of 1.25. This factor was based on the assessment of previous cost estimates provided by reactor design suppliers, where remaining equipment items contribute 20% of the installed equipment costs.

### 7.1.3 Indirect Costs

The capital required for construction overhead and other costs not included in the direct costs are included in the indirect costs. Given the early stage of HTGR design and costing efforts, it is necessary to estimate the indirect costs as a percentage of the direct costs based on previous reactor design supplier estimates and historical indirect costs for LWR designs. Indirect costs cover the following:

- Construction services: construction management, procurement, scheduling, cost control, site safety, and quality inspections

- Home and field office and engineering services: costs for estimating, scheduling, project expediting, project general management, design allowance, field office, field engineering, field drafting, field procurement, and project fees

- Owner's costs: project fees, taxes, and insurance; spare parts and other capital expenses; staff training and startup costs; and administrative and general expenses

- Design costs: covers conceptual, preliminary, and final design activities and R&D activities associated with these stages of reactor design and licensing. A breakdown of these components is provided in Table 7-2.

- R&D costs: covers the R&D needed to increase the TRLs for each HTGR system.

Table 7-2. Design costs.

| Phase | $ Million |
|---|---|
| Conceptual design | 90 |
| Preliminary design | 194 |
| Final design | 315 |
| R&D costs | 482 |
| **Total** | **1,081** |

### 7.1.4 Contingency

A project contingency of 20% was selected for the HTGR capital cost analysis for all project phases.

## 7.2 Operating Costs

Operating costs are estimated for the HTGTR and include O&M costs and refueling costs. O&M costs were estimated based on methodology presented for a study of advanced reactor technologies, specifically the study of O&M staffing and costs conducted by nuclear industry partners. O&M costs are assumed to include staffing requirements, fees, taxes and insurances, material supplies, outage costs, and administration and general cost overhead.

HTGR fuel costs were calculated for the prismatic fuel configuration provided by GA for the NGNP pre-conceptual design (INL 2007). It is assumed that the refueling cost is scaled linearly with the reactor power rating.

Table 7-1 shows that the standard cost model estimates the operating cost at $76 million per year. This does not include additional annual costs associated with test program activities (e.g., additional personnel and additional outage time for accessing loops), which could add another $25-$50 million to the annual costs (based on historical Fast Flux Test Facility data). Therefore, the total operating cost is estimated at $100-$125 million per year.

## 7.3 Assessment of Potential Revenue

A preliminary assessment of the potential revenue and resulting economic considerations associated with construction and operation of an HTGR was performed. The analysis assumed that 50% of the heat generated by the HTGR would be available to generate electricity. The remaining heat can be used for experimental setups or just dumped to the final heat sink. The results of the assessment are summarized in Table 7-3.

Table 7-3. Possible revenue generation for a HTGTR with Rankine cycle to generate electricity.

| Area | Selling Price of Electricity[a] ($/MWh) | Estimated Electrical Sales Revenue Generated[b] ($M) |
|---|---|---|
| Northwest U.S. | 22.75 | 6.3 |
| Northeast U.S. | 44.36 | 12.4 |

a. Selling price of electricity based on average January 2016 spot price from the Energy Information Administration website (www.eia.gov). The highest and lowest U.S. prices are presented in the table to illustrate the electricity selling price range.

b. Annual revenue from electricity sales for a 200-MW test reactor with a capacity factor of 80%, 50% of reactor power rating used to generate electricity, 39.8% efficiency of 550°C Rankine steam cycle to produce electricity (see Nelson et al. [2011] and electricity prices as noted in the table).

# 8. References

10 CFR 20, "Standards for Protection Against Radiation," *Code of Federal Regulations*, U.S. Nuclear Regulatory Commission.

10 CFR 50, "Domestic Licensing of Production and Utilization Facilities," *Code of Federal Regulations*, U.S. Nuclear Regulatory Commission.

10 CFR 100, "Reactor Site Criteria," *Code of Federal Regulations*, U.S. Nuclear Regulatory Commission.

DOE, 1986, *Preliminary Safety Information Document for the Standard MHTGR*, Stone & Webster Engineering Corp., report HTGR-86-024.

Gandrik, A.M., 2012, "Assessment of High Temperature Gas-Cooled Reactor (HTGR) Capital and Operating Costs," TEV-1196, Revision 1, Idaho National Laboratory, January 2012.

Gougar, H., 2014, *Baseline Concept Description of a Small Modular High Temperature Reactor*, INL/EXT-14-31541, Revision 1, Idaho National Laboratory, May 2014.

Gougar, H.D., et al, 2015, *Assessment of the Technical Maturity of Generation IV Concepts for Test and Demonstration Reactor Applications*, INL/EXT-15-36427, Revision 2, Idaho National Laboratory, October 2015.

INL, 2007, *Next Generation Nuclear Plant Pre-Conceptual Design Report*, INL/EXT-07-12967, Idaho National Laboratory, November 2007.

INL, 2015, *RELAP5-3D Code Manual, Volumes I-V*, INL/MIS-15-36723, Revision 4.3, RELAP5-3D Code Development Team, Idaho National Laboratory, October 2015.

Kinsey, J.C. and M.R. Holbrook, 2014, *Guidance for Developing Principal Design Criteria for Advanced (Non-Light Water) Reactors*, INL/EXT-14-31179, Revision 1, Idaho National Laboratory, December 2014.

Kinsey, J.C., 2015, *Advanced Reactor Technology – Regulatory Technology Development Plan (RTDP)*, INL/EXT-14-32837, Idaho National Laboratory, May 2015.

Mayer, J., L. Lommers, and F. Shahrikhi, 2015, *Design Attributes and Considerations for a Gas-Cooled Graphite Moderated Irradiation Test Reactor*, AREVA Inc., Technical Data Record 12-9247414-000, October 2015.

Mayer, J., L. Lommers, and F. Shahrikhi, 2016, *Steam Cycle - High Temperature Gas-Cooled Demonstration Reactor*, AREVA Inc., Technical Data Record 12-9251108-000, January 2016.

Nelson, L., et al. 2011, *Integration of High Temperature Gas-Cooled Reactors into Industrial Process Applications*, INL/EXT-09-16942, Revision 3, Idaho National Laboratory, September 2011.

NRC, 1996, *Guidelines for Preparing and Reviewing Applications for the Licensing of Non-Power Reactors*, NUREG-1537, U.S. Nuclear Regulatory Commission.

NRC, 2007, *Standard Review Plan for the Review of Safety Analysis Reports for Nuclear Power Plants: LWR Edition*, NUREG-0800, U.S. Nuclear Regulatory Commission.

Sterbentz, J.W. et al., *High Temperature Gas-Cooled Test Reactor Point Design: Summary Report*, INL/EXT-16-37661, Revision 1, Idaho National Laboratory, March 2016.

U.S. Energy Information Administration, Independent Statistics and Analysis, www.eia.gov.

X-5 Monte Carlo Team, 2003, *MCNP—A General Monte Carlo N-Particle Transport Code, Version 5*, Volume I (LA-UR-03-1987) and Volume II (LA-CP-03-0245), Los Alamos National Laboratory, April 2003.

# Appendix A

# Self-Assessment Against Test Reactor Metrics

# Appendix A. Self-Assessment Against Test Reactor Metrics

## Summary of Self-Assessment

| Metric | INL Score |
|--------|-----------|
| T1.1.1 | 1 |
| T1.1.2 | 5 |
| T1.1.3 | 9 |
| T1.1.4 | 9 |
| T1.1.5 | 9 |
| T1.2.1 | 9 |
| T1.2.2 | 9 |
| T1.2.3 | 9 |
| T2.1.1 | 5 |
| T2.1.2 | 5 |
| T2.2.1 | 5 |
| T2.3.1 | 5 |
| T3.1.1 | 9 |
| **Total** | **89/117 (76%)** |

Metric T1.1.1. Fast-flux conditions.

| Metric | $>5 \times 10^{15}$ n/cm$^2$-s fast (>0.1 MeV) | $5 \times 10^{14}$ to $5 \times 10^{15}$ n/cm$^2$-s fast (>0.1 MeV) | $<5 \times 10^{14}$ fast (>0.1 MeV) |
|--------|--------|--------|--------|
| INL Score | — | — | 1 |

Metric T1.1.2. Thermal flux conditions (0.625 eV).

| Metric | $>5 \times 10^{14}$ n/cm$^2$-s thermal | $1–5 \times 10^{14}$ n/cm$^2$-s thermal | $<1 \times 10^{14}$ n/cm$^2$-s thermal |
|--------|--------|--------|--------|
| INL Score | — | 5 | — |

Metric T1.1.3. Irradiation volumes and length for largest test location.

| Metric | Volume >10 L Length >2 m | Volume 5–10 L Length 0.5–2 m | Volume <5 L Length <0.5 m |
|--------|--------|--------|--------|
| INL Score | 9 | — | — |

Metric T1.1.4. Maximum sustainable time at power, to provide a time-at-power for a single irradiation (i.e., cycle length).

| Metric | >90 Days | 45–90 Days | <45 Days |
|--------|--------|--------|--------|
| INL Score | 9 | — | — |

Metric T1.1.5. Provisions for testing prototypic and bounding conditions (temperature, coolant, chemistry).

| Metric | Prototypic and bounding for different reactor coolant types | Prototypic and bounding for base coolant | Not prototypic and bounding |
|---|---|---|---|
| INL Score | 9 | — | — |

Metric T1.2.1. Number of test zones.

| Metric | >25 Locations | 10–25 Locations | <10 Locations |
|---|---|---|---|
| INL Score | 9 | — | — |

Metric T1.2.2. Number and type of distinct irradiation test loops each with a different cooling system independent of the primary reactor coolant.

| Metric | 3 or More | 1 or 2 | None |
|---|---|---|---|
| INL Score | 9 | — | — |

Metric T1.2.3. Ability to insert/retrieve irradiation specimen while staying at power.

| Metric | At Power (e.g., rabbit) | Limited Handling Capability | Only at Shutdown |
|---|---|---|---|
| INL Score | 9 | — | — |

Metric T2.1.1. Project cost.

| Metric | <$2.5 B | $2.5–4 B | >$4.0 B |
|---|---|---|---|
| INL Score | — | 5 | — |

Metric T2.1.2. Project schedule.

| Metric | <10 Years | 10-15 Years | >15 Years |
|---|---|---|---|
| INL Score | — | 5 | — |

Metric T2.2.1. Annual operating costs.

| Metric | <$100 M/year | $100–150 M/year | >$150 M/year |
|---|---|---|---|
| INL Score | — | 5 | — |

Metric T2.3.1. Availability factor.

| Metric | >80% | 60–80% | <60% |
|---|---|---|---|
| INL Score | — | 5 | — |

Metric T3.1.1. Secondary missions.

| Metric | Sale of Energy Products | Other Secondary Missions | None |
|---|---|---|---|
| INL Score | 9 | — | — |

# Appendix B

# Computer Code Input Models

# Appendix B. Computer Code Input Models

Descriptions of the input models and modeling assumptions used for the MCNP and RELAP5-3D calculations are provided.

## MCNP Input Model

Reactor physics calculations have been performed using the MCNP5/1.60 computer code on the INL's supercomputer systems. Fully explicit, three-dimensional core models were constructed for the core physics calculations that included both 1/12-core models and full-core models. The 1/12-core models were used to perform all parametric studies and the detailed depletion calculations. The full-core models were used to perform the control rod worth calculations. A reflective boundary condition was applied to the radial sides of the 1/12-core model in order to create a geometry- and reactivity-equivalent full-core model.

Figures B-1 and B-2 are MCNP cross sectional plots of the 1/12-core model and the full-core MCNP model of the 6+6-column core configuration.
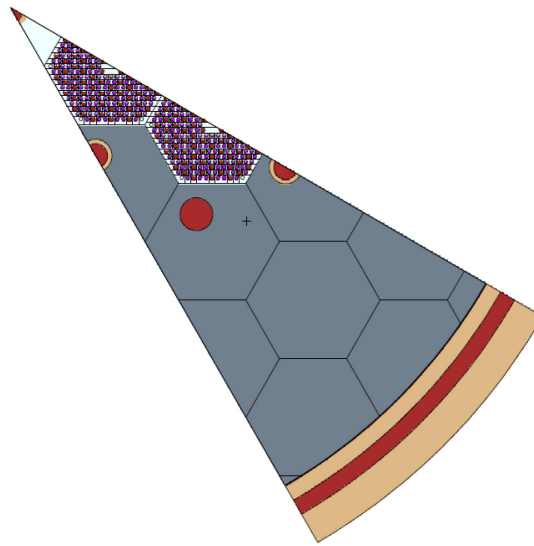


Figure B-2. 1/12-core MCNP model of the 6+6-column core configuration.

Figure B-4 is an MCNP plot of the 1/12-core model showing an axial view of the 6+6-column core configuration. Each fuel column consists of eight fuel blocks stacked vertically. Other configurations of the 6+6-column core considered cores with 4, 5, 6, and 7 block-high fuel columns. The top and bottom graphite reflectors are also shown, along with the inner and outer reflectors, core barrel, and reactor pressure vessel. The outer diameter of the outer reflector, core barrel, and reactor pressure vessel were modelled at 339.6, 350.0, and 380.0 cm, respectively.
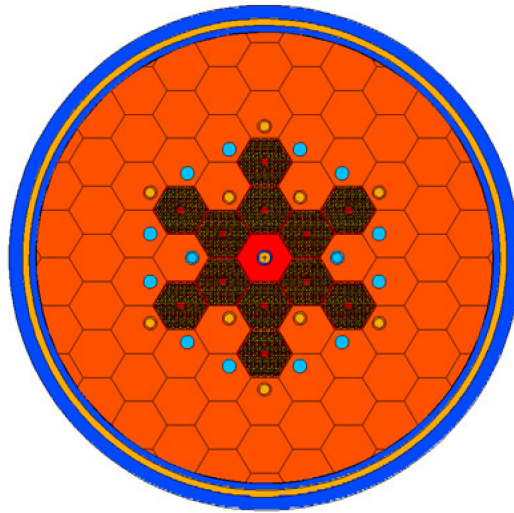
Figure B-3. Full-core MCNP model of the 6+6-column core configuration.
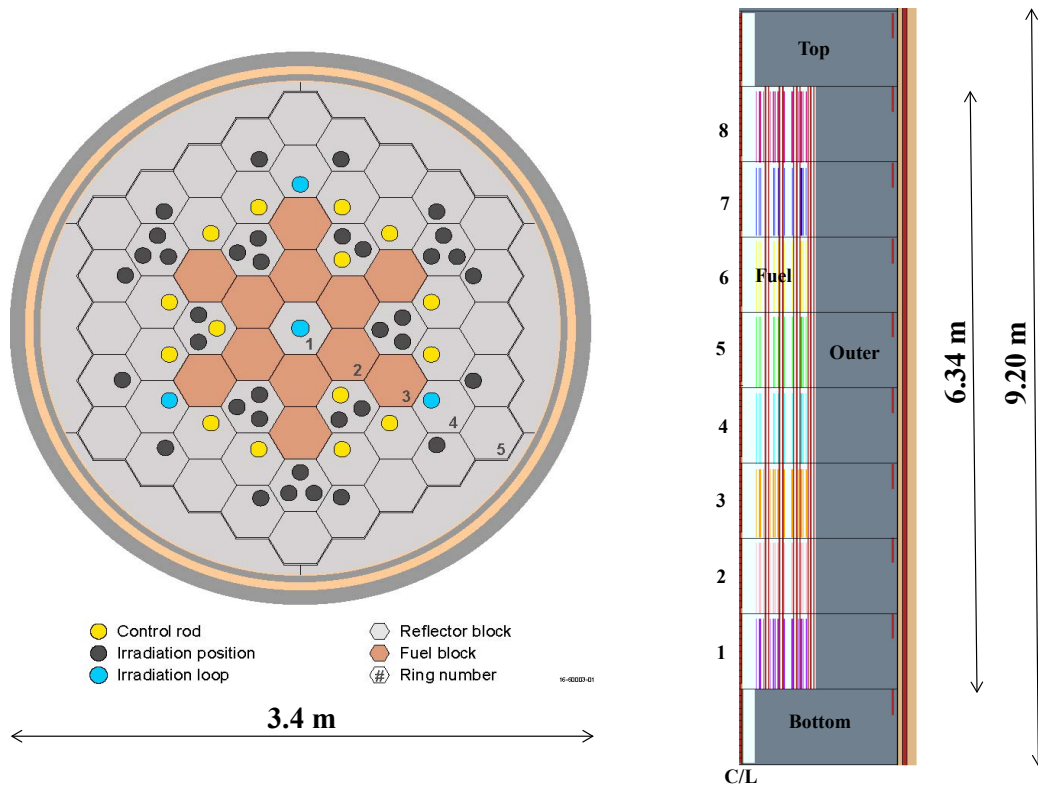


Figure B-4. Cross section and axial views of the final 6+6-column core configuration.

The fuel and reflector blocks are solid hexagonal prismatic graphite blocks. The HTGTR block design and dimensions were based on the FSV block design (Figure B-5). The block flat-to-flat dimension is 35.996 cm with a height of 79.299 cm. All blocks have a handling and tooling hole in the top and bottom center of each block. The fuel blocks have 210 fuel rod positions, 108 helium coolant channels, six burnable poison locations, and the two handling and tooling holes. The fuel rod holes are 1.27 cm in diameter (0.635-cm radius) on a 1.88-cm triangular pitch. The coolant channels are 1.588 cm in diameter with a 3.256-cm triangular pitch. Both fuel and coolant channels are drilled holes in the graphite blocks. The fuel channel holes do not penetrate the bottom of the block. Fuel compacts are loaded into each fuel hole and sealed with a screw cap, leaving a gas plenum space. The coolant channels are drilled straight through the graphite block.
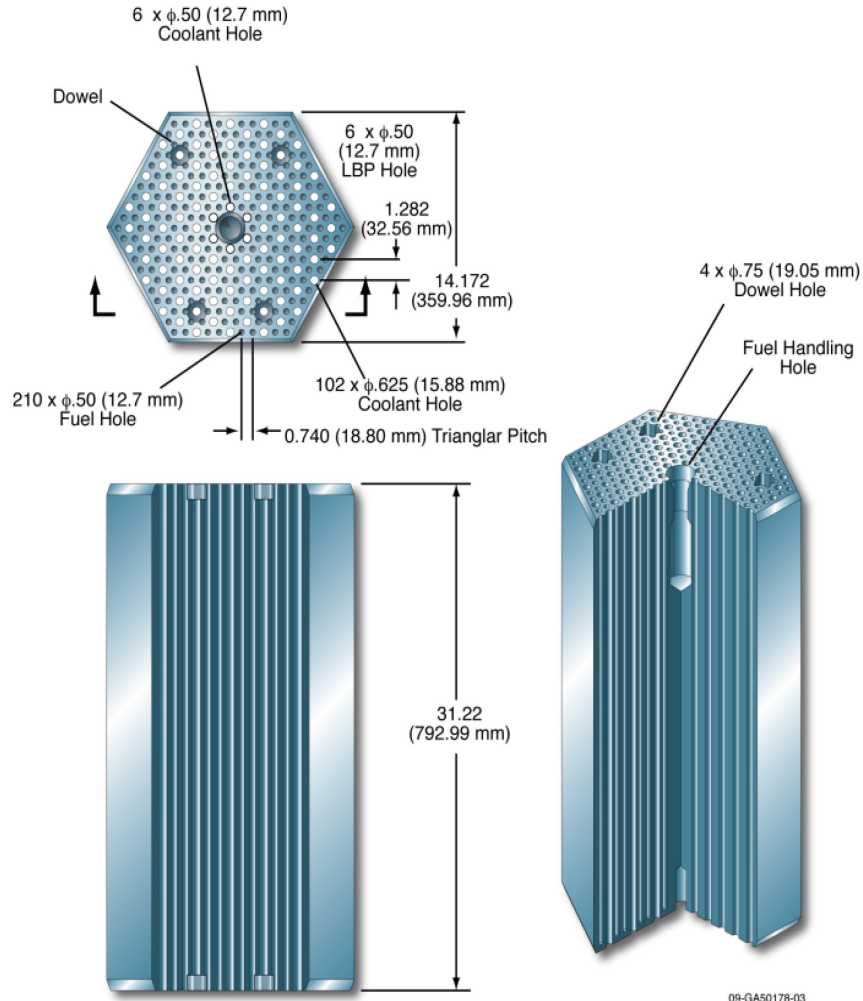


Figure B-5. FSV fuel block.

The MCNP core models explicitly represent fuel and reflector block features and dimensions per the FSV block specifications. Figure B-6 shows an MCNP cross section plot of a fuel block from one of the full-core models. The 210 fuel rods are shown as red circles, the coolant channels as yellow circles, and the bulk graphite block is green. The bulk graphite was assumed to have a density of 1.83 g/cm$^3$ and the compact binder matrix graphite a density of 1.70 g/cm$^3$. The helium gas was assumed to be pure $^4$He at a pressure of 7.12 MPa.
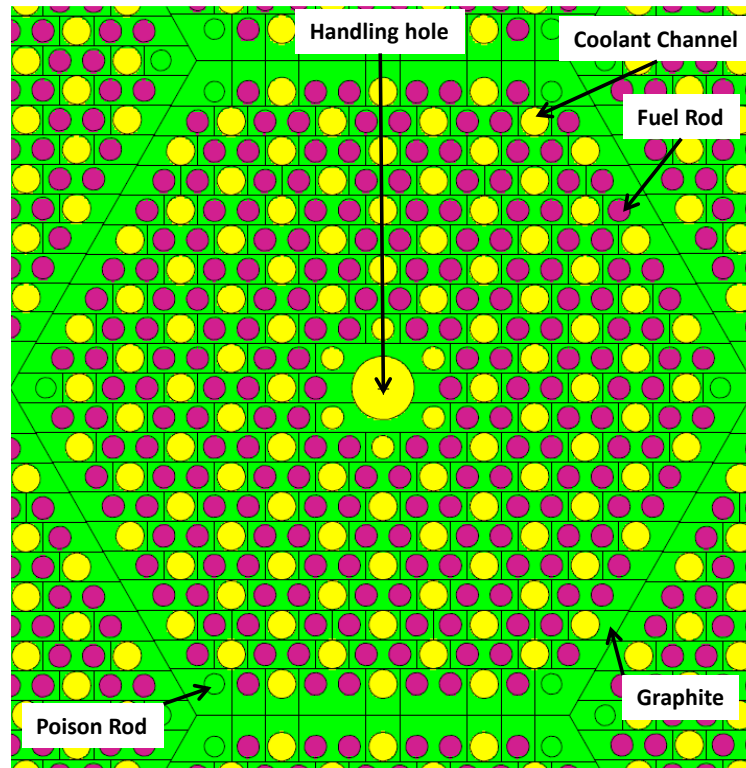
Figure B-6. MCNP fuel block model.

All of the physics models used neutron cross section data from the ENDF-7 library. Temperature-dependent cross section libraries for important actinides were generated at specific temperatures that corresponded approximately to the fuel and reflector block temperatures at each axial fuel block level. The axial fuel block and reflector block level temperatures were calculated by the thermal-hydraulic analyses. Graphite temperature-dependent thermal neutron $S(\alpha,\beta)$ scattering data or endf70sab library data were available from the MCNP-distributed ACER cross section library data at a variety of temperatures: 293.6, 400, 500, 600, 700, 800, 1000, 1200, 1600, and 2000 K. These $S(\alpha,\beta)$ data libraries were matched to the thermal-hydraulic-calculated graphite temperatures.

The following physics modelling assumptions were also made which simplified the physics parametric analyses:

(1) Uniform particle PF in all fuel compacts and across the core
(2) No particle PF grading
(3) No enrichment grading
(4) No burnable poisons
(5) Homogenized compacts
(6) Un-rodded core for most analyses, except in the control rod studies

The single particle PF assumption is tantamount to assuming a uniform particle distribution across the entire core, uniform uranium block loadings, and identical compacts throughout the core. It is anticipated that compacts with more than one PF will be used in the final HTGTR design. Compacts with different PFs will be useful to reduce peak particle power and extend burnup in specific areas of the active core. In other words, PF grading in coordination with strategically placed burnable poisons will play an important role in the core performance.

A single qualified TRISO particle with a single enrichment (15.5 wt%) may preclude enrichment grading as an option in future physics design work.

Burnable poisons were not used in the models or the physics design analysis of the HTGTR point design. However, strategic placement of burnable poisons in the core will eventually play an important role in holding down excess core reactivity at beginning-of-cycle, releasing reactivity over the course of the power cycle, and affecting the number, placement, worth, and design of the control rods.

Homogenized number densities were used in the MCNP models. Compact cells were assigned homogenized number densities that effectively smeared the UCO kernel, particle coatings, and compact matrix graphite. Homogenization simplified the complexity of the MCNP core models by avoiding the full and explicit descriptions of each particle in every compact. However, by not modelling the individual TRISO particles in each compact, the double heterogeneity effect of the lumped fuel kernels was not captured in the calculations. The double heterogeneity effect or modelling the TRISO particles explicitly in a regular particle array or in a random-distribution in the compacts would have had the effect of increasing the calculated core reactivity by approximately 5-7%, the result of which would be a comparable increase in the effective power cycle length. For the basic physics scoping parametric studies associated with the HTGTR point design, the additional burden and complexity of modeling the individual TRISO particles would have been prohibitive.

Table B-1 provides homogenized compact number densities as a function of particle PF for beginning-of-cycle or fresh fuel compacts, assuming a fuel compact diameter of 1.245 cm (radius = 0.6225 cm). Table B-2 provides basic TRISO particle parameters used in the physics analysis.

Table B-1. Homogenized compact number densities (a/b/cm) versus PF.

| Isotope | PF=10% | PF=15% | PF=20% | PF=25% | PF=30% | PF=35% | PF=40% |
|---------|--------|--------|--------|--------|--------|--------|--------|
| $^{235}$U | 4.785E-5 | 7.178E-5 | 9.571E-5 | 1.196E-4 | 1.436E-4 | 1.675E-4 | 1.914E-4 |
| $^{238}$U | 2.576E-4 | 3.864E-4 | 5.152E-4 | 6.439E-4 | 7.728E-4 | 9.015E-4 | 1.030E-3 |
| C | 8.316E-2 | 8.213E-2 | 8.109E-2 | 8.005E-2 | 7.902E-2 | 7.798E-2 | 7.695E-2 |
| O | 4.582E-4 | 6.872E-4 | 9.163E-4 | 1.145E-3 | 1.374E-3 | 1.604E-3 | 1.833E-3 |
| Si | 8.824E-4 | 1.324E-3 | 1.765E-3 | 2.206E-3 | 2.647E-3 | 3.088E-3 | 3.530E-3 |

Table B-2. TRISO particle parameters.

| Kernel/Coating | Thickness (μm) | Inner Radius (μm) | Inner Radius (μm) | Density (g/cm$^3$) |
|----------------|----------------|-------------------|-------------------|--------------------|
| Fuel kernel (UCO) | 429.7 | 0.0 | 214.85 | 10.820 |
| Carbon buffer | 100.0 | 214.85 | 314.85 | 1.050 |
| Inner pyrolytic graphite | 40.0 | 314.85 | 354.85 | 1.900 |
| Silicon carbide | 35.0 | 354.85 | 389.85 | 3.203 |
| Outer pyrolytic graphite | 40.0 | 389.85 | 429.85 | 1.900 |

The diameter of the UCO spherical kernel in each TRISO particle is assumed to be 429.7 μm, which is the nominal kernel diameter of TRISO particles in the Advanced Gas Reactor-5/6/7 qualification experiment planned to begin irradiation in 2017. In this report, the UCO kernel is usually stated to be 425 μm in diameter, but in the physics analyses the 429.7-μm diameter is actually used.

# RELAP5-3D Input Model

The RELAP5-3D input model includes the primary structures and flow paths within the reactor vessel; a nodalization diagram is shown in Figure B-7. A cross section of the core was presented in

Figure B-3 and is the basis for the RELAP5-3D model. Component 100 represents the vessel inlet region, Component 110 is the annulus between the core barrel and reactor vessel, and Component 120 is the upper plenum region. A number of parallel flow paths are modeled between the upper and lower plenum (Component 195): fuel block coolant holes (Components 140 and 150), the gaps between the hexagonal blocks (Components 135, 145, 155, 165, 175, and 185), the gap between the PSR and the core barrel (Component 190), the gap between the center irradiation tube and the central reflector block (Component 130), the gaps around the irradiation tubes in Ring 3 (Component 160), and the gaps around the control rods and irradiation tubes in the first ring of the side reflector (Component 170).
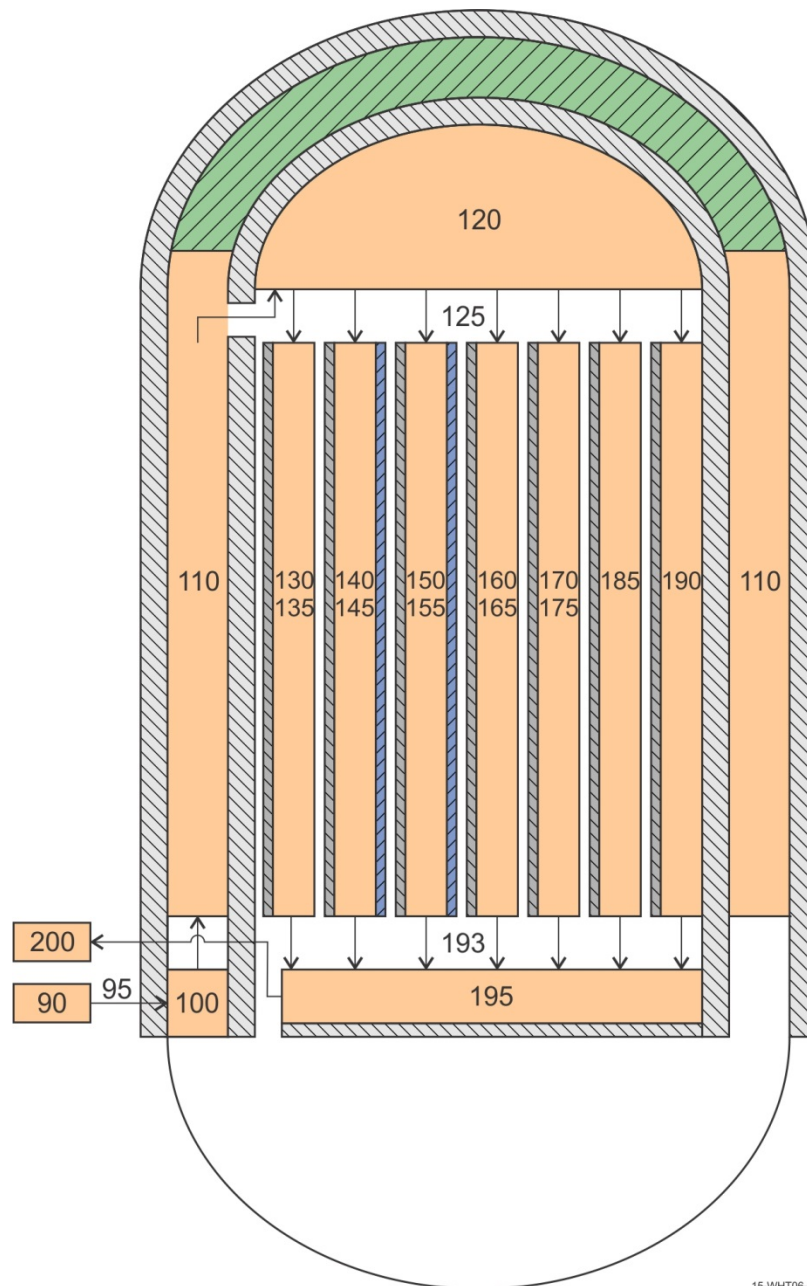


Figure B-7. Nodalization of the reactor vessel for the gas test reactor RELAP5-3D input model.

119

The fuel blocks are modeled using unit cells centered on the coolant holes, with a cylindrical graphite structure around the hole preserving the graphite mass in the block. The fuel rods are modeled as solid cylinders with a helium annulus between them and the graphite, with radiation modeled between the fuel rod and the graphite. Separate heat structures model the central reflector, the reflector blocks in Ring 3, the outer reflector rings, and the PSR. The core barrel and reactor vessel cylinder and upper head are included in the model, as are the upper plenum shield, some upper plenum internals, and the floor of the lower plenum.

The center irradiation loop is modeled as an 11.43-cm diameter (outer) tube with a 2.54-mm gap around it. The control rod and irradiation loop holes in the outer reflector are all assumed to have diameters of 10.16 cm with a control rod or flow tube outer diameter of 8.89 cm. A once-through helium flow of 0.1 kg/s, entering at 27°C, is modeled on the inside of the tube.

In the outer reflector, the holes in the blocks for accommodating control rods and irradiation tubes have a diameter of 10.2 cm. The control rods and tubes in the holes have an outer diameter of 8.89 cm, leaving a gap of 6.55 mm.

A thin layer of graphite, referred to as a sheath, was modeled on the surface of all fuel blocks and on the surface of the reflector blocks in Ring 3. These structures were needed to allow the graphite to have convective heat transfer to the coolant channels, the helium gap around the fuel rods, and the helium gap between adjacent blocks, and to better model radiation across the gaps around the fuel blocks. The sheaths are in conduction enclosures with the blocks, and in radiation enclosures that include sheaths on other blocks and the central and outer reflector blocks in the rings adjacent to the fueled rings. The conduction area factor for the sheaths was made as large as practical to keep their temperature as close to that of the graphite next to them as possible, but not so large that numerical instabilities were encountered.

Crossflow was modeled between the channels representing the gaps between blocks. Leakage from the coolant channels to the gaps, which may occur in the horizontal gap between two stacked blocks, was not modeled.

The RCCS is modeled as flat panels facing the reactor vessel, arranged in a square whose side length is twice the vessel diameter and whose height is slightly larger than that of the reactor vessel. Cooling water flows on the inside of the panels, with the back side (away from the vessel) having an insulated boundary. The flow is driven by natural convection, with a large water volume above the panels providing colder water to the bottom of the panels and accepting the heated water as it exits the RCCS panels. The space between the vessel and the RCCS panels is modeled as a large air-filled volume.

Control systems are used to establish steady-state conditions. The outlet pressure is controlled to provide a vessel inlet pressure of 7.0 MPa, and the coolant flow rate is controlled to provide a coolant temperature of 650°C in the lower (outlet) plenum; the coolant inlet temperature is 325°C. A flat axial and radial power profile was modeled in the fuel for most of the calculations. Heating rates for the reflector blocks were developed from MCNP calculations for a 100-MW core with 4-8 axial levels.

# Appendix C

# Initial Scoping Analyses

# Appendix C. Initial Scoping Analyses

Reactor physics and thermal-hydraulic calculations were performed on several different core configurations at the beginning of the project to better understand the implications of a compact, high-flux test reactor based on HTGR technology. Information gathered from these initial core analyses led to the final 6+6-column core configuration. Calculated results from these scoping analyses are provided below.

## Reactor Physics Analyses

Five core configurations were considered as potential point designs for the HTGTR. The five configurations are shown in Figure C-1. The basic difference between these designs is the number of fuel columns (6, 7, 12, and 18 fuel columns) and their arrangement in the core. The fewer the number of fuel columns, the higher the achievable core power density and the higher the irradiation fluxes. However, power densities are limited by particle power and fuel temperature. Plus, higher irradiation fluxes can be obtained by lower particle PFs in the compacts, but particle power and fuel temperature limits must be considered, and lower particle PFs reduce cycle length and core reactivity. The core designs had to balance these variables.
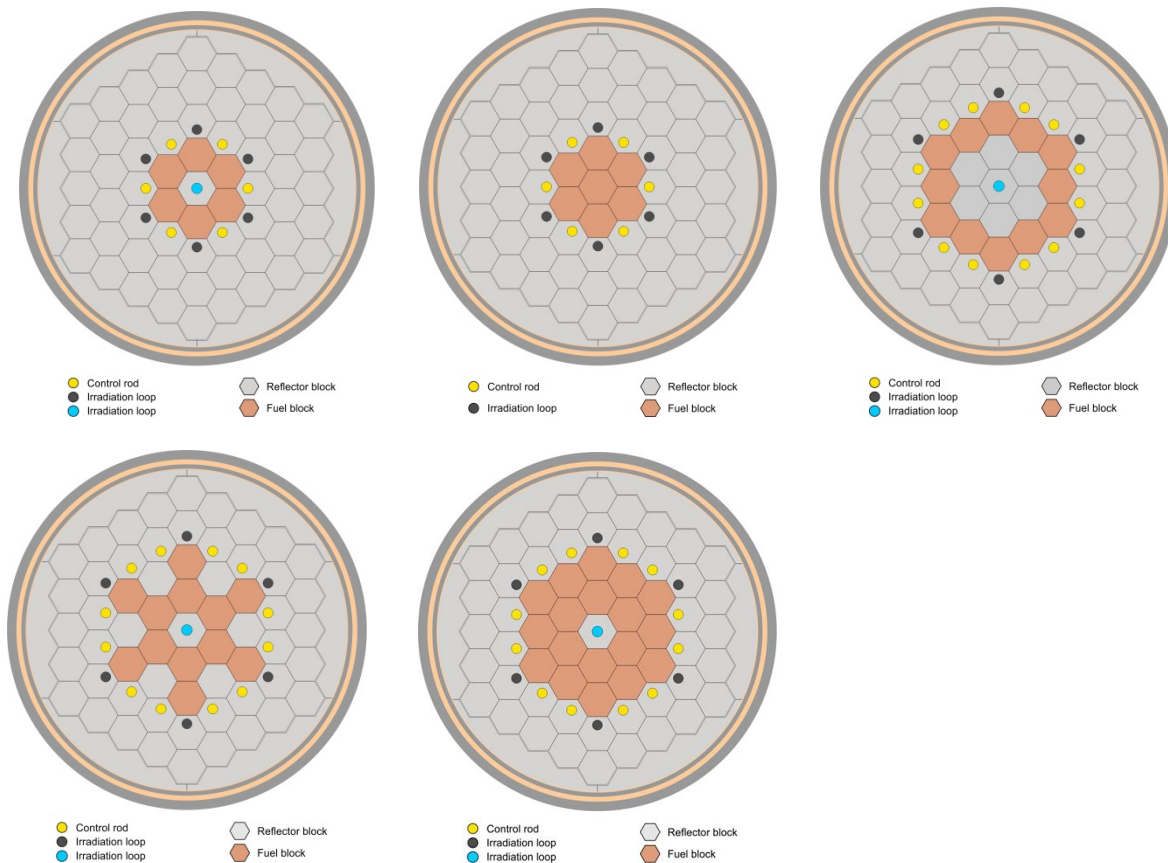


Figure C-1. Cross section views of the 6, 7, 12, 6+6, and 18-fuel column core configurations evaluated in the scoping analyses.

The 6+6-column core configuration (a core with 12 fuel columns) was ultimately adopted as the final design configuration. The 6+6-column, 200-MW core is a relatively compact design with relatively high power density, competitive irradiation fluxes, particle powers and fuel temperatures below performance limits, low PF, and a long cycle length (basically a well-balanced design).

However, one issue that was not fully investigated in this point design study was the potential for top-head penetration crowding, which might be a more immediate concern for the radially smaller, more compact core designs. If top-head crowding is later identified as an issue, and engineering solutions are not forthcoming, annular cores with larger diameters (e.g., inner fuel ring starting in Ring 3) and consequently more fuel columns may need to be considered. One example of such a core configuration is a 12+6-column or a 12+12-column core with the first 12 columns in Ring 3 and the rest in Ring 4 symmetrically spaced with outer reflector graphite blocks. However, assuming top-head crowding is not an issue, the more compact the core, the higher the achievable power density and flux for a fixed total core power. Plus, a smaller compact core with fewer fuel columns requires fewer fuel blocks, which translates directly into lower fuel costs and shorter refueling times.

The five core configurations considered in the scoping analyses assume an 8-block high fuel column, although 4, 5, 6, 7, and 8-block high fuel columns were evaluated in the final evaluation of the 6+6-column core configuration. The 8-block high fuel column, however, was ultimately chosen for the 6+6-column core in order to keep the maximum TRISO particle temperature below 1250°C.

The first core evaluated was the 18-column core configuration. Each of the 18 fuel columns consisted of a vertical stack of eight hexagonal fuel blocks, with a top and bottom graphite block acting as a reflector. In the 18-column core, there are a total of 610 hex block locations, plus the irregularly-shaped PSR blocks, or 18x8=144 fuel blocks, plus 466 graphite reflector blocks. Each fuel block in the stack is assigned a level number. For example, the fuel blocks at the bottom of each stack are referred to as Level 1 and the fuel blocks at the top of the stack are Level 8. The core is annular with both an inner and outer graphite reflector, although the inner reflector is just a single graphite block column with a central irradiation facility or hole. The 18 outer reflector blocks of Ring 4 provide 6 blocks for irradiation test loops and 12 blocks for control rods.

The 18-column core has five radial rings of blocks and a PSR that forms the outer circular geometry of the core, and the core barrel and reactor pressure vessel beyond the PSR. The five core configurations all have the same outer reflector, core barrel, and pressure vessel dimensions. The primary difference between the five configurations is then the number and location of the fuel columns. In addition, the irradiation test facilities and control rod locations in the outer reflector are also different between the five configurations. The central loop facility, however, is common to all configurations.

A full-core 18-column MCNP model would require depletion of all 144 fuel blocks with 210 fuel rods or 30,240 depletion cells. This would be a relatively complex and lengthy calculation. In order to reduce the size and run time of the Monte Carlo depletion calculations, all five core configurations used 1/12-core models instead of the full-core models. These un-rodded models were not only useful for depletion simulations, but also for running large numbers of parametric calculations on the five cores studied to evaluate the core physics characteristics. Parametric design variables and their ranges that were considered in the design evolution of the HTGTR included the following:

(1) Total core power (50-400 MW)
(2) TRISO particle PF (5-50%)
(3) Number of fuel columns (6, 7, 12, or 18)
(4) Number of fuel blocks per column (4, 5, 6, 7, or 8)
(5) Arrangement of the fuel columns in the core.

The thermal-hydraulic analyses provided block-average temperatures for the fuel and graphite reflector blocks. These temperatures were coupled into the MCNP physics models by using the corresponding temperature-dependent, Doppler-broadened, neutron cross-section library data for the specific actinide and fission product nuclides, along with the temperature-dependent thermal neutron scattering data or $S(\alpha,\beta)$ data for the bulk and compact matrix graphite. The fuel rod temperatures and bulk graphite block temperatures were assumed to be constant over the axial length of each block.

## Criticality

The first scoping calculations involved determining how many fuel columns and at what particle PF the core configurations would go critical. The number of fuel columns considered was 6, 7, 12, and 18, or 48, 56, 96, and 144 total fuel blocks in the core, respectively, assuming 8 block-high fuel columns. The ten specific particle PFs considered were 0.05, 0.10, 0.15, 0.20, 0.25, 0.30, 0.35, 0.40, 0.45, and 0.50. Table C-1 gives the beginning-of-cycle fuel block $^{235}$U loadings as a function of PF for the FSV fuel block, plus the total $^{235}$U core loadings for each of the five cores.

Table C-1. FSV fuel block $^{235}$U loading (gram/block) versus PF (%).

| PF | FSV Block $^{235}$U Mass (g/block) | 6-column $^{235}$U Mass (kg/core) | 7-column $^{235}$U Mass (kg/core) | 12-column $^{235}$U Mass (kg/core) | 6+6-column $^{235}$U Mass (kg/core) | 18-column $^{235}$U Mass (kg/core) |
|---|---|---|---|---|---|---|
| 0.05 | 175.21 | 8.41 | 9.81 | 16.82 | 16.82 | 25.23 |
| 0.10 | 350.41 | 16.82 | 19.62 | 33.64 | 33.64 | 50.46 |
| 0.15 | 525.62 | 25.23 | 29.43 | 50.46 | 50.46 | 75.69 |
| 0.20 | 700.83 | 33.64 | 39.25 | 67.28 | 67.28 | 100.92 |
| 0.25 | 876.03 | 42.05 | 49.06 | 84.10 | 84.10 | 126.15 |
| 0.30 | 1,051.24 | 50.46 | 58.87 | 100.92 | 100.92 | 151.38 |
| 0.35 | 1,226.45 | 58.87 | 68.68 | 117.74 | 117.74 | 176.61 |
| 0.40 | 1,401.66 | 67.28 | 78.49 | 134.56 | 134.56 | 201.84 |
| 0.45 | 1,576.86 | 75.69 | 88.30 | 151.38 | 151.38 | 227.07 |
| 0.50 | 1,752.07 | 84.10 | 98.12 | 168.20 | 168.20 | 252.30 |

Figure C-2 is a plot of the core k-effective versus particle PF for the five core configurations. The particle PF is assumed to be the same in all fuel rods and fuel blocks throughout the core. A stainless steel 316L pressure tube was modelled in Ring 1 (inner graphite reflector). This central test loop facility was present in every core configuration and MCNP model. This particular pressure tube had an assumed diameter of 11.43 cm (4.5 in.) and a wall thickness of 1.349 cm (0.531 in.). The other six irradiation loop test facilities in the outer reflector (OR) were assumed to contain a carbon or graphite flow tube. These hypothetical flow tubes had an outer diameter of 10.16 cm (4.0 in.) and a wall thickness of 1.349 cm (0.531 in.). Because these tubes were assumed to be pure carbon, thermal neutron absorption was low and did not impact the overall core reactivity. In later parametric studies, the tube material was changed to include stainless steel (316L) and titanium.

All five cores are critical for PF>5%, except the 6-column core, which only goes critical for PF>9%. As the PF is further increased, the core k-effective continues to increase and reaches a maximum before decreasing. In the case of the 6+6-column core, a maximum k-effective of approximately 1.32 is achieved at a PF between 30 and 35%. This is a reactive core with approximately $35 of positive excess reactivity. The 12- and 18-column cores are similarly reactive at the higher PFs.

Figure C-3 again shows the core k-effective versus PF, but this time with the six carbon tubes in the outer graphite reflector replaced with 1.349 cm (0.531 in.) thick stainless steel 316L pressure tubes for loop facilities. These outer reflector stainless steel tubes correspond to the central loop tube dimensions.
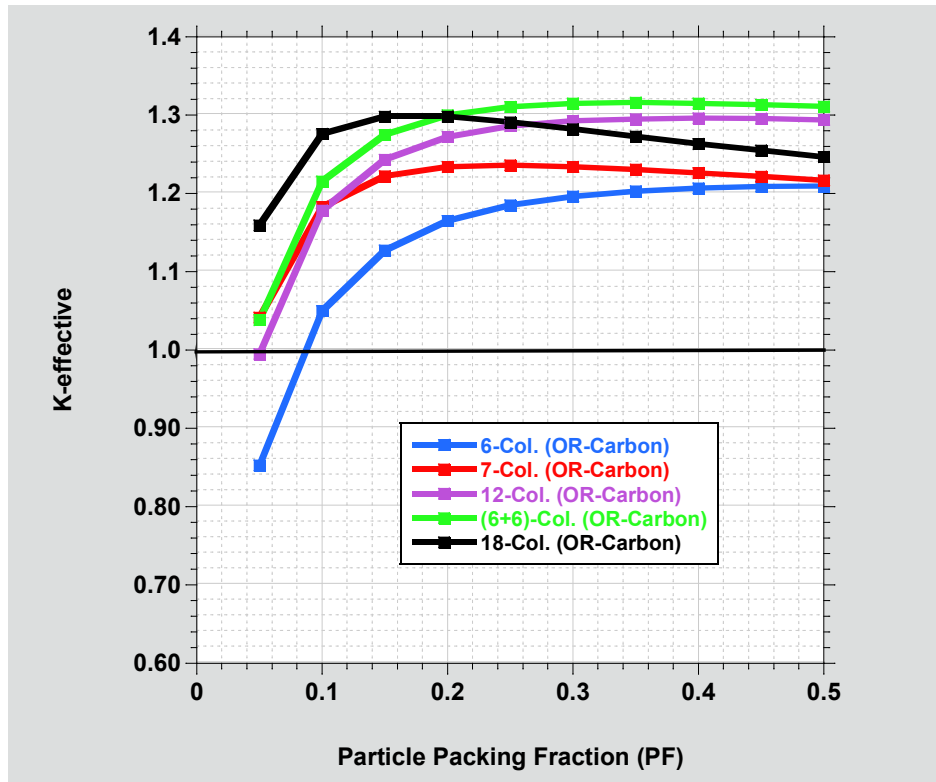
Figure C-2. Core k-effective versus PF for the five core configurations with carbon flow tubes in the outer reflector.
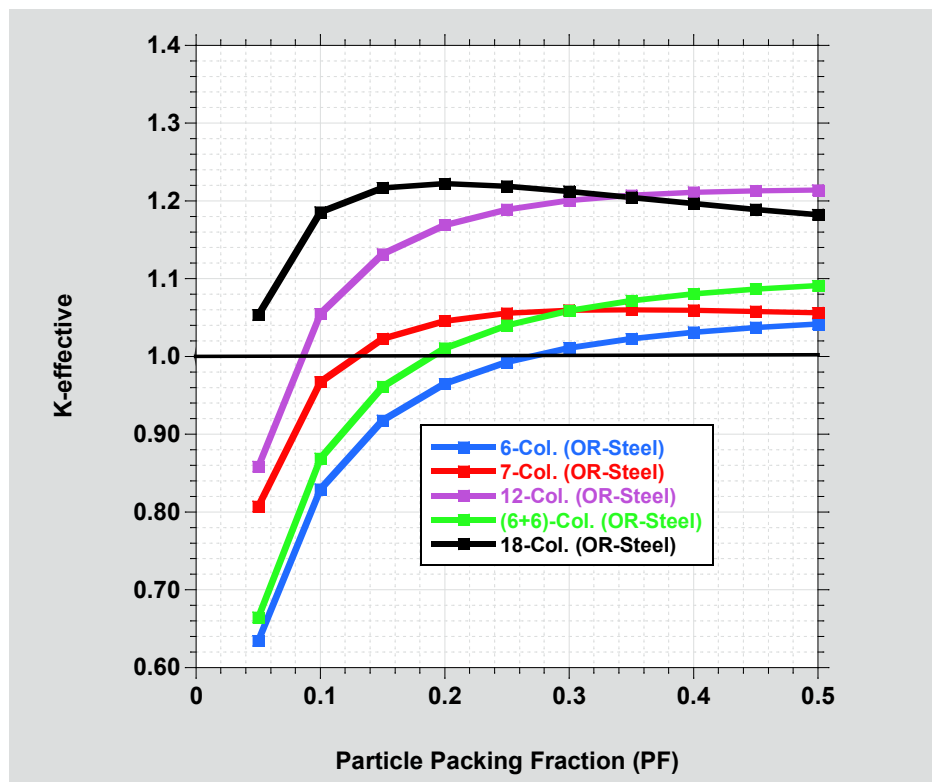


Figure C-3. Core k-effective versus PF for the five core configurations with thick-walled stainless steel (316L) pressure tubes for loop facilities.

The strong thermal neutron absorption of the stainless steel tubes is evident. The thick metallic tubes significantly reduce the core k-effective and the overall core reactivity. The design of the HTGTR will probably have to limit the number of these outer reflector pressure tubes or loop test facilities. In addition, for the non-loop facilities, the wall thickness of any metallic flow tubes should be minimized.

Figure C-4 is a plot of the core k-effective versus total $^{235}$U mass loading in the core for the case of all carbon flow tubes in the outer reflector irradiation positions. The PF variable on the x-axis of these figures has been replaced with the total $^{235}$U core mass loading. These 10-point curves correspond directly to the ten PFs on the matching curves in Figure C-2. From these curves, a rough estimate of the minimum PF for a desired cycle length and total core power can be obtained. As an example, if the total core power is assumed to be 100 MW and the desired cycle length is one year (365 days), approximately 100 g of $^{235}$U will be depleted per day, or approximately 36.5 kg $^{235}$U per year. Therefore, roughly a minimum of 50 kg $^{235}$U in an initial core load will be required to maintain criticality over the cycle. This translates into minimum PFs:

<div style="text-align:center">

6-column core:  PF>30%
7-column core:  PF>25%
12-column core:  PF>15%
6+6-column core:  PF>15%
18-column core:  PF>10%.

</div>

As will be shown later, as the PF decreases, the irradiation flux intensity will increase. Since the primary goal of the HTGTR design is to maximize the irradiation flux, going to smaller PFs will reduce the power cycle length. These three variables need to be balanced in order to optimize the test reactor design.
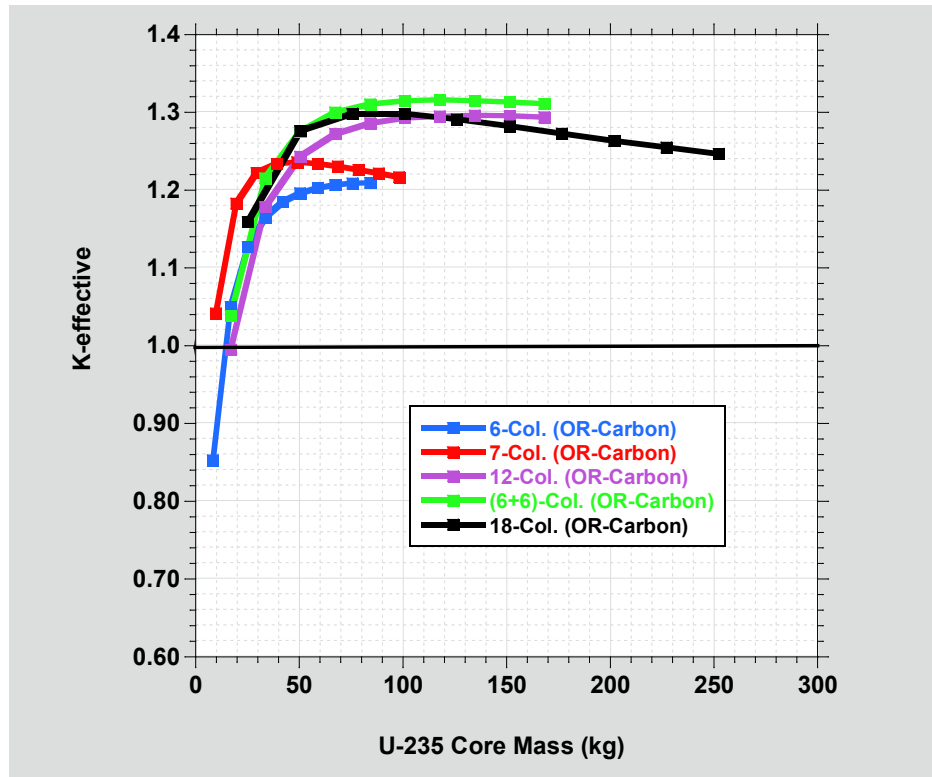


Figure C-4. Core k-effective versus the total $^{235}$U core mass loading for the five core configurations with carbon flow tubes in the outer reflector.

Figure C-5 is again a plot of the core k-effective versus total $^{235}$U mass loading in the core, but this time with stainless steel pressure tubes in the outer reflector irradiation positions. For the same example above, the minimum PFs change as follows:

6-column core:  PF>45%
7-column core:  PF>30%
12-column core:  PF>20%
6+6-column core:  PF>30%
18-column core:  PF>15%.

All PFs must increase to compensate for the loss of reactivity due to the stainless steel pressure tubes. The smaller fuel column cores are impacted the most.
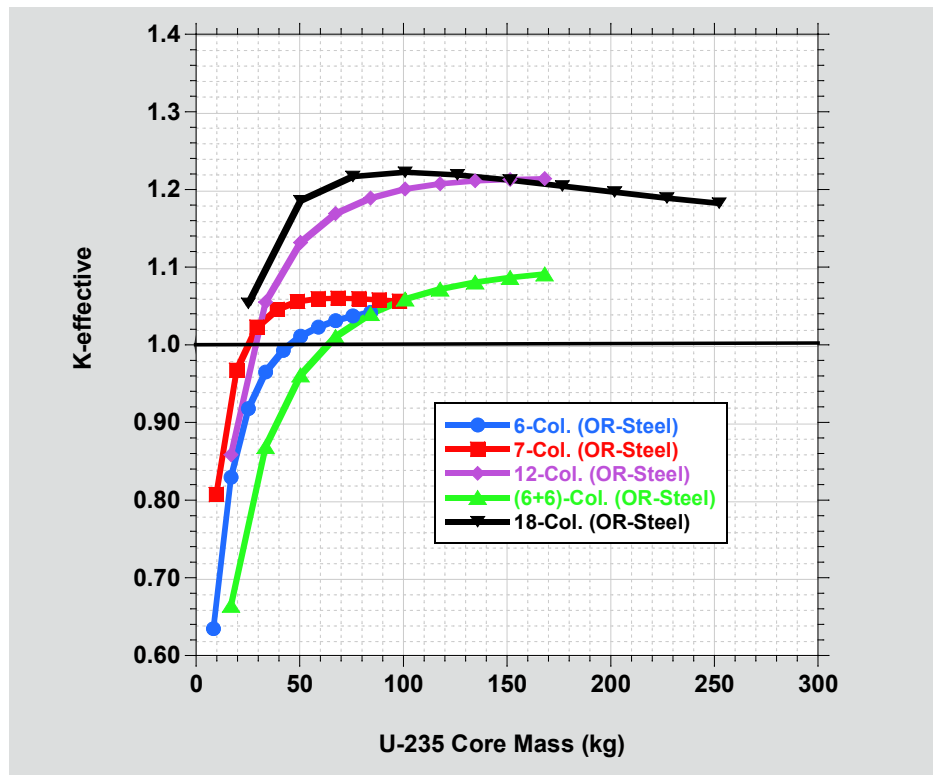


Figure C-5. Core k-effective versus the total $^{235}$U core mass loading for the five core configurations with stainless steel (316L) pressure tubes in the outer reflector.

One additional criticality study was performed to better understand the reactivity consequences of maintaining the 0.6225 cm fuel rod radius from the FSV fuel block design. K-effective was calculated as a function of PF for different fuel rod radii (0.6225, 0.55, 0.50, and 0.40 cm).

Figure C-6 is a plot of k-effective versus PF and fuel rod radius for just the 18-column core with graphite-filled irradiation test positions in the outer reflector. As the fuel rod radius is decreased, the core k-effective maximum increases, and increases substantially for the higher PFs, as noted by the upward shift in the curves. In addition, the curves shift to the right or to higher PFs for decreasing fuel rod radius. For PFs>28%, k-effective clearly increases with decreasing fuel rod radius. For example, at a PF=30%, k-effective increases from 1.31 to 1.37 for fuel radii of 0.6225 and 0.40, respectively. Therefore, maintaining the FSV lattice pitch, but reducing the fuel rod radius, may allow for a boost in core reactivity.
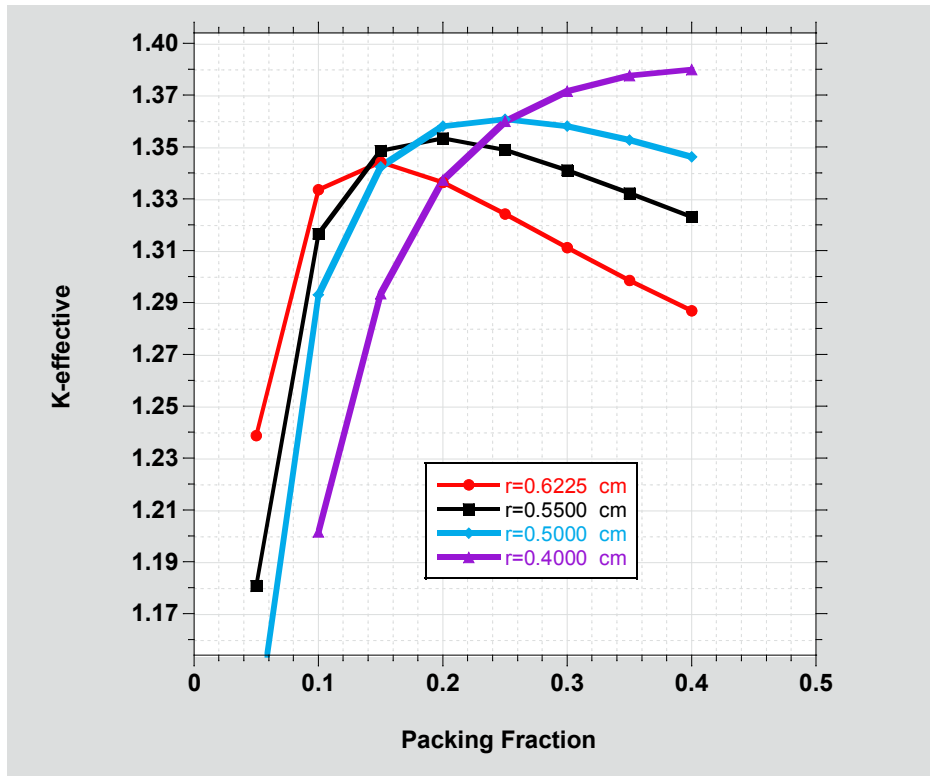
Figure C-6. Core k-effective versus PF and fuel rod radius for the 18-column core.

The triangular lattice pitch and fuel rod radius in the FSV block is typically under-moderated for prismatic core PFs and corresponding [235]U block loadings. Decreasing the fuel rod radius increases the neutron moderation and gives a boost to core reactivity. Therefore, the fuel rod radius could be an optimization parameter in future block and core designs.

## Steel Flow Tubes

The central test facility has preliminarily been designated to be a test loop facility with a pressure boundary isolating it from the test reactor's high-pressure helium primary coolant system. The loop will then require a relatively thick-walled single or double tube system. Currently it is envisioned to be double tube system where test fluids other than helium would enter from the top of the reactor vessel head, flow downward between the inner and outer annuli formed by the two tubes, turn around at the bottom of the outer tube and flow back upward through the inner tube and back out the vessel head. The loop tubes were assumed to be stainless steel (316L) and with a relatively thick outer tube wall thickness of 1.349 cm (0.531 in.).

Although the central facility does not have to be a loop facility, for the HTGTR point design it was decided to make this facility a dedicated loop facility. Therefore, in all point design MCNP models, the central test facility is a loop facility with a thick-walled stainless steel (316L) tube. Other loop facilities can be incorporated into the HTGR point design and in fact, three additional loop facilities have been identified and located in the outer reflector in Ring 4 of the 6+6-column core configuration. These three outer reflector loop facilities have been placed in Ring 4 to relieve potential top head crowding, since the control rods are also located in Rings 3 and 4 of the outer reflector.

The use of stainless steel pressure tubes for loop facilities has a relatively large negative reactivity impact on overall core reactivity, as shown in the section on criticality. The final point design is a relatively reactive core and can easily support four loops. However, the negative reactivity of these four loops will shorten the power cycle length, which could require an increase in PF to increase the

beginning-of-cycle uranium loading and extend the cycle length at the expense of slightly reduced irradiation flux levels.

The k-effective or reactivity impact of the six outer reflector loop pressure tubes (Rings 3 and 4) as a function of tube material for the 18-column core configuration was also calculated. The tube materials considered are carbon, stainless steel, and titanium. Figure C-7 shows core k-effective for the 18-column core with six pressure tubes in the outer reflector (Ring 4) as a function of PF.
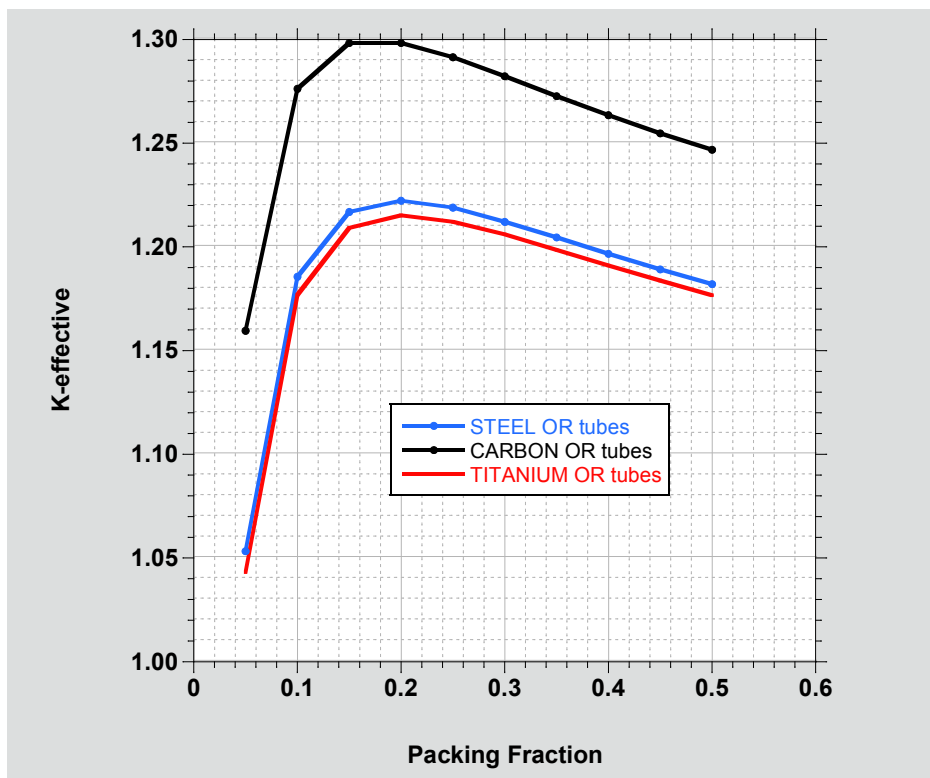


Figure C-7. Core k-effective versus PF and pressure tube material for the 18-column core.

The six stainless steel tubes introduce approximately $6.91 of negative reactivity into the core relative to the carbon tubes. The negative reactivity is relatively insensitive to PF, as noted by the similar curve shapes of both carbon and steel over the PF range. Also, the six titanium pressure tubes would insert almost the same amount of negative reactivity as the stainless steel tubes. An 18-column core with just three stainless steel tubes in the outer reflector (Ring 4) would introduce approximately $3.5 worth of negative reactivity.

Figure C-8 shows core k-effective core versus PF for 0, 6, or 12 stainless steel pressure tubes in the outer reflector (rings 3 and 4) for the 6+6-column core. The blue curve is for zero steel tubes or all carbon tubes, and hence is the most reactive. As stainless steel pressure tubes are added to the outer reflector, six to Ring 4 (black) or six to Ring 3 (red) or six to both Ring 3 and 4 (purple), the curves shift downward as negative reactivity is increased. At a PF=15%, the negative reactivity of six stainless steel tubes in Ring 4 is approximately -$7.9. For the final 6+6-column final point design core with just three stainless steel pressure tubes for loop facilities in the outer graphite reflector, the negative reactivity impact to the core would only be about -$4.0. In a highly reactive core, such as the 6+6-column final point design core with $35 of positive excess reactivity, accommodating the central loop facility, plus an additional three stainless steel pressure tubes would be feasible.

Non-loop flow tubes or non-pressure boundary tubes could be placed in the multitude of other potential irradiation test positions in the outer graphite reflector. These non-pressure tubes could be
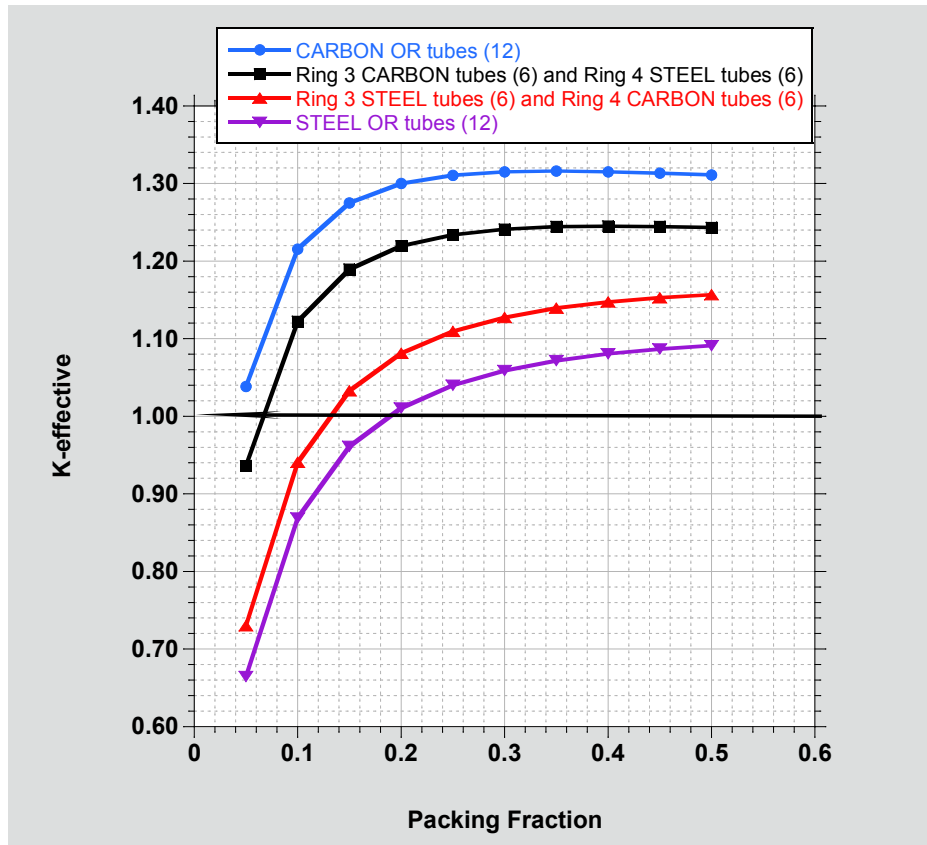
Figure C-8. Core k-effective versus PF and number of carbon versus steel pressure tubes in 12 of the outer reflector irradiation positions for the 6+6-column core.

thinner-walled tubes in order to minimize negative reactivity. With sufficient cooling, thinner-walled stainless steel flow tubes could be used along with tubes made out of titanium or zirconium.

## Irradiation Flux

The magnitudes of the calculated thermal and fast irradiation fluxes are presented for the five core configurations. For each core configuration, fast (>0.1 MeV) and thermal (<2.0 eV) fluxes are calculated at three radial locations: (1) Ring 1 central irradiation loop facility at core center, (2) Ring 3 outer reflector block irradiation positions, and (3) Ring 4 outer reflector block irradiation positions. The irradiation fluxes were calculated parametrically as a function of PF and normalized to a total core power of 100 MW. The five core configurations assume 8-block high fuel columns, a stainless steel pressure tube in the central loop facility, and carbon tubes in the outer reflector blocks. Tables C-2 through C-6 give the thermal and fast irradiation fluxes for the 6, 7, 12, 6+6, and 18-column active core configurations. Note that the fluxes in Table C-5 for the 6+6-column core are doubled for 200-MW operation.

These tables provide a good one-to-one comparison of the thermal and fast fluxes between the five configurations assuming a fixed total core power of 100 MW. In general, the smaller the core or the more compact the core, or the core with the fewest fuel columns, the higher the irradiation flux. In addition, the lower the TRISO particle PF or the smaller the beginning-of-cycle fuel block [235]U mass loading, the higher the irradiation flux. The maximum calculated flux in all irradiation positions occurs at an axial position that lines up with the middle of the fuel block at Level 5, just above the core midplane. This maximum axial flux position is due to both the axial temperature gradient in the core and the lack of control rods (un-rodded condition) in these MCNP models.

130

Table C-2. Maximum thermal and fast flux (n/cm$^2$/s) for the 6-column core.

| PF | Thermal Central Loop Facility (Ring 1) | Fast Central Loop Facility (Ring 1) | Thermal Outer Reflector (Ring 3) | Fast Outer Reflector (Ring 3) | Thermal Outer Reflector (Ring 4) | Fast Outer Reflector (Ring 4) |
|---|---|---|---|---|---|---|
| 0.05 | 3.67E+14 | 6.97E+13 | 7.78E+14 | 3.91E+13 | ---- | ---- |
| 0.10 | 2.11E+14 | 5.52E+13 | 4.60E+14 | 3.22E+13 | ---- | ---- |
| 0.15 | 1.60E+14 | 5.08E+13 | 3.55E+14 | 3.06E+13 | ---- | ---- |
| 0.20 | 1.33E+14 | 4.84E+13 | 3.01E+14 | 2.99E+13 | ---- | ---- |
| 0.25 | 1.18E+14 | 4.73E+13 | 2.69E+14 | 2.97E+13 | ---- | ---- |
| 0.30 | 1.06E+14 | 4.63E+13 | 2.46E+14 | 2.96E+13 | ---- | ---- |
| 0.35 | 9.82E+13 | 4.52E+13 | 2.30E+14 | 2.96E+13 | ---- | ---- |
| 0.40 | 9.25E+13 | 4.46E+13 | 2.18E+14 | 2.97E+13 | ---- | ---- |
| 0.45 | 8.69E+13 | 4.44E+13 | 2.08E+14 | 2.98E+13 | ---- | ---- |
| 0.50 | 8.33E+13 | 4.41E+13 | 2.00E+14 | 3.00E+13 | ---- | ---- |

Table C-3. Maximum thermal and fast flux (n/cm$^2$/s) for the 7-column core.

| PF | Thermal Central Loop Facility (Ring 1) | Fast Central Loop Facility (Ring 1) | Thermal Outer Reflector (Ring 3) | Fast Outer Reflector (Ring 3) | Thermal Outer Reflector (Ring 4) | Fast Outer Reflector (Ring 4) |
|---|---|---|---|---|---|---|
| 0.05 | 7.27E+14 | 1.58E+14 | 6.17E+14 | 2.71E+13 | ---- | ---- |
| 0.10 | 3.49E+14 | 1.31E+14 | 3.82E+14 | 2.48E+13 | ---- | ---- |
| 0.15 | 2.25E+14 | 1.21E+14 | 3.03E+14 | 2.45E+13 | ---- | ---- |
| 0.20 | 1.64E+14 | 1.15E+14 | 2.63E+14 | 2.50E+13 | ---- | ---- |
| 0.25 | 1.28E+14 | 1.11E+14 | 2.39E+14 | 2.55E+13 | ---- | ---- |
| 0.30 | 1.05E+14 | 1.08E+14 | 2.22E+14 | 2.60E+13 | ---- | ---- |
| 0.35 | 8.75E+13 | 1.06E+14 | 2.10E+14 | 2.65E+13 | ---- | ---- |
| 0.40 | 7.54E+13 | 1.04E+14 | 2.01E+14 | 2.69E+13 | ---- | ---- |
| 0.45 | 6.51E+13 | 1.02E+14 | 1.93E+14 | 2.73E+13 | ---- | ---- |
| 0.50 | 5.75E+13 | 1.00E+14 | 1.86E+14 | 2.76E+13 | ---- | ---- |

Table C-4. Maximum thermal and fast flux (n/cm$^2$/s) for the 12-column core.

| PF | Thermal Central Loop Facility (Ring 1) | Fast Central Loop Facility (Ring 1) | Thermal Outer Reflector (Ring 3) | Fast Outer Reflector (Ring 3) | Thermal Outer Reflector (Ring 4) | Fast Outer Reflector (Ring 4) |
|---|---|---|---|---|---|---|
| 0.05 | 1.57E+14 | 1.73E+12 | ---- | ---- | 3.47E+14 | 1.58E+13 |
| 0.10 | 9.98E+13 | 1.47E+12 | ---- | ---- | 2.05E+14 | 1.35E+13 |
| 0.15 | 8.17E+13 | 1.44E+12 | ---- | ---- | 1.57E+14 | 1.29E+13 |
| 0.20 | 7.21E+13 | 1.39E+12 | ---- | ---- | 1.34E+14 | 1.27E+13 |
| 0.25 | 6.61E+13 | 1.40E+12 | ---- | ---- | 1.19E+14 | 1.26E+13 |
| 0.30 | 6.25E+13 | 1.40E+12 | ---- | ---- | 1.09E+14 | 1.27E+13 |
| 0.35 | 5.95E+13 | 1.39E+12 | ---- | ---- | 1.02E+14 | 1.27E+13 |

Table C-4. (continued).

| PF | Thermal Central Loop Facility (Ring 1) | Fast Central Loop Facility (Ring 1) | Thermal Outer Reflector (Ring 3) | Fast Outer Reflector (Ring 3) | Thermal Outer Reflector (Ring 4) | Fast Outer Reflector (Ring 4) |
|---|---|---|---|---|---|---|
| 0.40 | 5.79E+13 | 1.36E+12 | ---- | ---- | 9.63E+13 | 1.29E+13 |
| 0.45 | 5.59E+13 | 1.38E+12 | ---- | ---- | 9.15E+13 | 1.28E+13 |
| 0.50 | 5.46E+13 | 1.39E+12 | ---- | ---- | 8.78E+13 | 1.29E+13 |

Table C-5. Maximum thermal and fast flux (n/cm$^2$/s) for the 6+6-column core.

| PF | Thermal Central Loop Facility (Ring 1) | Fast Central Loop Facility (Ring 1) | Thermal Outer Reflector (Ring 3) | Fast Outer Reflector (Ring 3) | Thermal Outer Reflector (Ring 4) | Fast Outer Reflector (Ring 4) |
|---|---|---|---|---|---|---|
| 0.05 | 1.85E+14 | 3.09E+13 | 4.71E+14 | 3.33E+13 | 3.01E+14 | 1.31E+13 |
| 0.10 | 1.07E+14 | 2.54E+13 | 2.64E+14 | 2.78E+13 | 1.81E+14 | 1.16E+13 |
| 0.15 | 8.02E+13 | 2.32E+13 | 1.95E+14 | 2.62E+13 | 1.41E+14 | 1.14E+13 |
| 0.20 | 6.66E+13 | 2.26E+13 | 1.61E+14 | 2.53E+13 | 1.21E+14 | 1.14E+13 |
| 0.25 | 5.86E+13 | 2.20E+13 | 1.39E+14 | 2.48E+13 | 1.08E+14 | 1.16E+13 |
| 0.30 | 5.30E+13 | 2.14E+13 | 1.24E+14 | 2.44E+13 | 9.94E+13 | 1.17E+13 |
| 0.35 | 4.87E+13 | 2.11E+13 | 1.14E+14 | 2.43E+13 | 9.35E+13 | 1.19E+13 |
| 0.40 | 4.55E+13 | 2.09E+13 | 1.06E+14 | 2.39E+13 | 8.88E+13 | 1.21E+13 |
| 0.45 | 4.31E+13 | 2.06E+13 | 9.95E+13 | 2.38E+13 | 8.51E+13 | 1.22E+13 |
| 0.50 | 4.08E+13 | 2.05E+13 | 9.46E+13 | 2.39E+13 | 8.21E+13 | 1.24E+13 |

Table C-6. Maximum thermal and fast flux (n/cm$^2$/s) for the 18-column core.

| PF | Thermal Central Loop Facility (Ring 1) | Fast Central Loop Facility (Ring 1) | Thermal Outer Reflector (Ring 3) | Fast Outer Reflector (Ring 3) | Thermal Outer Reflector (Ring 4) | Fast Outer Reflector (Ring 4) |
|---|---|---|---|---|---|---|
| 0.05 | 1.27E+14 | 1.95E+13 | ---- | ---- | 2.26E+14 | 9.15E+12 |
| 0.10 | 7.72E+13 | 1.76E+13 | ---- | ---- | 1.42E+14 | 8.74E+12 |
| 0.15 | 5.99E+13 | 1.70E+13 | ---- | ---- | 1.14E+14 | 9.03E+12 |
| 0.20 | 5.14E+13 | 1.68E+13 | ---- | ---- | 1.00E+14 | 9.28E+12 |
| 0.25 | 4.56E+13 | 1.66E+13 | ---- | ---- | 9.14E+13 | 9.55E+12 |
| 0.30 | 4.18E+13 | 1.67E+13 | ---- | ---- | 8.57E+13 | 9.88E+12 |
| 0.35 | 3.91E+13 | 1.67E+13 | ---- | ---- | 8.14E+13 | 1.01E+13 |
| 0.40 | 3.71E+13 | 1.66E+13 | ---- | ---- | 7.83E+13 | 1.05E+13 |
| 0.45 | 3.51E+13 | 1.65E+13 | ---- | ---- | 7.56E+13 | 1.07E+13 |
| 0.50 | 3.32E+13 | 1.66E+13 | ---- | ---- | 7.37E+13 | 1.09E+13 |

The consequence of fewer fuel blocks is higher core power density and a higher average TRISO particle power. The consequence of lower beginning-of-cycle [235]U block mass loading is higher average TRISO particle power. Hence, as the design irradiation flux and power density is increased, TRISO particle temperature and power limits are encountered that ultimately limit the maximum achievable

irradiation flux in the HTGTR. Particle power as a function of core configuration, total core power, and number of fuel block levels will be presented below. Compact fuel temperatures are discussed in the thermal-hydraulic results section.

In general, it is noted that the central irradiation facility has a slightly lower flux than the outer graphite reflector irradiation facilities with the exception of the 7-column core configuration. This is because the outer reflector block irradiation positions are right up against the outer ring of fuel blocks. In the case of the 6+6-column core, the outer reflector irradiation positions (Ring 3) are not only right against the fuel blocks, but are surrounded on four sides by fuel blocks. Plus, these irradiation positions are located in the thermal neutron peak in the outer reflector.

Although not presented here, an interesting observation is that the highest fast flux actually occurs at the centers of the fuel blocks. An irradiation hole in the middle of a fuel block will have a relatively hard spectrum with a 1:1 fast-to-thermal ratio where only 23% of the total flux are thermal neutrons ($E_n$<2.0 eV), whereas the outer reflector holes will have a much softer spectrum with a 1:7 fast-to-thermal ratio and approximately 66% of the total flux being thermal neutrons ($E_n$<2.0 eV). Unfortunately, although this observation would seem to provide the impetus to place irradiation facilities at the fuel block centers, thermal-hydraulic simulations have shown that under off-normal conditions, temperatures would be excessive for metallic structures in these locations.

## Axial Flux Profiles

This section presents examples of both thermal and fast axial flux profiles for the 6+6-column core with 8-block high fuel columns and carbon flow tubes in the outer reflector irradiation positions. Figures C-9 through C-11 are axial thermal flux profiles for the central loop facility, Ring 3 outer reflector irradiation positions, and Ring 4 outer reflector irradiation positions, respectively. Figures C-12 through C-14 are the corresponding axial fast flux profiles. The axial elevation at 0.0 cm is the bottom of the active core or bottom of the Level 1 fuel block and 634.4 cm is the top of the active core or top of the Level 8 fuel block. The axial flux profiles are presented parametrically as a function of PF. Although similar plots were made for the other four core configurations, those plots will not be presented here due to similar-looking axial profile characteristics. The plots here are all for the un-rodded core, hence the cosine-shaped axial profiles.

Core midplane is at 317.2 cm, which is between the top of the Level 4 fuel blocks and the bottom of the Level 5 fuel blocks. The maximum thermal and fast fluxes occur over the axial extent of the Level 5 fuel block due to the axial temperature gradient. The helium coolant flows into the top of the core and then downward through the active core and heats up. Therefore, the active core is cooler at the top and hotter at the bottom. The lower the fuel temperature the more reactive the fuel, which tends to draw power upward to the cooler core regions above midplane, which in turn results in higher fission rates and thermal and fast fluxes above core midplane.

The thermal flux profile curves are relatively smooth, making it hard to discern the individual fuel blocks. The fast flux profiles on the other hand are quite wavy, with individual blocks identified by the flux depressions at the block interfaces.

## Fast Flux Boost

The HTGTR is a thermal reactor. The large graphite mass efficiently moderates fast fission neutrons, thus limiting the test reactor's ability to achieve significant and competitive fast neutron irradiation fluxes. One means to increase the fast flux in the central test loop facility would be to reduce the graphite block density or simply remove graphite mass from the Ring 1 graphite inner reflector blocks. Removing the moderating graphite material between the loop facility and the inside surface of the annular core would allow inward directed fast fission neutrons to reach the central test loop and boost the fast flux in the loop facility. Because the graphite blocks are relatively long at approximately 80 cm in height,
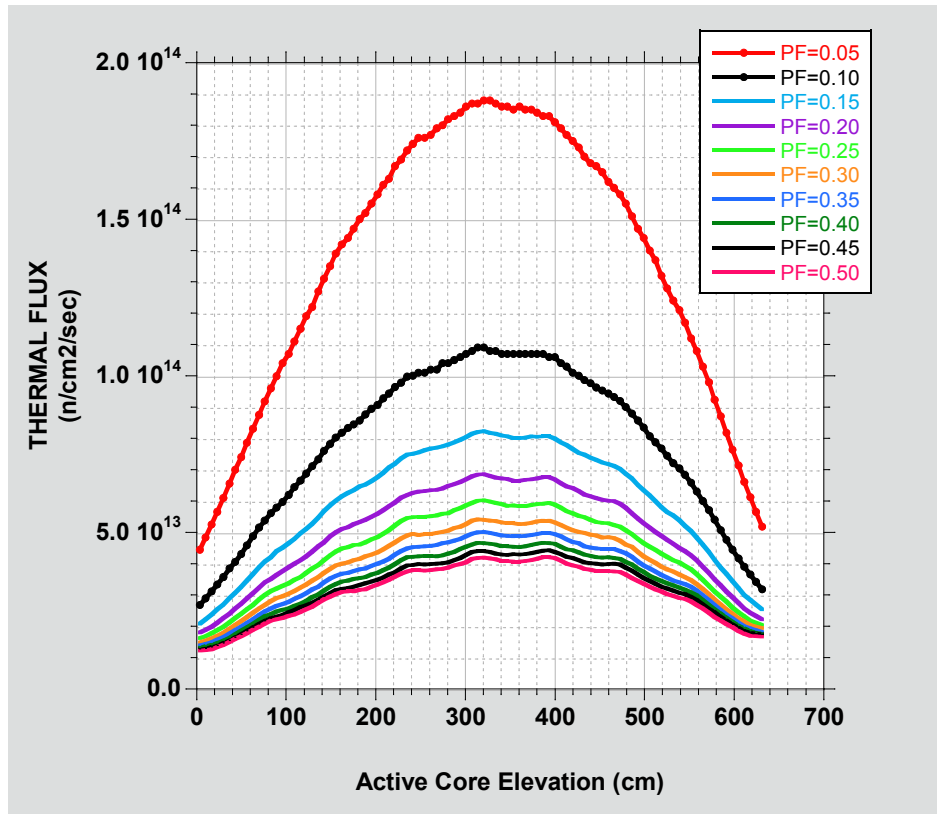
Figure C-9. Thermal neutron axial flux profile in the central loop test facility for the 6+6-column core.
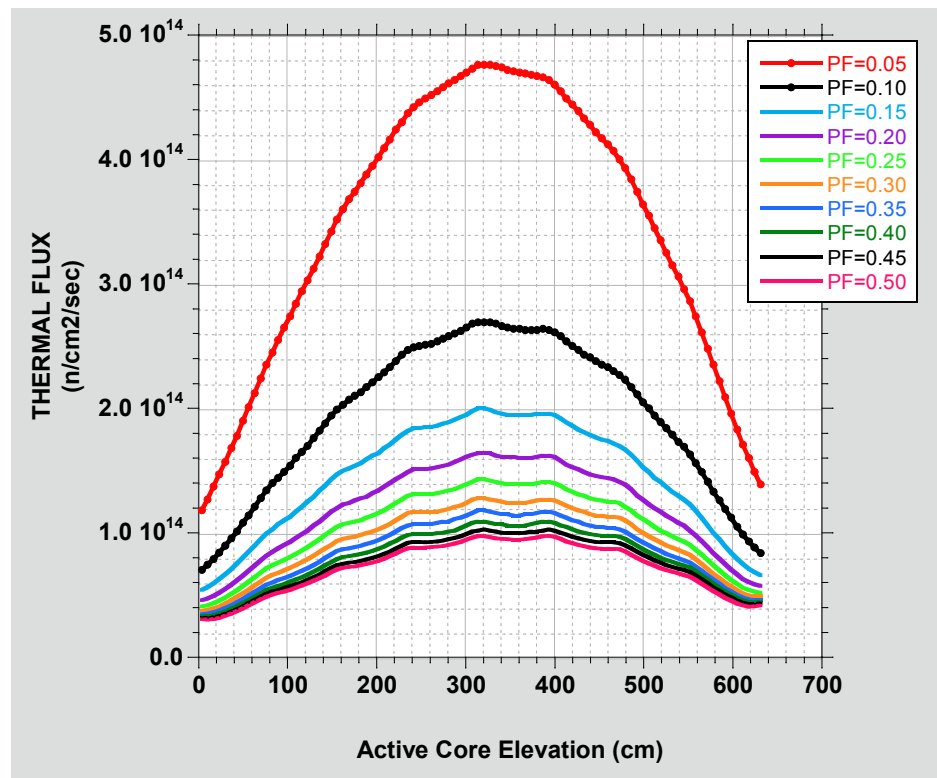


Figure C-10. Thermal neutron axial flux profile in the Ring 3 outer reflector irradiation positions for the 6+6-column core.
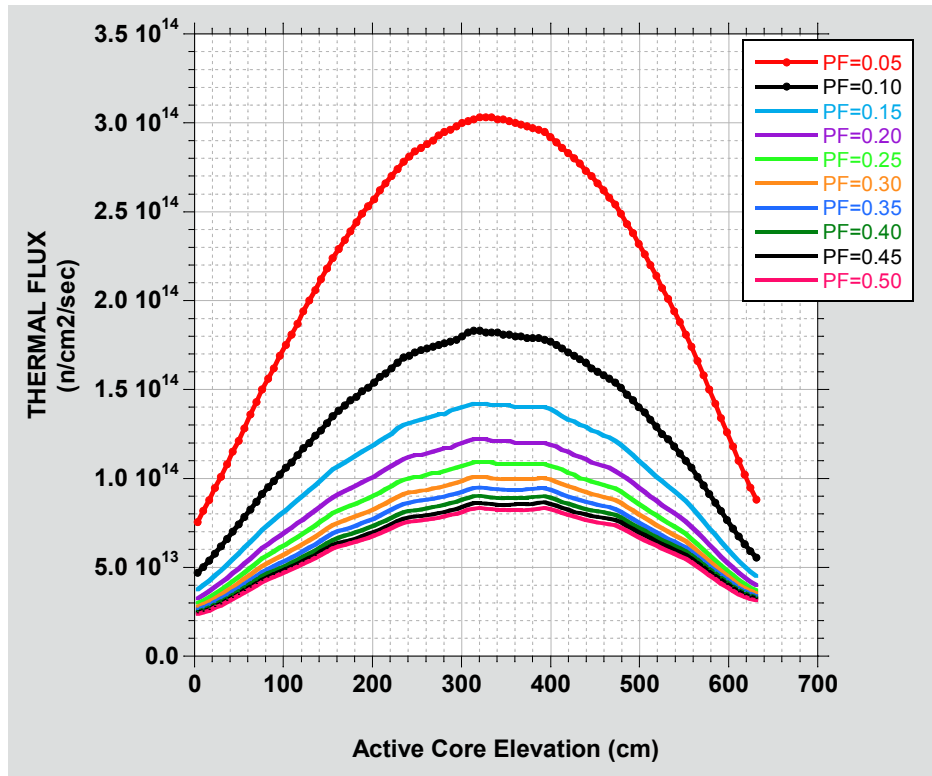
Figure C-11. Thermal neutron axial flux profile in the Ring 4 outer reflector irradiation positions for the 6+6-column core.
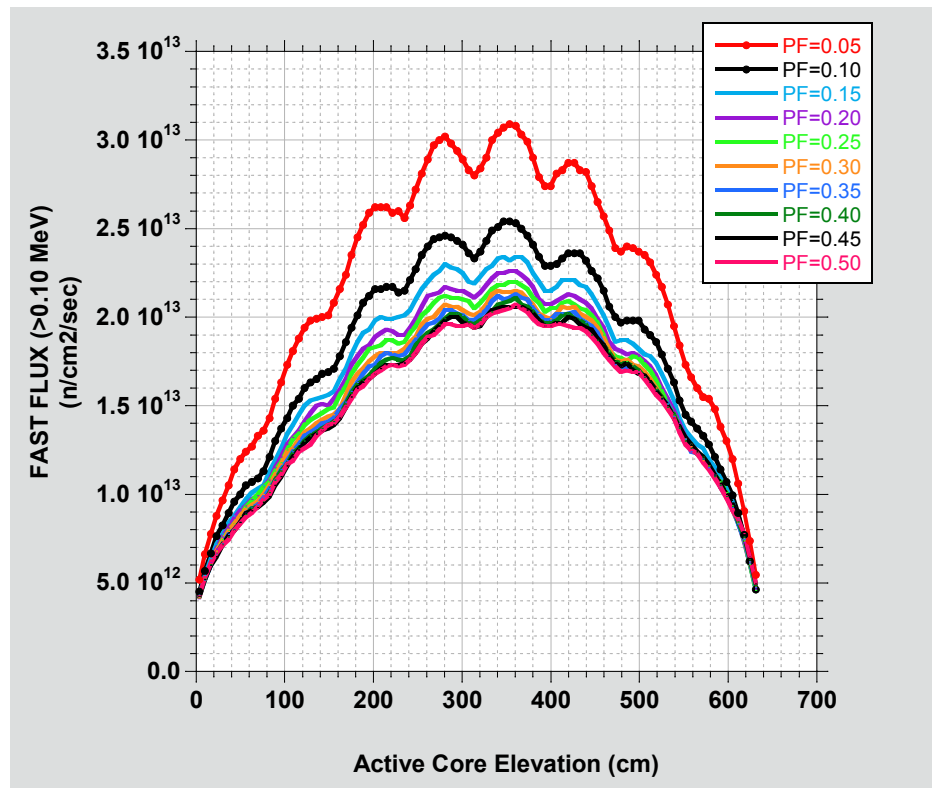


Figure C-12. Fast neutron axial flux profile in the central loop test facility for the 6+6-column core.
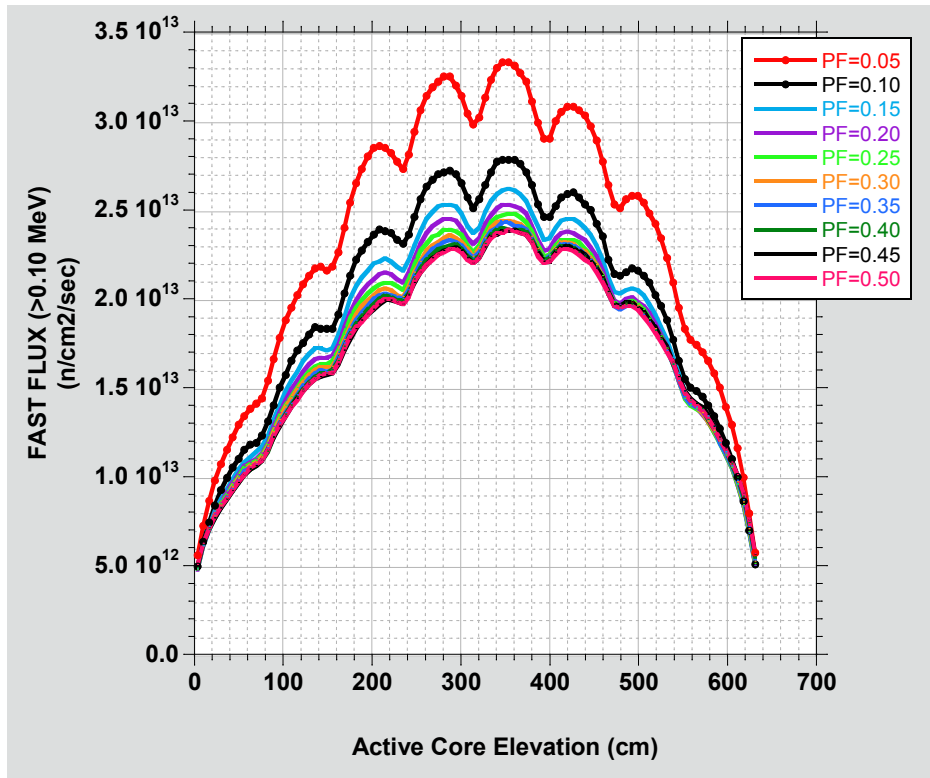
Figure C-13. Fast neutron axial flux profile in the Ring 3 outer reflector irradiation position for the 6+6-column core.
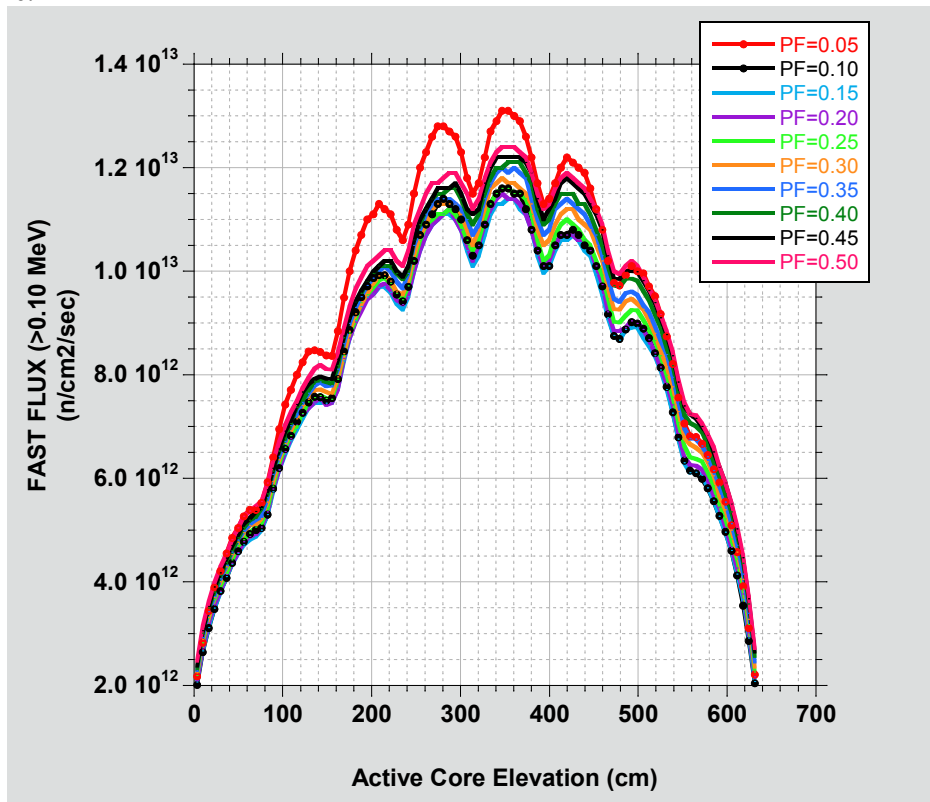


Figure C-14. Fast neutron axial flux profile in the Ring 4 outer reflector irradiation positions for the 6+6-column core.

perhaps some and not all the Ring 1 reflector blocks would need to be special reduced graphite blocks, it would depend on the central loop experiment needs.

To demonstrate the maximum achievable fast flux increase in the central loop facility, the graphite was removed from the Ring 1 graphite blocks surrounding the central test loop facility in the 6+6-column core for PF=15% and 100 MW total core power. Table C-7 presents the thermal and fast fluxes in the central loop facility and the outer reflector irradiation positions in Ring 3 and Ring 4. The first row of data is for the core with normal or full density graphite blocks in Ring 1 and the second row with graphite completely removed from the Ring 1 graphite blocks. Thermal and fast fluxes in the outer reflector remain relatively unchanged, but the fast flux ($E_n > 0.1$ MeV) in the central loop increases by a factor of >2.5. This is a significant increase in the available fast flux. Presumably similar results could be obtained in the outer reflector blocks in Ring 3 which are surrounded on four sides by fuel blocks. Doubling the core power to 200 MW, the maximum fast flux is approximately 1.17E+14 n/cm$^2$/s.

Table C-7. Maximum thermal and fast flux (n/cm$^2$/s) for the 6+6-column core with reduced graphite.

| Ring 1 Inner Reflector Graphite | Thermal Central Loop Facility (Ring 1) | Fast Central Loop Facility (Ring 1) | Thermal Outer Reflector (Ring 3) | Fast Outer Reflector (Ring 3) | Thermal Outer Reflector (Ring 4) | Fast Outer Reflector (Ring 4) |
|---|---|---|---|---|---|---|
| Normal | 8.02E+13 | 2.32E+13 | 1.95E+14 | 2.62E+13 | 1.41E+14 | 1.14E+13 |
| Reduced | 7.21E+13 | 5.84E+13 | 2.04E+14 | 2.67E+13 | 1.49E+14 | 1.21E+13 |

### Thermal-to-Fast Ratios

The HTGTR is a thermal reactor and thermal neutrons tend to dominate throughout the core. Thermal-to-fast flux ratios should therefore be expected to be slanted in favor of the thermal neutrons. In this section thermal-to-fast flux ratios are presented for the 6+6-column core; these ratios are typical of the other four core configurations as well. Also, the ratios are relatively constant over the axial length of the active core. Table C-8 gives the thermal-to-fast flux ratios for the central test loop facility in Ring 1 and the outer reflector irradiation positions in both Ring 3 and Ring 4.

Table C-8. Thermal-to-fast flux ratios for the 6+6-column core.

| Central Loop Facility (Ring 1) | Outer Reflector (Ring 3) | Outer Reflector (Ring 4) |
|---|---|---|
| 4.2 | 9.0 | 14.7 |

The central loop facility has the smallest ratio, or hardest neutron spectrums. If graphite is removed from the Ring 1 inner graphite reflector blocks, the thermal-to-fast flux ratio can get as small as 1.4 for complete graphite removal from these blocks.

## Test Loop Fluids

Part of the HTGTR mission is to irradiate other advanced reactor technologies, including alternative coolant fluids which might include: (1) liquid sodium, (2) liquid salts, (3) light water, and (4) helium and other gases including steam. This study evaluated the reactivity impact of some of these fluids on the 6+6-column core with 8-block high fuel columns and a PF=35%. These alternative fluids were placed in the central test loop facility at prototypical fluid conditions for the intended reactor. Fluid operating conditions and density are given in Table C-9 along with the MCNP-calculated core k-effective and corresponding reactivity change.

The core reactivity impact is negative and relatively small in magnitude for all five fluids considered. Liquid sodium and enriched FLiBe have essentially a negligible reactivity impact. The higher thermal neutron absorbing FLiBe with natural lithium (7.5 atom percent $^6$Li) and light water with hydrogen result in less than $1.50 in negative reactivity. Other gas coolants (e.g. He, $CO_2$, steam) are expected to have negligible reactivity impacts too. The HTGTR helium coolant served as the reactivity baseline.

Table C-9. Coolant fluid properties and reactivity impact on the 6+6-column core.

| Fluid | Temperature (°C) | Pressure (MPa) | Density (g/cm3) | Core k-effective | Reactivity ($) |
|---|---|---|---|---|---|
| Helium | 600 | 7.12 | 0.003194 | 1.316085 | ---- |
| Na | 327 | 0.1014 | 0.927 | 1.314354 | -0.11 |
| FLiBe[a] | 548 | 0.3 | 2.012 | 1.297682 | -1.48 |
| FLiBe[b] | 548 | 0.3 | 2.012 | 1.314099 | -0.16 |
| H2O | 329 | 15.0 | 0.654 | 1.300288 | -1.26 |

a: LiF-BeF$_2$ natural lithium
b: LiF-BeF$_2$ enriched lithium (enriched in $^7$Li to 99.99%)

## Core-Average Particle Powers

Particle power is an important parameter to consider when boosting core power density. Excessive particle powers lead to excessive kernel burnups and particle temperatures that can lead to particle failures. Balancing particle, compact, and fuel rod power throughout the core will lead to a more uniform burnup and temperature distributions, extending particle in-core life and integrity. A single TRISO particle has a 400-mW power limit.

The core average particle power here is simply calculated by dividing the total core power by the total number of TRISO fuel particles in the core, and for the five core comparison, the total core power will be assumed to be 100-MW total core power and 8-block high fuel columns. Tables C-10 through C-14 give the core-average particle powers for the five core configurations as a function of PF.

In all cases, as expected, the core-average particle powers decrease with increasing PF. The greater the number of particles in the core, the lower the average power load on each individual particle. This is also emphasized by the fact that the 6-column core has the highest average particle powers of the five cores at a given PF. The 6-column core has only 48 fuel blocks. At the PF=0.05, the average particle power is 739 mW/particle or well above the 400-mW threshold. However, for PF≥0.20, the core-average particle powers are all <200 mW or comfortably below the 400-mW limit for all cores. The 6+6-column core with a PF=15% would have an average particle power of just 123 mW/particle.

Table C-10. Average TRISO fuel particle power estimates in the 6-column core.

| PF | Total Number of Particles in Core | Particle Power (mW/particle) |
|---|---|---|
| 0.05 | 1.3534E+08 | 739 |
| 0.10 | 2.7069E+08 | 369 |
| 0.15 | 4.0603E+08 | 246 |
| 0.20 | 5.4137E+08 | 185 |
| 0.25 | 6.7672E+08 | 148 |
| 0.30 | 8.1206E+08 | 123 |
| 0.35 | 9.4740E+08 | 106 |
| 0.40 | 1.0827E+09 | 92 |
| 0.45 | 1.2181E+09 | 82 |
| 0.50 | 1.3534E+09 | 74 |

Table C-11. Average TRISO fuel particle power estimates in the 7-column core.

| PF | Total Number of Particles in Core | Particle Power (mW/particle) |
|---|---|---|
| 0.05 | 1.5790E+08 | 633 |
| 0.10 | 3.1580E+08 | 317 |
| 0.15 | 4.7370E+08 | 211 |
| 0.20 | 6.3160E+08 | 158 |
| 0.25 | 7.8950E+08 | 127 |
| 0.30 | 9.4740E+08 | 106 |
| 0.35 | 1.1053E+09 | 90 |
| 0.40 | 1.2632E+09 | 79 |
| 0.45 | 1.4211E+09 | 70 |
| 0.50 | 1.5790E+09 | 63 |

Table C-12. Average TRISO fuel particle power estimates in the 12-column core.

| PF | Total Number of Particles in Core | Particle Power (mW/particle) |
|---|---|---|
| 0.05 | 2.7069E+08 | 369 |
| 0.10 | 5.4137E+08 | 185 |
| 0.15 | 8.1206E+08 | 123 |
| 0.20 | 1.0827E+09 | 92 |
| 0.25 | 1.3534E+09 | 74 |
| 0.30 | 1.6241E+09 | 62 |
| 0.35 | 1.8948E+09 | 53 |
| 0.40 | 2.1655E+09 | 46 |
| 0.45 | 2.4362E+09 | 41 |
| 0.50 | 2.7069E+09 | 37 |

Table C-13. Average TRISO fuel particle power estimates in the 6+6-column core.

| PF | Total Number of Particles in Core | Particle Power (mW/particle) |
|---|---|---|
| 0.05 | 2.7069E+08 | 369 |
| 0.10 | 5.4137E+08 | 185 |
| 0.15 | 8.1206E+08 | 123 |
| 0.20 | 1.0827E+09 | 92 |
| 0.25 | 1.3534E+09 | 74 |
| 0.30 | 1.6241E+09 | 62 |
| 0.35 | 1.8948E+09 | 53 |
| 0.40 | 2.1655E+09 | 46 |
| 0.45 | 2.4362E+09 | 41 |
| 0.50 | 2.7069E+09 | 37 |

Table C-14. Average TRISO fuel particle power estimates in the 18-column core.

| PF | Total Number of Particles in Core | Particle Power (mW/particle) |
|---|---|---|
| 0.05 | 4.0603E+08 | 246 |
| 0.10 | 8.1206E+08 | 123 |
| 0.15 | 1.2181E+09 | 82 |
| 0.20 | 1.6241E+09 | 62 |
| 0.25 | 2.0301E+09 | 49 |
| 0.30 | 2.4362E+09 | 41 |
| 0.35 | 2.8422E+09 | 35 |
| 0.40 | 3.2482E+09 | 31 |
| 0.45 | 3.6543E+09 | 27 |
| 0.50 | 4.0603E+09 | 25 |

The core-average particle power is relatively sensitive to the PF variable and will be useful for future fine-tuning of the HTGTR core.

By multiplying the core-average particle powers in this section by the fuel rod power-peaking factors in the next section, a maximum or peak particle power can be obtained. Peak TRISO fuel particle powers are constrained to be ≤400 mW.

## Power-Peaking Factors

Fuel rod power-peaking is an important physics parameter. A core power map of each fuel rod power can be used to identify regions of the core that have the potential to over-power TRISO particle compacts and lead to excessive TRISO particle powers. In the design of the HTGTR, a maximum TRISO particle power design constraint of <400 mW per particle has been established. This constraint basically limits core power density and in turn constrains the maximum achievable irradiation fluxes.

Using the five MCNP core models with carbon tubes in all the outer reflector irradiation positions, it is possible to calculate the average fuel rod power in every fuel block in each core and derive a peak-to-average value or power-peaking factor for each fuel rod. Mitigation of power-peaking and peak particle power can be accomplished through coordinated strategic placement of burnable poisons in the corner positions of the hexagonal fuel blocks along the core-reflector interfaces and appropriate particle PF grading in the first four rows of fuel pins at the interface.

Table C-15 gives the maximum power-peaking factor in each of the five cores as a function of PF. The greatest power-peaking occurs at the core-reflector interfaces; the maximum can occur at either interface. For example, maximum power-peaking occurs at the inner core-reflector interface for the 12-column core and at the outer core-reflector interface for the 6-column and 18-column cores. The peak rod is typically near the corner of a fuel block whose corner is projected the furthest into the graphite reflector.

Maximum or peak particle powers can be estimated by multiplying the core-average particle powers estimated in the last section by the power-peaking factors or peak-to-average fuel rod powers presented in this section. As an example, the maximum or peak particle power for the 6+6-column core with 8-block high fuel columns and a PF=0.15 is 202 mW based on a core-average particle power of 123 mW/particle (Table C-13) and a peak-to-average fuel rod power of 1.64 (Table C-15). The maximum or peak TRISO particle power then is estimated to be (123 mW/particle)x(1.64) = 202 mW per particle. This 202 mW peak particle power is based on the 6+6-column core operating at 100 MW.

Mitigation of power-peaking and peak particle power can be accomplished through coordinated strategic placement of burnable poisons in the corner positions of the hexagonal fuel blocks along the core-reflector interfaces and appropriate particle PF grading in the first four rows of fuel pins at the interface.

Table C-15. Fuel rod maximum peak-to-average powers for the five core configurations with 8-block high fuel columns.

| PF | 6-column | 7-column | 12-column | 6+6-column | 18-column |
|---|---|---|---|---|---|
| 0.05 | 1.46 | 1.44 | 1.63 | 1.57 | 1.44 |
| 0.10 | 1.56 | 1.54 | 1.77 | 1.59 | 1.56 |
| 0.15 | 1.71 | 1.69 | 1.90 | 1.64 | 1.72 |
| 0.20 | 1.78 | 1.83 | 2.01 | 1.75 | 1.88 |
| 0.25 | 1.88 | 1.96 | 2.13 | 1.85 | 2.01 |
| 0.30 | 1.96 | 2.09 | 2.23 | 1.94 | 2.15 |
| 0.35 | 2.05 | 2.20 | 2.32 | 2.04 | 2.27 |
| 0.40 | 2.13 | 2.31 | 2.42 | 2.12 | 2.38 |
| 0.45 | 2.21 | 2.41 | 2.50 | 2.20 | 2.50 |
| 0.50 | 2.28 | 2.50 | 2.59 | 2.27 | 2.60 |

## Fuel Column Height

The 8-block high fuel column was initially based on preliminary thermal-hydraulic considerations. An 8-block high fuel column of FSV blocks makes the active core height 6.34 m (~20 ft). It was recognized that a shorter core with fewer than 8-block high fuel columns could have beneficial attributes, particularly in terms of achieving higher core power densities which in turn would produce higher irradiation fluxes for the same total core power. In addition, a reduction in the number of core fuel blocks would reduce fuel costs and shorten re-fueling times. Also, a shorter core could potentially make loading and unloading experiments easier and reduce the length of the control rods. Higher core power densities would, however, potentially reduce the power cycle length, but increases in PF would be able to extend the cycle length at moderate penalty in irradiation flux intensity. The potential benefits of a reduced core height were worth exploring.

The fuel column height study here focused primarily on the 6+6-column core configuration. The 6+6-column core configuration had emerged as the most viable and highest scoring configuration relative to the four core configurations. For this study, the 6+6-column core configuration was evaluated with fuel column heights of 1, 2, 3, 4, 5, 6, 7, and 8-blocks (levels) and PFs of 0.15, 0.25, 0.35, and 0.45. This study was intended mainly to determine the minimum number of fuel blocks and PF that could achieve criticality and sufficient uranium loadings to achieve a 90-day operating cycle.

Figure C-15 shows the core k-effective versus the fuel block levels or number of fuel blocks stacked vertically in each fuel column. It is clear that 1 and 2 block high fuel column in all cores will simply not go critical for the PF range considered. Sensitivity to PF appears to be very small. Although the 3-block high cores will go critical, the fuel block loading for PF=15 to 25% is too low to sustain a >90-day fuel cycle length at 100 MW. The 4-block high core at a PF=15% is the minimum core height and PF that can reach a >90-day fuel cycle length at 100 MW. PFs greater than 15% can also reach a >90-day fuel cycle length at 100 MW, but the thermal and fast irradiation fluxes are slightly lower.

Table C-16 gives the total core $^{235}$U mass loading as a function of fuel column height or number of stacked fuel blocks and PF. The numbers highlighted in red are cores that could potentially sustain a >90 day fuel cycle length at 100 MW. Of these cores, those with the lowest PFs will have higher

irradiation fluxes; for example, the 4-block high core with PF=15% will have the highest fast and thermal irradiation fluxes.
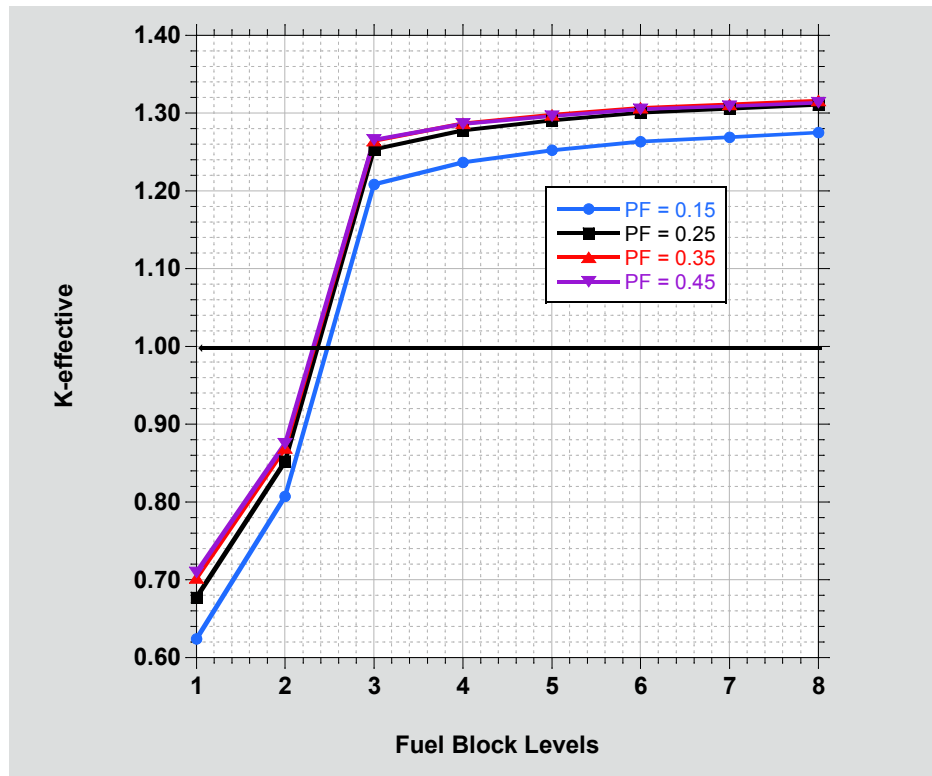


Figure C-15. Core k-effective versus fuel block levels and PF.

Table C-16. Core loading (kg $^{235}$U) versus fuel column block height and PF.

| PF | Fuel Column Block Height | | | | | | | |
|------|-------|-------|-------|-------|-------|--------|--------|--------|
| | 1 | 2 | 3 | 4 | 5 | 6 | 7 | 8 |
| 0.15 | 6.31 | 12.61 | 18.92 | **25.23** | **31.54** | **37.84** | **44.15** | **50.46** |
| 0.20 | 8.41 | 16.82 | **25.23** | **33.64** | **42.05** | **50.46** | **58.87** | **67.28** |
| 0.25 | 10.51 | 21.02 | **31.54** | **42.05** | **52.56** | **63.07** | **73.59** | **84.10** |
| 0.30 | 12.61 | 25.23 | **37.84** | **50.46** | **63.07** | **75.69** | **88.30** | **100.92** |
| 0.35 | 14.72 | 29.43 | **44.15** | **58.87** | **73.59** | **88.30** | **103.02** | **117.74** |
| 0.40 | 16.82 | 33.64 | **50.46** | **67.28** | **84.10** | **100.92** | **117.74** | **134.56** |
| 0.45 | 18.92 | 37.84 | **56.77** | **75.69** | **94.61** | **113.53** | **132.46** | **151.38** |

Another interesting parametric investigation was the calculation of the maximum thermal and fast irradiation fluxes for different fuel column heights and PFs at 100 MW total core power. The calculated results will be presented for just the 6+6-column core configuration. The variable ranges include: (1) fuel column height (number of fuel blocks) from 3-8 block-high columns and (2) PF from 0.15 to 0.45. Both fast flux (>0.1 MeV) and thermal flux (<2.0 eV) are presented in Tables C-17 through C-19 for the central test loop facility with stainless steel pressure tube and Ring 3 and Ring 4 outer reflector irradiation positions with carbon flow tubes, respectively.

The thermal and fast irradiation fluxes increase as both active core height and PF decrease. At a fixed total core power of 100 MW, as the core height decreases, the core power density increases which in turn leads to increased irradiation fluxes. Since maximizing the irradiation flux was the main physics design goal, reducing the core height from 8 to 4 fuel blocks became a clear direction to investigate. The

Table C-17. Maximum thermal and fast irradiation fluxes in the central test loop facility for different fuel column heights and PF.

| | Maximum Thermal Flux (n/cm$^2$/s) | | | | Maximum Fast Flux (n/cm$^2$/s) | | | |
|---|---|---|---|---|---|---|---|---|
| Levels | PF=15% | PF=25% | PF=35% | PF=45% | PF=15% | PF=25% | PF=35% | PF=45% |
| 8 | **8.24E+13** | 6.02E+13 | 5.02E+13 | 4.41E+13 | 2.34E+13 | 2.20E+13 | 2.13E+13 | 2.06E+13 |
| 7 | 9.29E+13 | 6.80E+13 | 5.67E+13 | 5.04E+13 | 2.67E+13 | 2.48E+13 | 2.36E+13 | 2.30E+13 |
| 6 | 1.06E+14 | 7.76E+13 | 6.49E+13 | 5.71E+13 | 3.04E+13 | 2.82E+13 | 2.75E+13 | 2.64E+13 |
| 5 | 1.23E+14 | 9.07E+13 | 7.55E+13 | 6.65E+13 | 3.62E+13 | 3.36E+13 | 3.21E+13 | 3.12E+13 |
| 4 | **1.53E+14** | 1.11E+14 | 9.29E+13 | 8.17E+13 | 4.35E+13 | 4.01E+13 | 3.89E+13 | 3.75E+13 |
| 3 | 1.93E+14 | 1.39E+14 | 1.15E+14 | 1.01E+14 | 5.85E+13 | 5.37E+13 | 5.11E+13 | 4.96E+13 |

Table C-18. Maximum thermal and fast irradiation fluxes in the Ring 3 outer graphite reflector irradiation positions for different fuel column heights and PF.

| | Maximum Thermal Flux (n/cm$^2$/s) | | | | Maximum Fast Flux (n/cm$^2$/s) | | | |
|---|---|---|---|---|---|---|---|---|
| Levels | PF=15% | PF=25% | PF=35% | PF=45% | PF=15% | PF=25% | PF=35% | PF=45% |
| 8 | **2.00E+14** | 1.43E+14 | 1.18E+14 | 1.03E+14 | 2.62E+13 | 2.48E+13 | 2.33E+13 | 2.29E+13 |
| 7 | 2.26E+14 | 1.62E+14 | 1.33E+14 | 1.17E+14 | 2.95E+13 | 2.79E+13 | 2.71E+13 | 2.67E+13 |
| 6 | 2.58E+14 | 1.84E+14 | 1.51E+14 | 1.32E+14 | 3.36E+13 | 3.17E+13 | 3.03E+13 | 2.98E+13 |
| 5 | 2.98E+14 | 2.13E+14 | 1.75E+14 | 1.53E+14 | 4.01E+13 | 3.78E+13 | 3.66E+13 | 3.59E+13 |
| 4 | **3.67E+14** | 2.62E+14 | 2.15E+14 | 1.88E+14 | 4.79E+13 | 4.47E+13 | 4.34E+13 | 4.28E+13 |
| 3 | 4.56E+14 | 3.22E+14 | 2.63E+14 | 2.30E+14 | 6.44E+13 | 5.99E+13 | 5.79E+13 | 5.68E+13 |

Table C-19. Maximum thermal and fast irradiation fluxes in the Ring 4 outer graphite reflector irradiation positions for different fuel column heights and PF.

| | Maximum Thermal Flux (n/cm$^2$/s) | | | | Maximum Fast Flux (n/cm$^2$/s) | | | |
|---|---|---|---|---|---|---|---|---|
| Levels | PF=15% | PF=25% | PF=35% | PF=45% | PF=15% | PF=25% | PF=35% | PF=45% |
| 8 | **1.42E+14** | 1.09E+14 | 9.49E+13 | 8.65E+13 | 1.14E+13 | 1.12E+13 | 1.14E+13 | 1.22E+13 |
| 7 | 1.60E+14 | 1.24E+14 | 1.07E+14 | 9.80E+13 | 1.29E+13 | 1.31E+13 | 1.34E+13 | 1.37E+13 |
| 6 | 1.82E+14 | 1.40E+14 | 1.22E+14 | 1.11E+14 | 1.46E+13 | 1.45E+13 | 1.49E+13 | 1.56E+13 |
| 5 | 2.10E+14 | 1.61E+14 | 1.40E+14 | 1.27E+14 | 1.75E+13 | 1.76E+13 | 1.79E+13 | 1.84E+13 |
| 4 | **2.56E+14** | 1.96E+14 | 1.70E+14 | 1.55E+14 | 2.06E+13 | 2.07E+13 | 2.11E+13 | 2.18E+13 |
| 3 | 3.18E+14 | 2.42E+14 | 2.08E+14 | 1.89E+14 | 2.74E+13 | 2.74E+13 | 2.79E+13 | 2.84E+13 |

maximum thermal fluxes in these tables almost doubled (red highlighted values in each table) in going from 8- down to 4-block high cores as might be expected. For the 6+6-column core configuration, the peak TRISO particle power, however, would also double to approximately 404 mW per particle, or at the 400-mW limit. However, the thermal-hydraulic analysis predicted fuel temperatures in excess of the 1250°C maximum fuel temperature limit for this core.

The thermal irradiation flux (3.67E+14 n/cm$^2$/s) in Ring 3 of the 4-block high 6+6-column core (PF=15%) is, however, competitive with the Advanced Test Reactor and the High-Flux Isotope Reactor and therefore a potentially attractive and desirable feature for the HTGTR. But because the predicted fuel temperatures exceeded 1250°C, the 4-block high core was not feasible. However, the same high thermal flux can be obtained with the 8-block high core by doubling the total core power from 100 to 200 MW. Now the maximum fuel temperatures are below the 1250 °C limit, and this particular core design became the final HTGTR point design. This final core design can, however, certainly be optimized further.

## Fuel Cycle Length

A fuel cycle length >90-days satisfied the maximum design metric. The HTGTR was assumed to operate in a single-batch fuel cycle mode; reloading of used fuel blocks was not considered.

Detailed depletion calculations were delayed until near the end of the design when the final 6+6-column HTGTR design began to mature. The bulk of the physics parametric design studies were performed prior to the detailed depletion studies. This was done for two reasons: detailed depletion calculations are complex and time-consuming, and reasonable estimates of cycle length could be obtained directly from the criticality studies. These estimates used the fuel block and core mass loadings of $^{235}$U for the assumed total core power and estimated $^{235}$U depletion rates over a 90-day period. Detailed depletion calculations were used primarily to obtain exact cycle lengths for the final 6+6-column designs and to verify the cycle lengths for the other core configurations. It should be noted that the approximate cycle length estimates proved to be quite accurate when ultimately compared to the detailed depletion calculations.

The detailed depletion calculations are based on a Monte Carlo depletion methodology. Both the MCNP and ORIGEN2.2 computer codes are used in the depletion methodology. The depletion calculations for the 6+6-column core configuration used 1/12-core MCNP models and depleted 2 half-fuel blocks at each of the 8 levels or 1680 full-length fuel rods. The 1/12-core MCNP models are assumed to be un-rodded.

Results will be presented for just the 6+6-column core configuration. The first set of results in the form of k-effective versus burnup, or reactivity letdown versus number of effective full power days (EFPDs) of reactor operation, will be for the 6+6-column core with 8-block high fuel columns. Parametric variables include PF and total core power. The depletion analysis assumes the core to be un-rodded with no burnable poisons.

Figure C-16 shows five reactivity letdown curves for the 6+6-column, 8-block high core for PFs of 15%, 25%, and 35% and total core powers of 150, 200, and 260 MW. At 200 MW, cycle lengths of 110, 210, and 280 EFPDs can be achieved for PFs = 15, 25, and 35%, respectively. Basically, increasing the PF will increase the cycle length. Also shown in this figure is the effect of total core power versus EFPDs. Three letdown curves for fixed PF=15% show the decrease in cycle length with increasing power. Cycle lengths of 148, 110, and 84 EFPDs were calculated for 150, 200, and 260 MW, respectively.

Figure C-17 shows results from detailed depletion calculations for the 6+6-column core, but with 4-block high fuel columns as a function of PF. Total core power is 100 MW. Again cycle lengths increase with increasing PF. For PFs of 15, 25, 35, and 45%, cycle lengths of 92, 182, 252, and 300 EFPDs can be achieved. At PF=15%, the 100 MW and 4-block core meets the >90-day cycle length, maximizes the irradiation fluxes, and has half the fuel blocks in the core relative to the 8-block high core. The only problem with this 6+6-column, 4-block high core design was the TRISO fuel temperature exceeded 1250°C under normal steady-state conditions. Otherwise this core would have been selected as the final design. In the next phase, or conceptual phase, a smaller core height of 5- or 6-block high fuel columns will be an interesting option to consider.
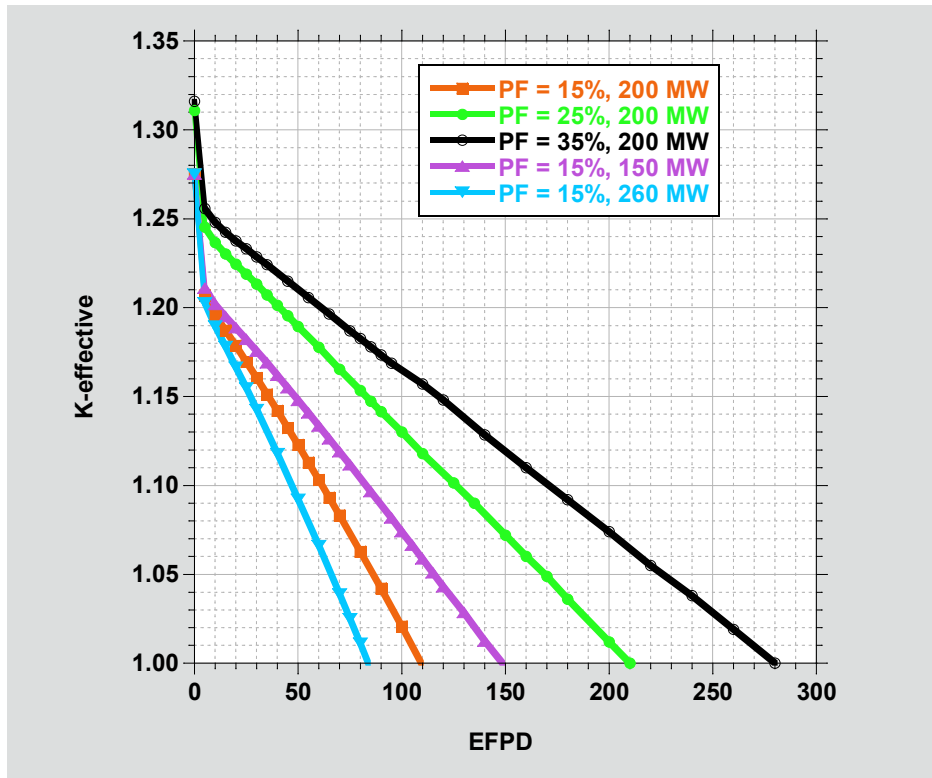
Figure C-16. Reactivity letdown versus burnup (EFPD) and PF and total core power for the 6+6-column core with 8-block high fuel columns.
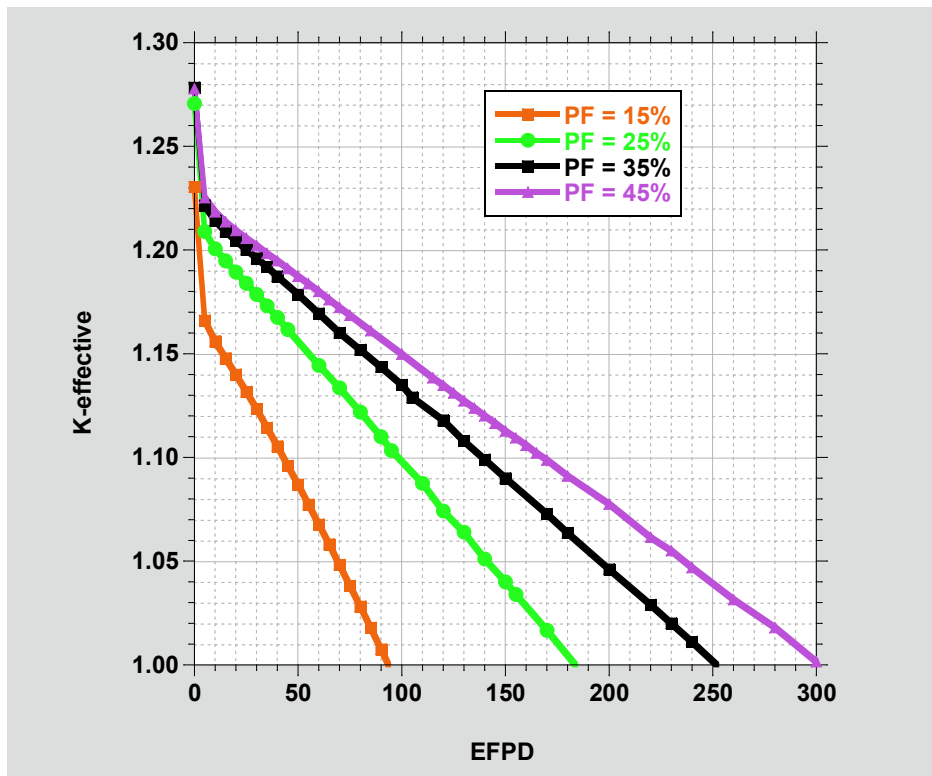


Figure C-17. Reactivity letdown versus burnup (EFPD) and PF for the 6+6-column core with 4-block high fuel columns.
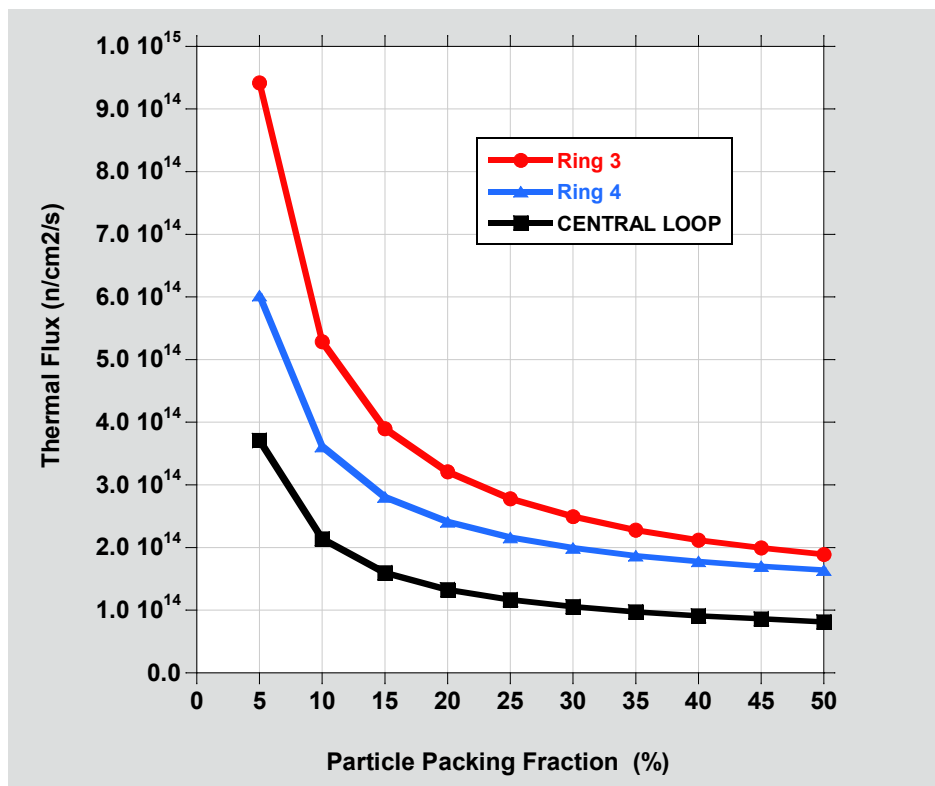
Figure C-18. Maximum thermal neutron flux versus PF for the 6+6-column core at 200 MW.

## Thermal Neutron Flux versus Packing Fraction

Previous physics parametric studies have indicated that reducing the TRISO particle PF in the fuel compact increases the thermal and fast irradiation fluxes. For the 200 MW, 6+6-column core configuration with 8-block high fuel columns and carbon flow tubes in the outer reflector, Figure C-18 shows the thermal neutron flux as a function of PF at three locations in the core. The thermal flux increases substantially for PF<15%. Unfortunately, core criticality (k-effective) falls rapidly for PF<10%, plus the cycle length decreases with decreasing PF, limiting the minimum PF to around 15%. One interesting feature of these curves is the thermal flux does not decrease substantially with increasing PF above 15%. This implies that the overall core PF could be increased, resulting in a significant increase in fuel cycle length, while accepting a proportionately smaller decrease in the available thermal neutron flux intensity. For example, if the current PF=15% were increased to 25% or 35%, the thermal neutron flux in Ring 3 would decrease from approximately 3.9E+14 n/cm$^2$/s to 2.8E+14 and 2.3E+14 n/cm$^2$/s, respectively, or by factors of 1.39 and 1.70. The fuel cycle length however would correspondingly increase from 110 to 210 and 280 days, respectively, or by factors of 1.91 and 2.55. So, if an increased cycle length beyond the maximum 90-day goal became important, the HTGTR could easily achieve a higher cycle length with minimal reduction in irradiation flux intensity.

## Control Rod Worth

Preliminary control rod studies have been performed on the final 6+6-column core configuration with 8-block high fuel columns and PF=15%. The control rod studies used a rudimentary control rod design and focused primarily on the determination of how many control rods were needed to shut down the reactor and their placement in the outer graphite reflector. Control rods were not placed in the inner reflector in order to prevent top head crowding. Control rods were also not placed inside fuel block columns, because under accident conditions, temperatures might exceed metallic structural integrity limits. Therefore, placement of control rods was limited to the outer reflector, and specifically to the outer

146

reflector blocks bordering the outermost ring of fuel blocks (Rings 3 and 4), where both the thermal neutron flux and control rod worth would be at a maximum. The preliminary control rod design assumes a metallic sheath (alloy 800H) containing 100% enriched boron carbide.

Figure C-19 shows the 6+6-column core configuration with 15 control rods in the outer reflector (yellow circles). Three high-worth control rods are in Ring 3, and twelve control rods are located in Ring 4. The twelve rods in Ring 4 are labelled either CR4.1 or CR4.2, six of each, in order to differentiate the two groups of control rods by worth and azimuthal location relative to their proximity to either a Ring 3 control rod (CR3), or a Ring 3 irradiation test facility in a corresponding position.
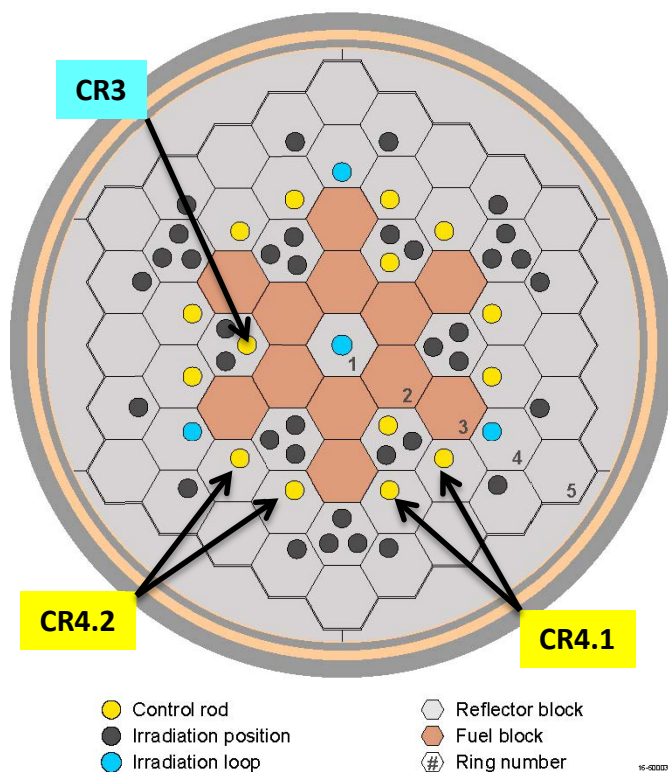


Figure C-19. Control rod arrangement in the 6+6-column core configuration showing all 15 control rods.

In the MCNP full core models, the control rods were assumed to extend from the top of the top reflector to the bottom of the active core. Although the boron carbide ($B_4C$) was assumed to be 100% enriched in $^{10}B$, lower $^{10}B$ enrichments would have been acceptable as well with only small differences in worth predictions.

Figure C-20 shows k-effective versus $^{10}B$ enrichment in the $B_4C$ control rod material for the 6+6-column core configuration with 14 of the 15 control rods fully inserted (one high-worth Ring 3 control rod is withdrawn). There is essentially no additional negative reactivity gain for $^{10}B$ enrichments above 60%. From 19.9% (natural) to 60%, only a -$1.7 of negative reactivity is gained. In the concept design phase, it should be possible to design control rods with much lower concentrations of $^{10}B$, especially in conjunction with the placement of burnable poisons throughout the core.

The calculated worth of the 15 control rods fully inserted into a fresh, beginning-of-cycle (BOC) core was calculated to be approximately -$50.2. The BOC core is quite reactive with essentially no parasitic structures in the outer reflector, and only the central loop facility in Ring 1. In the MCNP models for the control rod study, the assumption was made to use graphite (carbon) flow tubes in all of the outer reflector irradiation positions and no burnable poisons. This condition resulted in maximum core excess reactivity and therefore a maximum number of required control rods to shut down the core. In the concept

design phase, the addition of outer reflector loops and flow tubes, plus the strategic placement of burnable poisons in certain fuel block corners to reduce fuel rod power-peaking will significantly reduce the beginning-of-cycle core excess reactivity and hence the control rod worth requirement.
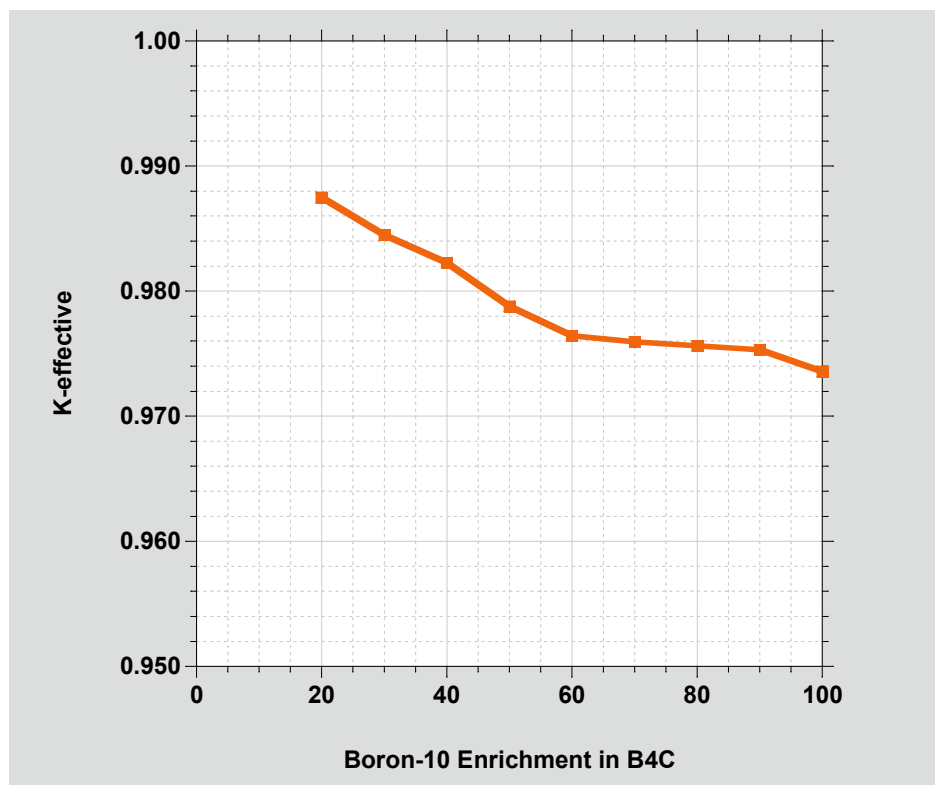


Figure C-20. Core k-effective versus [10]B enrichment.

Table C-20 gives calculated parametric results for number and type of control rods inserted, the corresponding core k-effective, the combined worth of the control rods fully inserted under cold shutdown conditions (most reactive).

The cold, BOC, un-rodded core has an excess reactivity of approximately +$35.0. The hot, BOC, un-rodded core has an excess reactivity of approximately +$29.6. The combined worth of all 15 control rods is approximately -$50.2 which implies not all 15 rods are required for cold shutdown. In fact, only two of the three Ring 3 control rods and 9-10 of the Ring 4 control rods are required to achieve cold shutdown.

Single rod worths are also given for the three differentiated control rods (CR3, CR4.1, and CR4.2).

In addition, a parametric study was performed for a variety of different control materials to see if there was a more effective control rod material than $B_4C$. The study considered gadolinia ($Gd_2O_3$), natural gadolinium metal, natural hafnium metal, silver-indium-cadmium (Ag-In-Cd), and samaria ($Sm_2O_3$). Enriched boron carbide was the best of the control rod materials considered in the study.

## Temperature Coefficients of Reactivity

Isothermal, fuel, and moderator temperature coefficients of reactivity were calculated for the 6+6-column core. Figure C-21 shows the three coefficients as a function of temperature. All three are strongly negative. The isothermal coefficient is essentially the sum of the fuel (Doppler) and moderator (graphite temperature). Table C-21 gives the coefficient magnitudes and applicable temperature range. The helium coolant void coefficient is negligibly small, but negative.

Table C-20. Control rod worth results for cold shutdown conditions.

| Rods Inserted | | | | Reactivity* |
| CR3 | CR4.1 | CR4.2 | k-effective | ($) |
| --- | --- | --- | --- | --- |
| 0 | 0 | 0 | 1.34296 | ---- |
| | | | | |
| 3 | 6 | 6 | 0.90031 | -50.15 |
| 3 | 5 | 6 | 0.91001 | -48.53 |
| 3 | 6 | 5 | 0.91765 | -47.28 |
| 3 | 6 | 1 | 0.99384 | -35.83 |
| 3 | 0 | 5 | 0.98186 | -37.51 |
| 3 | 1 | 4 | 0.99085 | -36.25 |
| | | | | |
| 2 | 6 | 6 | 0.97357 | -38.70 |
| 2 | 5 | 6 | 0.98042 | -37.72 |
| 2 | 6 | 5 | 0.98953 | -36.43 |
| 2 | 6 | 4 | 0.99583 | -35.56 |
| 2 | 3 | 6 | 0.99445 | -35.75 |
| | | | | |
| 1 | 0 | 0 | 1.248869 | -7.69 |
| 0 | 1 | 0 | 1.322029 | -1.62 |
| 0 | 0 | 1 | 1.306258 | -2.87 |
| *Beta-effective = 0.0073* | | | | |

Table C-21. Temperature coefficients of reactivity.

| Temperature Coefficients of Reactivity | Magnitude and Range (pcm/°C) | Temperature Range (°C) |
| --- | --- | --- |
| Isothermal | −9.7 to −8.0 | 20 to 1400 |
| Fuel | −4.9 to −2.4 | 20 to 2500 |
| Moderator | −3.2 to −5.2 | 20 to 1800 |

## TRISO Fuel Burnup and Neutron Fast Fluence

TRISO fuel burnup is only presented for the final HTGTR 6+6-column core configuration with 8-block fuel columns, 200 MW, PF=15%, and a cycle length of 110 days. Burnups for other core configurations can be estimated by appropriately scaling the burnup results (%FIMA) here to the total core power and number of fuel columns in the core.

Table C-22 gives the minimum, average, and maximum fuel compact burnup in percent of fissions of initial heavy metal atoms (%FIMA) and the maximum fast fluence for the HTGTR along with comparative burnup and fluence values from the TRISO particle tests AGR-2 and AGR-5/6/7. All data are calculated results. The AGR-2 experiment was irradiated in the Advanced Test Reactor for 12 cycles. The AGR-5/6/7 experiment has not been built yet, but is projected to be irradiated for 12 or 13 cycles in ATR. The AGR-2, AGR-5/6/7, and the HTGTR TRISO particles are all similar with a nominal 425 μm diameter uranium oxycarbide kernel, coatings of the same materials and nominal thicknesses, and enrichments of 15.5 wt% [235]U, although AGR-2 had an enrichment of 14%. Compact particle PFs are,
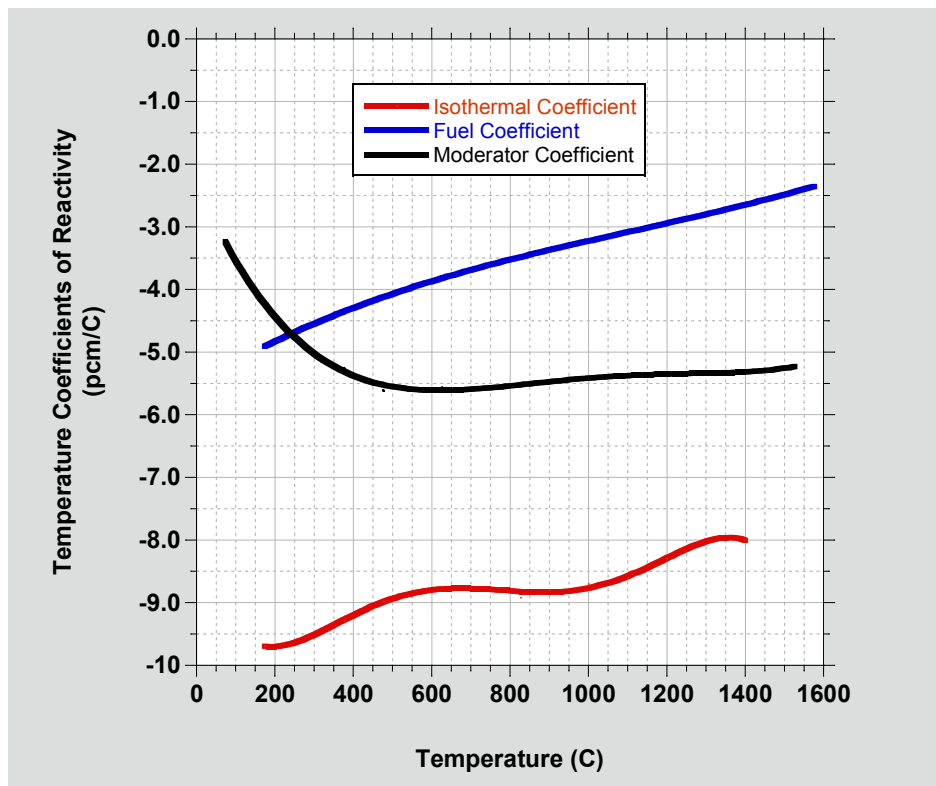
Figure C-21. Isothermal, fuel, and moderator coefficients of reactivity for the 6+6-column core.

however, different. The HTGTR uses a PF=15%, whereas AGR-2 had a PF=36%, and AGR-5/6/7 is projected to use compacts with PFs of both 25% and 35%.

Table C-22 data shows that the HTGTR fuel burnup ranges from 4.62 to 9.56% FIMA with an average burnup of 7.36% FIMA. These burnups are not excessive and are quite comparable to the AGR-2 burnups and slightly less. The AGR-5/6/7 TRISO particle tests are aiming for much higher maximum burnups as part of the margin test which was designed to push the TRISO particle performance to projected limits. The HTGTR maximum fuel rod burnup (9.56% FIMA) occurred in a corner fuel rod at the outer core-reflector interface in level 5 (fuel block just above the core midplane).

The maximum fast neutron fluence ($E_n$>0.1 MeV) for the HTGTR was calculated to be 1.72E+21 n/cm$^2$. Again this fluence is comparable to the AGR-2 experiment maximum of 2.53E+21 n/cm$^2$, but slightly less. The maximum fluence for the AGR-5/6/7 test is projected to be substantially larger at 7.35E+21 n/cm$^2$. Again, the AGR-5/6/7 maximum fluence is part of the margin test program.

Table C-22. Fuel compact burnup (%FIMA) for the 6+6-column core.

| Reactor/ Experiment | Burnup (%FIMA) | | | Fast Fluence (n/cm$^2$) |
|---|---|---|---|---|
| | Minimum | Average | Maximum | Maximum |
| HTGTR | 4.62 | 7.36 | 9.56 | 1.72E+21 |
| AGR-2 | 4.90 | 8.18 | 10.30 | 2.53E+21 |
| AGR-5/6/7 | 8.01 | 9.56 | 18.60 | 7.35E+21 |

The TRISO particle and fuel compact burnups are reasonable and within the bounds of recent TRISO particle experiments from the AGR tests. The same is true for the particle fast fluence exposure. The burnups are for a once-through or single-batch mode of operation for the HTGTR.

# Thermal-Hydraulics Analyses

RELAP5-3D was used to perform the thermal-hydraulic calculations. The input model was similar to that used for the final calculations, with changes reflecting the different fuel block arrangements. Sensitivity calculations addressed the impacts of different parameters on the steady-state operating conditions, and design-basis conduction cooldown transients were simulated.

## Steady-State Simulations

Calculations have been performed to determine the steady state conditions in the reactor vessel. Scoping sensitivity calculations were performed to address different irradiation loop sizes and contents. Sensitivity calculations were also performed to investigate the flow in the gaps between the blocks and the effects of reflector heating.

### *Scoping Sensitivity Studies*

These simulations were performed using a simple core model with only fuel and reflector blocks, with no control rod or irradiation holes in the outer reflector. These calculations addressed the effect of different diameter fuel rods and the size of the irradiation loop in the center of the core and the gas gap around it. In all of the calculations, the core power was 100 MW with flat axial and radial power profiles. The gap between blocks was 1.0 mm. The coolant inlet and outlet temperatures were 350°C and 750°C, respectively.

The first parameter varied was the fuel rod diameter. Diameters of 11.0, 11.5, 12.0, and 12.5 mm were modeled. The fuel rod holes in the core blocks had a constant diameter of 12.7 mm.

The fuel temperatures in the two rings of fuel were within a few degrees of each other. Table C-23 presents the axial fuel temperatures in the inner fueled ring for the four cases. The fuel temperatures decreased as the diameter increased because there was more fuel volume available for the same amount of power. The effect on the reflector temperatures was small, indicating that nearly all of the power is being removed by convection in the coolant channels, with only a small portion being radiated to the reflectors.

The size of the hole in the center of the central reflector block was varied next. For these calculations, a steel tube was assumed to be in close contact with the graphite reflector. The tube contained either water at typical pressurized water reactor conditions (15 MPa, 327°C) or molten salt (FLiBe) at 0.20 MPa and 547°C. Table C-24 presents the results of these calculations; the basis for comparison was a solid graphite block.

Table C-23. Inner core ring fuel rod average temperatures from the fuel diameter sensitivity calculations.

| Core block | D = 11.0 mm | D = 11.5 mm | D = 12.0 mm | D = 12.5 mm |
|:---:|:---:|:---:|:---:|:---:|
| 8 | 759°C | 715°C | 669°C | 648°C |
| 7 | 793°C | 750°C | 704°C | 678°C |
| 6 | 834°C | 794°C | 750°C | 720°C |
| 5 | 877°C | 839°C | 798°C | 765°C |
| 4 | 920°C | 885°C | 846°C | 810°C |
| 3 | 963°C | 930°C | 893°C | 850°C |
| 2 | 1005°C | 973°C | 935°C | 883°C |
| 1 | 1036°C | 1004°C | 964°C | 903°C |

Table C-24. Center irradiation hole size sensitivity calculation results.

| Nominal Tube Size (in.) | Test Loop Fluid | Center Reflector T$_{ave}$ (°C) | Change from Solid (°C) |
|---|---|---|---|
| None | None | 645 | 0 |
| 3 | Water | 473 | -173 |
| 4 | Water | 458 | -187 |
| 3 | Molten salt | 594 | -51 |
| 4 | Molten salt | 589 | -56 |

The results showed that flow through the test loop reduced the average temperature of the central reflector graphite, with a water loop causing a significant reduction. The temperature reduction is less with the molten salt because a higher loop temperature is needed to keep the salt molten. While the larger hole resulted in lower temperatures in the graphite, because there is less graphite to heat, the temperature difference is not considered significant.

The large reduction in temperature with a water loop may be a concern from the graphite standpoint, but it should be noted that there was no gap between the piping and the graphite block; a gap would be expected to be present in the reactor. Therefore, calculations were performed with different size gaps between the tube and the graphite. The gap contained helium flowing in parallel with the rest of the primary coolant flowing down through the core. Radiation was modeled between the flow tube and the graphite. Since the water loop had a greater impact, it was used as the base case.

Table C-25 shows the results of these calculations. The average graphite temperature increased significantly with the gap modeled, with the presence of the gap being more significant than its size.

Table C-25. Sensitivity on gap size around a water-filled center irradiation tube.

| Nominal Tube Size (in.) | Gap around Tube (mm) | Center Reflector T$_{ave}$ (°C) | Change from No Gap (°C) |
|---|---|---|---|
| 3 | 0.0 | 473 | 0 |
| 3 | 2.54 | 572 | 99 |
| 3 | 5.08 | 589 | 117 |
| 3 | 12.7 | 595 | 123 |
| 3 | 25.4 | 602 | 129 |
| 4 | 0.0 | 458 | 0 |
| 4 | 2.54 | 561 | 103 |
| 4 | 5.08 | 580 | 122 |
| 4 | 12.7 | 603 | 145 |
| 4 | 25.4 | 608 | 150 |

After these calculations were completed, it was noted that there is no Schedule 160 4-in. (10.2 cm) outside diameter piping; it was assumed that this piping grade will be used to accommodate high-pressure water. Subsequent analyses assumed a water-filled 4.5-in. (11.4 cm) outside diameter flow tube with a 2.54-mm. gap around it.

### Steady State

Steady-state calculations were performed using the baseline input model. Two basic calculations were performed, one with and one without direct heating of the reflectors. These calculations assumed a 1-mm gap existed between all of the core and reflector blocks, a 2.54-mm gap around the 11.43-cm diameter center irradiation loop, and a 6.35-mm gap around the 8.89-cm diameter control rods or irradiation tubes in the side reflector. The center irradiation loop contains water at 15.0 MPa and 327°C, with a velocity of

5.0 m/s that makes the water essentially isothermal over the core height. The results of the steady-state calculations are summarized in Table C-26. Axial average temperatures in the table are over the height of the fueled length.

Table C-26. Steady-state conditions.

| | 18 Columns | | | |
| | No Reflector Heating | With Reflector Heating | 12 Columns | 6 Columns |
| Parameter | | | | |
|---|---|---|---|---|
| Total power (MW) | 100 | 100 | 100 | 100 |
| Power in fuel (MW) | 100 | 98.2 | 97.4 | 98.3 |
| Coolant inlet temperature (°C) | 350 | 350 | 350 | 350 |
| Coolant outlet temperature (°C) | 750 | 750 | 750 | 750 |
| Primary coolant flow rate (kg/s) | 47.9 | 47.8 | 47.8 | 47.8 |
| Peak fuel temperature (°C) | 1048 | 1039 | 1166 | 1521 |
| Axial average temperature (°C) | | | | |
|   Central reflector | 393 | 490 | 489 | 483 |
|   Ring 2 graphite | 775 | 770 | 640 | 1040 |
|   Ring 2 fuel | 877 | 871 | -- | 1277 |
|   Ring 3 graphite | 775 | 769 | 838 | 384/372[a] |
|   Ring 3 fuel | 877 | 870 | 978 | -- |
|   Ring 4 graphite | 364/353[a] | 382/378[a] | 463/385 | 383 |
|   Ring 5 graphite | 351 | 368 | 364 | 361 |
|   Permanent side reflector | 351 | 361 | 361 | 356 |
|   Core barrel | 352 | 355 | 355 | 353 |
|   Reactor vessel | 340 | 341 | 341 | 340 |
| RCCS heat removal (MW) | 0.51 | 0.51 | 0.51 | 0.51 |
| RCCS inlet temperature (°C) | 27 | 27 | 27 | 27 |
| RCCS flow rate (kg/s) | 125 | 125 | 125 | 125 |
| Reactor cavity air temperature (°C) | 111.5 | 111.5 | 111.5 | 111.4 |

a. Split ring showing temperatures of the inner/outer half

A little less than 2% of the total power is deposited directly in the reflectors in this simulation; it should be noted that there was no iteration between the physics and thermal-hydraulics to address how the changes in reflector temperatures would affect the neutron and gamma heating. The largest effect of the reflector heating was seen in the central reflector, whose temperature increased by nearly 100°C. Much smaller increases were calculated for the outer reflector rings. The peak and average fuel temperatures decreased less than 10°C.

### Sensitivity Analyses

Several sensitivity studies were performed using the 18-column core input model. They addressed core bypass flow and gap crossflow.

The size of the gap between blocks in the core will likely vary over time, as the graphite blocks shrink and expand as they are irradiated at elevated temperatures. The first set of calculations examined gap widths of 1.0, 1.5, 2.0, 2.5, and 3.0 mm.

The effect of these gaps on the core bypass flow and the peak fuel temperature are shown in Table C-27. The bypass flow is defined as all coolant flow not passing through the coolant channels in the fuel blocks. While the peak fuel temperature increased as the bypass flow increased, because less coolant was flowing through the fuel block coolant channels, the increase was not very large.

Table C-27. Block-to-block gap width sensitivity study results.

| Gap Width (mm) | Bypass Flow (%) | | | | Peak Fuel Temperature (°C) |
| | Block-to-Block gaps | Tube and Control Rod Gaps | PSR-to-Core Barrel | Total | |
|---|---|---|---|---|---|
| 1.0 | 3.2 | 8.0 | 4.6 | 15.9 | 995 |
| 1.5 | 5.2 | 7.9 | 4.6 | 17.7 | 1000 |
| 2.0 | 8.0 | 7.7 | 4.4 | 20.1 | 1012 |
| 2.5 | 11.3 | 7.5 | 4.3 | 23.1 | 1024 |
| 3.0 | 14.9 | 7.2 | 4.1 | 26.3 | 1039 |

One deficiency noted in the steady-state results is the temperature difference between the gap flow channels around the fueled region. The modeling approach does not present a good method for attaching the gaps to both the fueled blocks and the adjacent ring of reflector blocks, which results in temperatures that are likely too hot in the core gap and too cold in the nearest reflector gaps. To try to increase the gap temperatures, crossflow connections were made at each axial level between the fuel region gap channel and the gap channels in the central reflector and the first ring of the side reflector. The first calculation modeled the crossflow area based on a 3-mm gap between each of the blocks in the fuel rings. The second calculation increased this area by a factor of ten. The results of these steady-state calculations are presented in Table C-28, where it is seen that the increase in the reflector gap outlet temperatures was not very large and increasing the crossflow area had no effect.

Table C-28. Effect of crossflow on gap outlet temperature (°C).

| Coolant gap | Without Crossflow | With Smaller Crossflow | With Larger Crossflow |
|---|---|---|---|
| Central reflector-to-Ring 2 | 598 | 599 | 599 |
| Ring 2-to-Ring 3 | 860 | 862 | 862 |
| Ring 3-to-Ring 4 | 470 | 482 | 482 |
| Ring 4-to-Ring 5 | 379 | 382 | 382 |
| Ring 5-to-PSR | 368 | 369 | 369 |
| PSR-to-core barrel | 369 | 369 | 369 |

## Transient Simulations

Two simulations of a depressurized conduction cooldown (DCC) transient were performed to investigate the response of the system during a design-basis accident. Both calculations imposed a 5-s blowdown on the system. In Case 1, only the outlet plenum was open to atmospheric pressure, and a 5-s flow coastdown was imposed at the reactor vessel inlet. In Case 2, both the vessel inlet and outlet were open to atmospheric pressure, so that once-through flow through the core could occur. As will be seen in the figures, there was essentially no difference between the two cases. The transient simulations covered 7 days.

Figure C-22 presents the peak fuel temperatures in the two fueled rings for both transient simulations. The temperatures dropped quickly at the beginning of the transient, as heat was redistributed from the bottom of the core toward the top; this is shown in Figure C-23 for the inner core ring graphite. As the
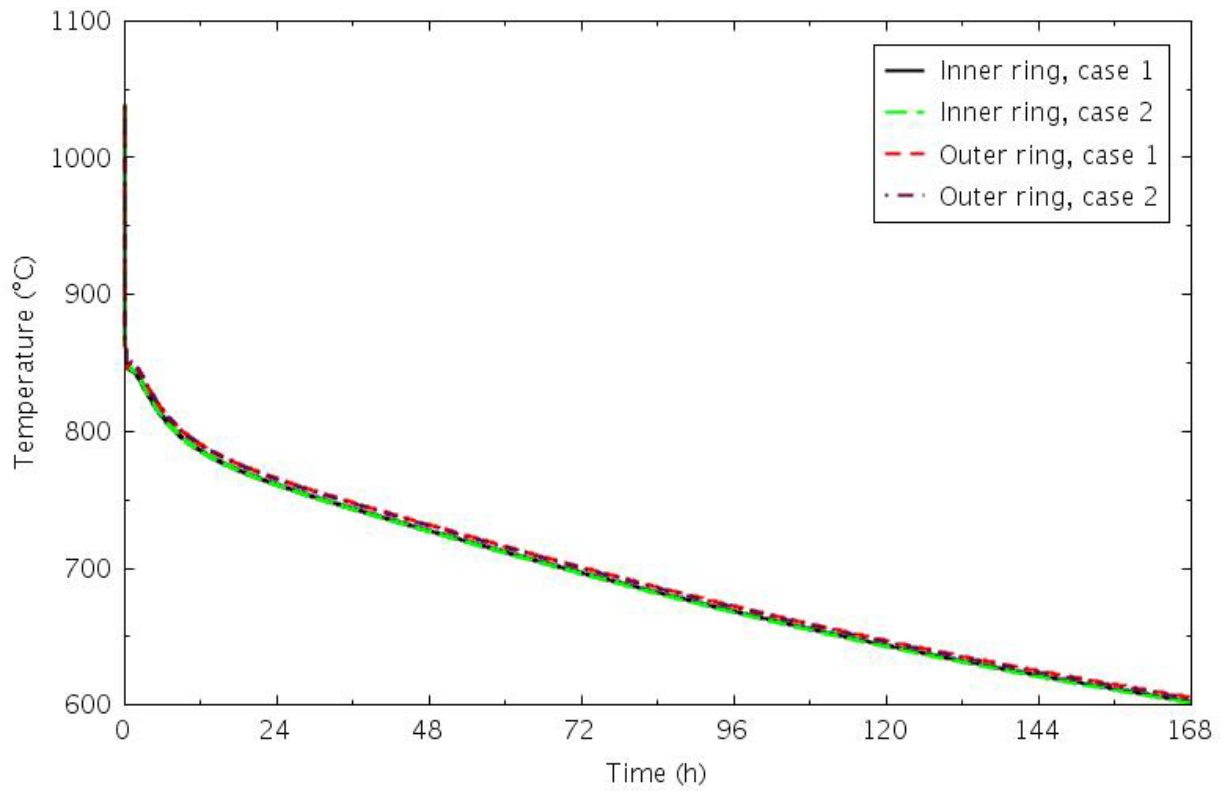
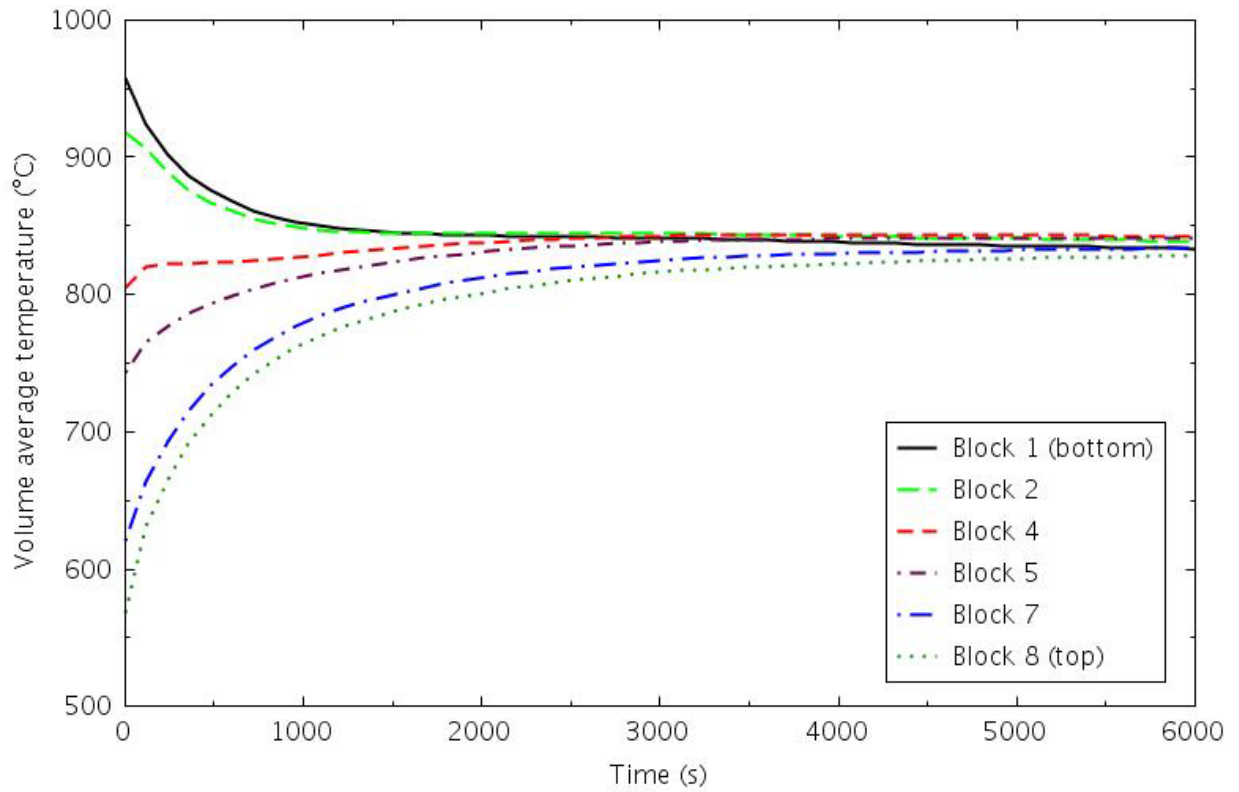Figure C-22. Peak fuel temperatures for the DCC transients.



Figure C-23. Axial temperature distribution in the inner fuel ring graphite for DCC transient Case 1.

transient progressed, the peak fuel temperatures decreased continuously. Axial average fuel temperatures are presented in Figure C-24. After the initial decrease following scram, a modest increase in temperature occurs, although the maximum temperatures are well below the steady-state values.

Figures C-25 through C-27 show the radial temperature distribution across the reactor vessel heat structures. These temperatures are axial averages over the fueled length of the core. The central reflector and fuel ring temperatures peaked very early in the transient, and the peaks occurred progressively later moving radially outward from the center of the vessel, with the reactor vessel reaching its maximum temperature after about two days.

The power generated in the core and heat removed by the RCCS are shown in Figure C-28. The powers were fairly well matched after about four days. Figure C-29 presents the coolant temperature at the outlet of the RCCS. The small temperature change over the course of the transient indicates that there was more than enough flow in the RCCS to remove the heat reaching the surface of the cooling panels.

The temperature in the reactor cavity is presented in Figure C-30. No ventilation of the cavity was included in the model, so the steady-state value is higher than would be expected in an operating facility.

Overall, the transient simulations showed a very coolable reactor. The heat from the fuel rings was quickly redistributed axially, then effectively removed radially. Peak fuel temperatures during the transient were lower than during steady-state operation.
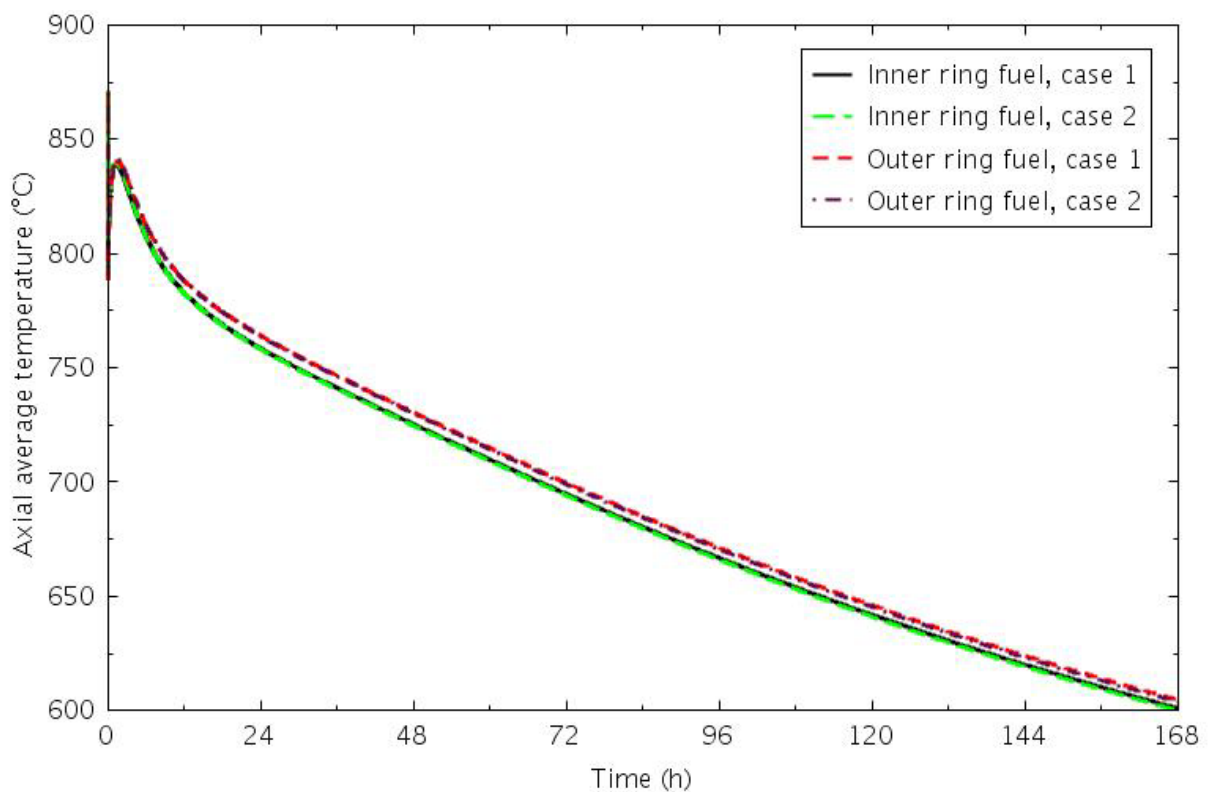


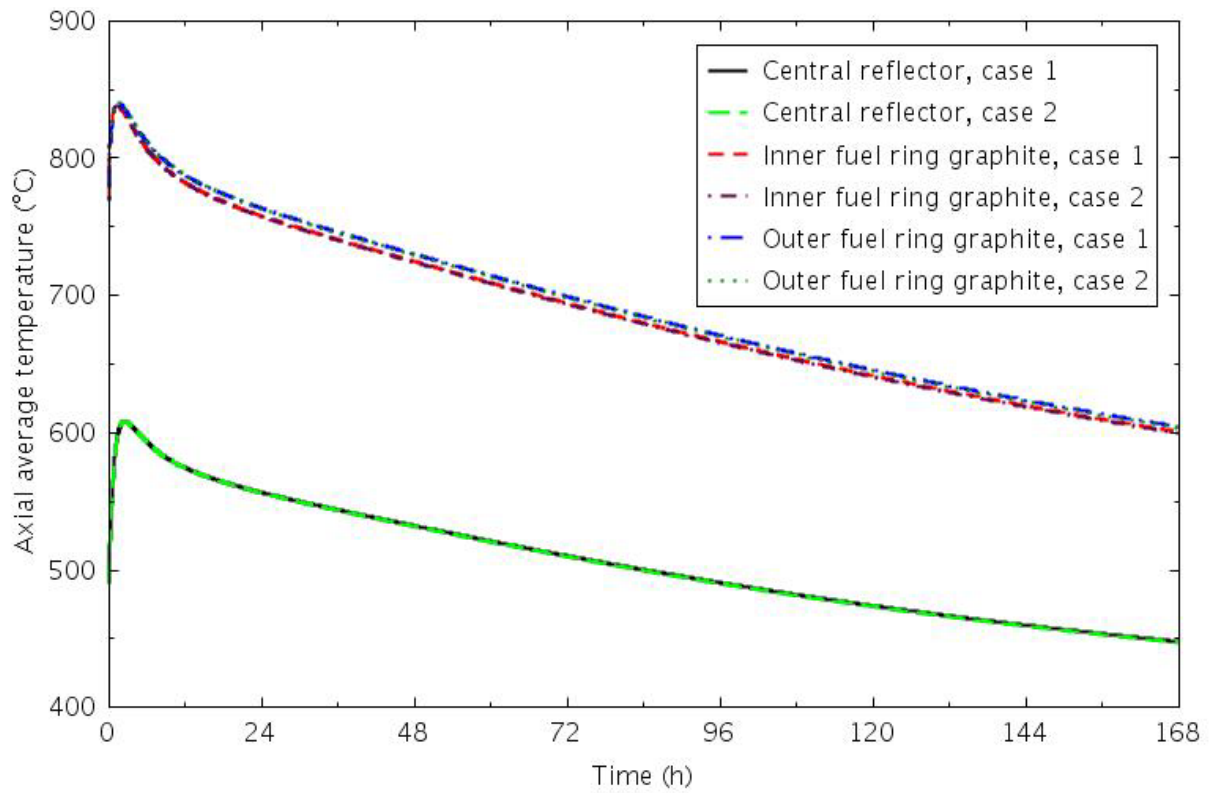Figure C-24. Average fuel temperatures for the DCC transients.

Figure C-25. Temperatures in the central reflector and fuel ring graphite for the DCC transients.
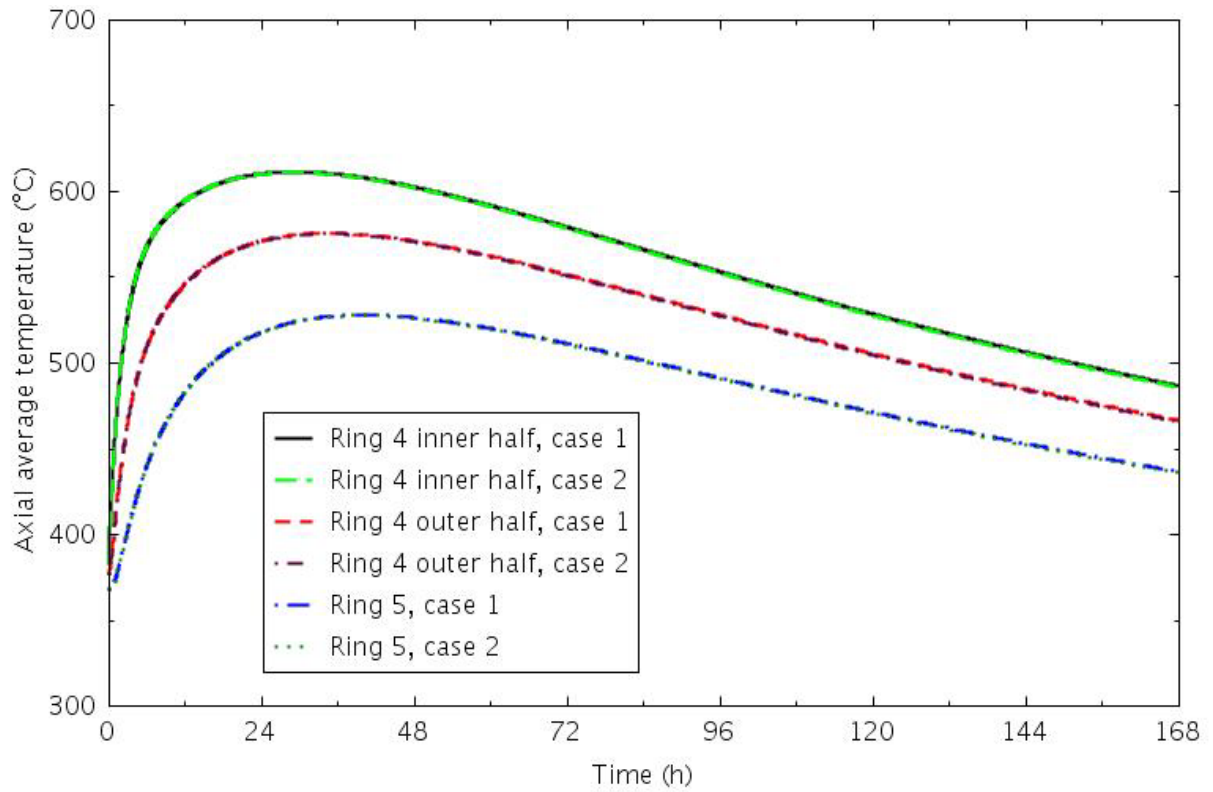


Figure C-26. Temperatures in the outer reflector for the DCC transients.
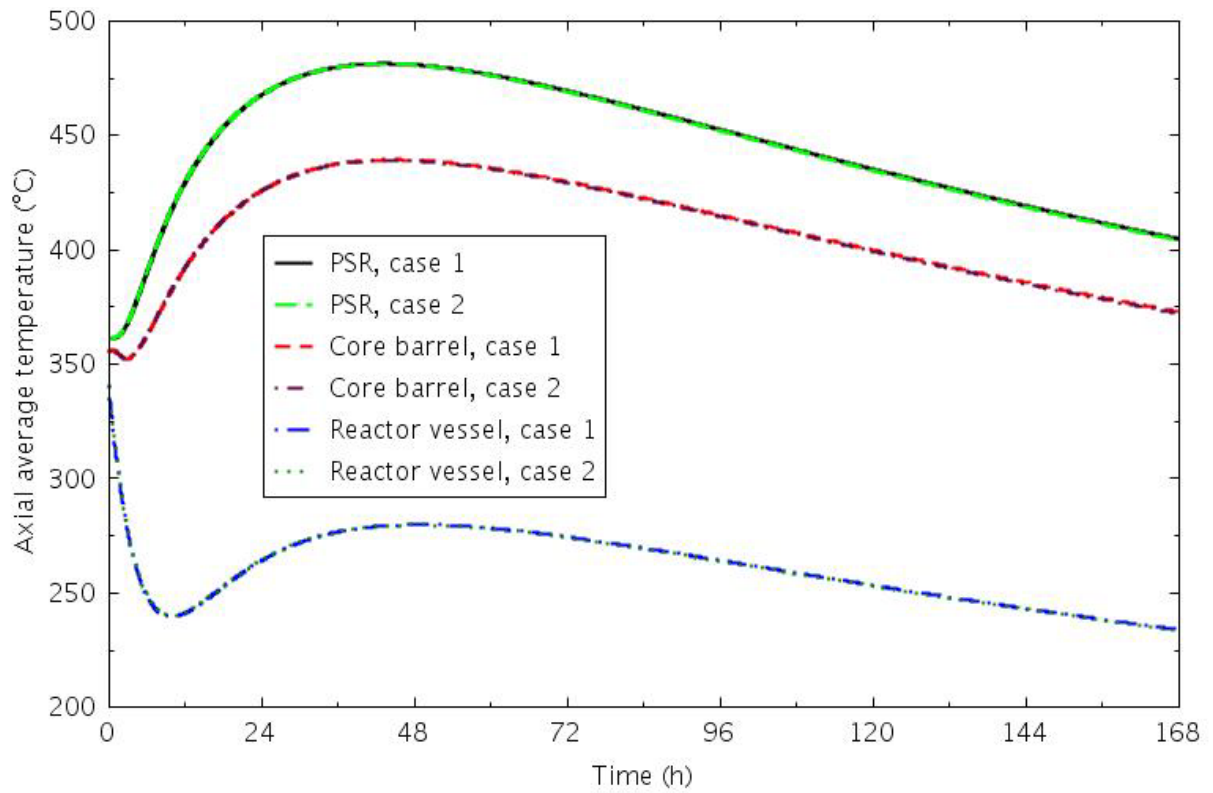
Figure C-27. Temperatures in the PSR, core barrel, and reactor vessel for the DCC transients.
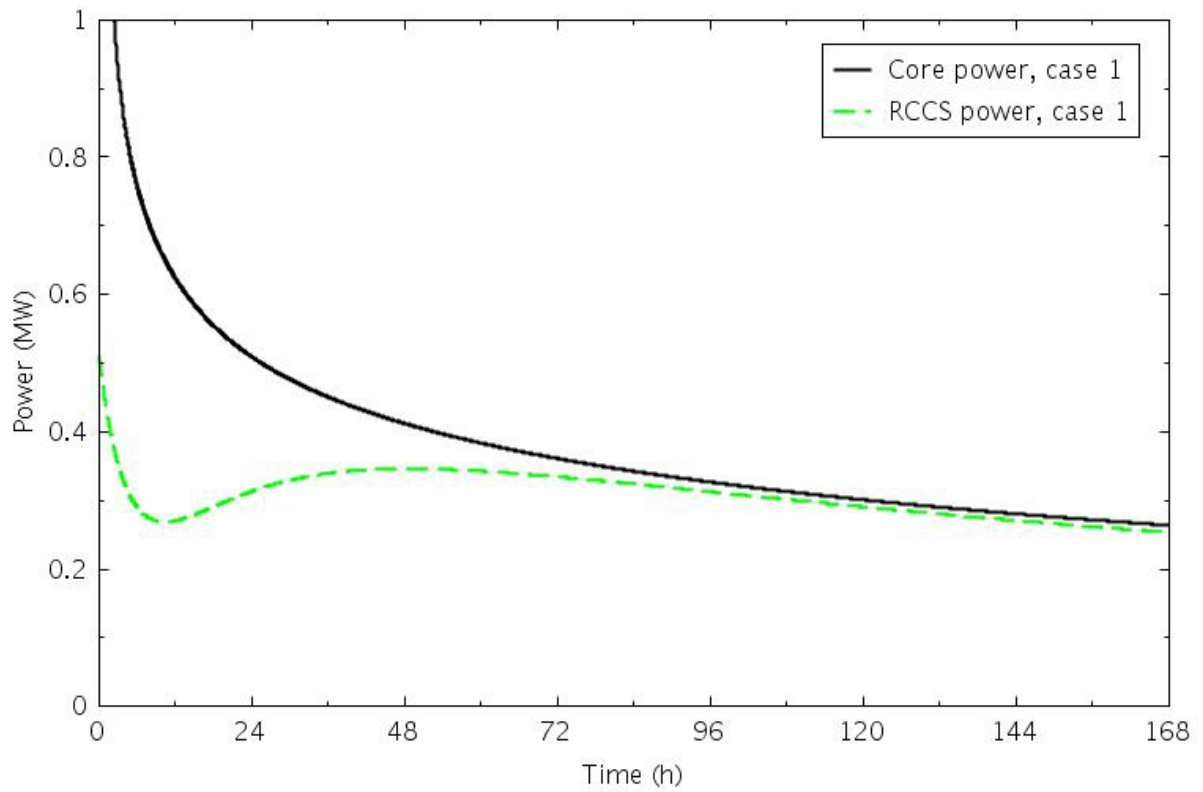


Figure C-28. Core heat generation and RCCS heat removal for the DCC transients.
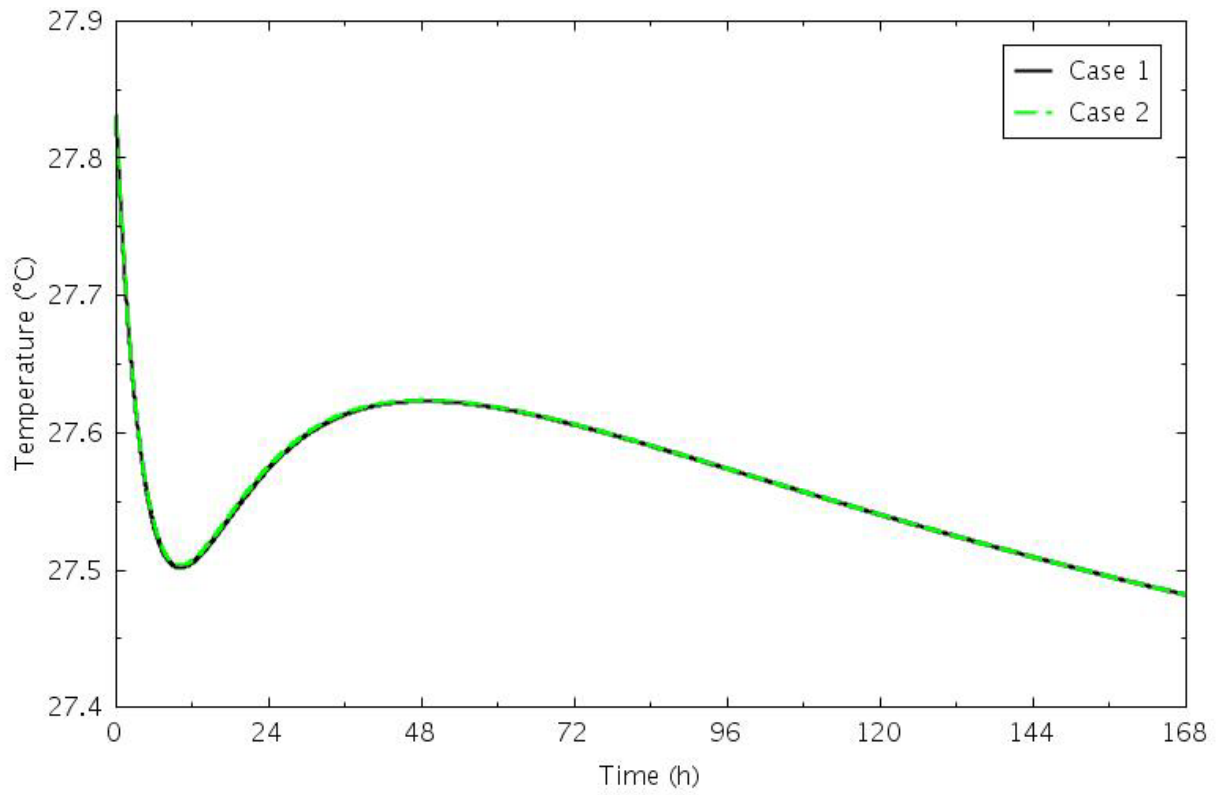
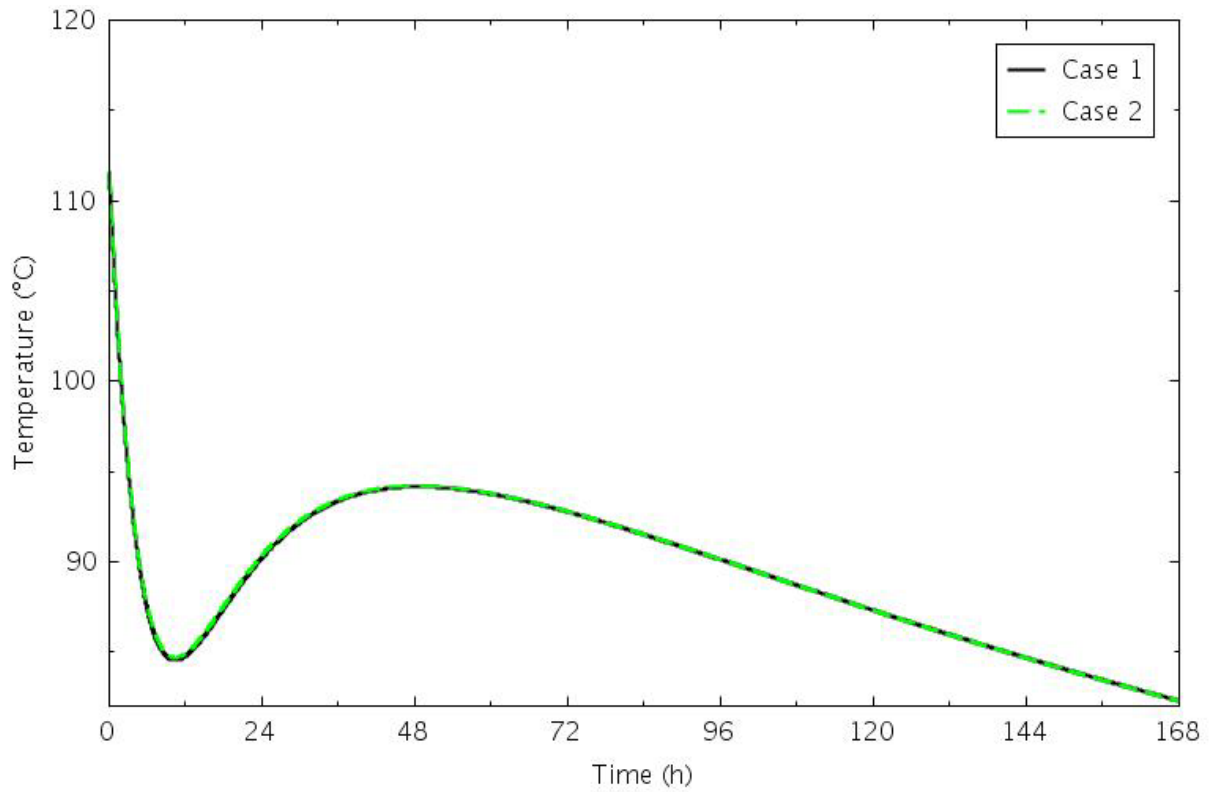Figure C-29. RCCS coolant outlet temperature for the DCC transients.



Figure C-30. Reactor cavity gas temperature for the DCC transients.

159